INVESTIGATION OF TERNARY LAYERED THIN FILM MATERIALS

By

MELLIE LEMON

A DISSERTATION

Presented to the Department of Chemistry and Biochemistry and the Division of Graduate Studies of the University of Oregon
in partial fulfillment of the requirements for the degree of
Doctor of Philosophy

June 2023

DISSERTATION APPROVAL PAGE

Student: Mellie Lemon

Title: Investigation of Ternary Layered Thin Film Materials

This dissertation has been accepted and approved in partial fulfillment of the requirements for the Doctor of Philosophy degree in the Department of Chemistry and Biochemistry by:

Shannon Boettcher	Chairperson
David C. Johnson	Advisor
Amanda Cook	Core Member
Benjamin J. McMorran	Institutional Representative

and

Krista Chronister	Vice Provost for Graduate Students

Original approval signatures are on file with the University of Oregon Division of Graduate Studies.

Degree awarded June 2023

DISSERTATION ABSTRACT

Mellie Lemon

Doctor of Philosophy

Department of Chemistry and Biochemistry

June 2023

Title: Investigation of Ternary Layered Thin Film Materials

This dissertation focuses on the use of the modulated elemental reactants synthesis method to target previously unknown, metastable compounds. The nucleation and growth of the compounds discovered were monitored via x-ray characterization techniques, leading to insights on the reaction pathways and parameters for trapping kinetic products. The insights about the growth technique contribute to the goal of materials discovery by design. The exploration of the physics behind Laue oscillations and the incorporation of Laue oscillation fitting into GSAS-II is an advance in x-ray characterization techniques, and enabled a deeper, fundamental understanding of the growth of layered compounds.

This thesis begins with background and motivation for thin film synthesis before delving into an in-depth description of the modulated elemental reactants synthesis method. An exploration of the reaction pathways of MER precursors as they crystallize into metastable products is described, with three novel materials presented as experimental examples. For $Fe_{0.8}V_{0.2}Se_2$, nucleation of VSe_2 grains during the deposition kinetically favor the growth of highly Fe-substituted VSe_2. For $(PbSe)_{1+\delta}(FeSe_2)_2$, interlayer interactions with PbSe stabilize the formation of a novel,

hexagonal $FeSe_2$ phase. For $(Pb_3Mn_2Se_5)_{0.6}(VSe_2)$, finite size effects and interlayer stabilization promote the formation of a novel, quintuple layer $Pb_3Mn_2Se_5$ unit cell. In each example, nucleation during the deposition controls the formation of the targeted metastable phases.

The second section describes how to extract the maximum amount of structural information from Laue oscillations in thin film samples. Laue oscillations are theoretically explored to understand how to distribution of domains sizes impact their intensities. Laue oscillation fitting is incorporated into the crystallography data analysis software GSAS-II. Laue oscillations are key in the development of an approach to determine the distribution and extent of substitution and/or intercalation of dopant atoms, which is demonstrated for $Fe_xV_{1-y}Se_2$ samples.

The remainder of this thesis focuses on the experimental synthesis and characterization of novel Fe-containing phases from MER precursors. This includes the synthesis of a $Pb_{1-x}Fe_xSe$ phase, a range of $Fe_xV_{1-y}Se_2$ compounds with more Fe incorporation than had previously been achieved, and a family of $(PbSe)_{1+\delta}(FeSe_2)_n$ heterostructures.

CURRICULUM VITAE

NAME OF AUTHOR: Mellie Lemon

GRADUATE AND UNDERGRADUATE SCHOOLS ATTENDED:

University of Oregon, Eugene, OR
The University of the South, Sewanee, TN

DEGREES AWARDED:

Doctor of Philosophy, Chemistry, 2023, University of Oregon
Bachelor of Science, Chemistry, 2018, The University of the South

AREAS OF SPECIAL INTEREST:

Materials Science
Thin Film Synthesis and Characterization
Electron Microscopy

PROFESSIONAL EXPERIENCE:

Research Assistant, D. C. Johnson Research Group, University of Oregon, 2019 – 2023

FIB-SEM Assistant, Center for Advanced Materials Characterization in Oregon, University of Oregon, 2022-2023

Research Assistant, R. Pongdee Research Group, University of the South, 2016

PUBLICATIONS:

Lemon, M.; Harvel, F.; Gannon, R.; Rudin, S.P.; Lu, P.; Blackwood, H.; Johnson, D.C., 1T-$FeSe_2$ Layers in $(PbSe)_{1+\delta}(FeSe_2)_n$ – An Interlayer Stabilized 2D Structure, submitted to *Chem. Mater.* May **2023**

Lemon, M.; Harvel, F.; Gannon, R.; Lu, P.; Rudin, S.P.; Johnson, D.C., Targeted synthesis of predicted metastable compounds using modulated elemental reactants, *J. Vac. Sci. Technol. A* **2023**, 41, 022203
*Chosen as a featured article

Lemon, M.; Gannon, R.; Lu, P.; Battey, S.R.; Rudin, S.P.; Toby, B.H.; Johnson, D.C., A method to determine the distribution of substituted or intercalated ions in transition metal dichalcogenides: Fe_xVSe_2 and $Fe_{1-x}V_xSe_2$.

Chem. Mater. **2022**, *34* (19), 8528–8535
*Chosen to be spotlighted in edition of the Advances in Engineering series

Harvel, F.; Lemon, M**.**; Gannon, R.; Bardgett, D.; Humphrey, M.; Johnson, D.C.; Investigation of the Pb–Fe–Se Ternary System and the Synthesis of a Ternary $Pb_{1-x}Fe_xSe$ Phase. *Chem. Mater.* **2022**, *34* (14), 6339–6344

Miller, A.M.; Lemon, M.; Choffel, M.A.; Rich, S.R.; Harvel, F.; Johnson, D.C. Extracting information from X-ray diffraction patterns containing Laue oscillations. *Zeitschrift für Naturforschung B*, **2022**, *77*, 313

ACKNOWLEDGMENTS

I would like to acknowledge the many wonderful people who I have worked with and been supported by during my time at UO. Firstly I would like to thank my advisor, Professor David C. Johnson. I sincerely appreciate all of your guidance over the past four years. You have helped shape the way I think and have helped me to grow as a scientist while working in your group. I would also like to express my gratitude for my colleagues – Dr. Marisa Choffel, Dr. Renae Gannon, Dr. Aaron Miller, Hannah Blackwood, Sarah Rich, and Fischer Harvel. I have loved working with y'all and truly appreciate your support and encouragement. I would especially like to thank Fischer Harvel for letting me turn every project into OUR project. To the undergraduate researchers I have mentored – Sarah Chu, Taylor Hulbert, Kikachi Akpakwu – thank you for all of your hard work, for helping me to grow as a teacher, and for always joking with me. Thank you to the previous DCJ lab members for building a foundation of research that I could build my thesis on top of.

I would also like to thank the folks at CAMCOR and the UO machine shop for their knowledge and support. Thank you to Steve Weimholt for your plethora of knowledge that you share with us every time we knock on your door. Thank you to Jeffrey Garman and John Boosinger for keeping our lab running when things break. I would also especially like to thank Valerie Brogden for mentoring me on focused ion beam techniques. You have been so generous with your time, effort, and advice and I truly appreciate it.

My research would not have been possible without my national and international collaborators. I have thoroughly enjoyed working with Dr. Sven P. Rudin

and Dr. Samuel R. Battey, who provided guidance through theoretical calculations and predictions, as well as Dr. Ping Lu for his expertise on electron microscopy methods. I would especially like to thank Dr. Brian Toby, who has been endlessly patient with me and giving with his time aiding me in research.

I would like to acknowledge funding from the U.S. Department of Energy (DOE), Office of Science, Basic Energy Sciences (BES) under Award #DE-SC0020095. A portion of this work was performed at the Center for Integrated Nanotechnologies, an Office of Science User Facility operated for the U.S. Department of Energy Office of Science by Los Alamos National Laboratory under contract 89233218NCA000001. Sandia National Laboratories was instrumental for HAADF-STEM images. Sandia National Laboratories is a multimission laboratory managed and operated by National Technology and Engineering Solutions of Sandia, LLC, a wholly owned subsidiary of Honeywell International Inc. for the U.S. Department of Energy's National Nuclear Security Administration under contract DE-NA0003525. This paper describes objective technical results and analysis. Any subjective views or opinions that might be expressed in the paper do not necessarily represent the views of the U.S. Department of Energy or the United States Government.

Thank you to all of my past professors and graduate and undergraduate mentors. Your guidance has been invaluable and has helped shape me into the scientist I am today.

To my committee members, thank you for pushing me to reach my potential, and thank you for all your advice. Thanks to the Department of Chemistry and Faculty for support and guidance.

Finally, I could not have made it here without the love and support from my partner, my mom, my siblings, my nieces and nephews, and my friends. Thank you all for always listening and being encouraging and for all your love.

To my Dave, for changing your name to Dale when I got a PI named Dave,
and also for everything else
(I love you)

TABLE OF CONTENTS

Chapter Page

LIST OF FIGURES

LIST OF TABLES

CHAPTER I

INTRODUCTION

1.0 Authorship Statement

This chapter was written for this work alone with no intention of publishing it elsewhere. I am the primary author and wrote the following with assistance from my advisor David C. Johnson.

1.1 Overview

The discovery of new materials with useful properties is pivotal for the advancement of modern technology. New materials are needed to make devices that are more energy efficient, cheaper, and smaller. The drive to discover new materials has led to a boom in theoretical research efforts focused on calculating the formation energies of potential novel phases and predicting their properties.[1–4] The theoretically predicted stable phases become targets for experimental synthesis. However very few novel phases, relative to the number of predicted phases, have been experimentally realized.[5–7] Many of the predicted phases are metastable, which leads to challenges in synthesizing them without first forming more thermodynamically stable products. This is particularly true for classical solid state synthesis methods which rely on high temperature melts. In order to form metastable phases, a better understanding of solid state reaction pathways must be developed to gain control over the nucleation and growth of targeted products during synthesis. Formation of metastable ternary or higher order phases is dependent on control over the reaction pathway so that more thermodynamically stable binary phases are avoided.

Research into 2D layered materials and heterostructures is particularly promising for applications in modern thin film technologies due to the discovery of emergent properties at or near the monolayer limit.[8–11] and because it is possible to tune the properties of these materials through intercalation or substitution, varying layer thicknesses, or stacking with different layers.[12–18] Layered heterostructures are underexplored in computational calculations due to challenges in calculating their stability. However, it is logical that

undiscovered ternary phases consisting of alloys or intergrowths of 2D layers exist as local minima in ternary free energy landscapes. Layered materials such as 2D heterostructures, consisting of intergrowths of 2D layers, are a promising avenue for the discovery of novel materials, as the interlayer interactions can also be used to stabilize non-thermodynamic products. Typical synthesis techniques for forming metastable, layered materials include epitaxial growth based methods such as molecular beam epitaxy (MBE) and vapor transport based methods such as chemical vapor deposition (CVD) and physical vapor deposition (PVD).[19] Each of these techniques offer unique advantages and limitations, which have been reviewed extensively, and will be briefly described here.[20–24]

Epitaxial growth has been utilized to synthesize thin films for decades, and MBE has been extensively studied for the synthesis of III-V semiconducting films and numerous oxide thin films with a broad spectrum of electronic properties.[25,26] MBE can be used to create specific phases of compounds through layer by layer growth of the individual components. MBE is effective in avoiding secondary phases by utilizing a specific sequence of deposition of components to facilitate procession through a certain path on the phase diagram.[27] This method highlights the importance of stabilization through interactions at the interface of the substrate or between layers, which affect the nucleation and crystallographic structure of grown compounds. During MBE growth, the system will rearrange to minimize the energy, which is accomplished by forming coherent or semi-coherent interfaces at the substrate through distortion from the regular crystal structure of deposited compounds.[28] These low-energy interfaces lead to stabilization of metastable, unstable, or nonequilibrium phases of compounds. Potential phases for formation via MBE can be predicted based on the diffusion coefficients of the components and lattice parameters of the substrate and desired phase.[27]

Although the free energy minimization via formation of coherent or semi-coherent interfaces provides an explanation for the stabilization of metastable or unstable phases, the exact structural mechanism of stabilization during epitaxy remains unclear.[29] This has caused limitations in expanding the method towards compounds that are less predictable than oxides. Furthermore, during MBE growth bulk diffusion rates must be sufficiently small to limit the movement of atoms between the surface and interface of the layer so that the system cannot segregate into thermodynamic, binary products.[26,28] Metastable phases are formed via surface diffusion throughout each epitaxially grown layer. However, it can be experimentally

challenging to find the correct conditions for MBE growth, especially for targeted compounds that require sources with significant differences in vapor pressure, such as transition metal dichalcogenides.[30,31]

In vapor transport based synthesis methods such as CVD, gaseous phases of materials react on the surface of substrates to form solid products that are deposited onto the substrate. The nucleation and growth of 2D materials through CVD is controlled by several parameters including temperature, pressure, substrate choice, amount of source materials, and gas flow rate.[21,32,33] Varying these parameters allows for control over the final structure of deposited films. The morphology and orientation, number of layers, and layer size in deposited films are all dependent on the growth parameters. Defects and dopants can also be intentionally introduced by controlling the deposition parameters. These advantages make CVD a promising candidate for exploring fundamental insights on reaction mechanisms of 2D layered materials. However, direct growth of metastable phases by CVD is experimentally difficult because the growth parameters must be controlled to create an environment where the targeted material is thermodynamically stable at that condition. In order to form metastable phases, samples prepared by CVD must be post-treated via techniques such as plasma treatment, laser irradiation, mechanical force, or alkali metal intercalation.[21,32] Additionally, the growth of continuous films with large grains is challenging via CVD, which limits the growth of vertically stacked layered materials since complete monolayers across the substrate are seldom formed.

An alternative thin film synthesis method, modulated elemental reactants (MER), utilizes layered, mostly amorphous precursors with designed nanoarchitectures to target metastable materials. The precursors are composed of atomically thin elemental layers that are stacked in a manner to mimic the nanoarchitecture of targeted products. The determination of the number of atoms per unit area in the precursors from XRF measurements allows for precise control over the deposition. The precursors are deposited onto a nominally room temperature substrate, limiting diffusion to avoid the formation of thermodynamically stable products. Low temperature annealing of the designed precursors promotes the formation of targeted products if they are in a free energy minimum. Several parameters can be controlled to influence the nucleation and growth of products from MER precursors, including layer thickness, layer sequence, and post deposition processing

parameters. Annealing studies of the precursors are carried out to promote formation of products, and characterization of the film structure, thickness, and composition is carried out after each annealing step to monitor the nucleation and growth of the films. This leads to insight on reaction pathways, which further informs the parameters used in the preparation of precursors to target metastable products while avoiding global free energy minima. More details on the formation of metastable layered materials prepared by MER synthesis will be discussed in the following chapter.

1.2 Dissertation Overview

This dissertation describes the synthesis of ternary layered thin film materials via the modulated elemental reactants (MER) method and details the characterization of these materials through advanced x-ray techniques. This dissertation is separated into three sections. The first section containing Chapters I-III reviews the techniques used for synthesis and characterization of the films presented in this thesis. Chapter I provides a brief overview of the motivations for forming layered thin films and summarizes selected thin film synthesis techniques. Chapter II details how the MER method can be used in combination with an "island" approximation for predicting metastable structures to target novel, layered materials. This chapter provides insight into how nucleation of products can be controlled through the design of MER precursors and describes how the nucleation sites affect the growth of metastable structures. Chapter III summarizes the relevant experimental techniques used for synthesis and characterization of the thin film samples presented in subsequent chapters.

The second section of this dissertation containing Chapters IV-VI describes the advancement of x-ray diffraction (XRD) techniques to characterize samples containing Laue oscillation. Chapter IV delves deeper into physics behind Kiessig fringes and Laue oscillations present in x-ray reflectivity (XRR) and specular XRD patterns. Three different experimental systems are presented as examples to showcase the structural information that can be extracted from XRR and XRD patterns containing Laue oscillations. Chapter V continues the theoretical investigation of Laue oscillations and details how the Laue oscillation theory was utilized when programming Laue oscillation fitting into the crystallography data analysis software GSAS-II. Chapter VI includes the analysis of Laue oscillations in a combinatorial approach for determining the extent of substitution and/or

intercalation in a layered film. The x-ray fluorescence (XRF), Kiessig fringe, Laue oscillation, and XRD data were all used in this synergistic approach. A $Fe_xV_{1-y}Se_2$ compound was used to demonstrate this approach.

The third section of this thesis containing chapters VII-X describes the synthesis of metastable phases from MER precursors. Chapter VII contains information on the synthesis and characterization of layered $Fe_xV_{1-y}Se_2$ compounds with Fe content up to x = 0.8. Chapter VIII explores another ternary system containing Fe, Pb, and Se. This chapter details the investigation of the ternary Pb-Fe-Se phase diagram and the synthesis of a novel $Pb_xFe_{1-x}Se$ compound. Chapter IX further explores the ternary Pb-Fe-Se phase space. This chapter describes the synthesis of layered $(PbSe)_{1+\delta}(FeSe_2)_n$ heterostructures with n = 1, 2, and 3. These heterostructures contain a novel, metastable 1T-$FeSe_2$ compound that is stabilized by interlayer interactions with PbSe.

1.3 Bridge

Chapter I contains a brief, unpublished overview of relevant background for this dissertation and an overview of the dissertation contents. This chapter was written primarily by myself and edited by my advisor David C. Johnson. The following chapter, published in the *Journal of Vacuum Science and Technology A*, continues the discussion of thin film synthetic techniques and provides experimental examples of the different ways the modulated elemental reactants synthesis method can be utilized to form metastable structures predicted by computational calculations.

CHAPTER II

TARGETED SYNTHESIS OF PREDICTED METASTABLE COMPOUNDS USING MODULATED ELEMENTAL REACTANTS

2.0 Authorship Statement

Chapter II was published in the *Journal of Vacuum Science and Technology A* in 2023. I am the primary author of the manuscript. Fischer Harvel aided in sample preparation and data analysis. Renae Gannon prepared cross sections for HAADF-STEM imaging. Ping Lu collected HAADF-STEM images and EDS data. Sven Rudin performed theoretical calculations of predicted metastable compounds. David C. Johnson acted as my advisor and helped to edit the manuscript.

2.1 Introduction

Advances in technology beyond current limitations in speed, energy efficiency, size, and price depend on the discovery of new materials with useful functionality.[1] To speed up the discovery of such materials, computational calculations have been developed to predict stable compounds with unique properties.[2–5] Despite the large number of novel materials that have been predicted, the percentage that have been successfully synthesized remains small.[6] Experimental synthesis is the rate limiting step in turning predictions into usable new materials.[7] The main synthetic challenge for discovering new, predicted materials is that they are often metastable, and it is experimentally challenging to avoid more easily accessible thermodynamically stable phases. To access metastable phases, synthetic approaches must be developed that can target specific local free energy minima in the energy landscape while avoiding the global minimum.[8] This fundamentally requires control over initial nucleation such that a targeted structure forms and control over subsequent growth so that more thermodynamically stable products do not nucleate while atoms diffuse to the growth front.[9]

Classical synthetic techniques (flux synthesis, vapor transport, direct reaction of elements) were developed to overcome the slow solid-state diffusion through use of a fluid phase and/or high temperatures.[10] The composition of the reaction mixture and synthetic

parameters such as temperature and pressure are typically used to find reaction conditions where a targeted product is thermodynamically stable. This permits the growth of single crystals of a targeted compound, which enables the structure to be determined and the physical properties to be measured. Finding such reaction conditions for predicted compounds, however, can be incredibly challenging.

Synthetic techniques developed more recently facilitate the growth of compounds with targeted structures by controlling reaction kinetics. Molecular beam epitaxy (1960's) is perhaps the most widely known and best understood synthesis approach used to prepare metastable phases by controlling reaction kinetics.[11] MBE controls nucleation by providing a substrate with an epitaxial relationship with the targeted compound. During MBE growth, the deposition rates of different elements and the temperature of the substrate, which governs the desorption rate of the atoms, are used control the surface composition. Conditions are varied to find rates and temperatures where heterogeneous nucleation of the targeted structure from the epitaxial substrate is favored. Growth occurs as deposited atoms diffuse laterally and attach to the edges of growing layers. Conditions are controlled such that diffusion along the surface favors the growth of already nucleated crystal planes rather than nucleation of unwanted phases, reaction with the substrate, or reaction with previously deposited layers.[12] It can be quite challenging to find the appropriate conditions to nucleate and grow a targeted compound, especially when the deposited elements have large differences in their vapor pressures. For example, growing transition metal dichalcogenides becomes more difficult as the chalcogen becomes more volatile, with sulfur being particularly challenging.[13,14]

An alternative kinetically controlled synthesis approach developed over the last 4 decades, modulated elemental reactants (MER), also controls nucleation but does so by controlling local composition and limiting long range diffusion.[15] MER is based on preparing precursors with designed composition profiles at the nanoscale, which control what nucleates. The precursors consist of repeating sequences of thin elemental layers, which are deposited on non-epitaxial substrates kept near room temperature, limiting the extent of both bulk and surface diffusion.[16] In the simplest case of MER synthesis, the elemental layers remain amorphous after the deposition. The amorphous intermediate formed will, in principle, provide access to the highest number of possible metastable crystalline compounds.[17] Nucleation of compounds that have stoichiometries that are close to the local

composition are favored, especially if diffusion rates are low, since reaction pathways are determined by the fastest reduction in Gibbs free energy.[18–20] Forming the thermodynamic ground state compound or mixture of compounds is inhibited by the longer diffusion lengths that are required to "unmix" the precursor.[18] Nucleation depends on both the difference in Gibbs free energy between the existing state and potential products and the magnitude of the rearrangements required. The free energy difference generally is proportional to the extent of undercooling of the metastable state.[21,22] MER precursors are significantly "undercooled" and the nanoarchitecture of the precursor favors formation of the targeted compound because the local composition profile matches the targeted compound rather than the thermodynamic ground state.[9]

A significant recent advance in targeting metastable materials through MER synthesis is a theoretical approach that evaluates the kinetic stability of "nuclei" of different structures. This approach utilizes a model in which an "island" of a potential phase is embedded between crystalline layers.[23] Islands that are stable under these conditions become synthetic targets using MER.[24] The theoretical calculations inform the experimental parameters chosen to favor formation of the targeted structures, such as the layering sequence targeted local stoichiometries.

Here we illustrate the ability to kinetically trap metastable compounds by designing MER precursors that match the nanoarchitecture of targeted products. Three examples are presented. The first example is $Fe_xV_{1-x}Se_2$, where we extend the solid solution range from the $x = 0.3$ compound possible using conventional synthesis techniques to $x = 0.8$ using MER. The increased value for x results from low diffusion rates during processing that prevent unmixing during growth. The second example is the preparation a quintuple layer thick rock salt structured $Pb_3Mn_2Se_5$ block in a heterostructure. Despite PbSe and MnSe being immiscible, this ordered alloy layer, which was predicted to be kinetically stable by the "island" approach, can be trapped from a designed precursor. The third example is the synthesis of a metastable $(PbSe)_{1+\delta}(FeSe_2)_2$ heterostructure, where the $FeSe_2$ layers have a structure that differs from known binary iron selenides. The structure is kinetically trapped by the stabilizing interaction between PbSe and $FeSe_2$ layers. The confined two-dimensional geometry of the precursor layers favors formation of a layered solid with low energy interfaces. These examples illustrate the ability of MER synthetic parameters (local

composition, diffusion lengths, layer sequences) to control the reaction pathway, avoiding more thermodynamically stable products as reaction intermediates.

2.2 Experimental Set-up and Rationale

The synthesis method, modulated elemental reactants, involves the repeated physical vapor deposition of elemental layers in designed sequences onto an unheated substrate to form a layered precursor, which is then annealed to low temperatures to promote crystallization (see Figure 1). The sequence of elemental layers controls the composition profile of the precursor, which influences which compounds initially nucleate. The individual elemental layer thicknesses are typically very thin (less than a nanometer) to create ultrashort diffusion distances to form targeted products. The number of atoms deposited in adjacent elemental layers is controlled to target the number required to form a single crystalline layer of a proposed structure. These conditions kinetically favor the nucleation and growth of targeted products if annealing temperatures – typically between 100°C and 700°C – can be found that enable atoms to locally rearrange into the desired structures without diffusing longer distances to form the thermodynamically stable products.[9]

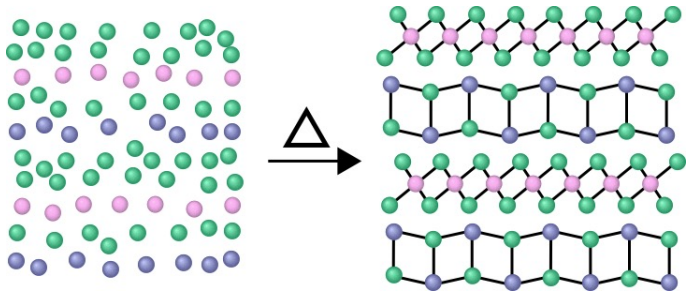

Fig. 2.1. Schematic of an idealized MER precursor that evolves to form a heterostructure during low temperature annealing.

A cryopumped high vacuum custom-built physical vapor deposition chamber was used to deposit the precursors from elemental sources. An ion gauge was used to measure the pressure of the chamber during the deposition, which remained below 3 x 10^{-7} Torr. The temperature of the shield that separates the sources from the substrates was measured with a thermocouple, and these temperatures were between 25-80°C. The precursors were deposited

onto (100) oriented Si wafers, which do not have an epitaxial relationship with the targeted crystalline layers. The native oxide on the Si wafer surface was not removed before deposition. A Knudson effusion cell was used to evaporate Se (99.995%, Alfa Aesar) from an alumina crucible. Electron-beam guns were used to evaporate Fe (99.95%, Kurt J. Lesker), V (99.995%, Alfa Aesar) Pb (99.8%, Alfa Aesar) and Mn (99.9%, Alfa Aesar). The Pb source was placed in an alumina crucible for the deposition. All other sources were placed directly on the electron-beam gun hearth. The deposition rates of the elements were monitored by quartz crystal microbalances located above each source and controlled to be 0.2-0.9 Å/sec. The sequence and thickness of the deposited elemental layers were controlled by the programmed opening and closing of pneumatic shutters positioned between the elemental sources and the unheated spinning substrate.

To prepare the metastable alloy $Fe_xV_{1-x}Se_2$, 50 repeats of a V|Fe|Se sequence of layers were deposited to yield a targeted total film thickness of ~30 nm. The crystal structure of VSe_2[25] was used to calculate the number of atoms of each element in the V|Fe|Se sequence required to form a monolayer of $Fe_xV_{1-x}Se_2$. The ratio of the number of V and Fe atoms in the sequence was controlled to target a specific value of x. Approximately 10% excess Se was deposited as this was reported to produce larger crystalline domains[26] and also compensates for Se evaporation during annealing. The V|Fe|Se layering sequence was chosen because VSe_2 is known to nucleate and grow during the deposition under the conditions described.[27] Since Fe was deposited directly after V, the short diffusion paths of Fe to the growing VSe_2 crystallites were expected to kinetically favor the addition of Fe to VSe_2 rather than the nucleation of thermodynamically stable binary Fe_xSe_y compounds.

For the $(Pb_3Mn_2Se_5)_{1+\delta}(VSe_2)$ heterostructure, precursors were prepared by depositing the elemental layers for 13 repeat units in the following sequence: V|Se|Pb|Se|Mn|Se|Pb|Se|Mn|Se|Pb|Se. The thicknesses of the V|Se layers were controlled to target enough atoms to form a single hexagonal 1T-structured Se-V-Se trilayer. The thicknesses of each of the Pb|Se layers were controlled to target enough material to form a single PbSe monolayer with a 100 orientation of the crystallographic planes of its rock salt structure with respect to the substrate. The Mn|Se layers were deposited between Pb|Se layers with thicknesses targeting enough atoms to form a single MnSe monolayer with the same lattice parameter of the 'host' PbSe rock salt matrix. The layering sequence and layer

thicknesses were chosen because PbSe is known to form crystallographically aligned with a dichalcogenide during deposition and VSe_2 is known to crystallize in a hexagonal structure during deposition.[28] The presence of Mn and Se in between the Pb|Se layers was expected to kinetically favor the formation of an alloyed $Pb_3Mn_2Se_5$ rock salt structure layer over the thermodynamically favored segregation into binary products. The crystalline VSe_2 layers located on either side of the sequence of Pb|Se and Mn|Se layers have a stabilizing interaction with the $Pb_3Mn_2Se_5$ layer and limit the diffusion of the reactants perpendicular to the substrate. The MnSe layers were expected to stabilize the surface puckering distortion of the outside PbSe monolayers.[29]

A precursor was prepared to target the ternary heterostructure $(PbSe)_{1+\delta}(FeSe_2)_2$ by depositing elemental layers in the sequence Fe|Pb|Fe|Se for 20 repeat units. The thicknesses of the elemental layers in each repeating unit were designed to provide enough material to form a rock salt structured PbSe bilayer and two hexagonal structured $FeSe_2$ trilayers with lattice parameters near those of VSe_2. Based on previous studies, we expected that PbSe would crystallize during the deposition,[30] confining the Fe and remaining Se to the finite space between the planes of PbSe. The "island" approach calculations indicated that the crystalline PbSe layers would stabilize a layered $FeSe_2$ structure rather than formation of known binary Fe_xSe_y compounds with more 3-dimensional structures.

The prepared samples were stored in a nitrogen glovebox (<0.2 ppm O_2) to prevent oxidation and were taken out as needed for characterization. Annealing studies were carried out on the deposited precursors to monitor the reaction mechanism and to determine the optimal temperature for formation of the targeted phases. The samples were heated to sequentially higher temperatures for 5 to 60 minutes with or without a Se atmosphere on a calibrated hot plate in the nitrogen glovebox. The annealing temperatures reported correspond to the temperature of the hot plates surface measured with a thermocouple. The annealing lengths reported refer to total amount of time from when the samples were placed on the hot plate surface to when they were removed.

The as-deposited and annealed samples were characterized using multiple X-ray techniques including X-ray reflectivity (XRR), specular X-ray diffraction (XRD), in-plane X-ray diffraction, and X-ray fluorescence (XRF). The XRR, specular XRD, and in-plane XRD patterns were collected on a Rigaku Smartlab diffractometer equipped with Cu Kα radiation.

The XRR and specular XRD scans were run in θ−2θ locked-coupled scan mode over a 2θ range of 0-11° for XRR and 5-65° for XRD. The total film thicknesses were determined from the XRR patterns using a modified version of Bragg's law to account for refraction.[31] The in-plane XRD patterns were run in grazing-incidence mode over a 2θ range of 15-110° 2θ. Lebail fits of the specular and in-plane XRD patterns and one-dimensional Rietveld refinements of the specular XRD patterns were carried out using the crystallography data analysis software, GSAS-II.[32]

The actual amount of each element deposited was measured using X-ray fluorescence spectroscopy (XRF) collected on a Rigaku Primus II spectrometer. The proportionality constant between the total number of atoms per unit area of an element and the intensity of its characteristic XRF signal was determined using a method developed by Hamann et al.[33] The average local compositions of the layers were calculated by dividing the total amount of each element by the number of layers deposited.

A cross-section of the $(PbSe)_{1+\delta}(FeSe_2)_2$ sample was prepared with an FEI Helios NanoLab 600i DualBeam focused ion beam scanning electron microscope (FIB-SEM) using standard lift out procedures.[34] High-angle annular dark-field scanning transmission electron microscopy (HAADF-STEM) images with atomic resolution and energy-dispersive X-ray spectroscopy (EDS) maps of the prepared cross-section were obtained using a Titan G2 80-200 STEM with a Cs-probe corrector and ChemiSTEM technology (X-FEG and SuperX EDS with four windowless silicon drift detectors) at 200kV.

Potential metastable phases were explored through theoretical calculations. The theoretical approach used relies on density functional theory (DFT) calculations using the VASP code.[35,36] DFT calculations rely on several well-controlled approximations that make the application workable. For the current applications these include the projector augmented wave (PAW)[37] method and the generalized gradient approximation to the functional.[38] The van der Waals interactions between layers were approximated with the method of Tkatchenko and Scheffler.[39]

For the $(Pb_3Mn_2Se_5)_{0.6}VSe_2$ and $(PbSe)_{1+\delta}(FeSe_2)_2$ heterostructures, the calculations were carried out using an "island approximation" in which potential phases are modeled as a finite island located between infinite 2D slabs of known thermodynamically favorable binary phases. The "islands" begin as a configuration of atoms with varying stoichiometries and

structures, which are allowed to relax between the adjacent crystalline layers. The free space around the islands allows the atoms to diffuse into more favorable configurations to lower the overall energy. This includes the freedom of the system to find previously unknown lattice parameters. During relaxation the atoms either diffuse into a recognizable, periodic pattern – an "island of promise" – or into a disordered dispersion – an "island of disaster."[23] The stoichiometry, the initial configuration, and the interfacial interactions with adjacent layers all influence whether an "island of promise" forms. The geometries of the stable islands are used to estimate the potential crystalline layer's lattice constants. Then structures containing both crystalline constituent layers are constructed and relaxed in DFT calculations to obtain formation energies. The information obtained about the energy landscape provides potential targets and parameters (local compositions and predicted structures) that aid the design of MER precursors.

2.3 Results and Discussion

2.3.1 $Fe_xV_{1-x}Se_2$

We first discuss the synthesis of a metastable dichalcogenide alloy $Fe_xV_{1-x}Se_2$ containing a significantly higher amount of Fe (x = 0.8) than has been previously reported using bulk synthesis approaches.[40,41] Theoretical calculations predicted that metastable $Fe_xV_{1-x}Se_2$ alloys would be kinetically stable with higher Fe concentrations.[42] To test these predictions, we prepared a precursor for $Fe_{0.8}V_{0.2}Se_2$ by depositing a repeating sequence of V|Fe|Se layers 50 times. The total number of atoms/Å^2 of each element in the as-deposited precursor was determined using XRF and yielded a composition of $Fe_{0.80(3)}V_{0.20(2)}Se_{2.2(1)}$. The expected nucleation of VSe_2 during deposition was anticipated to kinetically favor the inclusion of both Fe and V during the growth of the dichalcogenide.

XRR, specular XRD, and in-plane XRD scans of the as-deposited precursor (Figure 2.2) were carried out to probe whether crystalline domains formed during the deposition. The XRR pattern contains a sequence of regularly spaced Kiessig fringes, which were used to calculate the total film thickness of 308(1) Å. The specular XRD pattern shows a family of 00*l* Bragg reflections yielding a *c*-axis lattice parameter of 6.05(1) Å. The in-plane XRD pattern shows two relatively sharp *hk*0 reflections that can be indexed to a hexagonal structure with an *a*-axis lattice parameter of 3.36(1) Å. These values are near the *a*- and *c*-

axis lattice parameters of VSe_2 (a = 3.359 Å, c = 6.108 Å),[25] suggesting that domains of a dichalcogenide structure form crystallographically aligned to the substrate during the deposition, as shown schematically in Figure 2.3. The area of the unit cell's basal plane determined from the in-plane lattice parameter was multiplied by the number of atoms per unit area determined from the XRF data to yield the number of unit cells each element could potentially form. There was enough V to form 10(1) layers, enough Fe to form 40(1) layers, and enough Se to form 56(2) layers of dichalcogenide, indicating that there were enough atoms in each of the 50 V|Fe|Se layer sequences to form one layer of the targeted dichalcogenide.

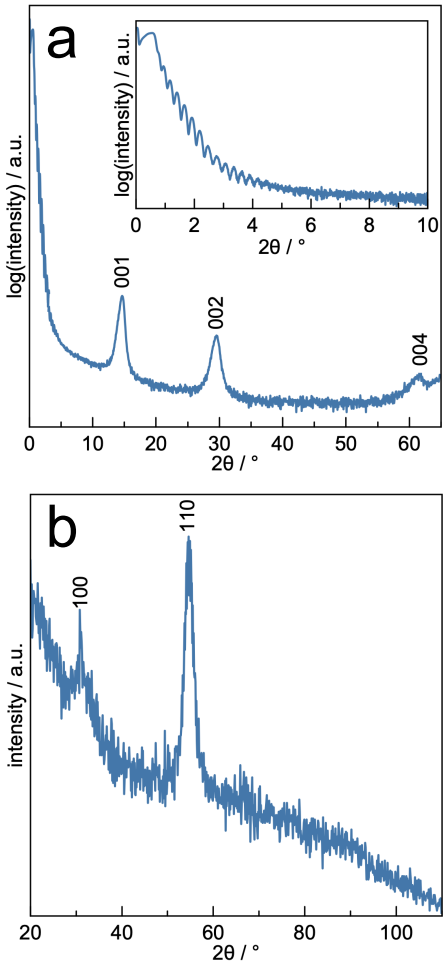

Fig. 2.2. a) X-ray reflectivity scan and specular XRD scan of the as-deposited $Fe_{0.80(3)}V_{0.20(2)}Se_{2.2(1)}$ sample. The inset shows a magnification from 0-10° 2θ. b) The in-plane XRD scan of the as-deposited $Fe_{0.80(3)}V_{0.20(2)}Se_{2.2(1)}$ sample. The hexagonal indices used to calculate lattice parameters are shown above each reflection.

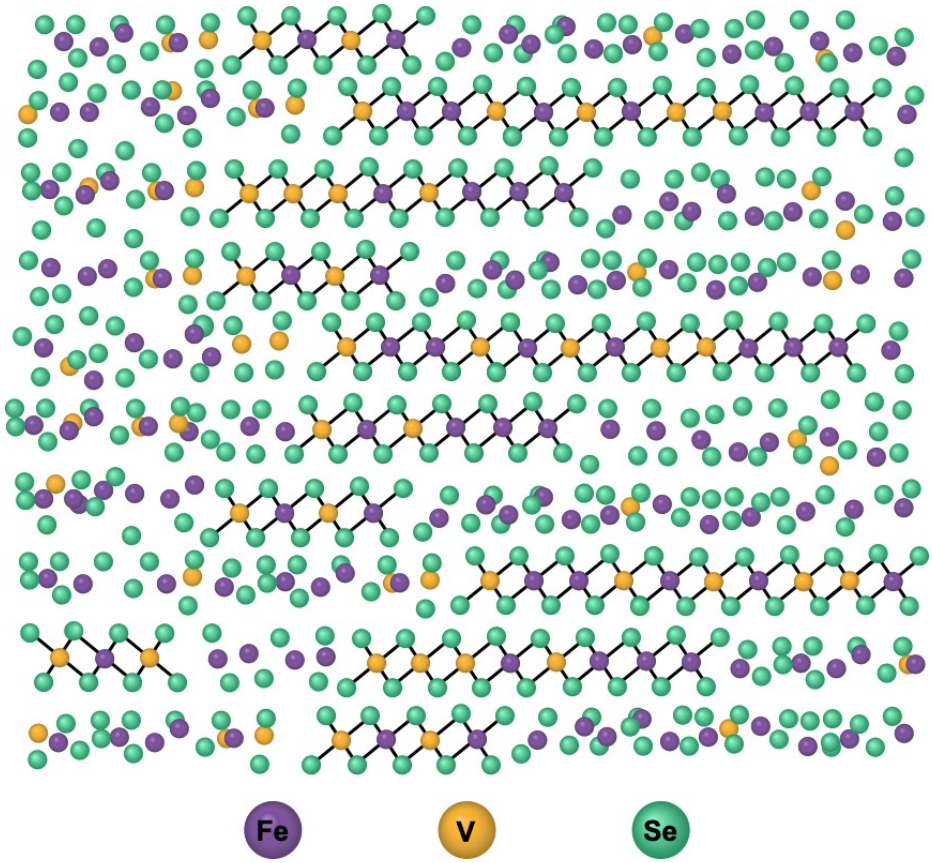

Fig. 2.3. Schematic of the as-deposited structure of ten representative layers of the $Fe_{0.8}V_{0.2}Se_2$ precursor. Nucleation and growth of a layered dichalcogenide occurs during deposition. The precursor contains crystalline domains of the dichalcogenide and amorphous regions.

An annealing study was carried out on the as-deposited sample with XRR, specular XRD, in-plane XRD, and XRF data taken after each annealing step to follow changes in composition and structure. See supplementary material for the annealing study data and discussion. The data showed that $Fe_{0.80(3)}V_{0.20(2)}Se_2$ grows as the annealing temperature is increased up to 300°C. Annealing to 400°C results in the formation of an intercalated dichalcogenide with a metal to selenium ratio greater than one. Based on this data, a piece of the precursor was annealed directly to 350°C for 15 minutes under Se atmosphere to promote crystallization of the substituted product. The specular and in-plane XRD patterns of the annealed sample are shown in Figure 4. The specular XRD pattern contains 4 00*l* reflections

yielding a *c*-axis lattice parameter of 5.766(5) Å. The in-plane XRD pattern contains *hk*0 reflections that can be indexed to a hexagonal unit cell with an *a*-axis lattice parameter of 3.381(5) Å.

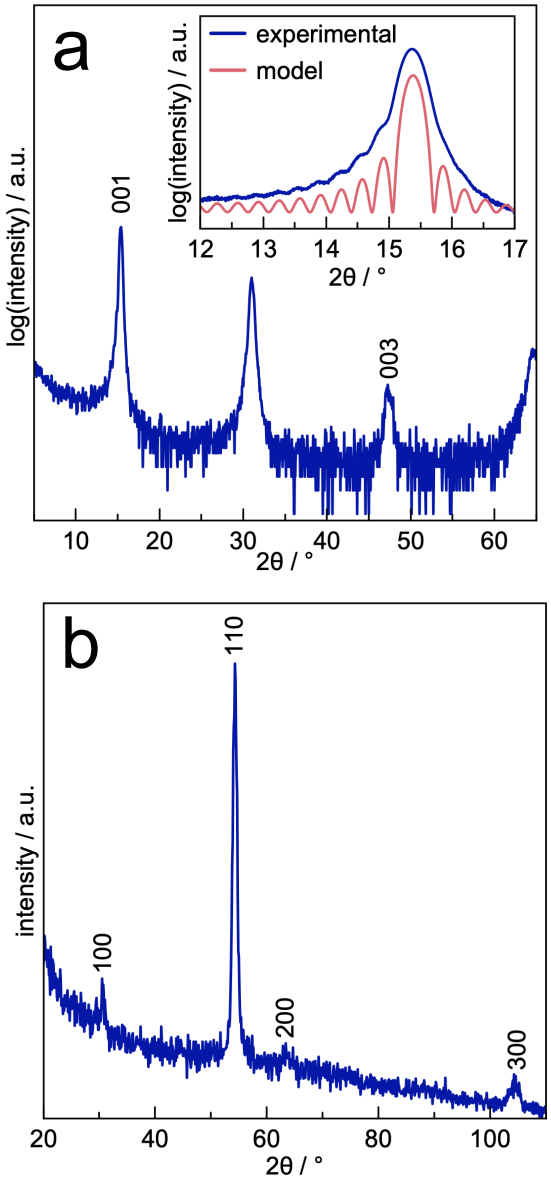

Fig. 2.4. a) Specular XRD pattern for the $Fe_{0.8}V_{0.2}Se_2$ annealed to 350°C under Se atmosphere. The inset shows a closeup of the 001 reflection with the experimental data in blue and the modeled data in pink. b) In-plane XRD pattern for the sample annealed to 350°C under Se atmosphere.

Laue oscillations are present on either side of the 001 reflection in the specular XRD pattern (Figure 4a), which indicate that most of the sample is composed of coherently diffracting crystalline domains with a similar, finite number of unit cells. The observation of Laue oscillations in grown films is generally only used to indicate the high crystalline quality of samples.[43] Laue oscillations, however, also contain information about the average number of coherently diffracting unit cells in the crystalline domains and an estimate as to the width of the distribution determined from the intensity decay of the oscillations as one moves away from the reflection.[44,45] For this sample we find an average of 47 +/- 1 unit cells result in the observed Laue oscillations. Multiplying the *c*-axis lattice parameter by the number of layers gives the average thickness of these coherently diffracting crystalline domains, 271(6) Å. Since the total thickness of the annealed film determined from the Kiessig fringes in the XRR pattern is 271.2(8) Å, the coherent crystalline domain accounts for the total film thickness and for almost all the atoms in the film. Therefore, the composition of the sample from the XRF data is the composition of the crystalline phase, which is $Fe_{0.81(4)}V_{0.21(2)}Se_2$ when normalized to the amount of Se. Multiplying the atoms per unit area of the annealed sample by the area of the unit cell basal plane indicates that there is enough Se present to form 48(2) unit cells, enough V present to form 10(1) unit cells, and enough Fe present to form 39(1) unit cells. The XRR, XRD, XRF, and Laue oscillation data yield a consistent picture of a crystalline $Fe_{0.8}V_{0.2}Se_2$ structure. These data were used to create an initial, constrained model of the structure and composition of the sample that was used as a starting point for a one-dimensional Rietveld refinement of the specular XRD pattern. See supplementary material for details on the parameters used for the Rietveld refinements. The refinement provided a good fit of the measured intensities as shown in Figure 5. This confirms the formation of a substituted $Fe_xV_{1-x}Se_2$ structure with more than three times the Fe content than has previously been achieved by direct reaction of the bulk elements.

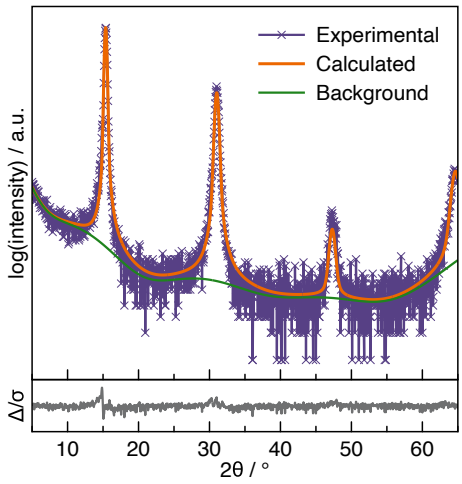

Fig. 2.5. Rietveld refinement of the specular XRD pattern of the $Fe_{0.8}V_{0.2}Se_2$ sample created from an initial, constrained model determined by the combination of XRR, XRD, Laue oscillation, and XRF data.

2.3.2 $(Pb_3Mn_2Se_5)_{0.6}VSe_2$

The MER method also provides opportunities to target constituent layers in heterostructures that have compositions and structures not found as bulk compounds. This is possible because interfacial interactions with adjacent layers in a heterostructure can stabilize metastable compounds. The finite thicknesses of layers in MER also impact the kinetics of crystal growth, influencing what forms. The synthesis of $(Pb_3Mn_2Se_5)_{0.6}VSe_2$, a member of the homologous series $(Pb_nMn_2Se_{n+2})_{0.6}VSe_2$, illustrates our ability to design a precursor to kinetically favor formation of a targeted, metastable product. The 0^{th} member of this family, $(Pb_2MnSe_3)_{0.6}VSe_2$,[24] has a central MnSe layer in rock salt structured trilayer which stabilizes a puckering distortion that occurs at the surface of finite thickness PbSe layers in a heterostructure.[29] Computational studies that probed the kinetic stability of Pb-Mn-Se islands with different structures placed between VSe_2 layers suggested that islands of $Pb_3Mn_2Se_5$ would also be kinetically stable.[24] In the predicted structure of the $Pb_3Mn_2Se_5$ layer – shown schematically in Figure 6 – 1T-VSe_2 layers are located on either side of an alloyed rock salt $Pb_3Mn_2Se_5$ layer with the MnSe planes adjacent to the outer PbSe planes, stabilizing the surface puckering.

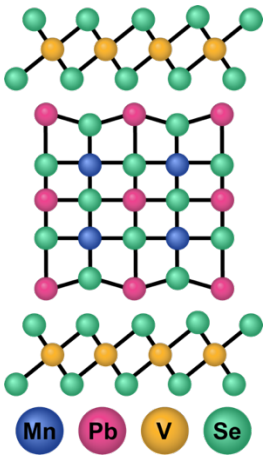

Fig. 2.6. A schematic of the structure of the targeted $(Pb_3Mn_2Se_5)_{0.6}VSe_2$ heterostructure with the puckering of the outer PbSe layers exaggerated to make it more visible.

A precursor targeting $(Pb_3Mn_2Se_5)_{0.6}VSe_2$ was prepared by depositing 13 repeat units of the elemental layering sequence V|Se|Pb|Se|Mn|Se|Pb|Se|Mn|Se|Pb|Se. The V|Se layers were designed to provide enough V and Se to form a trilayer of hexagonal structure 1T-VSe_2. The VSe_2 layers limit the diffusion of the Mn|Se and Pb|Se reactants perpendicular to the substrate and likely have a stabilizing interaction with the $Pb_3Mn_2Se_5$ layer. Each of the interweaved Mn|Se or Pb|Se layers was designed to provide enough atoms of each element to form a monolayer of a rock salt structure. The ultrathin layering would kinetically favor the formation the alloyed $Pb_3Mn_2Se_5$ structure rather than the segregation of the metals to form the thermodynamically favored mixture of PbSe and MnSe. The composition determined from the XRF indicated that the sample was near the targeted stoichiometry with a slight excess of Pb. The number of atoms per unit area from the XRF data was multiplied by the expected basal plane area for the Pb_2MnSe_3 and VSe_2 constituents of $(Pb_2MnSe_3)_{0.6}VSe_2$ to estimate the number of possible unit cells. The precursor contained enough V to form 12(1) VSe_2 layers, enough Pb to form 16(1) $Pb_3Mn_2Se_5$ layers, enough Mn to form 13(1) $Pb_3Mn_2Se_5$ layers and enough Se to form 12(1) layers of $(Pb_3Mn_2Se_5)_{0.6}VSe_2$.

XRR, specular XRD, and in-plane XRD data were collected to probe the structure of the as-deposited sample. The XRR pattern (Figure 7a) contains two narrow Bragg reflections at ~4° and ~8° that arise from the periodic modulation of electron density throughout the precursor, indicating that significant interdiffusion of the elements did not occur. The

modulation length in the precursor was calculated to be 21(1) Å. The "flat" appearance of the first Bragg peak potentially results from additional intensity from small crystalline domains of the targeted $(Pb_3Mn_2Se_5)_{0.6}VSe_2$ heterostructure. The broad reflection at 29° and a weaker reflection at 34° in the specular XRD pattern could be indexed as 00*l* reflections, yielding a *c*-axis lattice parameter of 21.3(1) Å which supports the formation of crystalline domains of the targeted heterostructure during the deposition. The in-plane XRD pattern contains peaks that can be indexed as *hk*0 reflections of a cubic structure and a hexagonal structure with *a*-axis lattice parameters of 5.95(1) Å and 3.43(6) Å, respectively. The lack of reflections that can be indexed to a separate Mn_xSe_y phase suggests that the $Pb_xMn_ySe_z$ structure is kinetically favorable. The XRR and XRD data suggest that small grains of the targeted heterostructure nucleate and grow within the layered precursor during the deposition, as illustrated schematically in Figure 8.

An annealing study was carried out on the as-deposited precursor, which showed that $(Pb_3Mn_2Se_5)_{0.6}VSe_2$ grains grow when the sample is annealed at 250°C or below. See supplementary material for details on the annealing study data and discussion. Annealing at 300°C or higher results in the formation of binary impurity phases and decomposition of the heterostructure. Based on the results of this annealing study, a second piece of the precursor was annealed to 250°C for 25 min in a N_2 atmosphere. The XRR and specular XRD pattern for the annealed sample (Figure 9a) contain a family of 00*l* reflections yielding a *c*-axis lattice parameter of 21.21(1) Å. The higher order 00*l* reflections remain broader than the first two Bragg reflections, indicating that noncrystalline regions with the original modulation in electron density remain. The in-plane XRD pattern for the annealed sample contains reflections that can be indexed as *hk*0 reflections of a cubic phase and a hexagonal phase with *a*-axis lattice parameters of 6.065(3) Å and 3.42(2) Å, respectively. The *a*-axis lattice parameters are near those for the $(Pb_2MnSe_3)_{0.6}VSe_2$ constituent layers, and the *c*-axis lattice parameter is near that estimated from the addition of two ~3 Å thick rock salt structured monolayers to the 14.96 Å $(Pb_2MnSe_3)_{0.6}VSe_2$ structure. This data indicates that the targeted heterostructure forms crystallographically aligned to the substrate after annealing at 250°C.

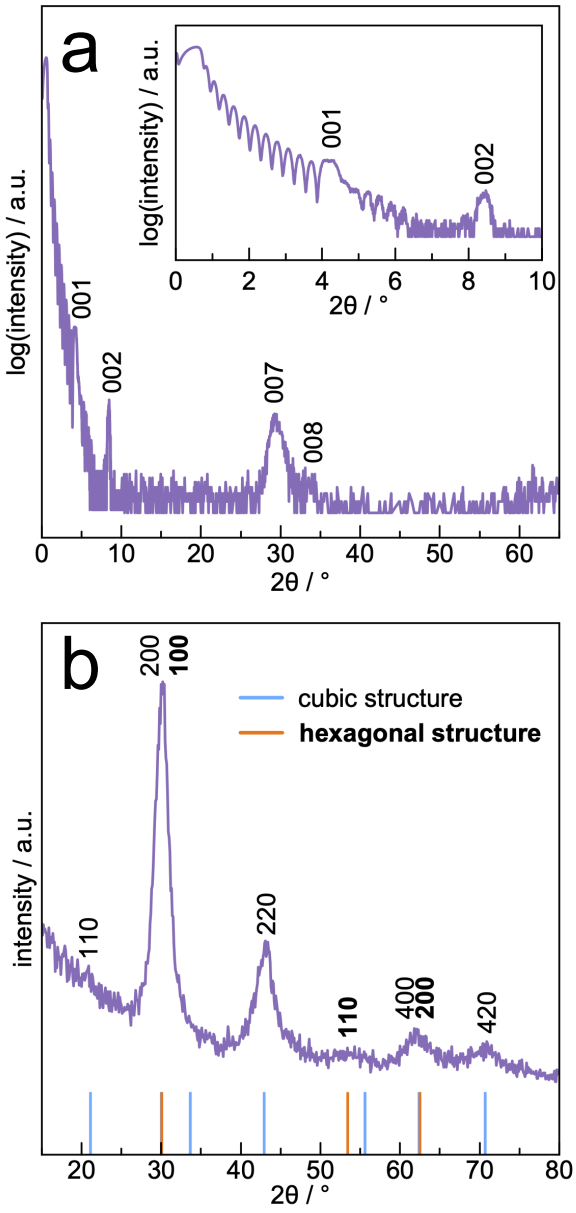

Fig. 2.7. a) The specular XRD and XRR patterns and b) the in-plane diffraction pattern of the as-deposited $(Pb_3Mn_2Se_5)_{0.6}VSe_2$ precursor. Indices are shown above the reflections. Locations of peaks for the cubic and hexagonal phases determined from a Lebail fit of the data are indicated by the blue and orange lines below the pattern.

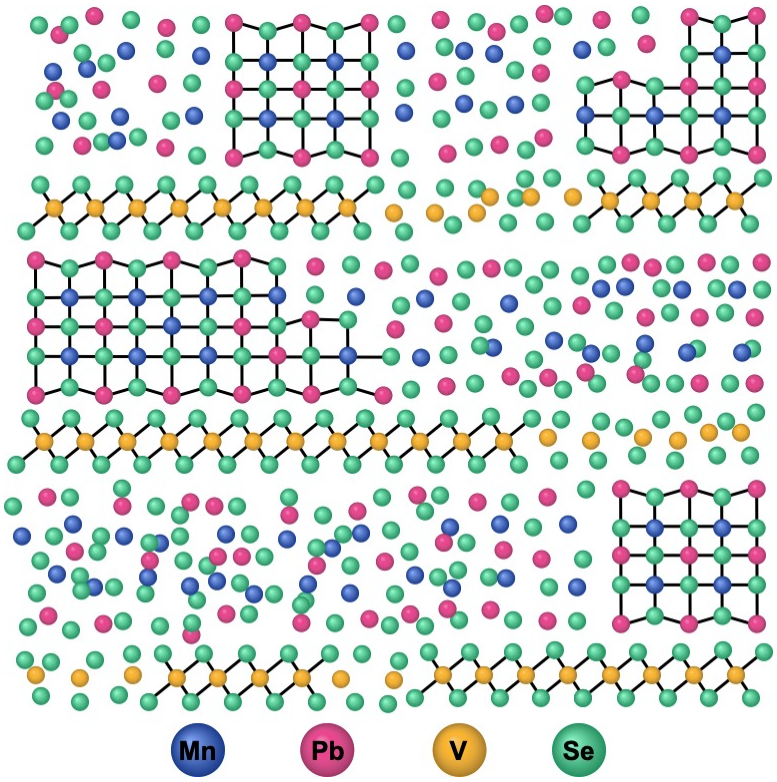

Fig. 2.8. Schematic of the as-deposited structure of 3 representative repeat units of the $(Pb_3Mn_2Se_5)_{0.6}VSe_2$ precursor. Some grains of VSe_2 and the alloyed $Pb_xMn_ySe_z$ structure form on deposit, and the artificial layering of the elemental layers is retained in the amorphous regions.

The XRR pattern also contains Laue oscillations which appear around the 2nd order Bragg reflection, indicating that the majority of the sample forms uniformly sized, coherently scattering domains of the kinetically stable heterostructure. The 10 maxima and 11 minima between the 1st and 2nd order Bragg reflections suggest that 12 unit cells of the heterostructure form. The number of unit cells was multiplied by the *c*-axis lattice parameter to determine the average crystalline domain thickness of 254(5) Å, which is smaller than the total film thickness calculated from the Kiessig fringes of 278(2) Å. This indicates that ~10% of the sample consists of impurity phase(s). A model was created to fit the Kiessig fringes and Laue oscillations present in the XRR pattern (Figure 10a). The model consists of 12 coherently diffracting unit cells of the $(Pb_3Mn_2Se_5)_{0.6}VSe_2$ heterostructure yielding a thickness of 257(2) Å and 22 Å of additional thickness consisting of a mixture of mostly

PbSe and some VSe_2 to yield the total film thickness of 278(2) Å. The amount of additional thickness is consistent with the number of excess Pb atoms measured by XRF.

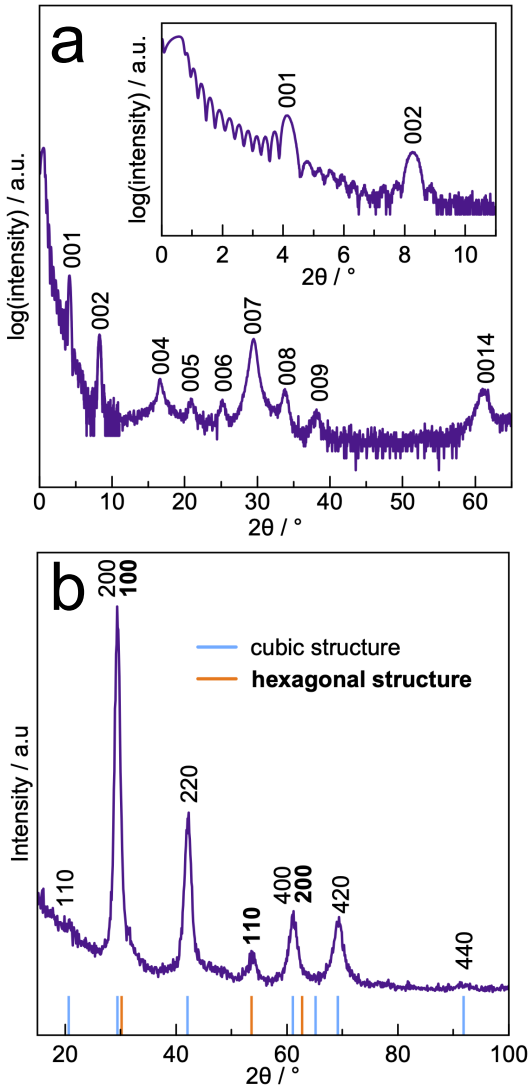

Fig. 2.9. a) The XRR and specular XRD pattern for the sample annealed to 250°C for 25 min. The inset shows a magnification from 0-10° 2θ. b) The in-plane XRD pattern for the annealed sample. Indices are shown above the reflections. Locations of peaks for the cubic and hexagonal phases determined from a Lebail fit of the data are indicated by the blue and orange lines below the pattern.

The presence of impurity phases and compositional variation within the $Pb_3Mn_2Se_5$ unit cell in the heterostructure limits the ability to perform a Rietveld refinement of the

diffraction data. However, a model of the $(Pb_3Mn_2Se_5)_{0.6}VSe_2$ structure was created based on the expansion of the $(Pb_2Mn_1Se_3)_{0.6}VSe_2$ structure by two additional ~3 Å thick monolayers to simulate the diffraction data (Figure 10b). See supplementary material for details on the parameters used for the model. The locations and intensities of the Bragg reflections from the modeled structure agree well with the experimental pattern observed for the specular XRD pattern after annealing the sample to 250°C for 25 min. This supports the formation of the novel $(Pb_3Mn_2Se_5)_{0.6}VSe_2$ heterostructure.

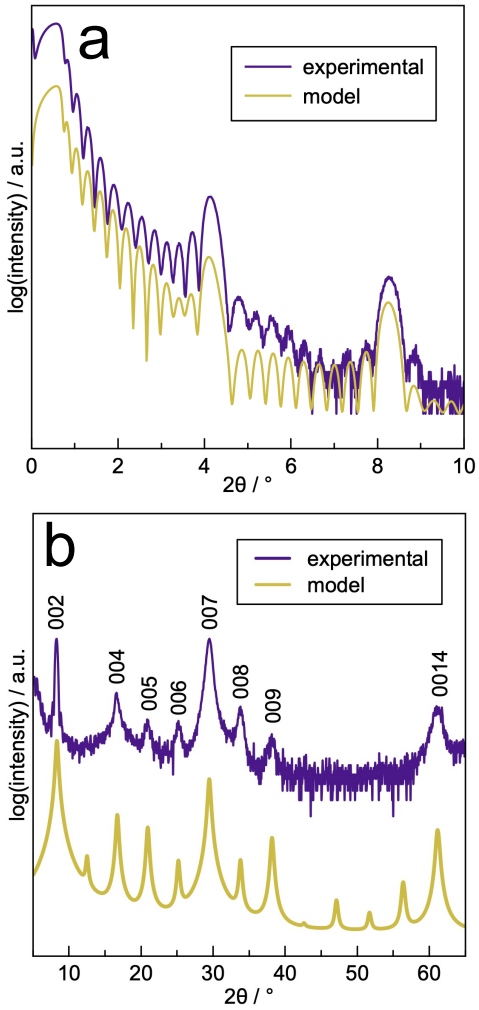

Fig. 2.10. a) A model of the Kiessig fringes and Laue oscillations present in the low angle XRR pattern for the $(Pb_3Mn_2Se_5)_{0.6}VSe_2$ sample after annealing at 250°C for 25 minutes. b) A simulated specular XRD pattern for a model of the structure of the $(Pb_3Mn_2Se_5)_{0.6}VSe_2$ heterostructure. The mustard curves are the modeled data, and the purple curves are the experimental data.

2.3.3 $(PbSe)_{1+\delta}(FeSe_2)_2$

The last example discussed is the synthesis of a ternary Pb-Fe-Se heterostructure. The Pb-Fe-Se phase diagram does not contain any known ternary compounds,[46] although several $Fe_xPb_ySe_z$ compounds have been computationally predicted to be stable. Experimental attempts to prepare the predicted ternary compounds via MBE, MER, or traditional approaches have resulted in only mixtures of binary compounds[6] or the formation of a metastable $Pb_{1-x}Fe_xSe$ alloy.[47] Heterostructures containing intergrowths of binary compounds are obvious possible ternary compounds in this and other empty phase diagrams, but their potential existence has not been extensively explored theoretically due to computational challenges. The "island" approach was used to computationally probe the kinetic stability of potential heterostructures in the Pb-Fe-Se system without having to distort the binary compounds to create a commensurate lattice. The kinetic stabilities of islands of iron selenide structures between rock salt structured PbSe bilayers were tested. These calculations showed that a distorted hexagonal 1T-$FeSe_2$ structure would be kinetically stable when layered with distorted rock salt structured PbSe bilayers, as shown in Figure 11. The structure of the PbSe layer is similar to that observed experimentally in thermodynamically stable heterostructures with the general formula $(PbSe)TSe_2$, where T = Ti, V, Nb, and Ta.[48–51] While there is still considerable debate as to the nature of the interaction between PbSe and dichalcogenide layers, the interaction must be strong enough to stabilize these unusual thermodynamically compounds.[52–57]

These calculations prompted us to prepare an MER precursor designed to kinetically favor the nucleation and growth of a heterostructure consisting of two hexagonal $FeSe_2$ layers stacked with a distorted rock salt structured PbSe layer. The precursor was deposited with the layering sequence Fe|Pb|Fe|Se for 20 repeat units. The number of atoms of each element in the repeat unit was designed to provide enough material to form one rock salt structured PbSe bilayer and two hexagonal structured $FeSe_2$ trilayers. The misfit parameter, 1.1, was approximated from the in-plane lattice parameters of PbSe and VSe_2. The layering sequence was chosen to reduce the amount of PbSe that formed during the deposition. The hypothesis is that the deposition sequence would confine the Fe and remaining Se to the finite space between the planes of PbSe, which would favor the formation of $FeSe_2$ with a layered structure.

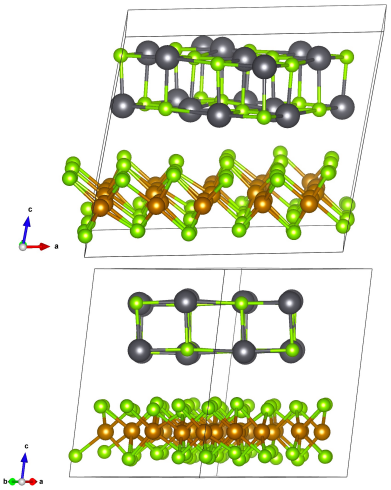

Fig. 2.11. Two different viewpoints of the computationally calculated structure for the $(PbSe)_{1+\delta}(FeSe_2)_n$ layered compound that was predicted to be a kinetically stable heterostructure.

The as-deposited precursor was characterized using XRF and XRR to probe the local composition and electron density profile from the elemental layering. The composition determined from the XRF data was $(PbSe)_{1.09(4)}(FeSe_{1.9(1)})_2$ when normalized to the amount of Fe and assuming a 1:1 stoichiometry for PbSe. This is within error of the targeted stoichiometry. Dividing the total number of atoms of each element by the number of layers deposited indicates that each repeat sequence of elemental layers contains enough atoms to form one unit cell of $(PbSe)_{1.1}(FeSe_2)_2$. The XRR pattern (Figure 12a) of the as-deposited precursor contains a narrow reflection at ~5° due to the periodic modulation of electron density from the elemental layering in the precursor, which yields a thickness of 18.4 Å. This indicates that significant inter-diffusion did not occur across the deposited repeat sequences, so the local composition profile is close to that of the targeted compound.

Specular and in-plane XRD data were collected on the as-deposited precursor to probe its structure. The specular XRD pattern (Figure 12a) contains a family of 00*l* reflections that yield a *c*-axis lattice parameter of 17.99(1) Å, which is near that estimated for the targeted heterostructure based on a 6.1 Å thick rock salt PbSe bilayer and two 5.8 Å thick hexagonal $FeSe_2$ trilayers.[58] The in-plane XRD pattern (Figure 11b) contains *hk*0 reflections from a cubic phase and a hexagonal phase with *a*-axis lattice parameters of 6.06(5) Å and

3.39(5) Å, respectively. The cubic lattice parameter is near that expected for PbSe, but the weak intensity of the forbidden 110 reflection suggests that the structure is distorted from an ideal rock salt structure.[47] This data suggests that crystalline domains of the kinetically stable heterostructure form aligned to the substrate during the deposition, as illustrated schematically in Figure 13.

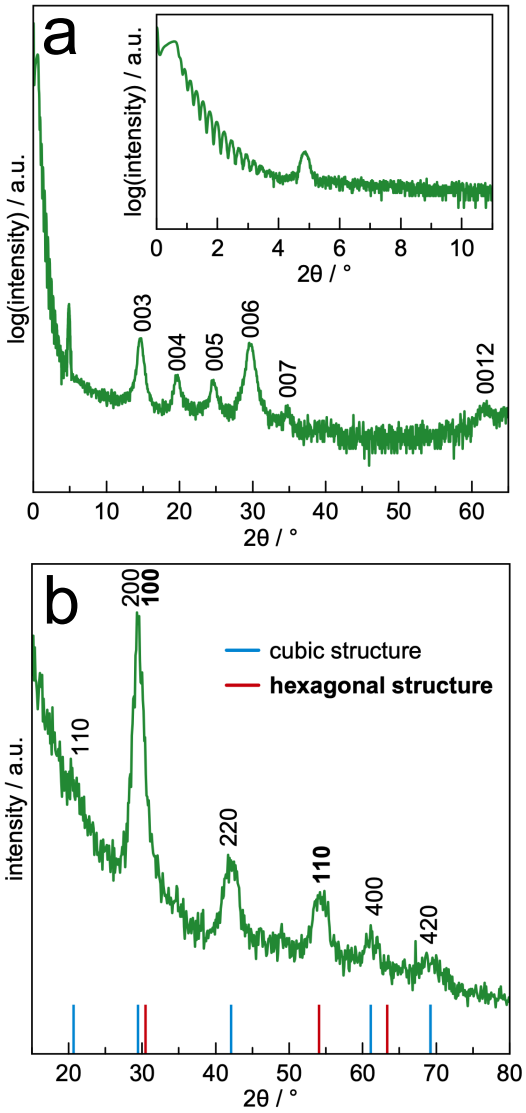

Fig. 2.12. a) XRR and specular XRD pattern for the as-deposited $(PbSe)_{1+\delta}(FeSe_2)_2$ precursor. The inset shows a magnification from 0-10° 2θ. b) In-plane XRD pattern of the as-deposited precursor. Locations of peaks for the cubic and hexagonal phases determined from a Lebail fit of the data are indicated by the blue and red lines below the pattern.

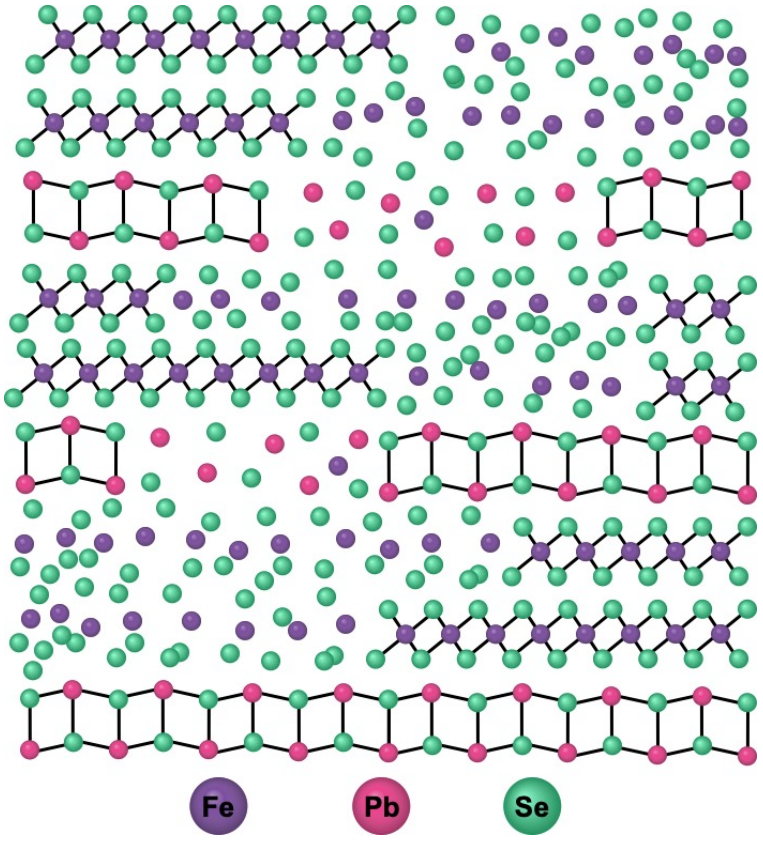

Fig. 2.13. Schematic of the as-deposited structure of 3 representative repeat units of the layering sequence and partial crystallization of the $(PbSe)_{1+\delta}(FeSe_2)_2$ precursor. Some grains of the heterostructure begin to form in the modulated amorphous matrix.

An annealing study carried out on the as-deposited precursor showed that significant crystal growth occurred during annealing at temperatures up to and including 200°C. See supplementary material at for the annealing study data and discussion. At 250°C, impurity phase(s) became present in the diffraction patterns, which are likely due to decomposition into thermodynamically stable binary phases, such as PbSe. The XRR, specular XRD, and in-plane XRD patterns for a piece of the precursor annealed to 200°C for 15 min are shown in Figure 14. The in-plane XRD pattern contains *hk*0 reflections that can be indexed to a cubic phase and a hexagonal phase with *a*-axis lattice parameters of 6.115(5) Å and 3.40(2) Å, respectively. Weak intensities observed for the 110 and 310 reflections, which are forbidden in the rock salt space group, indicate a distortion from the rock salt structure. The family of 00*l* reflections in the XRR and specular XRD pattern yield a *c*-axis lattice parameter of 17.592(5) Å. Laue oscillations are visible on each side of the 002, 003, and 004 reflections in

the specular XRD pattern, indicating that most of the sample consists of a similar, finite number of unit cells of the $(PbSe)_{1.1}(FeSe_2)_2$ heterostructure in coherently diffracting crystalline domains. The Laue oscillations do not extend further than a few degrees from each Bragg peak, indicating that there is a distribution of domain sizes. We estimate that there are 17 +/- 2 unit cells within the coherently diffracting domains.[43] This yields a thickness of 299(35) Å, which is less than the total film thickness calculated from the Kiessig fringes of 336(2) Å, suggesting that there is some thickness of impurity phase(s).

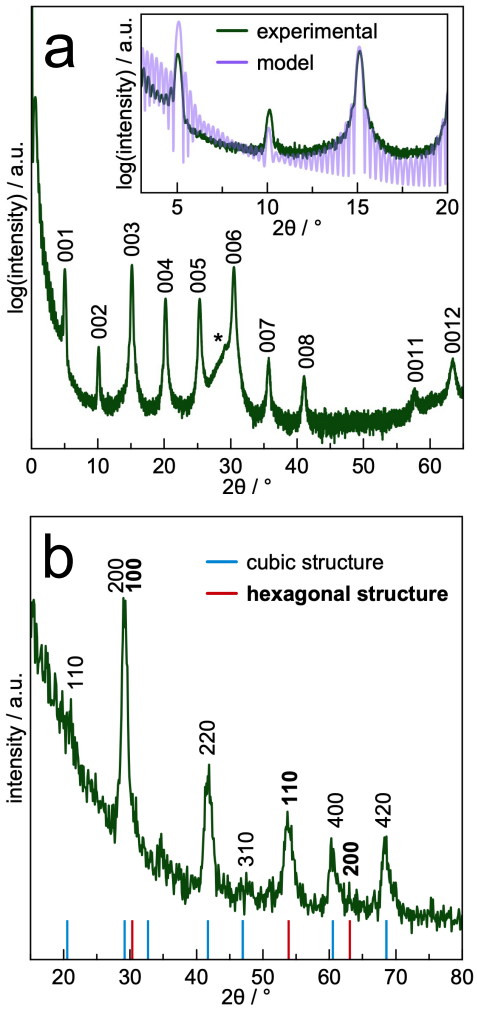

Fig. 2.14. a) XRR and specular XRD data for the $(PbSe)_{1.1}(FeSe_2)_2$ sample annealed to 200°C. The inset shows a close-up of the Laue oscillation observed from 3-20°. The reflection due to an impurity phase is indicated with * b) In-plane XRD data for the annealed sample. Locations of peaks for the cubic and hexagonal phases determined from a Lebail fit of the data are indicated by the blue and red lines below the pattern.

To further characterize the structure, cross-section lamellae of annealed samples were prepared by FIB-SEM for structural analysis via HAADF-STEM imaging and STEM-EDS mapping (Figure 15). The HAADF-STEM image of a representative cross-section shows 18 total repeat units consisting of one brighter Pb/Se layer and two darker Fe/Se layers. This is consistent with the number of unit cells determined from the Laue oscillations, indicating that this cross section is representative of the sample. The distribution of Pb, Fe, and Se throughout the sample was probed by STEM-EDS elemental mapping (Figure 15c), and the atomic plane positions were averaged across the unit cell by a method developed by Ping et al (Figure 15d).[59] The EDS line profiles show a repeat unit consisting of one primarily Pb and Se containing bilayer and two Se-Fe-Se trilayers. The Pb atoms in the bilayer are further apart then the Se atoms, indicative of the puckering distortion of the rock salt structure. A weak Fe peak located in the center of the PbSe bilayers suggests the presence of a small amount of Fe within the PbSe bilayer. The peak shape of the Fe layer is broader than that of Se and Pb, and slightly off center of the Se planes in the Se-Fe-Se region of the heterostructure. The broader line width may indicate that there is a distribution of Fe sites displaced from one another along the z-axis.

Rietveld refinements of the specular diffraction pattern were carried out using an initial model with atomic plane positions determined from the HAADF-STEM and STEM-EDS data. See supplementary material for details on the parameters used for the Rietveld refinements. A representative refinement of the XRD pattern and a schematic of the determined structure are shown in Figure 16. The refinement indicated that two phases were present: the $(PbSe)_{1.1}(FeSe_2)_2$ structure and an impurity PbSe phase indicated by the peak at ~29°. The Laue oscillations, diffraction data, HAADF-STEM image, STEM-EDS line profiles, and the Rietveld refinement are all consistent with one another and indicate that the novel, ternary $(PbSe)_{1.1}(FeSe_2)_2$ heterostructure formed.

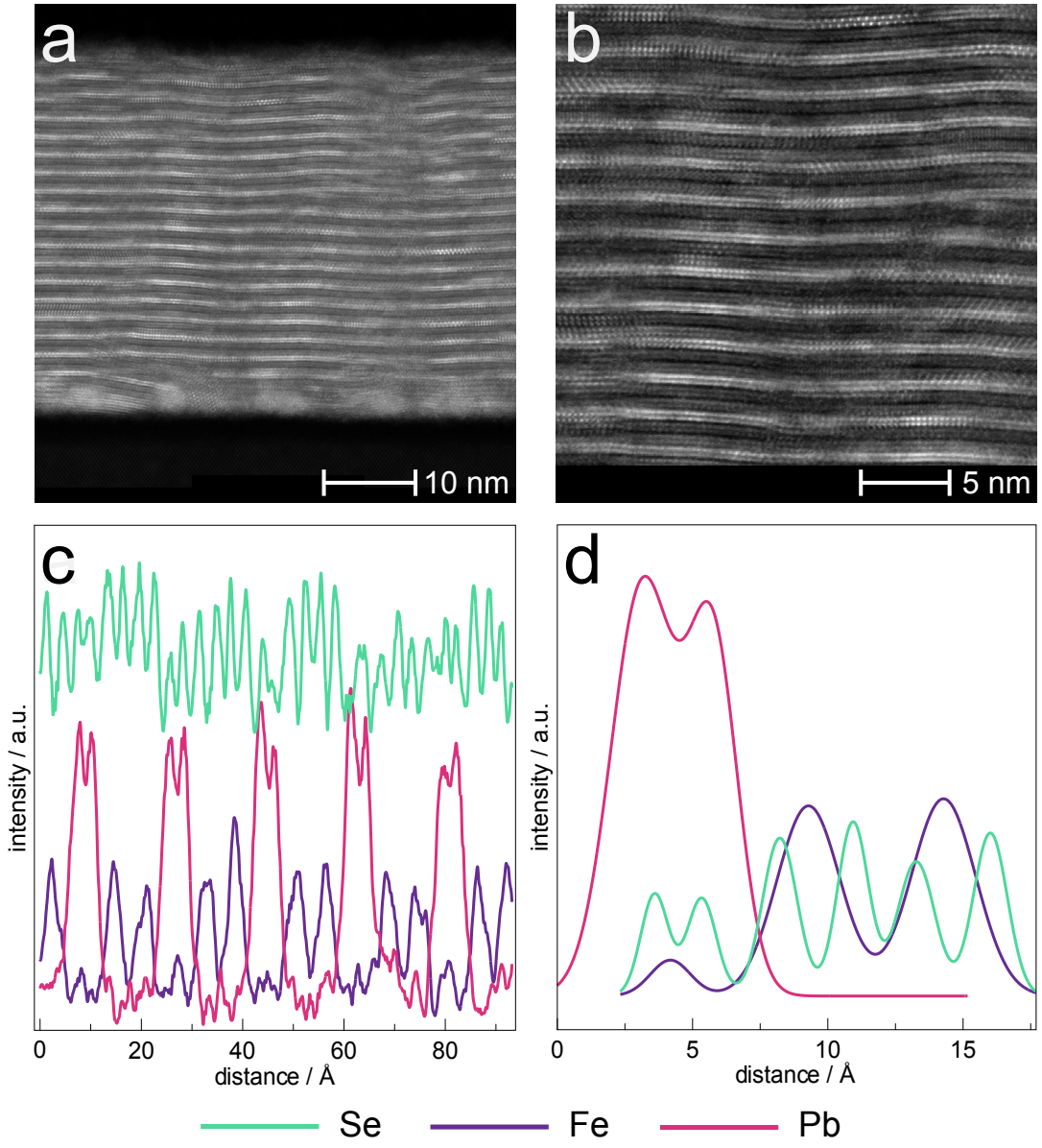

Fig. 2.15. a) HAADF-STEM image of a representative cross-section of the layered $(PbSe)_{1.1}(FeSe_2)_2$ sample b) close-up of the HAADF-STEM image showing individual layer structures c) EDS line profiles across the representative section of the sample and d) Gaussian fits of averaged EDS intensities.

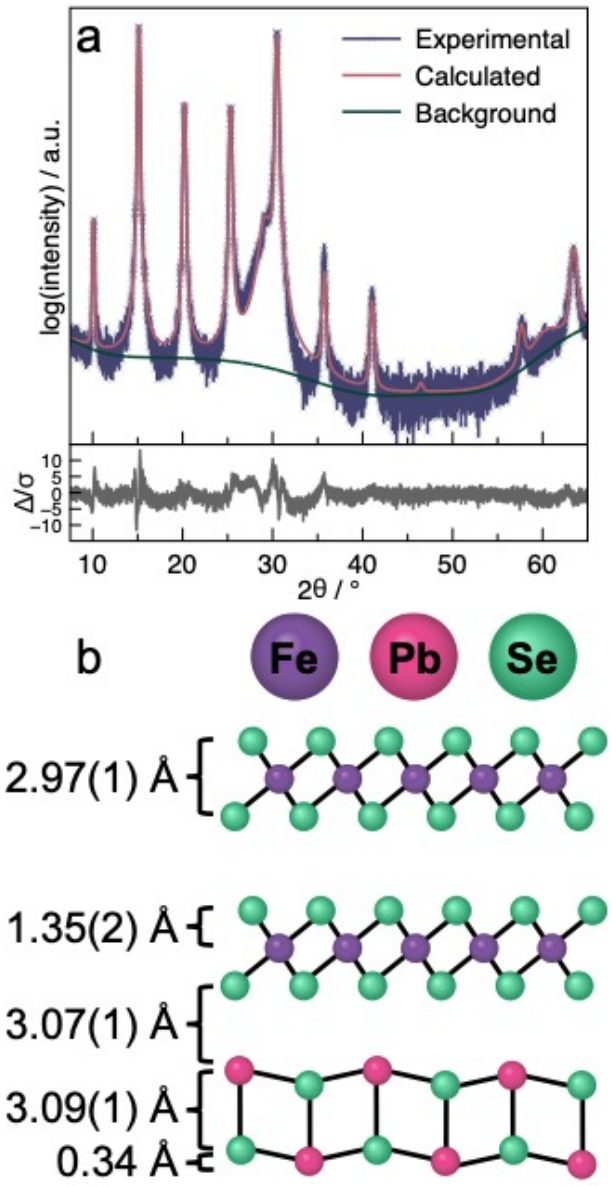

Fig. 2.16. a) Rietveld refinement of the specular XRD pattern of the $(PbSe)_{1.1}(FeSe_2)_2$ sample and b) a schematic of the structure determined from the refinement.

2.4 Conclusions

The three examples discussed in this manuscript demonstrate the ability to predict the kinetic stability of metastable compounds using the "island" approach and to prepare identified metastable compounds using MER. The preparation of a highly Fe-substituted VSe_2 sample, which is beyond the thermodynamically stable compositional range that can be achieved when forming $Fe_xV_{1-x}Se_2$ via traditional high temperature reaction of elemental

powders[40] and one-step chemical vapor transport,[41] demonstrates how local composition and small diffusion rates can be used to control the kinetics of nucleation and growth. The formation of the metastable $(PbSe)_{1.1}(FeSe_2)_2$ and $(Pb_3Mn_2Se_5)_{0.6}VSe_2$ heterostructures demonstrates how interfacial interactions between constituent layers can stabilize structures that differ from known binary or ternary compounds. Designing and depositing precursors that match the nanoarchitecture of the intended products favors their nucleation when annealed at low temperatures.

Preparing designed precursors has enabled the formation of compounds that are not found on equilibrium phase diagrams. We hypothesize that the local compositions and variation in composition within a deposited sequence of elemental layers promote the nucleation of targeted products as the system attempts to lower its free energy as rapidly as possible under the reaction conditions. Experimental parameters such as the amount of material deposited, the elemental layering sequence, and the processing conditions affect the nucleation, growth, and distribution of products – including impurity phases. The influence of these parameters on nucleation and growth is dependent on the topography of the free energy landscape, which is unique for each system. The "island" approach provides crucial estimates about the relative stability of nuclei of different structures in specific environments. Further examples are required to better understand how to use experimental parameters (elemental layer thicknesses, layer sequences, ratio of layer thicknesses, temperature, time) to control both nucleation and growth.

2.5 Bridge

This chapter presented examples and discussion of metastable structures formed via MER synthesis and described the characterization of the products. The following chapter provides a brief summary of the details on the experimental procedures used throughout this dissertation.

CHAPTER III

EXPERIMENTAL PROCEDURES

3.0. Authorship Statement

This chapter was written for this work alone with no intention of publishing it elsewhere. I am the primary author and wrote the following with assistance from my advisor David C. Johnson.

3.1. Synthesis of Designed Precursors via the MER method

All samples discussed throughout this thesis were prepared by the modulated elemental reactants (MER) synthesis method.[1,2] Precursors prepared by MER are designed to have very short (on the order of Angstroms) diffusion lengths to form targeted products. This reduces the energy barrier to form targeted products if they are local minima in free energy landscapes. The diffusion of the elements within the precursors is limited by maintaining room temperature conditions during the deposition and utilizing low temperature processing conditions post-deposition. This increases the energy barrier for precursors to un-mix to form more thermodynamically stable binary phases. This is shown pictorially in Figure 1.

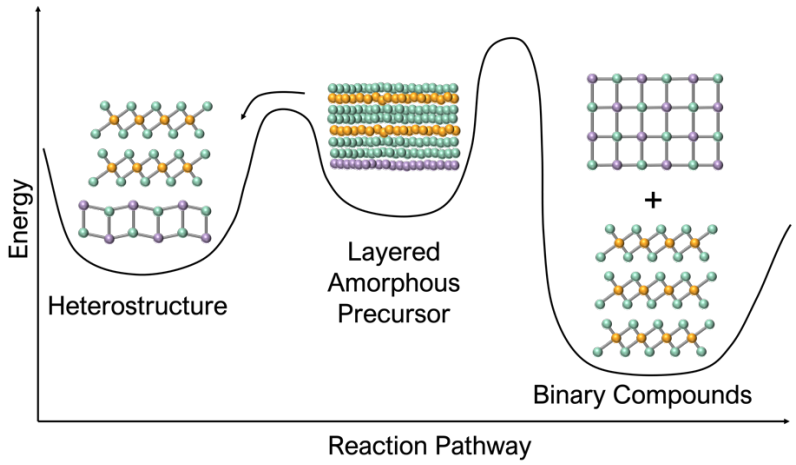

Fig. 3.1. Representation of the use of designed MER precursors to lower the energy barrier to form targeted layered materials and increase the energy barrier to segregate into binary phases.

MER precursors are deposited from elemental sources in a custom-built physical vapor deposition chamber. Pure metal sources are deposited using electron-beam guns, and selenium is deposited using a Knudson effusion cell. Viewports located above the electron-beam gun allow the user to monitor the state of metal sources in real time while depositing. Magnetic raster boxes are used to control the location of the electron beam and the amplitude of the beam sweeping. This is optimized so that the beam is centrally located on the metal source and the amplitude of the beam sweep covers ~80% of the source surface. The source surface topology affects the plume shape of the evaporated metals. Before the deposition of each sample, the beam sweep is reduced to a minimum and the electron beam is systematically moved across the source surface to smooth out any nonuniformity. Smoothing of the source surface increases the reproducibility of the deposition by maintaining a uniform plume shape.

The deposition rates of each of the elemental sources are monitored by quartz crystal microbalances located above each source. Evaporation rates of 0.2-0.9 Å/sec are maintained for each of the elements throughout the deposition. Computer-controlled shutters are located between each elemental source and the room temperature spinning sample substrate. The specific sequence and thickness of the deposited layers can be controlled. When the deposition begins, the computer controlled shutter for the first element in the sequence will open and the evaporation rate will be monitored to determine when the desired thickness has been deposited, which will cause the shutter to close. This is then repeated for each elemental source in the targeted sequence of layers. Nucleation and growth of products during the deposition is highly dependent on the layering sequence and layer thicknesses deposited. The deposited precursors are annealed to low temperatures (100-600°C) to promote crystallization.

3.2. X-ray Characterization Techniques

X-ray fluorescence spectroscopy is used for characterization of the composition of samples prepared by MER. All XRF measurements were collected with a Rigaku Primus-II wavelength dispersive x-ray fluorescence spectrometer with a Rhodium x-ray source. During XRF measurements, the samples are bombarded with high energy x-ray, which cause core electrons to be ejected. X-rays are then emitted as electrons from higher energy shells fall

down to fill the vacancy. The emitted x-rays are characteristic of both the specific element and specific orbital shell transitions. It was previously found by Hamann et al that at the thin film limit, absorption effects from XRF measurements could be ignored.[3] Therefore, the intensity of the XRF signal for a certain element is proportional to the number of atoms per unit area of that element in the film. In order to determine the proportionality constant between the XRF intensity and the amount of material in the film, films with known amounts of unit cells must be used to create a calibration curve for each element. This was carried out for binary and ternary Nb samples to create the calibration curve shown in Figure 2.

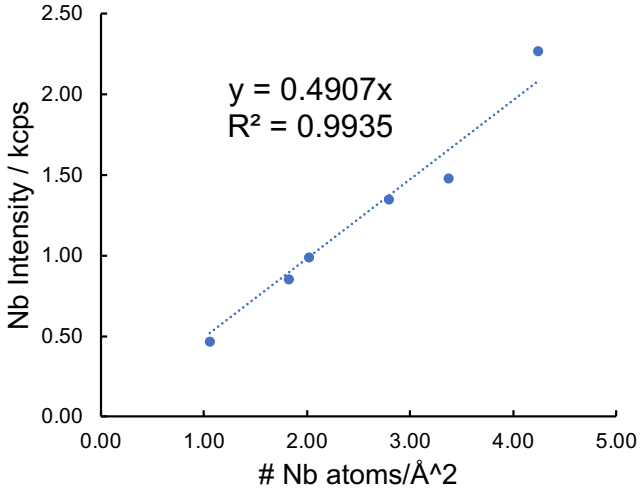

Fig. 3.2. Calibration curve created to determine the proportionality constant between the intensity of the Nb fluorescence peak and the absolute number of atoms/Å^2.

Multiple techniques are used to characterize the structure of samples prepared by MER including x-ray reflectivity (XRR), specular x-ray diffraction (XRD), and in-plane XRD. XRR, specular XRD, and in-plane XRD patterns for the samples presented in this thesis were collected on either a Bruker D8 or Rigaku Smartlab using Cu-Kα radiation.

X-ray reflectivity (XRR) measurements were carried out to determine film thickness. XRR patterns are collected in θ-2θ locked-coupled scanning mode from 0-10° 2θ along the axis perpendicular to the sample substrate. XRR patterns contain a critical angle, at which the X-ray begin to penetrate the surface of the sample. XRR patterns also contain Kiessig fringes, which arise from the constructive and destructive interference of x-rays reflected off

the top surface of the film and the interface of the film with the substrate. The critical angle location can be used to calculate the density of the thin film, and the locations of the Kiessig fringes can be used to calculate the total film thickness.[4] The angle at which the Kiessig fringes disappear can also offer information on the film "roughness" either at the surface or at the interface with the substrate.[5]

Specular XRD patterns are collected in θ-2θ locked-coupled scanning mode along the axis perpendicular to the sample surface along the range from 5-65° 2θ. For thin films that are crystallographically aligned perpendicular to the substrate, specular XRD patterns will contain only 00*l* Bragg reflections. The d-spacing calculated from the locations of the Bragg reflections can be used to determine the *c*-axis lattice parameter of the unit cell. The full-width at half-maximum (FWHM) of the Bragg reflections in the specular XRD pattern can be used to calculate the approximate grain size of crystalline domains along the *c*-axis.[6]

In plane XRD patterns are collected in grazing-incidence mode with the detector scanning across the axis parallel to the sample. For thin films that are crystallographically aligned perpendicular to the substrate that have turbostratic disorder, in plane XRD patterns contain *hk*0 Bragg reflections. For heterostructure samples containing more than one phase in the repeat unit, the reflections due to each phase will be present in the in plane XRD patterns. These reflections can be used to determine the unit cell type and the *a*- and *b*-axis lattice parameters of the phases in the repeat unit.

3.3. Bridge

The previous chapter describes the experimental procedures for synthesizing precursors via the modulated elemental reactants method and the most commonly used characterization techniques for MER samples. The following chapter discusses a method for extracting structural information from Kiessig fringes and Laue oscillations present in x-ray reflectivity and specular x-ray diffraction patterns.

CHAPTER IV

EXTRACTING INFORMATION FROM X-RAY DIFFRACTION PATTERNS CONTAINING LAUE OSCILLATIONS

4.0. Authorship Statement

Chapter IV This was published in *Zeitschrift für Naturforschung B* in 2022. The experimental work was performed either by me, A.M. Miller, or M.A. Choffel. S.R. Rich and F. Harvel contributed through research of relevant literature. A.M. Miller is the primary author. I aided in writing, editing, and interpretation of data. D.C. Johnson provided editorial assistance.

4.1. Introduction

Laue oscillations result from the incomplete destructive interference of a finite number of unit cells and occur when a sample consists of domains with the same number of unit cells across most of the area being probed. First predicted by Max von Laue, the Laue interference function relates the number of unit cells in the diffracting crystal to the distribution of diffracted intensity [1]. Generally, the presence of Laue oscillations are taken as confirmation that grown films are of high quality, homogenous, contain only the targeted compound, and have smooth and planar top and bottom interfaces [2–11]. The presence of Laue oscillations is frequently used as evidence of "the high crystallinity of samples" [12], "the uniformity of the film and smoothness of the interfaces" [13] or that "the out-of-plane order is high and coherent over the entire film thickness" [14].

While it is true that Laue oscillations are a qualitative indicator of sample quality, the presence of Laue oscillations also provides an opportunity to gain significant structural information about films. The most common quantitative analysis of Laue oscillations utilizes an equation derived from the Laue interference function to extract the total thickness of the crystalline phase [15–23, 24, 25]. The thickness obtained in this manner is often taken to be the total film thickness, which assumes that there is no additional thickness from amorphous or non-crystallographically-aligned layers present above and/or below the diffracting crystal.

There are only a few reports in the literature where both the oscillations in the X-ray reflectivity (XRR) at low diffraction angles and the Laue oscillations observed in the vicinity of a Bragg reflection are used to detect potential excess material. In these reports, differences between the total film thickness calculated from Kiessig fringes in the XRR data and the thickness of the crystalline layers obtained via the Laue oscillations were found [26,27]. Furthermore, the intensity of experimental Laue oscillations often differs from those predicted from the Laue function. The Laue function results in symmetric intensities of satellite reflections on either side of the Bragg maxima, but an asymmetric distribution of intensities on each side is also frequently observed [9,26–28]. In addition, the number of Laue oscillations observed on either side of the Bragg reflection varies significantly from sample to sample [2-28]. The extraction of structural information from Laue oscillations has been challenging due to the lack of a discussion of all relevant physical phenomena in a single reference that relates structural parameters to Laue intensities and provides examples illustrating the development of structural models from experimental data.

This paper addresses this challenge by presenting a summary of the relevant physical phenomena, showing how structural features in films impact the intensity and number of both Kiessig fringes and Laue oscillations that are observed, and provides examples of developing a structural model from experimental data. The first example illustrates an approach to simultaneously model reflectivity and diffraction patterns when these two phenomena are relatively uncoupled. The second example involves a more complex example where these two phenomena are both important in the same angular regions. Further efforts are required to create simulation software that enables the development of atom-level structural descriptions of films using the intensities of Kiessig fringes and Laue oscillations.

4.2. X-ray reflectivity and Kiessig Fringes

We begin this section with a short review of the physical origin of Kiessig fringes and show how increasing the structural complexity of films effects the intensity of the fringes with increasing angle using simulations. Examples show how to extract structural information from experimental data. Next, we discuss the origin of Laue oscillations and use examples to demonstrate how Laue oscillation intensities calculated using the Laue function

differ from experimental patterns. We illustrate how the interaction between reflectivity and diffraction effects cause the asymmetry in Laue intensities around the central Bragg reflection and use simulations to show the impact of structural imperfections on the intensities of Laue oscillations. We conclude by developing structural models from two experimental data sets where the total film thickness (calculated from the period of the Kiessig oscillations) is different from the thickness derived from the period of the Laue oscillations (defined as the product of the number of coherently diffracting unit cells and the *c*-axis lattice parameter).

Figure 1 shows XRR patterns for an experimental $TiSe_2$ film, along with simulated reflectivity patterns for 5.00 nm (*blue*) and 25.00 nm (*purple*) $TiSe_2$ films assuming a uniform electron density slab using the BedeREFS software [29]. The oscillations observed at low angles in these patterns are known as Kiessig fringes, first reported in 1931 [30], which result from interference between X-rays reflected off the top air/sample interface and those reflected off the sample/substrate interface. The position and spacing of the maxima (or minima) can be used to quantitatively determine the film thickness using a modified version of Bragg's law that includes a correction for refraction, as shown in eq. (1) [31].

$$sin^2\theta_i = {\theta_c}^2 + \frac{(n_i+\Delta n)^2\lambda^2}{4t^2} \qquad (1)$$

In this equation, θ_i is the angle of the observed Kiessig fringe maxima, θ_c is the critical angle, n_i is the index of the observed Kiessig fringe maxima, λ is the wavelength of the radiation utilized, and t is the total film thickness. As shown in Figure 1, the period of the observed Kiessig fringes is inversely related to the thickness of the films. The thickness of the experimental $TiSe_2$ film calculated using this equation is 50.10(5) nm (*black trace*).

An important point is that Kiessig fringes result solely from reflectivity phenomena - their presence and period do not depend on the crystallinity of the sample. Kiessig fringes will be observed in the reflectivity pattern for any thin enough sample with sufficiently smooth planar air/sample and sample/substrate interfaces, provided there is a difference in the index of refraction between the sample and the substrate. The intensity of the Kiessig fringes scales with the difference in electron density between the substrate and the film, with a larger difference producing more intense oscillations. Additionally, because the critical

angle for total internal reflection (θ_c) scales with electron density, the angle of each Kiessig fringe shifts depending on the average electron density of the film (eq. (1)).

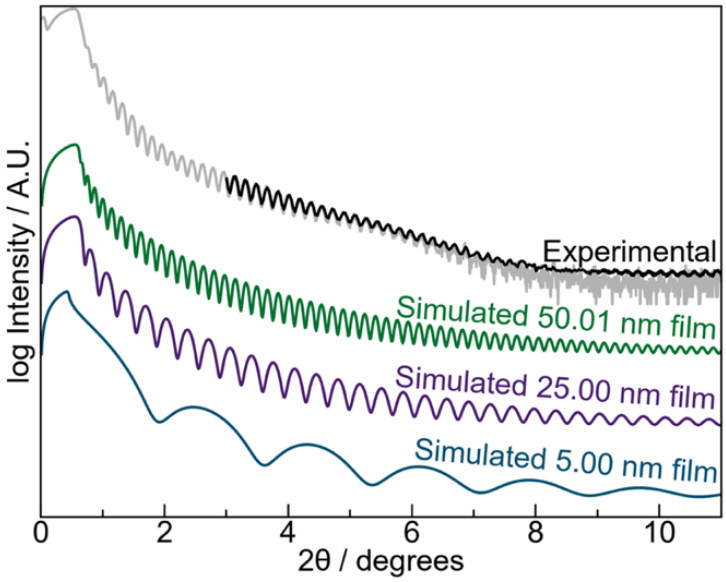

Fig. 4.1. Experimental x-ray reflectivity pattern of a 50.10(5) nm (black/grey) $TiSe_2$ film. Simulated reflectivity patterns from 50.1 nm (green), 25 nm (purple), and 5 nm (blue) $TiSe_2$ films are also shown. The period of the Kiessig fringes is inversely related to the film's thickness.

The rate of decay in the intensity of Kiessig fringes with increasing angle depends on interface roughness. Simulated reflectivity patterns from models containing atomically abrupt interfaces have Kiessig fringes that continue throughout the angular range, decreasing in intensity as the angle increases. The Kiessig fringes in the experimental pattern become unresolvable at an angle of ~7° 2θ. Parratt showed that the angle where Kiessig fringes are no longer visible depends on the sample's average top and bottom surface roughness and derived the relationship:

$$\Delta t = \frac{\lambda}{4(\theta_m{}^2 - \theta_c{}^2)^{1/2}} \qquad (2)$$

where θ_m is the angle of the last observed Kiessig maxima and θ_c is the critical angle [32]. The roughness of both the top and bottom interfaces controls the angle to which the Kiessig interference pattern will be visible. Figure 2 demonstrates how different amounts of

roughness in the bottom sample/substrate ($\sigma_{substrate}$) and the top air/sample (σ_{sample}) interfaces reduce the intensity of the Kiessig fringes. The slope of the initial decay of the intensity of the Kiessig fringes is different for the bottom and top interfaces. The shape of the intensity envelope can therefore be used to distinguish between roughness at the top or bottom interfaces. Kiessig fringes observed out to 7° 2θ correspond to an interfacial roughness of about 5 Å according to the Parratt relationship, eq. (2).

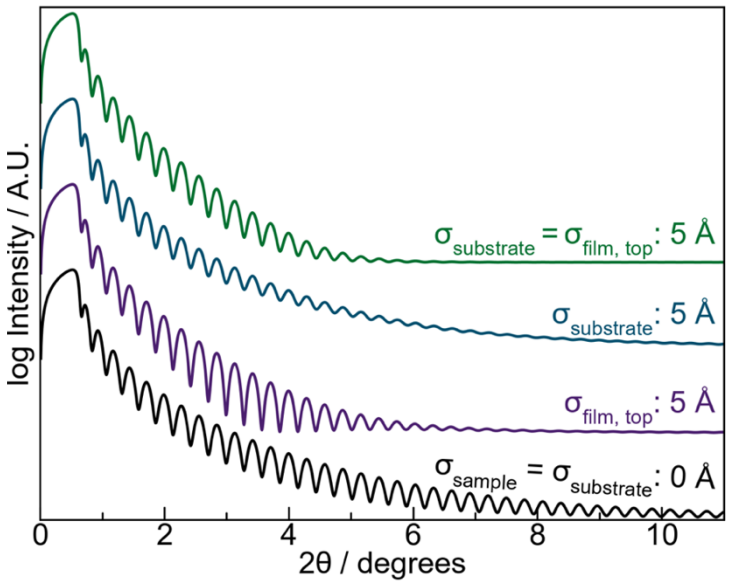

Fig. 4.2. The extent of interfacial roughness determines the maximum angle that the Kiessig interference fringes are visible. The shape of the intensity decay differs depending on whether the roughness is at the top or bottom interface.

Further information about a sample's structure can be extracted from deviations in the shape of its XRR pattern from that expected for a single layer [29]. The reflectivity from a film with a single constituent and perfect, planar interfaces is described by the Fresnel equations and the intensity decay is smooth, even, and continues to the angle at which the average scattered intensity is less than the background intensity [33]. If there are two layers in the film with different electron densities, Kiessig fringes from the two layers will both be apparent in the X-ray reflectivity scan. Figure 3 illustrates this effect, showing separate simulated reflectivity patterns for 2.42 nm TiO_2 and 50.05 nm $TiSe_2$ films, along with the calculated reflectivity patterns for a film containing a 2.42 nm TiO_2 layer on top of a 50.05

nm $TiSe_2$ film on a silicon (Si) substrate. The presence of oscillations with two different frequencies indicates that a second layer of material with a unique electron density and thickness is present in a film. Although somewhat subtler, the experimental pattern in Figure 1 also shows this effect, with a weak, low frequency oscillation apparent under the higher intensity oscillations from the total film thickness. The large period of the underlying oscillation suggests that the additional layer is much thinner than the $TiSe_2$ layer.

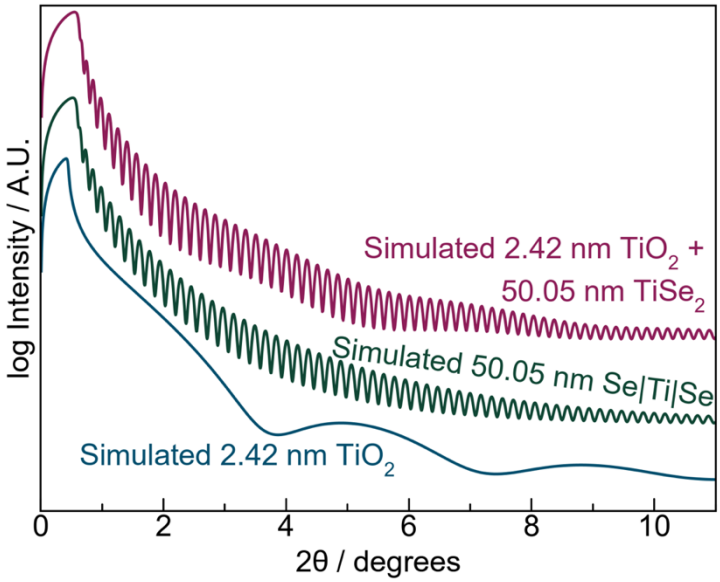

Fig. 4.3. Simulated XRR patterns of 2.42 nm TiO_2 (blue) and 50.05 nm $TiSe_2$ (red) films, along with the simulated pattern for a film containing 2.42 nm TiO_2 on top of 50.05 nm $TiSe_2$ (purple).

4.3. Laue Oscillations

If the sample consists of a crystallographically aligned film or contains a repeating sequence of deposited amorphous layers with different electron densities, the interference caused by the periodic changes in electron density results in Bragg reflections at angles given by Bragg's Law:

$$n\lambda = 2d\ sin(\theta) \qquad (3)$$

where n is an integer, and nλ is the difference in distance traveled by a wave scattered by repeating planes of equal electron density that are a distance (d) apart. The resulting evenly spaced set of reflections can be indexed as a one-dimensional crystal. Using Bragg's Law,

the thickness of the layers (or the size of the unit cell of crystals orientated perpendicular to the substrate) can be extracted from the diffraction pattern. Figure 4 shows the XRD pattern for a 79-layers thick $TiSe_2$ film, displaying four evenly spaced Bragg maxima, which can be indexed as 00*l* reflections consistent with those expected for a unit cell with a *c*-axis lattice parameter of 6.036(1) Å. The inset of Figure 4 expands the intensity and angular scale about the 001 reflection. The weak subsidiary maxima seen on the sides of this Bragg reflections are Laue oscillations. The positions and intensities of these satellite reflections are predicted by the Laue interference function:

$$I(Q) \propto \frac{\sin\left(\frac{N}{2}Qc\right)^2}{\sin\left(\frac{1}{2}Qc\right)^2} \qquad (4)$$

where c is the relevant lattice parameter, Q is the scattering vector, and N is the integral number of coherently diffracting unit cells [23,33]. Because Laue oscillations originate from the incomplete destructive interference of a finite number of diffracting unit cells between Bragg reflections, their presence suggests a low defect density.

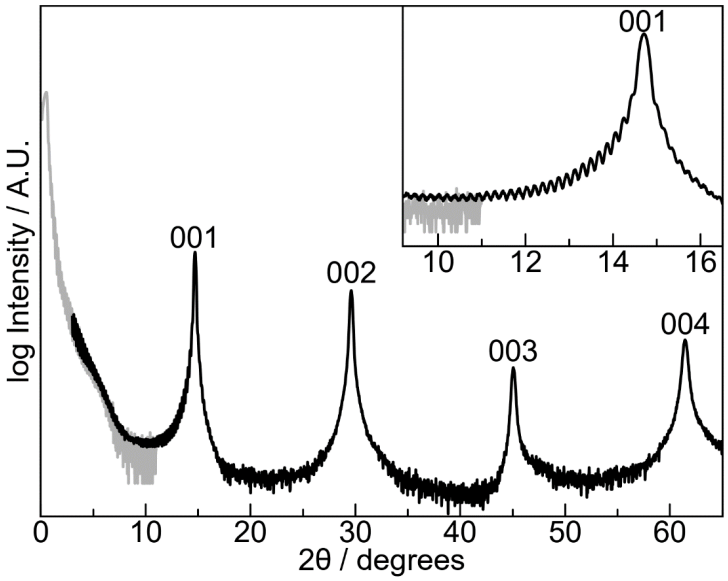

Fig. 4.4. Experimental XRR (gray) and XRD (black) patterns of a 79-layer crystalline $TiSe_2$ film. The four Bragg reflections can be indexed as 00l reflections yielding a c-axis lattice parameter of 6.036(1) Å. The inset highlights the Laue oscillations observed on the 001 reflection.

Kiessig fringes and Laue oscillations provide complementary structural information about the sample. The period of the Kiessig fringes determines the total film thickness (t_{sample}), inclusive of any impurity layers or amorphous material, while the period of the Laue oscillations determines the number of coherently diffracting unit cells in the film (N), which can be multiplied by the c-axis lattice parameter (c) to obtain the thickness of the coherently diffracting crystal.

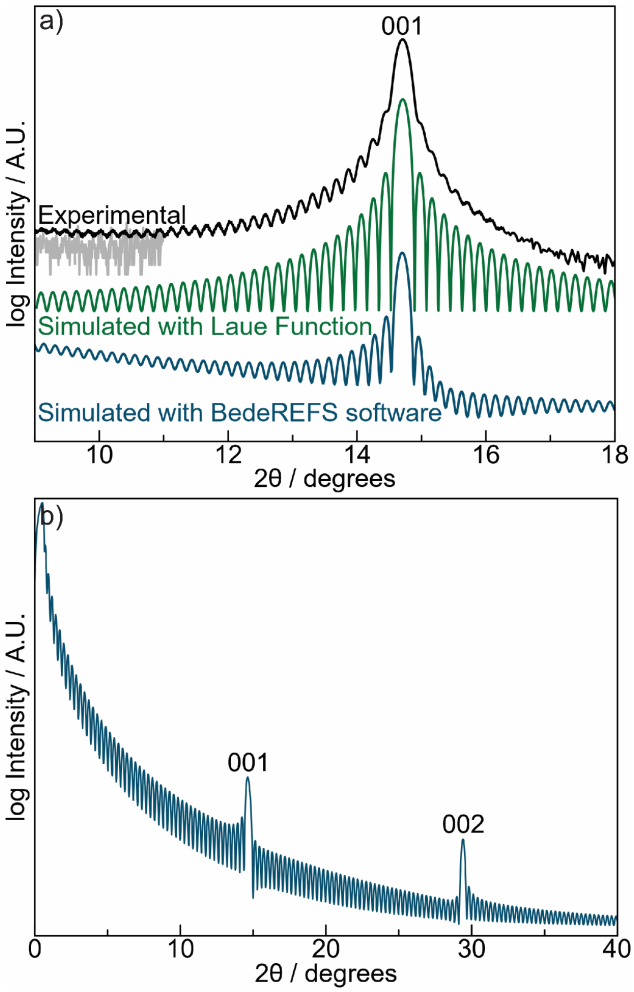

Fig. 4.5. (a) Comparison of the experimental Laue oscillations observed on either side of the 001 reflection of a $TiSe_2$ film with that calculated from the Laue interference function and a simulation that includes reflectivity using the BedeREFS simulation software. (b) A simulated XRR/XRD pattern of a 50-layer Se|Ti|Se film with a c-axis lattice parameter of 6.036 Å. The changing phase relationship between Kiessig fringes and Laue oscillations as the scattering angle moves through Bragg reflections is apparent in the lower average intensity between the 1st and 2nd Bragg reflections.

Structural defects typically prevent experimental diffraction data from exactly matching that expected for a perfect film. For example, the total amount of material in a film is difficult to control so the total film thickness is typically not equal to the thickness of the coherently diffracting crystal. Thus, the angular positions of the Kiessig fringes will differ from those calculated from the thickness of the coherently diffraction domain obtained from the Laue oscillations. The experimental amplitude of Laue oscillations is also typically much smaller than calculated, often asymmetric with respect to the Bragg reflection, and the rate of decay of the oscillations as one moves away from the main Bragg reflection varies significantly from sample to sample. These differences in amplitude are not often discussed when Laue oscillations are observed.

The Laue interference function predicts a symmetric distribution of satellite reflections centered on each Bragg maximum, as shown in Figure 5a (blue trace), but experimentally the intensity of the Laue oscillations is often different on either side of the Bragg reflection. Asymmetry of intensities was present in slightly more than half of the 27 representative reports we examined in a non-exhaustive literature search. This asymmetry occurs whether the Bragg reflection is dominated by the substrate, as in epitaxially grown films, or if the Bragg reflection is caused only by the film itself. The $TiSe_2$ film in Figure 5a (black trace) illustrates a typical intensity asymmetry around a Bragg reflection. The cause of the asymmetry in the intensity in this sample is the changing phase relationship between Kiessig fringes and Laue oscillations as the diffraction angle moves through that of a Bragg reflection. Figure 5b illustrates the effect of this changing phase relationship in a simulated diffraction pattern of a structurally perfect 301.8 nm thick film containing fifty 6.036 Å thick $TiSe_2$ layers. Here we use the approach of Zwiebler et. al., approximating the unit cell structure with slabs of the appropriate element in the simulation [34]. For the $TiSe_2$ layers, equal thickness slabs of Se, Ti, and Se were used totaling the thickness of the *c*-axis of the unit cell. Before the 001 reflection, the Kiessig and Laue effects are constructively interfering. Between the 001 and 002 reflections, the two are destructively interfering, resulting in the much lower average intensity between these reflections. The average intensity between the 2nd and 3rd reflections increases because the Kiessig and Laue effects are again constructively interfering. The bottom XRR pattern (black trace) in Figure 5 shows an expanded view of the oscillations around the 001 reflection, which are asymmetric.

Asymmetry caused by interference of the Kiessig and Laue effects is most likely to be observed for Bragg reflections at smaller 2θ values due to the decay of Kiessig fringe intensities as 2θ increases.

Experimentally observing the shift in phase between the Kiessig and Laue interference effects through Bragg reflections requires a film with extremely smooth interfaces, which is challenging to prepare experimentally. Figure 6 shows an experimental diffraction pattern where the changing sign relation between the two interference effects is clearly visible. This pattern also shows how the changing relative intensity of the Kiessig and Laue effects can cause a very weak Bragg reflection, resulting from the location of atoms in the unit cell, to appear split as the relative phase changes moving through the center of the 001 reflection.

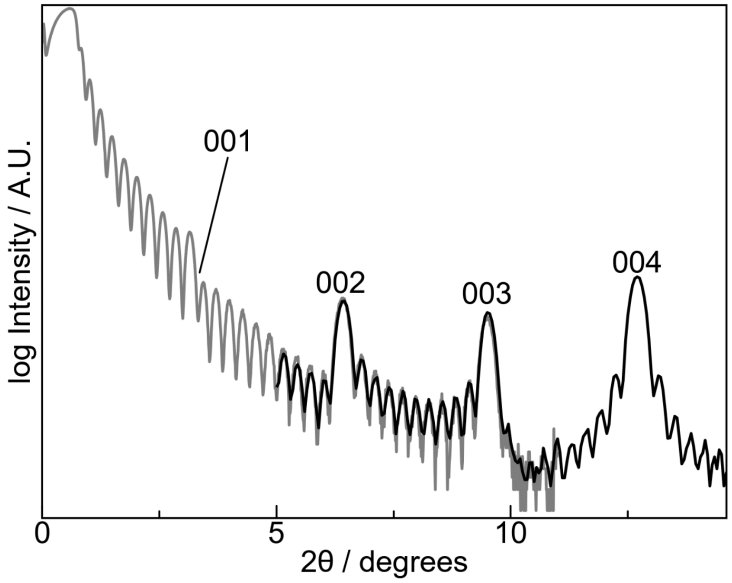

Fig. 4.6. Experimental diffraction data of a $(BiSe)_{0.97}(Bi_2Se_3)_{1.26}(BiSe)_{0.97}(MoSe_2)$ heterostructure.

The intensities of both Kiessig and Laue oscillations also depend on the abruptness and smoothness of the interfaces in the film. The relative magnitude of intensities of Kiessig oscillations depends on the smoothness of interfaces and the magnitude of the electron density differences between the constituents. The intensity of Laue oscillations depends on the percentage of the film that contains the dominant thickness of coherently diffracting

crystalline domains, the distribution of thickness of the crystalline domains (a form of roughness, as the entire area measured might contain several thicknesses), and the inherent intensity of the Bragg reflections, which depend on the location of atoms within the unit cell. Figure 7 shows the effects of increasing the substrate and sample interfacial roughness on the appearance of the interference pattern around the 001 reflection in simulated diffraction patterns of $TiSe_2$. The simulations approximate roughness by replacing an abrupt change in electron density at interfaces with a smooth gradient of width σ. Kiessig interference fringes are damped out as the magnitude of the roughness at the interfaces increases. Increasing roughness can damp out the Kiessig fringes enough that a symmetrical distribution of satellite reflections occurs around the Bragg maxima at higher angles. This infers that samples with an asymmetric distribution of the intensity Laue oscillations have smooth interfaces.

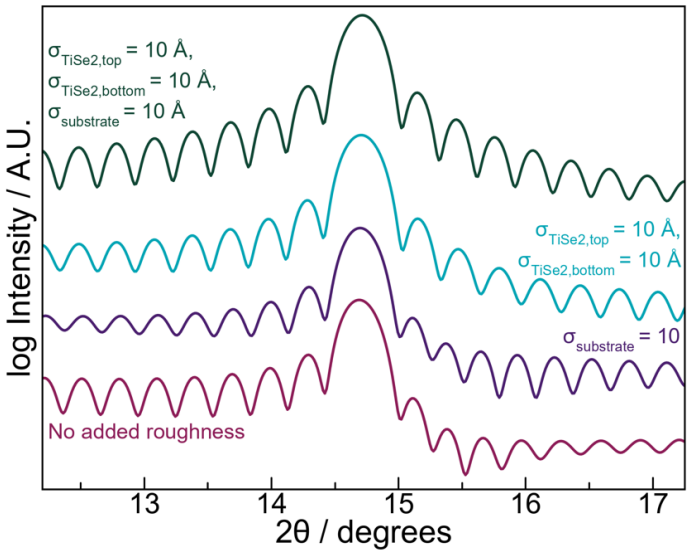

Fig. 4.7. Simulated XRR patterns of a 50-layer $TiSe_2$ film on a Si substrate illustrating how the roughness effects the symmetry of the satellite reflections around the Bragg reflections. Increasing roughness of the substrate and/or surface damps the intensity of the Kiessig fringes, making the Laue oscillations more symmetric.

The experimentally observed decrease in the intensities of Laue oscillations as one moves further away from the central Bragg maxima is typically much faster than predicted by the Laue oscillation function. While some of this intensity decrease is caused by substrate

and/or surface roughness of "extra" material, a distribution in the thickness of the coherently diffracting domain also contributes to this accelerated decrease in intensity. Figure 8 contains several simulations, where the percentage of coherent domains of different thicknesses was varied. If there are only two different thicknesses present, the interference pattern between the two different Laue oscillation functions is evident and the fringes closest to the Bragg maxima yield the average value of the coherent diffracting domain thicknesses. The fringes close to the Bragg maxima also yield the average value for the thickness for broader distributions, but the intensity of the oscillations decreases as one moves away from the Bragg maxima. These simulations suggest that the further the angular distance that Laue oscillations are observed from the Bragg maxima, the narrower the size distribution of coherently diffracting domains.

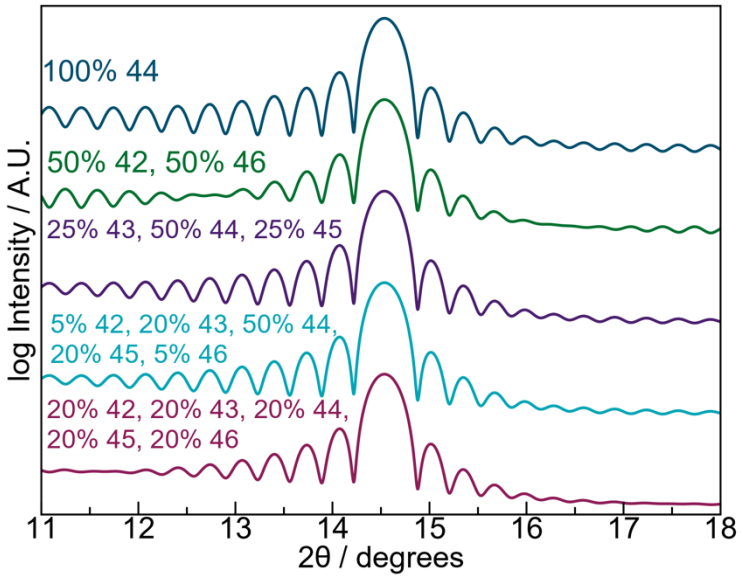

Fig. 4.8. Simulations of diffraction patterns from different distributions of coherently diffracting domains. The top simulation is from a sample with 44 $TiSe_2$ layers. The simulations below this are from different percentages of film area with the indicated number of $TISe_2$ layers in the coherently diffracting domain.

4.4. Developing Structural Models from Kiessig Fringes and Laue Oscillations

We conclude with two examples demonstrating how to systematically construct structural models using extracted structural information from X-ray reflectivity and X-ray

diffraction data on samples with both Kiessig fringes and Laue oscillations. The first example is an Fe-doped VSe_2 film whose XRR and XRD scans are shown in Figure 9. The total thickness of the film can be extracted from the Kiessig oscillations using eq. (1), yielding a film thickness of 271.0(2) Å. The Laue oscillations are used to determine the number of unit cells in the coherently diffracting domain from their positions. The Laue oscillations are consistent with 44 unit cells in the diffracting domain. The positions of the 00*l* Bragg reflections are used to determine the *c*-axis lattice parameter of 6.088(3) Å. The product of the number of unit cells (44) and the *c*-axis lattice parameter (6.088(3) Å) yields the thickness of the coherently diffracting domain – 267.9(1) Å. The Kiessig derived thickness is 3.1 Å larger, indicating that there is a thin layer of excess material. Independent corroborating evidence for a small amount of excess material was obtained from the absolute number of atoms / $Å^2$ of each element determined from X-ray fluorescence (XRF) data, which indicated that the excess material is vanadium oxide [35].

A structural model of the film to simulate the diffraction data below 20° 2θ was created from the data derived from the Kiessig and Laue oscillations. A model with a 267.9(1) Å thick $Fe_xV_{1-x}Se_2$ layer and top 3.1 Å thick surface layer of vanadium oxide was used to determine the top and bottom roughness of the film. Figure 9 shows the simulated pattern with interfacial roughness of σ_{VSe2} = 5.75 Å, σ_{oxide} = 5 Å, and $\sigma_{substrate}$ = 2.5 Å, which reasonably matches the low angle experimental reflectivity pattern. Dividing the 267.9(1) Å thick $Fe_xV_{1-x}Se_2$ layer into 44 explicit unit cells of $Fe_xV_{1-x}Se_2$ by using elemental slabs as discussed earlier provides a good fit to the experimentally observed positions of the Laue oscillations around the 001 reflection (see Figure 9). The intensities of the Laue oscillations, however, are too large, as the actual sample probably does not contain exactly 44 unit cells across the entire area probed by the X-ray beam, and we need to add the effect of substrate roughness. Including the substrate roughness determined from the $Fe_xV_{1-x}Se_2$ slab model does a reasonable job of matching the experimental pattern except that the Laue intensities are still too intense. The intensities of the Laue oscillations can be reduced by assuming that the film consists of regions that contain thinner coherently scattering domains, as discussed above. However, this will not yield a unique structural model for the film.

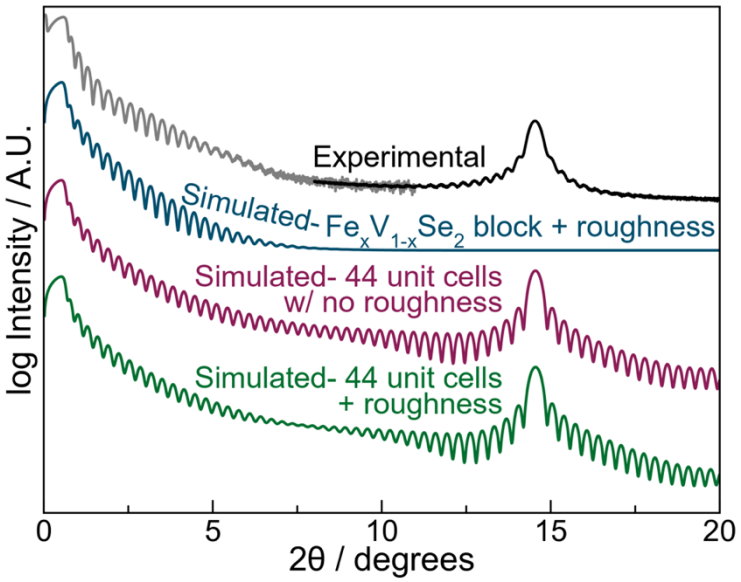

Fig. 4.9. (a) Experimental XRR (gray) and XRD (black) patterns of a 271.0(2) Å thick crystalline $Fe_xV_{1-x}Se_2$ film and simulated XRR pattern (teal) for a 267.9 Å thick $Fe_xV_{1-x}Se_2$ film consisting of 44 unit cells. The difference in Kiessig fringe period causes a poor fit of the simulated film above ~3 °2θ. (b) Including the excess material not incorporated into the coherent diffraction domain results in a simulated pattern that provides a reasonable fit over the entire range of the scan.

Diffraction patterns and their analysis become increasingly complicated as the Kiessig and Laue intensities interact across a large angular range. The XRR/XRD patterns collected of a $(BiSe)_{0.97}(Bi_2Se_3)_{1.26}(BiSe)_{0.97}(MoSe_2)$ heterostructure, displayed in Figure 10, illustrates these challenges [36]. The extracted total film thickness from the Kiessig fringes is 309.6(5) Å. From the period of the Laue oscillations at higher angles, it was determined that there are 10 unit cells in the coherently diffracting domains. The product of 10 unit cells times the *c*-axis lattice parameter (27.97 (10) Å) gives a crystal thickness of 279.7 Å. The difference between these two values is 29.9 Å. The question is how does one divide this thickness between the top and bottom of the crystalline domains? Figure 10 contains several simulated XRR patterns from models that distribute the 30 Å of excess material between the top and/or the bottom of the $(BiSe)_{0.97}(Bi_2Se_3)_{1.26}(BiSe)_{0.97}(MoSe_2)$ diffracting domain (Se was used as the excess material in these models). The simulated patterns are very sensitive to the exact distribution of the excess material between the front and back of the film. While we

assumed in these simulations that the composition of excess material at the bottom and the top were the same, this is not necessarily true, which adds another unknown parameter to potential models. This experimental pattern does not contain an explicit feature that allows us to estimate or separate the roughness of the substrate, the film, or the excess material. The large number of potential variables makes it currently impossible to extract additional information through simulations. Additional information, for example from HAADF-STEM images of film cross sections, is needed to limit the parameter space.

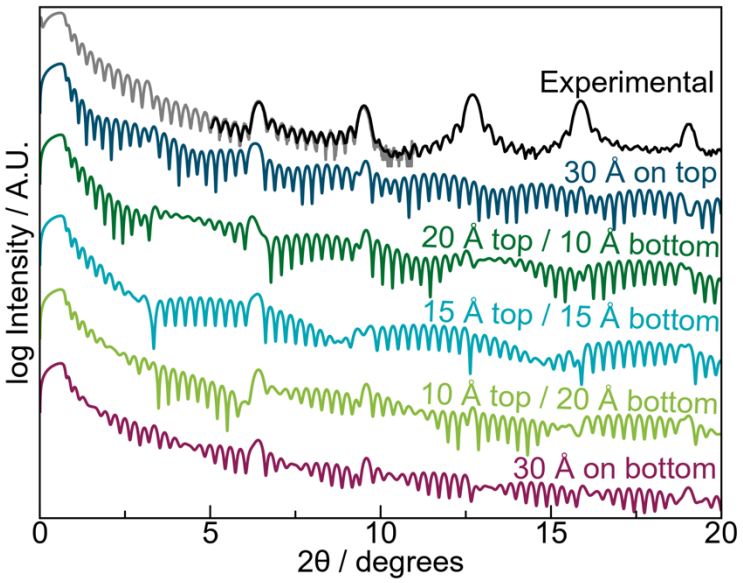

Fig. 4.10. Experimental XRR (grey) and XRD (black) patterns of a $(BiSe)_{0.97}(Bi_2Se_3)_{1.26}(BiSe)_{0.97}(MoSe_2)$ heterostructure, along with simulated patterns for models that consist of 10 unit cells of the targeted heterostructure, plus 30 Å of additional material distributed between either the top and/or the bottom of the heterostructure. No interfacial roughness was added to these models.

4.5. Conclusions

This manuscript shows how to extract quantitative structural information from Laue oscillations and Kiessig fringes. The thickness of the coherently diffracting domain can be calculated from the product of the *c*-axis lattice parameter and the number of unit cells present determined from the Laue oscillations. If there is extra material in the film, there will be a difference between total film thickness from the period of the Kiessig fringes and the

thickness of the coherently diffracting crystal domain. When the Kiessig fringes damp out before Laue oscillations are observed, it is possible to extract the roughness of the substrate and of the deposited layers. Samples with large differences between the total film thickness and crystal thickness are challenging to analyze, because the simulated patterns vary considerably as the extra thickness is partitioned above or below the coherently diffracting domain. Also challenging are samples with large angular regions where both the Laue and Kiessig interference effects contribute significantly. In films where Laue oscillations occur around reflections at high angles, however, the approach presented provides valuable additional information. Additional simulation tools need to be developed to get access to the additional structural information present in Laue oscillations obtained from experimental data.

4.6. Experimental

Films for this study were prepared using a custom high vacuum physical vapor deposition (PVD) chamber. Artificially layered precursors for binary thin films were prepared by repeatedly depositing M|Se bilayers, where ideally the number of atoms / $Å^2$ deposited in each bilayer is identical to the number required to form one unit cell of the targeted compound. Similarly, precursors for heterostructures were prepared by repeatedly depositing M|Se|M'|Se layers in the same manner. Metal layers were deposited using electron-beam guns, while Se was deposited with a Knudsen effusion cell. All precursors were deposited onto ⟨100⟩ Si substrates with a native SiO_2 layer. A pressure of less than 1×10^{-7} Torr was maintained during the deposition. In-house deposition software was used to control and monitor the amount of material deposited in each layer using pneumatic-controlled shutters and quartz crystal microbalances. After deposition, the precursors were removed from the vacuum chamber, briefly exposed to atmosphere, and brought into a dry-box (N_2 with <0.2 ppm O_2) where they were heated for 30 minutes at 500 °C and 350 °C for the Fe-doped VSe_2 and the $(BiSe)_{0.97}(Bi_2Se_3)_{1.26}(BiSe)_{0.97}(MoSe_2)$ films, respectively.

Structural characterization was carried out via XRR and XRD, while composition was determined using X-ray fluorescence (XRF). XRR and specular XRD patterns were collected on a Bruker D-8 Discover diffractometer. All diffraction measurements utilized a Cu K_α radiation source. Special care must be taken when aligning each sample to the diffractometer,

as the positions and intensities of reflectivity/diffraction features are extremely sensitive to sample alignment. To confirm the alignment of the sample in the goniometer, rocking curve scans were collected at two different small 2θ values. The maxima in both rocking curve scans occurring when the incident and exit angles are equal are evidence that the sample is correctly aligned in the center of the goniometer.

The absolute amount of each element deposited was determined using XRF data collected on a Rigaku ZSX Primus II with a rhodium source. Previously published calibration curves were used to relate the background-corrected integrated raw intensity to the atoms/Å^2 for each element [35]. Table 1 contains the calculated amount of each element required for the crystalline domains that contribute to the observed Laue oscillations along with the total number of atoms per unit area (areal density) of each element, as determined from the XRF measurements of each film.

Table 4.1. Experimental and target atomic areal density for the Fe-doped VSe2 and $(BiSe)_{0.97}(Bi_2Se_3)_{1.26}(BiSe)_{0.97}(MoSe_2)$ films as determined from XRF measurements.

Exp. V Atoms/Å^2	**Exp. Fe Atoms/Å^2**	**Exp. Se Atoms/Å^2**	**Target V Atoms/Å^2**	**Target Fe Atoms/Å^2**	**Target Se Atoms/Å^2**	**Target # of Unit Cells**
3.43(7)	1.4(1)	10.2(3)	3.43	1.71	10.29	44
Exp. Bi Atoms/Å^2	**Exp. Mo Atoms/Å^2**	**Exp. Se Atoms/Å^2**	**Target Bi Atoms/Å^2**	**Target Mo Atoms/Å^2**	**Target Se Atoms/Å^2**	**Target # of Unit Cells**
3.88(8)	1.15(2)	6.5(3)	3.37	1.18	6.8	10

Simulated XRR/XRD patterns were created using the BedeREFS software, which incorporates both reflectivity and diffraction physics that are required to accurately simulate thin film X-ray patterns [29]. BedeREFS uses “slabs” of electron density that are appropriately scaled to match the thickness and electron density of each layer in the film’s structure. Unless otherwise specified, the “slab” models created to simulate the reflectivity patterns, shown in Figures 1, 2, 3, 5, 7, 8, 9, and 10, had no added interfacial roughness, and were generated using a Si substrate with 10-20 Å of SiO_2.

4.7. Bridge

Chapter IV described a method to extract the maximum amount of structural information about a sample from a specular XRD pattern containing Laue oscillations. The discussion of the theory of Laue oscillations and how the sample structure influences their intensity will be continued in the next chapter. Chapter V describes how this theory was used to incorporate Laue oscillation fitting into the crystallography software GSAS-II.

CHAPTER V

LAUE OSCILLATION FITTING IN GSAS-II

5.0. Authorship Statement

Chapter V contains unpublished material that will be submitted to the *Journal of Applied Crystallography*. B.H. Toby and I are both primary authors. The experimental work and simulations were carried out by me. Coding of Laue oscillation fitting into GSAS-II was carried out by B.H. Toby. D.C. Johnson provided guidance and editorial assistance.

5.1. Introduction

Thin films are a broad area of considerable research interest due to their current and potential applications in technologies including photovoltaics, electronics, and memory devices.[1–5] This research effort has led to the development and optimization of many synthetic approaches to prepare films, including well known techniques such as CVD, ALD, PVD, and MBE.[6–11] Thin film samples of crystallographically aligned materials grown by these techniques can contain Laue oscillations in specular x-ray diffraction patterns. Laue oscillations occur due to the incomplete destructive interference between Bragg reflections caused by a finite number of unit cells and are commonly taken as an indicator of a high quality crystalline film. However, limited quantitative information about the film structure is typically extracted from the oscillation period and the decay of Laue oscillation intensity away from the main reflection.

For crystallographically aligned thin films, structural analysis can be performed by refining the intensity of the family of reflections present from the aligned grains in a specular XRD pattern. The simplest case is one-dimensional structural analysis of films with the unit cell *c*-axis aligned perpendicular to the substrate. In this case, only 00*l* reflections appear in the specular XRD pattern and their intensities are determined by the position of atomic planes along the z-axis. Constructing a model structure as an orthorhombic or tetragonal lattice with two very short in-plane lattice dimensions and the unit cell c-axis lattice parameter as the specular lattice dimension yields a simulated pattern containing only (00*l*)

reflections. The atomic plane positions determined by the distribution of the atoms along the unit cell *c*-axis can be included in the model to fit the specular XRD pattern using Rietveld analysis.[12] Rietveld analysis, however, cannot currently refine XRD patterns containing Laue oscillations because software packages assume an infinitely thick sample with zero intensity between Bragg reflections. To obtain a diffraction pattern without Laue oscillations for refinement, XRD scans are typically at a significant offset angle. The off-specular scattering obtains intensity from grains tilted from the surface of the substrate with a larger variation in grain sizes, which depresses the intensity of the Laue oscillations. Unfortunately, these grains may not be representative of most of the film. Ideally, a Rietveld refinement could be carried out on a specular pattern containing Laue oscillations to determine the structure of the highly ordered crystalline grains and to extract additional structural information from the Laue oscillations.

Calculating the intensity and positions of Laue oscillations is challenging because a variety of physical phenomena (strain, defects, non-abrupt interfaces, a distribution of the number of unit cells in the crystalline domains, and the position of the atoms within a unit cell) impact the intensity of Laue oscillations as a function of diffraction angle. The intensity of the Laue oscillations on the high-angle side of the Bragg reflection versus the low-angle side of the Bragg reflection is often asymmetric, which has been attributed to a variety of factors including interference with Kiessig fringes[13] and sample strain,[14-16] but can also be causes by the modulation of electron density within the unit cell. Herein we discuss the relevant theory behind Laue oscillations and discuss how the periodicity, intensity, asymmetry, and damping of Laue oscillations arise from the sample structure.

At present it is not clear how the effects of each physical phenomenon could be parameterized to calculate Laue intensity for implementation into Rietveld fitting. Therefore, we present an intermediate approach for fitting Laue oscillation peaks where the positions of Laue oscillation maxima are generated from a refinable number of unit cells in the coherently scattering domains, but reflection intensities are fitted as empirical least-squares parameters rather than derived from a structural model. This method has been implemented into the crystallography data analysis software, GSAS-II. Several empirical parameters are introduced into the fit for each reflection to account for peak shape, Laue oscillation damping, and the asymmetry of Laue oscillation intensities on either side of the Bragg

reflection. The empirical parameters introduced allow for more qualitative fitting of patterns containing Laue oscillations, but a quantitative interpretation of the relation between the parameters and the structural facets of the sample is not currently possible. This empirical approach to fitting Laue oscillations in GSAS-II represents a first step towards more quantitative structural analysis of films with XRD patterns containing Laue oscillations. The usefulness of our intermediate model is demonstrated by 3 example fits experimental patterns containing Laue oscillations.

5.2. Laue Oscillation Theory

For layered, crystallographically aligned thin film samples that are very high quality, on-specular x-ray diffraction patterns will contain Laue oscillations, which result from the incomplete destructive interference of X-rays diffracted from a finite number of unit cells in the direction perpendicular to the substrate surface. Laue oscillations can be modeled through a simple simulation based on the Laue equation:

$$I(Q) \propto \frac{\sin\left(\frac{N}{2}Qc\right)^2}{\sin\left(\frac{1}{2}Qc\right)^2} \qquad \text{(Eq. 1)}$$

where Q is the scattering momentum transfer, $Q = 4\pi \sin\theta \,/\, \lambda$, c is the lattice parameter in the direction perpendicular to the substrate, and N is the number of unit cells in the coherently scattering domain.

The Laue oscillation spacing is determined by the average number of unit cells in the coherently diffracting domain, *N*. Patterns of oscillations calculated for different values of N from equation 1 and the experimental *c*-axis lattice parameter can be compared with the experimental XRD pattern to determine N. The average thickness of the coherently scattering domain, obtained by multiplying the average number of unit cells by the lattice parameter perpendicular to the substrate, can be compared to the total film thickness derived from X-ray reflectivity patterns to calculate the fraction of the film composed of the coherently diffracting domain and impurity phase(s).[13]

In practice, Eq. 1 does not quantitatively match most experimental peak profiles (see Fig. 1) as it assumes the entirety of the sample has the same coherently scattering domain

size and that the substrate and top surface of the sample are atomically flat. The difference between simulated and experimental Laue oscillation patterns results from a variety of factors related to the "perfection" of the sample. Peak broadening is caused by several contributing factors including the finite thickness of the diffracting crystal, instrument broadening, local strain, and any curvature of the film.[17] In our discussion which follows, the effect of these factors will be categorized as those that cause "damping" and those that cause "asymmetry". "Damping" refers to the intensities of Laue oscillations decreasing more quickly than predicted by the Laue equation as the difference between the 2θ value and the position of the Bragg peak increases. "Asymmetry" refers to the tendency of Laue oscillations on the lower 2θ side of the Bragg peak to differ in intensity and/or periodicity from those on the higher 2θ side.

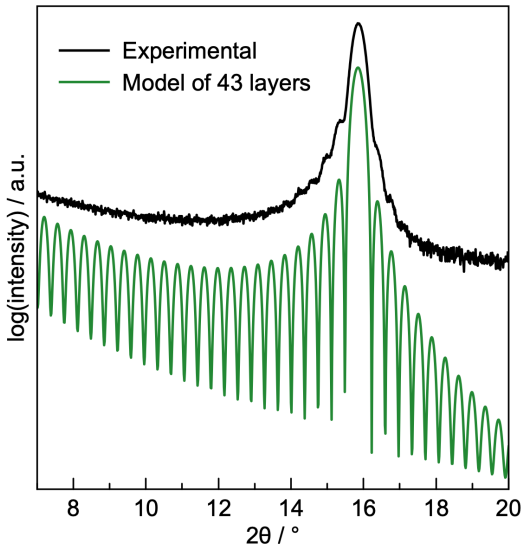

Fig. 5.1. Comparison of XRD pattern simulated from Laue oscillation equation with experimental XRD pattern containing Laue oscillations.

5.3. Asymmetry

5.3.1. Kiessig interference

Asymmetry in the intensity of Laue oscillations on either side of the Bragg reflection is frequently observed.[18-21] One factor that may result in asymmetry of Laue oscillations around Bragg reflections at low angles (<10° 2θ) is the interference between the Kiessig

fringes arising from the total film thickness and the Laue oscillations arising from the thickness of only the coherently diffracting domain. As has been discussed previously,[13] for films that are entirely composed of crystalline material, the location of the Kiessig fringes and Laue oscillations are identical. If the film thickness is greater than the size of the coherently diffracting domains, a phase shift between the Kiessig fringes and Laue oscillations occur as the scattering angle moves to 2θ values greater than the Bragg peak location. This phase shift can affect the intensities of the Laue oscillations on the high angle side of the Bragg peak relative to those on the lower angle side of the peak.

5.3.2. Electron Density Modulation

Asymmetry in the intensity of the Laue oscillations can also be caused by the variations in electron density of the unit cell inherent to the structure and crystallographic orientation of the coherently scattering domain. Figure 2 illustrates how the decay of the intensity of Laue oscillations can be asymmetric using a model containing different thicknesses of two elements with different electron densities. In this simple model, the electron density within the layers was modeled as uniform and continuous, and 50 unit cell layers were stacked on top of an infinitely thick Si substrate, as shown pictorially in Figure 2A. The continuous distribution of electron density within each constituent layer in the unit cell results in a square-wave function for the electron density as shown in Fig. 2C for the three different unit cells used. If the two layers are equal thickness, the asymmetry of the intensity of the Laue oscillations on either side of the Bragg reflection is minimized. If the more electron-rich layer is made thicker than the electron-poor layer, the Laue oscillations at angles less than the Bragg reflection are much more intense than those at angles greater than the Bragg reflection. The opposite is true if the more electron-rich layer is thinner than the electron-poor layer.

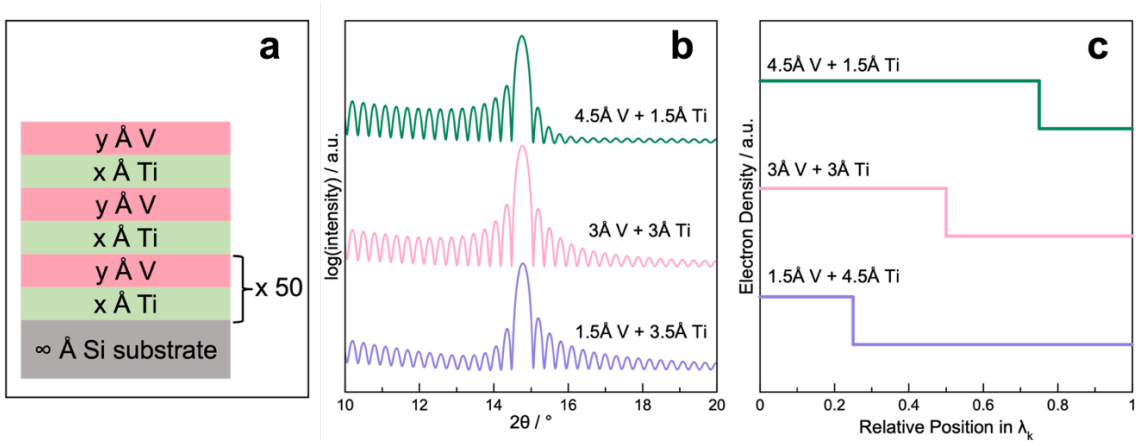

Fig. 5.2. a) Pictorial representation of the modeled unit cell used to simulate Laue oscillations consisting of an x Å thick electron-poor Ti layer with y Å thickness of an electron-rich V layer stacked on top. The ratio of x and y was varied, but the sum of x and y was kept constant equal to 6 Å. b) Simulated XRD patterns containing Laue oscillations for three modeled unit cells. c) A schematic representation of the electron density distribution in the modeled unit cells

5.3.3. Strain/Defects/non-uniform interfaces

Asymmetry in the intensity of the Laue oscillations can also arise from defects, non-abrupt interfaces, and strain. Strain has an effect both on peak broadening[17] and on the asymmetry of the intensities of the Laue oscillations. The effect of strain on the asymmetry of the intensity of the Laue oscillations across a Bragg reflection has been described previously with different approaches to calculate the diffraction intensity based on strain parameters proposed.[14-16] The damping and reduced intensity of the oscillations on the high angle side of the Bragg reflection relative to those on the low angle provides direct experimental evidence of dilatative strain normal to the film caused by displacement of atoms from their ideal lattice points. Displacement of atoms from their latticed points can cause phase shifts. For example, if the sample contained vacancies or inclusions of atoms in interstitial sites, the disorder caused by defects within the layers could cause a phase shift in the diffracted intensity, which would appear as asymmetry in the Laue oscillation pattern. This effect can also be thought of as arising from non-abrupt interfaces, which are typically used as an indicator of sample defects. However, non-abrupt interfaces may also arise

because of substrate roughness or from a non-uniform distribution of the film across the substrate.

5.4. Damping

5.4.1. Distribution of Crystalline Domain Sizes

One factor that can cause damping of Laue oscillations is a distribution of crystalline domain sizes around the average. This is especially applicable for films that are "rough," as thicknesses varying by +/- an integer number of unit cells will cause the film surface to be nonuniform. However, this effect can also be prevalent in films that do not appear significantly rough, as phases present above or below the coherently diffracting domains can lead to a smooth surface. Laue oscillations result from only the coherently scattering domains, and a distribution of domain sizes below the total thickness of the film will still lead to intensity damping. The effect of the interference is amplified for the intensities of Laue oscillations at 2θ values further from the Bragg reflection, which are significantly more damped than those at narrower 2θ values around the Bragg peak.

To demonstrate the impact of a distribution of domain sizes on the intensities of the Laue oscillations, we simulated the interference for different Gaussian distributions of 40-60 layer domains with a 6 Å unit cell length. The percentage contribution of intensity for each layer was calculated based on Gaussian distributions with standard deviation values of 1, 2, or 3 layers and an average of 50 layers. The scaled intensities of each pattern were then summed at each 2θ value to give the resulting Laue oscillation patterns (Fig. 3). A broader distribution of domain thicknesses, as given by the standard deviation, results in increased damping of the oscillations, especially at 2θ values furthest from the Bragg peak. For a standard deviation of 3 layers, oscillations are only observed in a narrow range of 2θ values around the Bragg reflection.

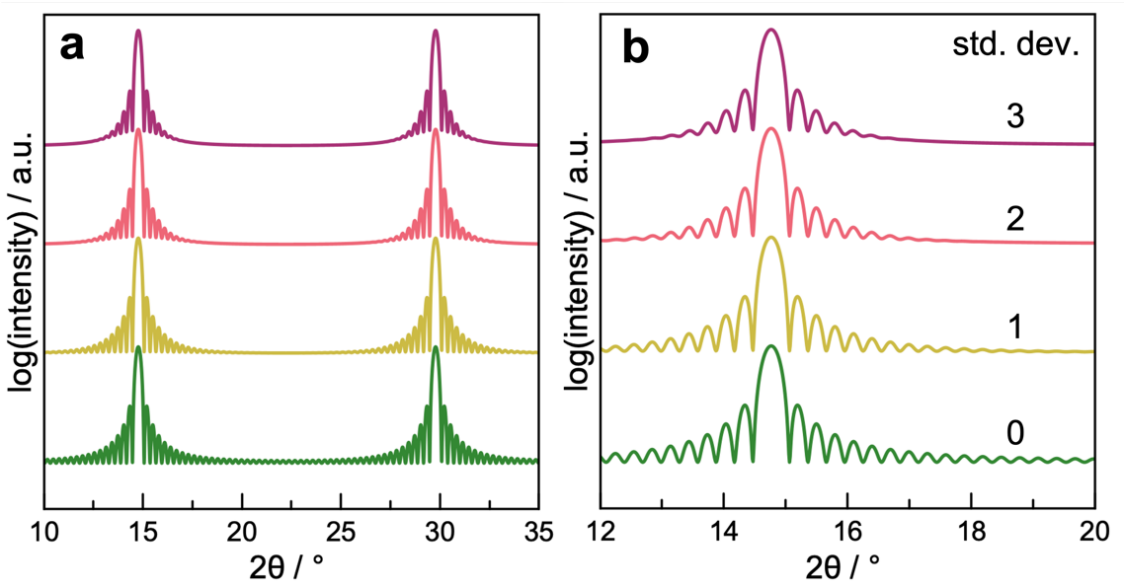

Fig. 5.3. Laue oscillations simulated for Gaussian distributions of the number of layers around an average of 50. The XRD patterns are displayed over a) broader and b) narrower 2θ ranges. The pattern with a standard deviation of zero is the Laue oscillation pattern for 50 layers.

5.4.2. Alignment to Substrate

Damping is also dependent on the crystallographic alignment of the film to the substrate and on the relative alignment of the crystalline domains. To visualize the effect of crystallographic alignment on the intensity and damping of the Laue oscillations, four different θ-2θ specular XRD patterns were collected on the same sample with a fixed "offset" between θ and 2θ (Figure 4). The offset was used to approximate the effect of increasing the number of domains with non-perfect crystallographic alignment to the substrate. The line width of the Bragg reflection is also an indicator of the film alignment, as a larger number of aligned crystalline domains will result in larger grain sizes and narrower Bragg reflections. For example, the pattern collected at an offset of 0.5° has a narrower Bragg reflection that the pattern collected at an offset of 0°, suggesting preferred alignment of the crystalline domains. The Laue oscillations nearest to the central Bragg peak remain visible even at an offset of 1.5°. This suggests that small differences in the alignment of the crystalline domains will not cause a large effect in the damping of the Laue oscillations nearest to the Bragg maxima.

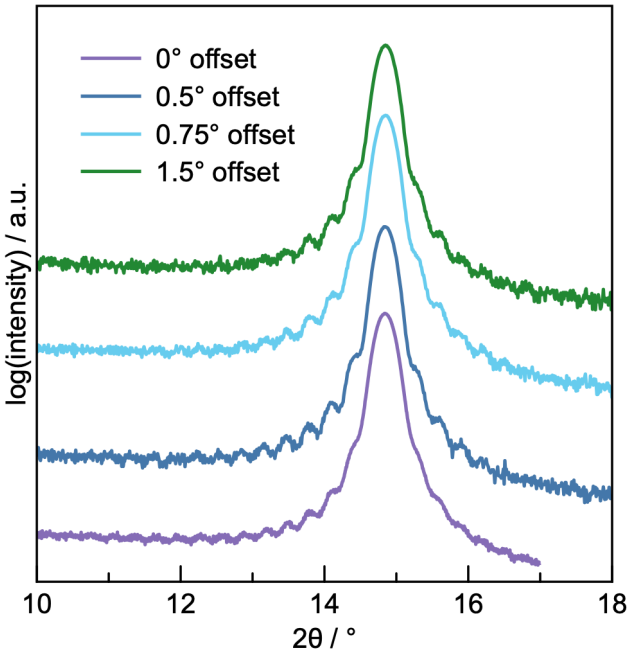

Fig. 5.4. Specular XRD patterns for the same sample with increasing offset between θ and 2θ.

5.5. Development of a Quantitative Laue Oscillation Profile Model

As has been described, the Laue oscillations computed with Eq. 1, while representative of the scattering to be seen under ideal circumstances, will not account for the finite resolution function of a powder diffractometer, nor the previously discussed materials imperfections or the asymmetry in the distribution of electron density in the unit cell. To generate a peak shape that can be used to fit observed peaks quantitatively, a new profile function has been introduced into the GSAS-II capability for fitting individual or groups of peaks in a selected region of a pattern. Specular diffraction scans, when read into GSAS-II are given a distinct tag (PLF) to designate that a special peak shape will be used, as described below.

To account for the faster falloff in the intensity of the oscillations, a negative exponential envelope term to damp the oscillations as a function of the distance from the peak position, Q_p, was added to Eq. 1. Further, to model the asymmetry in intensity between the two sides of the peak, two separate damping terms were used that affect the intensity of oscillations on the low-angle side or the high-angle side. Thus, Eq. 1 becomes:

$$I(Q) = \exp\left[-(10^d)(Q_p - Q_i)^n\right]\frac{\sin^2\left({}^{NQ_ic}/_2\right)}{\sin^2\left({}^{Q_ic}/_2\right)}$$

where *d* is the intensity damping for the oscillations. To allow for asymmetry between the two sides of the peak, one damping term 10^d is used on the low-angle side and another damping term 10^{d*} is used on the high-angle side. The exponentiation here allows relatively small changes in *d* to have significant changes in the profile, thus improving the refinement of these terms.

To account for the impact of the instrumental resolution, this damped Laue oscillation equation is convoluted with instrumental profile contributions using the NIST Fundamental parameters code.[22,23] This allows introduction of the following profile terms: a Gaussian peak with variance σ; a Lorentzian peak with FWHM γ; an emissions spectrum, which will account for the presence of multiple wavelengths, for example for $K\alpha_1$, α_2 spectrum. A correction for axial divergence could be included if a very long layer repeat distance were to create a very low angle peak.

Normally GSAS-II performs peak fitting with independent parameters for each peak's position and intensity. Peak widths in terms of Lorentzian and Gaussian contributions, σ and γ respectively, may be set individually, be determined from individually refined terms or be determined from U, V, W, X and Y (Rietveld-adapted Cagliotti profile terms) which are usually determined by instrument calibration or from instrumental fundamental parameters.[24,25] For Laue oscillation peak fitting, the peak positions are generated from a single lattice parameter, which may be refined. Likewise, only a single *N* value is specified for all peaks, but since this is an integer, it cannot be refined; instead a visualization mechanism is provided to show the positions for the oscillation fringes. Each peak does have an independent term for the peak area, and for *d* and *a*. As before the peak width terms σ and γ may be set individually, be refined or, optimally, determined from instrumental calibration.

5.6. Simulated and Experimental Examples

The newly implemented Laue oscillation fitting software was first tested on several simulated data sets, and two representative examples are shown in Figure 5. The simulated

XRD patterns were constructed from a model with either c = 8 Å and N = 10 layer (Fig. 5a) or c = 15 Å and N = 20 layers (Fig. 5b) and calculated via Eq. 1. The Laue oscillation fitting software implemented here was able to provide good fits of the data with the correct c and N values.

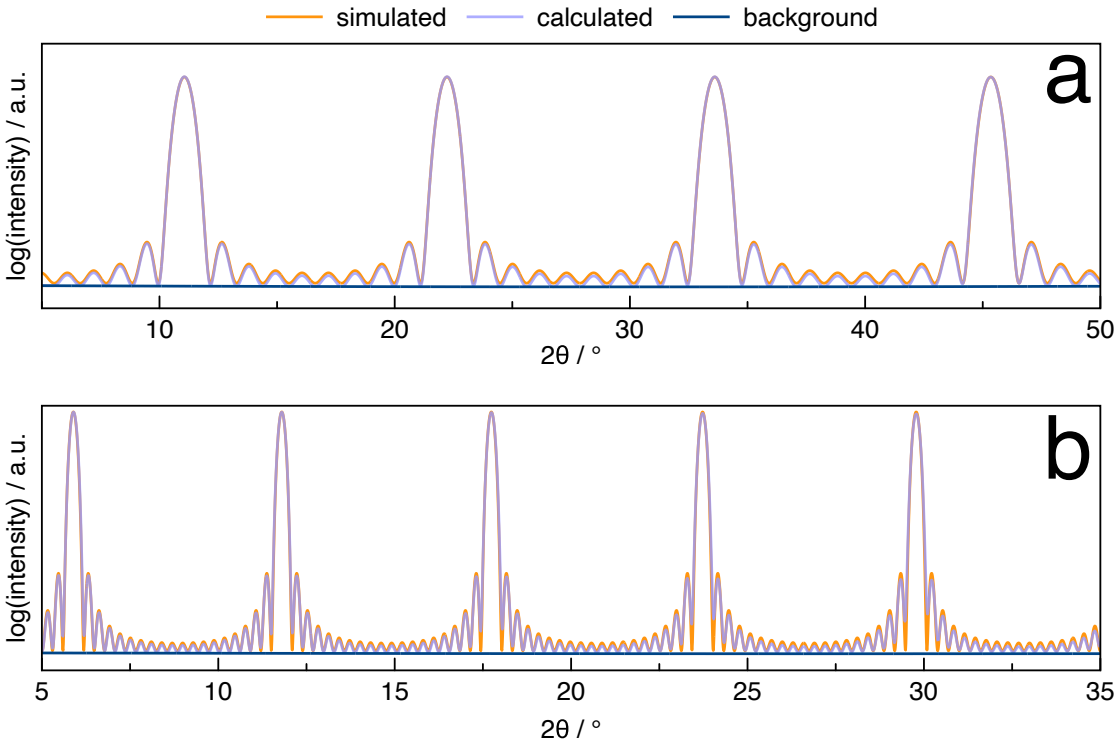

Fig. 5.5. Fits of simulated XRD patterns for a) a model with c = 8 Å and N = 10 layers and b) a model with c = 15 Å and N = 20 layers.

Given the success in fitting simulated XRD patterns for perfect samples, the Laue oscillation software was then used to fit a simulated pattern with intensity damping due to a distribution of the number of unit cells in the crystalline domains around an average of 50 with a standard deviation of 3. The calculated XRD pattern from a model with c = 6 Å and an average N = 50 and the fit provided by the software is shown in Figure 6. The abrupt damping in the simulated pattern could not be replicated by the software, but the minimally damped oscillations located nearest to the Bragg peak were fit reasonably well.

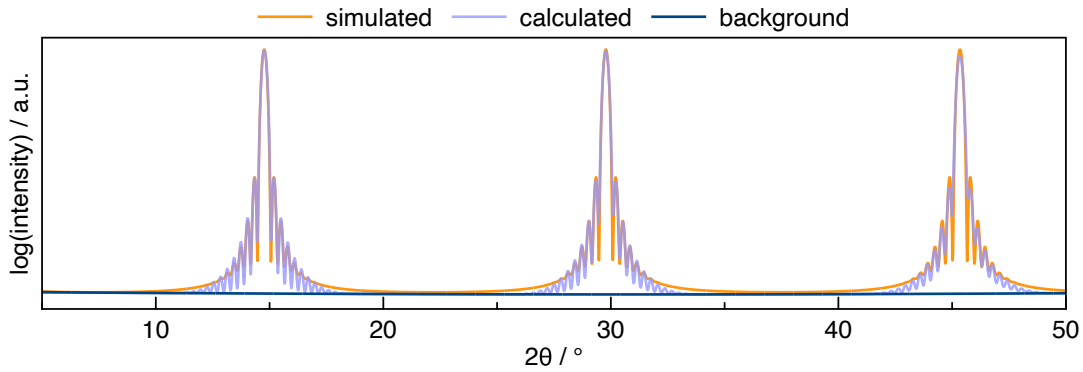

Fig. 5.6. Fit of simulated XRD pattern for a model with c = 6 Å and an average N = 50. The Laue oscillation damping in the simulated pattern was calculated by summing the weighted intensities given by a Gaussian distribution of patterns for models of 40-60 layers around an average of 50 layers with a standard deviation of 3 layers.

The Laue oscillation fitting software was then carried out for several experimental specular XRD patterns of crystallographically aligned thin film samples. Three examples are discussed below. The first example (Fig. 7) consists of a pattern for an Fe-substituted VSe_2 sample containing Laue oscillations on either side of the 001 Bragg reflection. The Laue function in GSAS-II was used to fit this pattern with N = 42 layers with a unit cell length of 6.097(5) Å. Since the Laue oscillations on the low angle side of the peak were more intense than those on the high-angle side, the "damping plus" parameter was refined to fit the asymmetry in intensity. The difference between the damping on the low and high angle side of the Bragg peak indicates that defects or strain are present in this film.

The second example consists of a specular XRD pattern for a VSe_2 thin film that contains significantly damped intensities leading to few Laue oscillations observed on either side of the 001 and 002 Bragg reflections (Fig. 8). The calculated c-axis lattice parameter was 6.126(1) Å, and similar fits were achieved with N = 12 and N = 13. This indicates that there are 12-13 layers on average in the coherently diffracting domains. However, very few Laue oscillations are observed, suggesting that the distribution around the average is relatively large.

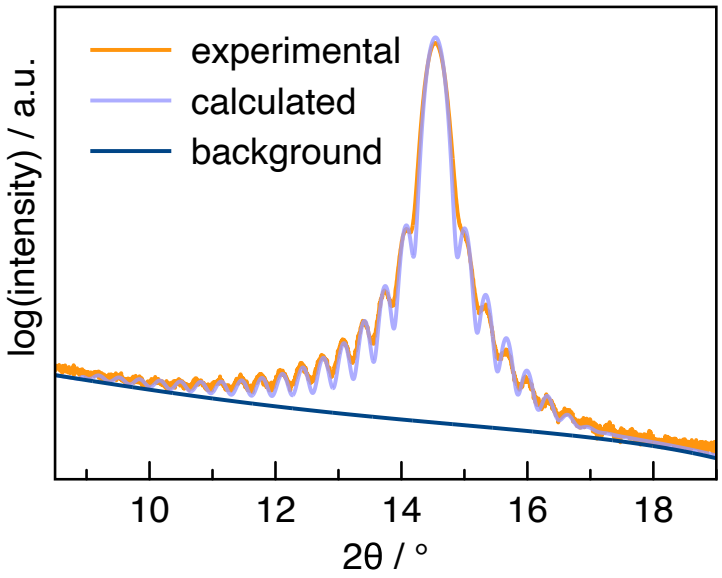

Fig. 5.7. Fit of experimental specular XRD pattern of an Fe-substituted VSe_2 film containing Laue oscillations on either side of the 001 peak.

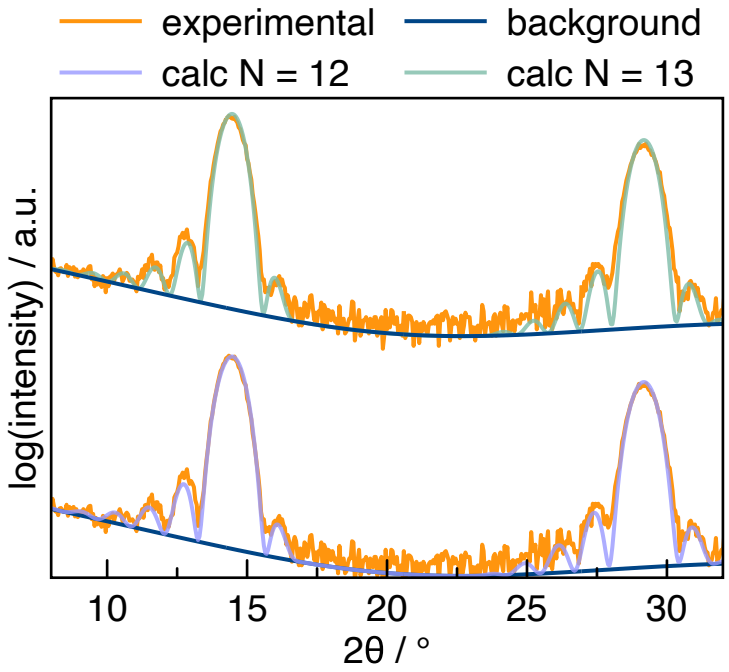

Fig. 5.8. Experimental specular XRD pattern of a VSe_2 film containing Laue oscillations on either side of the 001 and 002 peaks that was fit with N = 12 or N = 13.

The final example shown in Figure 9 consists of the specular XRD pattern for a $(PbSe)_{1+\delta}(VSe_2)_2$ heterostructure thin film containing very weak Laue oscillations on either side of the 006 Bragg reflection. The *c*-axis lattice parameter calculated by fitting the data was 18.42(1) Å, and the best fit was achieved with N = 14 layers. Although the broadness of the Bragg reflection causes the intensity of the Laue oscillations to appear weak, oscillations are observable for a 2θ range +/- 3° from the Bragg reflection. Additionally, modeling the patterns for N = 13 or 15 layers resulted in significantly worse fits of the experimental data. This suggests that the distribution of the number of unit cells around the average of 14 is relatively small, although additional models are necessary to determine the exact range. The observed Laue oscillations intensity damping is likely due to small grain sizes of the coherently diffracting crystalline domains, which causes significant peak broadening. The refinement of the damping parameters for the low-angle and high-angle sides of the Bragg peak resulted in values that were approximately equal, indicating that the oscillation intensities are symmetric. This suggests that significant strain is not present in the film.

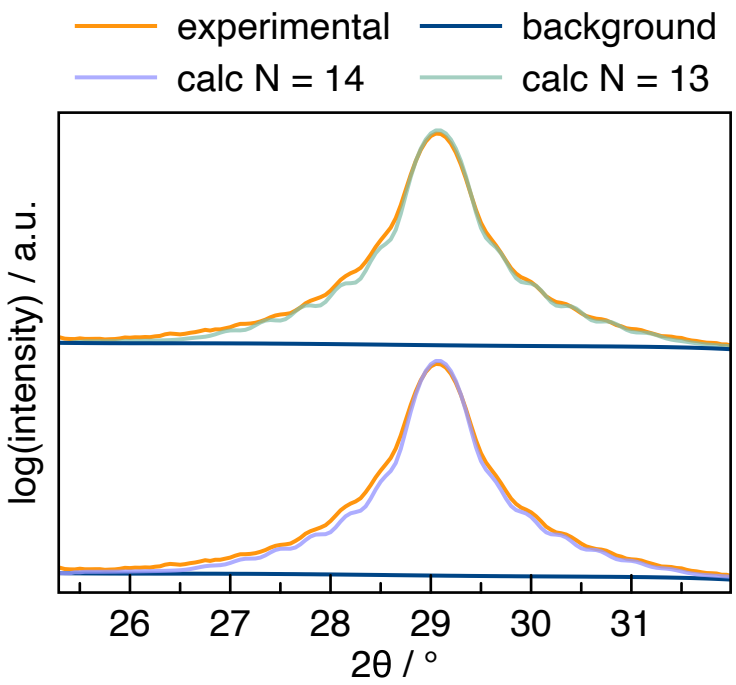

Fig. 5.9. Experimental specular XRD pattern for a $(PbSe)_{1+\delta}(VSe_2)_2$ heterostructure thin film containing Laue oscillations on either side of the 006 peak that was fit with N = 13 or N = 14.

5.7. Conclusions

As the work presented herein demonstrates, quantitative peak fitting of on-specular diffraction from thin film samples that exhibit Laue oscillations can provide valuable characterization information. Our work could potentially be extended to implement Rietveld fitting for 1D structural models. This would be similar to the peak-fitting process described here, but diffraction intensities would be computed from a refinable structural model. Implementation of Rietveld fitting requires a more comprehensive peak shape model that would use global fitting parameters for the damping of Laue oscillations rather than the peak-by-peak empirical terms introduced here. More experience with these empirical terms may allow this. Alternately, a theoretical model could be developed that would treat this. At the present, with the method presented here, trends seen in the as-fit intensities could be compared to intensities computed from different structural models. It is even possible to perform a secondary fit against those intensities, which will be statistically equivalent to a Rietveld fit, provided that the covariance matrix from the first fit is used in place of observation weighting.[26]

5.8. Bridge

Chapter V delved into details on experimental Laue oscillations and the effect of sample structure on the damping and asymmetry of their intensity. This was applied for the incorporation of Laue oscillation fitting in GSAS-II. The following chapter describes a method to distinguish between substitution and intercalation in transition metal dichalcogenides with Fe-doped VSe_2 used as an example. Laue oscillation fitting is a key component of this method.

CHAPTER VI

A METHOD TO DETERMINE THE DISTRIBUTION OF SUBSTITUTED OR INTERCALATED IONS IN TRANSITION METAL DICHALCOGENIDES: Fe_XVSe_2 AND $Fe_{1-X}V_XSe_2$

6.0. Authorship Statement

Chapter VI was published in *Chemistry of Materials* in 2022. I am the primary author and performed the experimental work. Rietveld refinements were carried out under the guidance of B.H. Toby. Theoretical calculations were carried out by S.R. Battey and S.P. Rudin. A sample lamella was prepared by R. Gannon for HAADF-STEM imaging and EDS mapping by P. Lu. D.C. Johnson provided editorial assistance.

6.1. Introduction

Transition metal dichalcogenides (TMDs) have historically garnered significant interest because of their layered architecture and the interesting properties that result from their two-dimensional structures.[1,2] The diverse and tunable properties of TMDs make them highly attractive materials for applications ranging from nanoelectronics and nanophotonics to catalysis and sensing.[3-5] An often-used strategy to tune the properties of these materials is by incorporating foreign atoms or ions that either substitute into the TMD structure or intercalate in the van der Waals gap between layers.[6-8] By varying the amount of substitution or intercalation of foreign atoms, it is possible to control the electronic, magnetic, optical, and morphological properties of TMDs.[8-12]

In common synthesis techniques used to prepare TMDs with incorporated guest species (direct reaction of elements, growth via physical vapor transport, and chemical vapor deposition[13,14]), the composition of the elemental or compound powder sources, the evaporation rates of precursors, or the growth conditions are assumed to control the extent of intercalation or substitution.[15] However, this assumption may not be valid in systems where the guest species is similar in size and/or valence to the metal or chalcogen because intercalation and substitution can occur.[16] For example, when incorporating Fe into 1T-TaS_2, the octahedral coordination of Ta allows for substitution of Fe onto Ta sites and an

unpredictable mix of both Ta and Fe intercalating into the van der Waals gap.[17-19] With V as a guest species in $TiSe_2$, substitution of V into the lattice is more stable than intercalation, so Ti atoms are more likely to intercalate.[20] Characterization of the composition and structure of final products is necessary to determine the extent of substitution and/or intercalation.

It is experimentally challenging to determine the amount and location of guest species in the host structures, so a variety of characterization techniques have been used. Small changes in lattice parameters are frequently used as evidence for intercalation and substitution. For intercalated TMDs, the lattice parameter generally varies linearly as intercalants are incorporated into the van der Waals gaps. When the maximum amount of intercalant incorporation is reached, the lattice parameter remains constant as excess foreign atoms form impurity phases.[7,11,12,21] However, substitution also causes systematic changes in lattice parameters.[22,23] Changes in the properties are also used as evidence of both substitution and intercalation, but the effect on the electrical, magnetic or catalytic properties is often similar or unpredictable for both.[8] The literature of Fe incorporation into VSe_2 demonstrates the challenges involved in determining the extent of substitution and/or intercalation, as the lattice parameters and the electrical and magnetic properties reported for intercalation ($Fe_{0.33}VSe_2$) and substitution ($Fe_{0.33}V_{0.67}Se_2$) are very similar to one another.[19,24] Other techniques used to differentiate between intercalated and substituted TMDs include electron microscopy, X-ray photoelectron spectroscopy, Raman spectroscopy, and angle-resolved photoemission spectroscopy. However, these techniques can be difficult to quantify or provide only indirect information about the extent of substitution and/or intercalation.[25-28] A direct method to determine the amount and site of guest species incorporation into the host lattice of TMDs would aid the development of structure-function relationship and accelerate the enhancement of properties for specific applications.

Here, we present an approach combining data from XRR, XRD and XRF measurements that directly establishes the amount of intercalation and/or substitution in transition metal dichalcogenides. Information on the amount of each element, limits on the amount of impurity phases present, and the number of unit cells of the dichalcogenide determine the amount of intercalation and/or substitution. The utility of this approach is demonstrated by characterizing $Fe_xV_ySe_2$ samples. The extent of substitution determined

using XRR, XRD and XRF data in these samples is supported independently by electron microscopy and Rietveld refinement of diffraction patterns.

6.2. Methods and Materials

6.2.1. Synthetic Procedures

The multilayer thin-film precursors were deposited onto (100) oriented Si wafers using a custom-built high vacuum ($<10^{-6}$ Torr) physical vapor deposition (PVD) chamber from elemental sources. Electron-beam guns were used to evaporate Fe (99.95%) and V (99.99%) from targets, and a Knudson effusion cell was used to evaporate Se (99.99%). The deposition rates were monitored by quartz crystal microbalances located above each elemental source. Pneumatic shutters positioned between the elemental sources and the spinning substrate were programmed to open and close to control the sequence and amount of each element deposited. Thin layers of V, Fe, and Se were deposited sequentially, and the number of repeat units was designed to yield a film thickness of approximately 300 Å. The bulk crystal structure of VSe_2 was used to calculate the desired amount of material in each layer such that the repeating V|Fe|Se layers in the substitution precursor had enough total metal atoms to form a single Se-M-Se trilayer of $Fe_xV_{1-x}Se_2$. In the intercalation precursor, each V|Se|Fe layer had enough V and Se to form a single Se-V-Se trilayer of VSe_2 and excess Fe. Prepared samples were stored in a nitrogen glovebox (>0.2 ppm O_2) to prevent oxidation.

Annealing of the samples took place inside the glovebox on a calibrated hot plate set to the desired temperature. The pieces were annealed for 15 minutes either in conditions open to the N_2 atmosphere or inside a closed container alongside a Se source to maintain a Se atmosphere and prevent Se loss. The samples were temporarily removed from the nitrogen glovebox as needed for characterization.

Two samples targeting either Fe-substituted or Fe-intercalated VSe_2 were prepared to illustrate our approach to determine the extent of intercalation/substitution of foreign atoms in TMDs. Annealing studies were carried out on both samples to determine the optimal conditions for crystallization of the targeted products with specular and in-plane XRD, XRR, and XRF data collected after each annealing step (SI).

6.2.2. Characterization

The amount of intercalation/substitution was determined through analysis of XRF, XRR and XRD data. X-ray fluorescence spectroscopy (XRF) data was collected on a Rigaku Primus II spectrometer. A technique previously described by Hamman, et al was used to determine the proportionality constant between intensity and the absolute number of atoms per unit area.[31] X-ray reflectivity (XRR) data and specular X-ray diffraction (XRD) data were collected on a Bruker D8 diffractometer equipped with Cu Kα radiation in θ−2θ locked-coupled scan mode over a 2θ range of 0-11° for XRR and 5-65° for XRD. The specular XRD scans are run in locked-coupled mode such that they will only show peaks in the 00*l* family of reflections for a sample aligned perpendicular to the substrate, which provides information about the *c*-axis lattice parameter. Film thicknesses were determined from the XRR patterns using a modified version of Bragg's law to account for refraction.[32] Laue oscillations present in the specular XRD patterns were used to calculate the number of unit cells in the coherently scattering domains.[29,30] Grazing incidence in-plane XRD patterns were collected on a Rigaku Smartlab diffractometer with Cu Kα radiation and parallel-beam/parallel slit analyzer (PB/PSA) optics over a 2θ range of 20-70°. In-plane scans are carried out in grazing incidence mode along the axis parallel to the substrate, which allows for *hk*0 reflections in the pattern and provides information about the *a*- and *b*-axis lattice parameters. Lebail fits of the specular and in-plane XRD patterns and one-dimensional Rietveld refinements of the specular XRD patterns were carried out using the crystallography data analysis software, GSAS-II.[33]

A cross-section of Sample A was prepared with an FEI Helios NanoLab 600i DualBeam focused ion beam scanning electron microscope (FIB-SEM) using standard lift out procedures.[34] A Titan^{TM} G2 80-200 STEM with a Cs-probe corrector and ChemiSTEM technology (X-FEG and SuperX^{TM} EDS with four windowless silicon drift detectors) was used to obtain atomic resolution HAADF-STEM images and EDS maps of the prepared cross-section at 200kV.

Computational calculations were carried out utilizing a density functional theory (DFT) framework comprised of the projector augmented wave (PAW)[35] method as implemented in the Vienna ab initio Simulation Package (VASP)[36,37] which has shown previous success when working with transition metal atoms and compounds.[38-40] In the PAW

method, all electrons appear as either adaptable in valance states or frozen in atomic core states. Many potentials are supplied within VASP with this work utilizing those that treat the 4s and 4p of Se and the 4s and 3d electrons of both V and Fe as valence electrons. The PAW sphere radii are 1.16, 1.32, and 1.30 Å for Se, V, and Fe respectively, which lead to no significant overlap between spheres. The plane wave energy cut-off is set to 520 eV, which converges energy differences to below 1 meV/atom. Exchange and correlation are treated in the generalized gradient approximations (GGA) with the PBE functionals of Perdew, Burke, and Ernzerhof.[41] For each system the k-point mesh was altered until the total energy (calculated using the linear tetrahedron method with the corrections of Blochl et. al.[42] converged within 1 meV/atom. This was achieved by using a 3x3x3 mesh and was consistently applied throughout this work. Unless otherwise stated, optimization of the individual superlattices began from the same basic pattern. A supercell was used for our calculations containing two 4x4 superlattice layers of VSe_2 each consisting of 16 vanadium atoms and 32 selenium atoms in a monolayer of VSe_2. The conjugate gradient algorithm in VASP was used to optimize cell parameters, atomic positions, spin, and magnetic moments.

6.3. Results and Discussion

The specular diffraction pattern for an annealed sample (500°C for 15 minutes in a Se atmosphere) targeting Fe-substituted VSe_2 ($Fe_{0.3}V_{0.7}Se_2$, Sample A) is shown in Figure 1a. Laue oscillations are clearly visible on either side of the 001 peak (Figure 1b). Laue oscillations arise from the incomplete destructive interference from a finite number of coherently diffracting unit cells and can be used to calculate the number of unit cells in a coherently diffracting domain (CDD).[43] The Laue oscillations in Figure 1b correspond to 44 unit cells in the coherently diffracting domain. The c-axis lattice parameter [6.088(3) Å] determined from the specular diffraction pattern multiplied by the number of unit cells yields the total thickness of the CDD [267.9(1) Å]. The Kiessig fringes, which are also apparent in Figure 1b at low angles, were used to calculate the total film thickness of 271.0(2) Å using a modified form of Bragg's law to account for refraction.[32,44] The difference between the total film thickness calculated from the XRR [271.0(2) Å] and the thickness of the CDD [267.9(1) Å] indicates that only ~1% of the sample is composed of impurity phases, and ~99% of the film consists of

coherently diffracting TMD layers. Hence, the total number of atoms per unit area calculated from the XRF data can be assumed to be the amount of each element in the dichalcogenide.

In-plane XRD data (Figure 1c) was collected and used to determine the in-plane lattice parameters [a = b = 3.367(1) Å], which combined with knowledge of the structure of the unit cell enables us to calculate the total number of atoms per unit area of each element for the number of unit cells determined from the Laue oscillations. Since the amount of chalcogen is constant whether intercalation or substitution is occurring, the amount of Se measured using XRF should be consistent with this calculated value. The sum of the amount of the metals would be expected to equal the amount calculated if only substitution was occurring and would be larger if some intercalation was occurring. For Sample A, the amount of Se is enough to form 45(1) unit cells and the total number of metal atoms present is enough to form 46(2) unit cells in the CDD. The number of V is enough to form 33(1) unit cells, and the number of Fe atoms is enough to form 13(1) unit cells, indicating a substituted TMD with the formula $Fe_{0.27(2)}V_{0.73(3)}Se_2$. The combination of information from XRR, XRD, and XRF data yields constrained values for the amount and extent of substitution and intercalation.

To obtain an independent measurement of the extent of Fe substitution in VSe_2, a cross section from a representative area of Sample A was prepared using FIB-SEM for structural analysis via HAADF-STEM imaging and STEM-EDS mapping. The HAADF-STEM image (Figure 2a) achieves atomic resolution across almost the entire area, revealing layers that are crystallographically aligned along the *c*-axis with the 1T hexagonal structure that is expected for VSe_2. Grain boundaries can be distinguished by changes in the orientation of the relative positions of the atoms both between layers and within a layer. There is a distinguishable van der Waals gap between each ~6 Å thick layer, and there are no regions with noticeable intensity within the van der Waals gaps, indicating that there is not significant intercalation of either V or Fe.

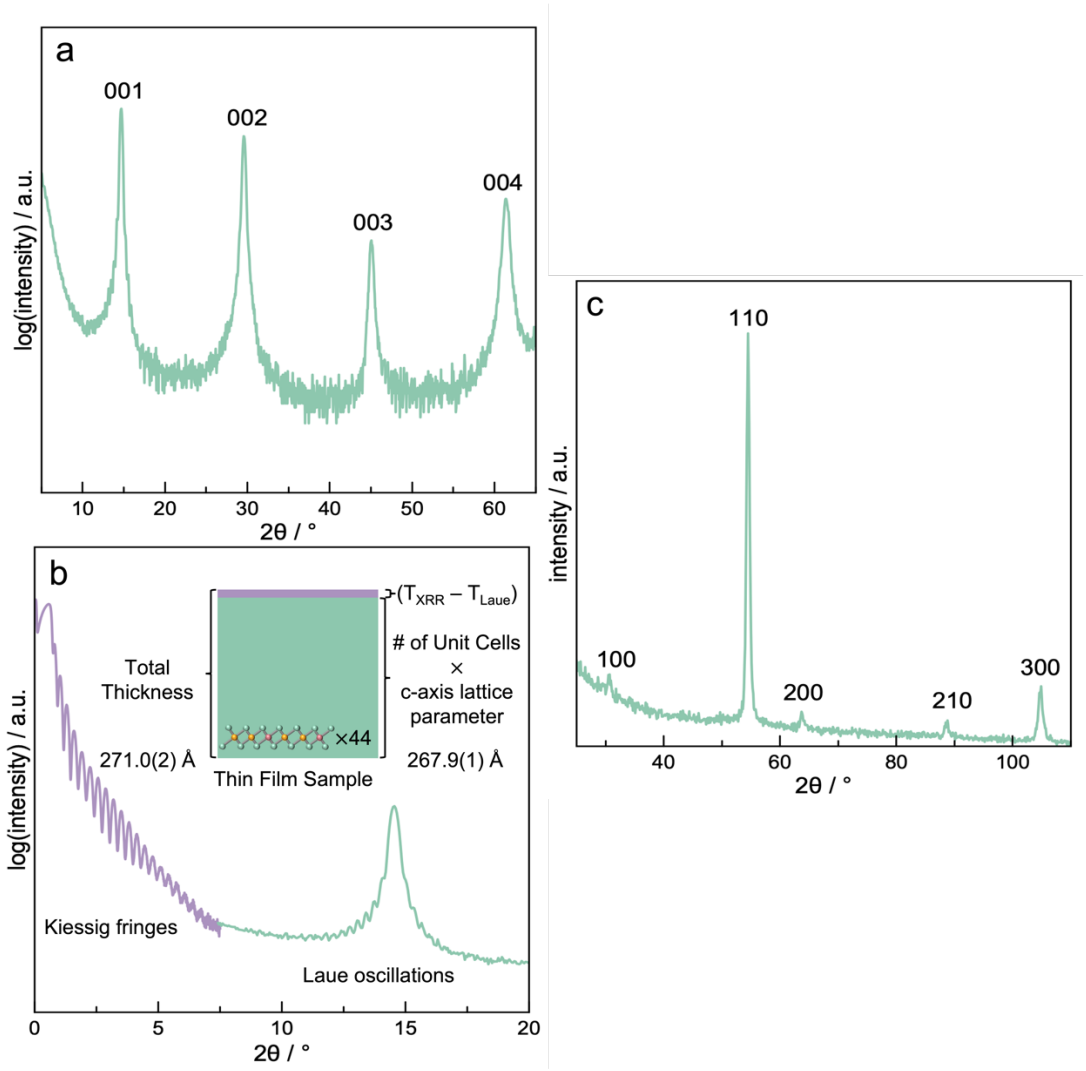

Fig. 6.1. Specular XRD pattern (a) XRR pattern and first Bragg reflection (b) and in-plane XRD pattern (c) for Sample A annealed at 500°C.

STEM-EDS elemental mapping (Figure 2b) probes the distribution of Fe and V within the film. The intensity profile of each element from EDS was utilized to determine the positions of the atomic planes via a method developed by Lu et. al. in which the intensity of each EDS peak is averaged across the map by lattice translations of the unit cell.[45] Averaging the peaks for the most well resolved unit cells yields a Gaussian distribution of intensity for each element (Figure 2c). The averaged Fe position is within error of the averaged V position with Se atomic planes located on either side, confirming that most of the Fe in the lattice is directly substituting for V.

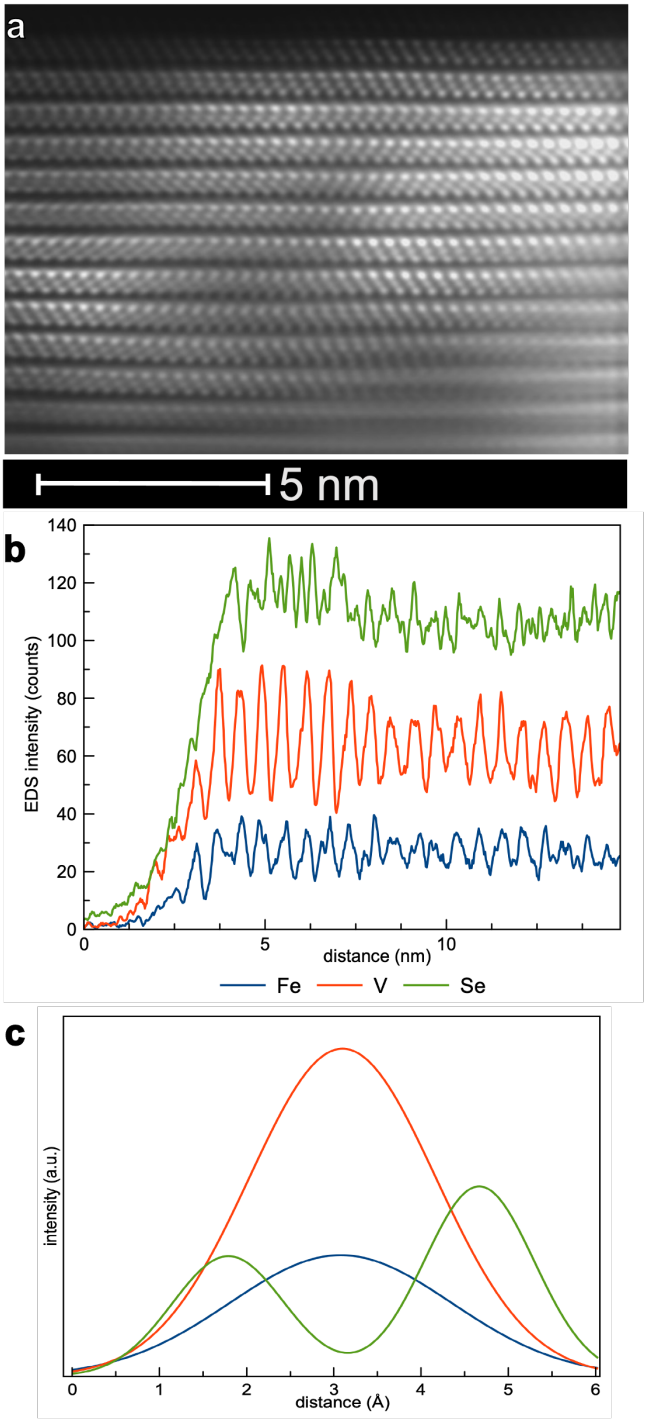

Fig. 6.2. Representative HAADF-STEM image of a cross section of Sample A (a); Elemental EDS line-profiles of a section of Sample A with intensity as a function of distance perpendicular to the substrate (b); and atomic plane positions determined by averaging the information in the EDS map (c)

Multiple Rietveld refinements of the specular XRD data for Sample A were also carried out to determine if the HAADF-STEM and STEM-EDS data was representative of the entire sample. A representative refinement is shown in Figure 3 (additional refinements are contained in the SI). Due to the crystallographic alignment of the sample to the *c*-axis, a one-dimensional refinement was carried out in which the x- and y-coordinates are held constant and only the z-coordinate is varied to refine the structure based on the intensity of the 00*l* reflections.[46] The initial parameters for the structure were constrained such that the atomic plane positions were near those determined from the HAADF-STEM and STEM-EDS data. Because of the similarity in atomic number between Fe and V, the refinement was not expected to be sensitive to the ratio of Fe to V, thus the initial parameters for the composition were constrained to be near those determined from XRF. For each refinement, upon releasing the constraints on the model, the parameters changed very little, confirming that the initial model is consistent with the STEM-EDS data.

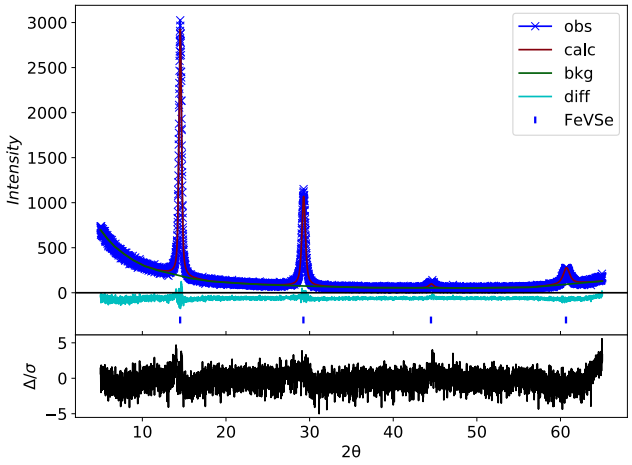

Fig. 6.3. Representative Rietveld refinement of specular XRD pattern of Sample A using the HAADF-STEM and STEM-EDS data for an initial model for the refinement.

Our new approach for determining the extent of foreign atom incorporation in TMDs was also applied to the sample targeting Fe-intercalated VSe_2 ($Fe_{0.3}VSe_2$, Sample B). The reflections in the as-deposited specular XRD pattern (Figure 4a) and the as-deposited in-plane XRD pattern (Figure 4b) for Sample B are much lower in intensity than those in the diffraction scan of Sample A, indicating that Sample B is less crystalline on deposit. The

three reflections observed in the as-deposited in-plane XRD pattern for Sample B cannot be indexed to a hexagonal unit cell, and because there are only three reflections present in the pattern, whether the sample contains one or more phases cannot be uniquely determined.

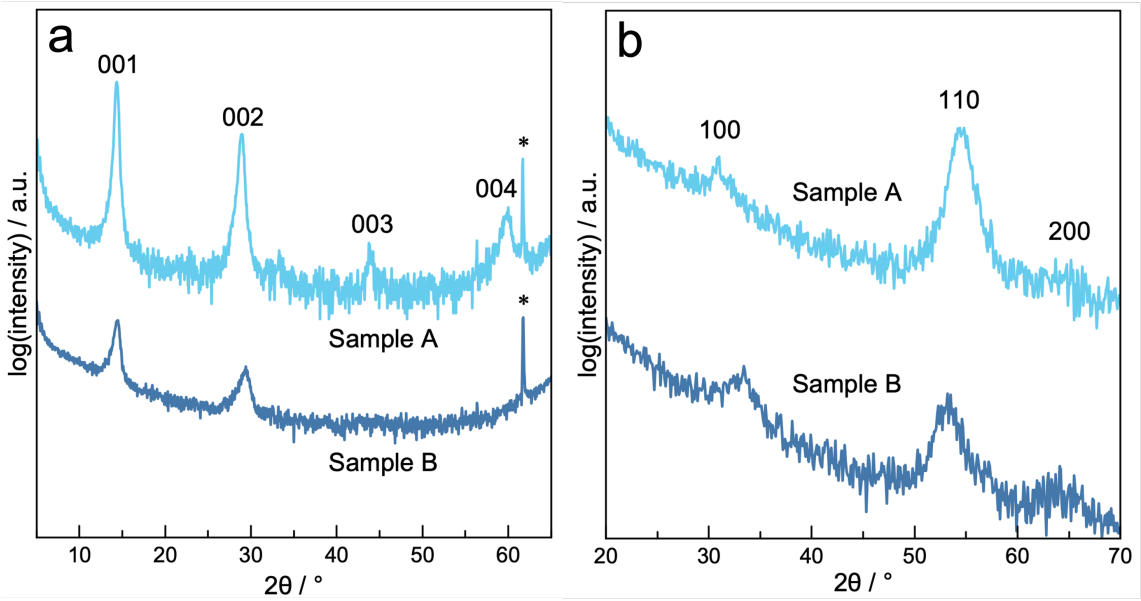

Fig. 6.4. Specular (a) and in-plane (b) XRD patterns of as-deposited precursors. Reflections marked with * are from the Si substrate.

Annealing Sample B to 400°C for 15 minutes in a N_2 atmosphere results in loss of Se due to evaporation, and the reflections in the specular XRD (Figure 5a) become sharper and shift to higher angles, corresponding to a c-axis lattice parameter of 5.839(1) Å. The reflections in the in-plane pattern (Figure 5b) also become sharper and can be indexed as *hk*0 reflections of a hexagonal unit cell with an *a*-axis lattice parameter of 3.498(5) Å. These lattice parameters are different from those expected from the literature values for an intercalated $Fe_{0.33}VSe_2$ sample (c = 6.056 Å, a = 3.356 Å).24 While Laue oscillations are not observed on the Bragg reflections, we can use the measured amount of Se to estimate the number of possible dichalcogenide unit cells. The estimated number of unit cells is 46(1), yielding a thickness of the dichalcogenide of 269(6) Å, which is within error of the total film thickness [274(1) Å]. Assuming excess metal is intercalated between layers, the calculated formula for Sample B at 400°C is $Fe_{0.28(5)}V_{1.1(1)}Se_2$.

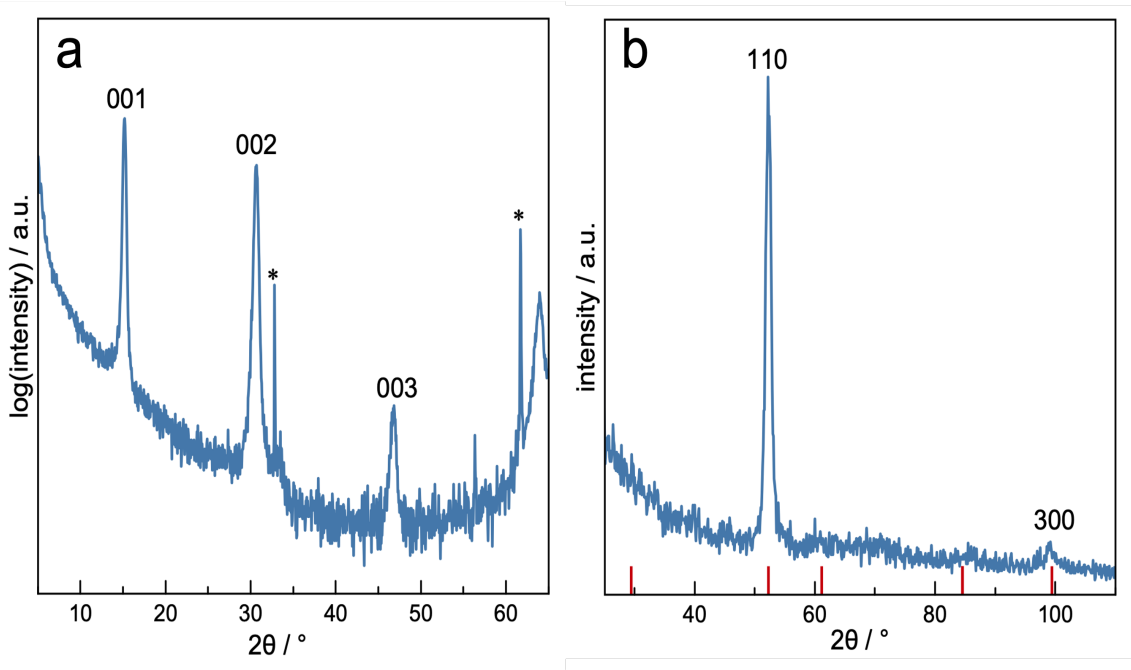

Fig. 6.5. Specular (a) and in-plane (b) XRD patterns for Sample B annealed to 400°C. Predicted locations for reflections calculated from the *a*-axis lattice parameter are indicated by the red lines in the in-plane XRD pattern. Reflections marked with * are from the Si substrate.

Several different Rietveld refinements of the specular XRD pattern for Sample B were carried out using multiple initial models with the composition $Fe_{0.28(5)}V_{1.1(1)}Se_2$. The initial constrained models (see SI) varied the amount of intercalated Fe, the amount of intercalated V and Fe, or the amount of intercalated and substituted Fe and V. However, the similar scattering power of Fe and V resulted in several solutions with similar goodness of fits for the unconstrained refinements, emphasizing the difficulty in distinguishing foreign atoms with similar atomic numbers to that of the host atoms. Even with the constraint on the total composition, false minima can be reached based on the assumption that the product is single phase and uniform in composition throughout the sample, as the actual sample could contain domains with different amounts of intercalated atoms. The ambiguity in these refinements emphasizes the challenge of using diffraction data and refinements to determine the extent of foreign atom incorporation.

To explore the relative stabilities of Fe-intercalated versus Fe-substituted VSe_2, computational calculations were carried out for two basic intercalated or substituted structural models (Figure 6) at a variety of Fe concentrations. Table 1 summarizes the lowest energies obtained for each composition investigated and the calculated lattice parameters. Both intercalation and substitution become less thermodynamically favorable as x increases, and for $x < 0.25$ substitution is preferred by 10-15 meV/Atom. At higher concentrations of Fe, the relative formation enthalpies are much closer, in some cases less than 5 meV/Atom apart, and the favored foreign atom incorporation switches to intercalation for $x = 0.38$ and 0.5. Further calculations are needed to describe the dynamic properties of a mixed addition method and/or material rearrangement.

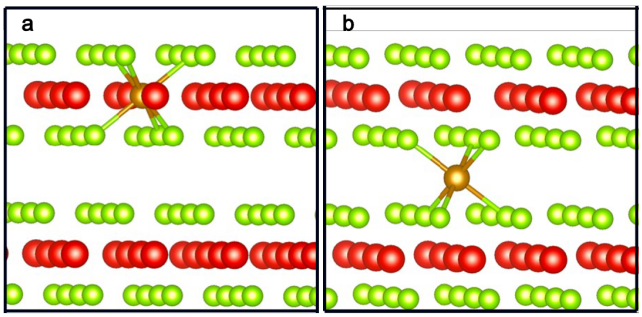

Fig. 6.6. Schematic of the structures used for Fe addition to the VSe_2 bilayer: substitution (a) octahedral intercalation (b)

When substituting Fe for V ($Fe_xV_{1-x}Se_2$), increasing x leads to a decrease in the calculated *c*-axis lattice parameter while the *a*-axis lattice parameter remains relatively constant. When intercalating Fe ($Fe_xV_1Se_2$), the calculated *c*-axis lattice parameter also decreases but the *a*-axis lattice parameter increases as x increases. The lattice parameters for $x = 0.25$-0.38 are slightly different than those determined for Sample A [a = 3.367(1) Å, c = 6.088(3) Å] and Sample B [a = 3.5(1) Å, c = 5.839(1) Å] in the substituted and intercalated structure, respectively. Since the lattice parameters calculated for each structure are very similar to one another, computational calculations were not carried out to investigate simultaneous substitution and intercalation. To experimentally explore the conversion of intercalated atoms to substituted atoms, a piece of Sample B was annealed in Se vapor. At temperatures above 300°C, the sample begins to react with the Se atmosphere, and

the lattice parameters calculated from the specular and in-plane XRD patterns (SI) shift towards those measured for Sample A. At 500°C, the lattice parameters for the piece of Sample B annealed in Se vapor [a = 3.36(1) Å, c = 6.080(4) Å] are within error of those of Sample A. These theoretical and experimental studies highlight the challenge in definitively distinguishing the site of foreign atom incorporation using lattice parameters alone.

Table 6.1. Formation enthalpies and lattice parameters calculated from DFT for increasing Fe-dopant concentrations for incorporation via substitution or intercalation into VSe_2

x	Formation Enthalpy (meV/Atom)	*a*-axis Lattice Parameter	*c*-axis Lattice Parameter
	Substitutional Addition		
0	-448	3.32	6.13
0.03	-437	3.31	6.13
0.09	-417	3.31	6.11
0.19	-381	3.32	6.07
0.25	-374	3.31	5.96
0.38	-327	3.30	5.94
0.5	-307	3.30	5.83
x	Intercalated Addition		
0.03	-440	3.32	6.11
0.09	-425	3.32	6.08
0.19	-397	3.34	6.06
0.25	-377	3.36	6.02
0.38	-333	3.39	5.87
0.5	-311	3.42	5.63

6.4. Conclusions

In this work, a definitive approach was demonstrated for characterizing the site and amount of foreign atom incorporation in a TMD. The presence of Laue oscillations allowed for a determinization of the number of unit cells in the coherently diffracting domain. Multiplying the number of unit cells by the *c*-axis lattice parameter gave the thickness of the coherently diffracting domain which could be compared to the total thickness calculated from

the XRR data. Since the difference between the coherently diffracting domain thickness and the total film thickness was small, the number of atoms of each element determined from XRF was representative of the number of atoms in the crystalline domain. For samples without Laue oscillations present, the number of unit cells possible from the amount of selenium measured in the XRF can be used to calculate a thickness which can be compared to the total thickness. In-plane lattice parameters allowed for the calculation of the amount of metal and selenium atoms necessary to form the number of unit cells in the crystalline domain. The ratio of metal atoms to chalcogen atoms calculated from the XRF data and number of unit cells determines the extent and site of foreign atom inclusion. This approach is a general method for characterizing foreign atom inclusion in layered TMDs.

6.5. Bridge

Chapter VI describes an approach to definitively determine the amount and site of foreign atom incorporation in transition metal dichalcogenides. The $Fe_xV_{1-x}Se_2$ system that was used to demonstrate this approach in Chapter VI is further explored in the next chapter. Chapter VII describes the exploration of this system through synthesis of $Fe_xV_{1-y}Se_2$ with a range of Fe content from x = 0-0.9. This chapter emphasizes the ambiguity in using lattice parameters to determine whether an atom is intercalated or substituted as well as the effect of processing parameters.

CHAPTER VII

USING SLOW SOLID STATE DIFFUSION RATES TO TRAP HIGHLY SUBSTITUTED TRANSITION METAL DICHALCOGENIDES

7.0. Authorship Statement

Chapter VII contains work that will be submitted to *Chemistry of Materials*. I am the primary author and performed the experimental work. P. Lu collected HAADF-STEM and STEM-EDS data. D.C. Johnson provided editorial assistance.

7.1. Introduction

There has been a tremendous surge of research on layered materials in the last few decades due to the discovery of emergent properties of monolayered materials and heterostructures containing designed sequences of 2D layers.[1,2] The layered transition metal dichalcogenides (TMDs) have been of particular interest to the 2D community due to their interesting electrical, optical, and mechanical properties,[3–5] which have resulted in TMDs being proposed for a wide range of technological applications including photonics and optoelectronics,[6–8] sensing,[9,10] and energy storage.[11] Historically, researchers have tuned the properties of TMDs for specific applications by the incorporation of guest species through substitution or intercalation.[12,13] For example, intercalation of Cr into $TiTe_2$ to form Cr_xTiTe_2 changes the electrical properties from conducting at small x to insulating above x = 0.3 and higher x values result in ferromagnetism.[14] Substituting half of the Te atoms in 1T-$PdTe_2$ for Se atoms leads to a significant enhancement of the superconducting transition temperature.[15] Increasing the amount of Fe substituted for V increases the effectiveness of $Fe_xV_{1-y}Se_2$ as a catalyst for the hydrogen evolution reaction up to the maximum value of x (0.3) that can be prepared using high temperature synthesis.[16] The ability to tune electrical, magnetic, and optical properties of TMDs by incorporation of a substituted or intercalated species has also been critical to understand the origin of many of their unique properties and broadens the range of properties available as constituents in heterostructures.[12,17,18]

.

Traditional techniques to prepare substituted or intercalated TMDs, such as repeated high temperature annealing after grinding, flux growth or vapor transport reactions, are carried out at high temperatures to increase diffusion rates and/or control the concentration of species in the fluid phase.[19] These methods rely on creating an environment where the intended product is the most thermodynamically stable under the reaction conditions, which are optimized depending on the relative thermodynamic stability of potential products and the reactivity of intermediate compounds formed during processing. For example, in synthesis via direct reaction of the elements at elevated temperatures, binary compounds are typically formed as reaction intermediates and must react to form potential ternary compound. Hence high reaction temperatures and repeated intermediate grinding steps are used to overcome slow solid state interdiffusion rates and reduce any potential distribution of compositions across a reacting interface.[20] With respect to forming substituted and/or intercalated dichalcogenides, the amount of substitution (*z*), intercalation (*y*) and the relative amount of each occurring in a reaction depends on the relative stability of each of the potential compounds (M_yTX_2, $M_zT_{1-z}X_2$ or $M_yM_zT_{1-z}X_2$) relative to other potential products and the reaction conditions used in the synthesis.[21] Determining the extent of substitution vs intercalation is particularly important in vapor transport reactions, where the crystals grown often have different compositions than the initial reacting charge. The maximum values of *y* and z are often limited by the formation of stable intermediate compounds and can vary depending on the overall composition of the reaction mixture.[18] Complicating the study of M_yTX_2, $M_zT_{1-z}X_2$ and $M_yM_zT_{1-z}X_2$) compounds is the experimental challenge of determining the values of y and z using traditional analytical techniques,[22–24] which has hindered determining the origin of properties reported for both intercalated and substituted compounds.[25,26]

In this report we show that it is possible to significantly increase the extent of substitution and/or intercalation by low temperature annealing of intimately mixed, mostly amorphous precursors prepared by sequentially depositing ultrathin elemental layers. Precursors were prepared targeting $Fe_x(Fe_yV_{1-y}Se_2)$ samples with Fe content up to x + y = 0.9. Slow solid state diffusion rates at low temperatures prevent the long range separation of the elements into a mixture of binary compounds, kinetically favoring formation of $Fe_x(Fe_yV_{1-y}Se_2)$ compounds with substitution dominating for low Fe content and a mix of

substitution and intercalation for higher Fe content. The extent of substitution and intercalation was shown to be sensitive to post deposition processing parameters. In our thin film samples, Laue oscillations present in specular diffraction patterns of the products combined with the measured amount of each element determined from XRF enable us to determine the extent of substitution/intercalation. The samples formed mixtures of VSe_2 and binary iron selenide compounds when annealed at higher temperatures, indicating that the products are only kinetically stable. This synthesis method creates opportunities to expand the range of substitution and/or intercalation in TMDs beyond those achieved from traditional synthetic methods since unmixing is limited by the slow diffusion rates at low temperatures. The ability to use Laue oscillations and XRF data to determine the relative amounts of intercalation and substitution creates opportunities to better understand structure/function relationships in M_yTX_2, $M_zT_{1-z}X_2$ and $M_{y+z}T_{1-z}X_2$ systems.

7.2. Results and Discussion

Nine precursors were prepared in this investigation by sequential deposition of V|Fe|Se elemental layers targeting compositions of substituted $Fe_zV_{1-z}Se_2$ compounds with z ranging from 0 to 0.9. Each V|Fe|Se repeat sequence targeted the amount of V, Fe and Se required to make a single Se-(V,Fe)-Se layer of a 1T dichalcogenide structure with 5-10% excess of Se atoms to account for Se loss during annealing. The V|Fe|Se layering sequences were repeated 50 times to produce films approximately 30 nm in total thickness. X-ray reflectivity (XRR) patterns were collected on the as-deposited samples to determine the total film thicknesses and X-ray fluorescence measurements were used to determine the number of atoms per unit area of each element in the as-deposited precursors (see SI).[27] Table 1 contains the measured compositions of each of the precursors. Samples **1** and **5** contained more than 1 metal atom per 2 Se atoms on average, which might favor intercalation of some metal atoms. The other samples contained 1-10% excess Se atoms relative to a 1:2 ratio of metal atoms to Se atoms except for Sample **9**, which contained 30% excess Se atoms relative to a 1:2 ratio of metal atoms to Se atoms.

Table 7.1. A summary of the as-deposited compositions and lattice parameters of the 9 samples prepared as part of this investigation. Vanadium was assumed to be substituted. Intercalation of iron was assumed to occur when the sum of vanadium and iron exceeded 1.

Sample	Avg composition Normalized to Se i.e. $Fe_x(Fe_yV_{1-y}Se_2)$				*c* - axis lattice parameter (Å)	*a* - axis lattice parameter (Å)
	Fe_x	Fe_y	V	V + Fe		
1	0	0	1.03(4)	1.03(4)	6.107(5)	3.37(1)
2	0	0.27(1)	0.66(2)	0.93(2)	6.175(6)	3.34(2)
3	0	0.31(1)	0.65(2)	0.97(2)	6.190(5)	3.36(1)
4	0	0.56(1)	0.44(2)	1.01(2)	6.15(1)	3.36(1)
5	0.11(1)	0.52(1)	0.48(2)	1.12(2)	6.18(2)	3.37(2)
6	0	0.63(1)	0.37(2)	0.99(2)	6.14(3)	3.35(1)
7	0	0.69(1)	0.27(2)	0.96(2)	6.110(5)	3.35(1)
8	0	0.73(1)	0.17(3)	0.90(3)	6.05(1)	3.36(1)
9	0	0.71(1)	0.06(2)	0.77(2)	6.03(5)	3.34(4)

The specular and in-plane XRD patterns of the as-deposited precursors are shown in Figure 1. The XRD patterns for precursors **2**-**9** each resemble those of the pure VSe_2 sample, precursor **1**. The specular XRD patterns contain a family of 00*l* Bragg reflections yielding *c*-axis lattice parameters of ~6 Å, which are near those reported for 1T-VSe_2. This indicates that small grains of $Fe_x(Fe_yV_{1-y}Se_2)$ nucleate and grow during the deposition. Fewer, broader, and less intense 00*l* reflections are present in the patterns for samples with higher Fe content, indicating fewer and smaller grains have formed. This suggests that it is more favorable to form $Fe_x(Fe_yV_{1-y}Se_2)$ grains when the surrounding matrix is more V-rich. Each in-plane XRD pattern contains broad reflections that can be indexed as *hk*0 reflections of a hexagonal unit cell with an *a*-axis lattice parameter near that of VSe_2. The presence of only 00*l* reflections in the specular pattern and only *hk*0 reflections in the in-plane pattern indicates that the domains are crystallographically aligned with respect to the substrate. The *a*- and *c*-axis lattice parameters calculated from the patterns contained in Table 1 are consistent with layered dichalcogenides, $Fe_x(Fe_yV_{1-y}Se_2)$, forming during the deposition. The as-deposited lattice parameters do not systematically vary with the average composition, however, reflecting that the domains formed may be more V rich than the amorphous matrix.

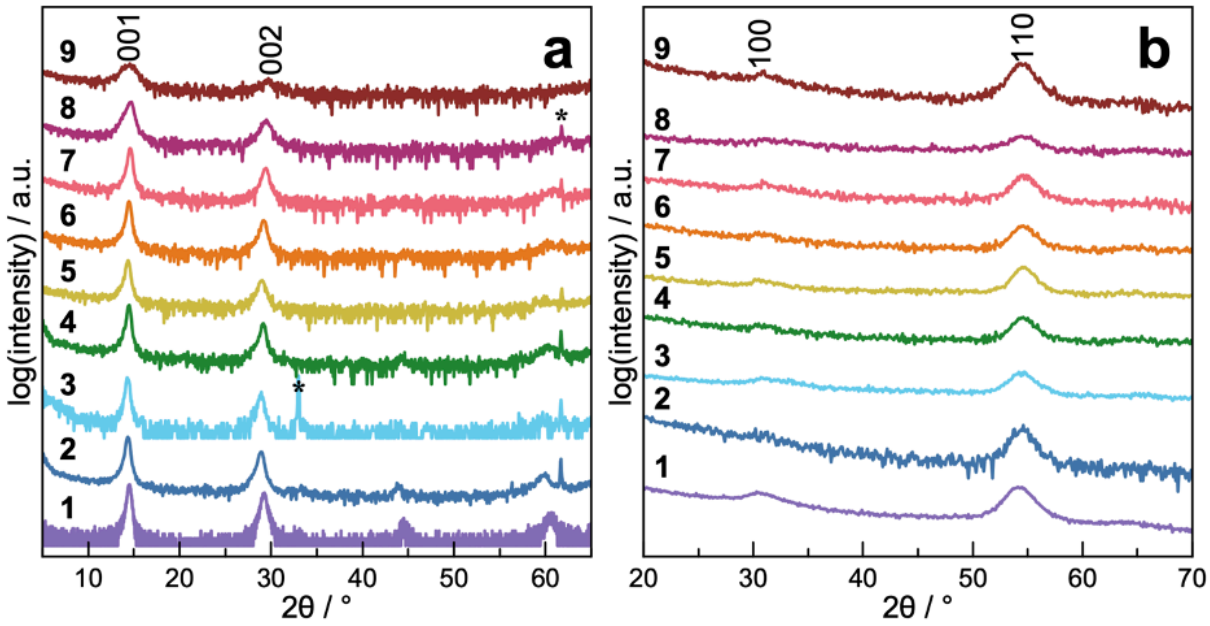

Fig. 7.1. a) Specular and b) in-plane XRD patterns of the as-deposited precursors prepared for this investigation. The hexagonal indices are given above each reflection. Reflections marked with * are due to the Si substrate.

XRD patterns were collected after annealing an iron-rich precursor (Sample **8**) and an iron-poor precursor (Sample **2**) at increasingly higher temperatures in 100°C steps to follow structural changes as the samples lower their free energy. Figure 2 contains the specular and in-plane XRD patterns collected from sample **8** after each annealing step. XRF data collected after each annealing temperature indicate that sample **8** systematically loses Se during the annealing steps. After each annealing step up to and including 300°C, the 00*l* reflections in the specular XRD and *hk*0 reflections in the in-plane XRD become narrower and more intense, indicating growth of larger crystalline domains of the hexagonal structure perpendicular to the substrate. The 00*l* reflections shift to higher angles as the annealing temperature increases, indicating a decrease in the *c*-axis lattice parameter. At 400°C, the peaks in the specular and in-plane XRD patterns become broader and asymmetric indicating that the crystalline domains become smaller and more heterogeneous. The abrupt shift in the diffraction angle of the reflections in both the specular and in-plane scans after annealing at 400°C indicates a significant change in lattice parameters, which is perhaps correlated with loss of Se. The black scan in Figure 2 was collected after annealing an as-deposited piece of

sample **8** directly to 350°C in a Se atmosphere for 15 minutes. The diffraction patterns are very similar to the scan collected after annealing at 300°C.

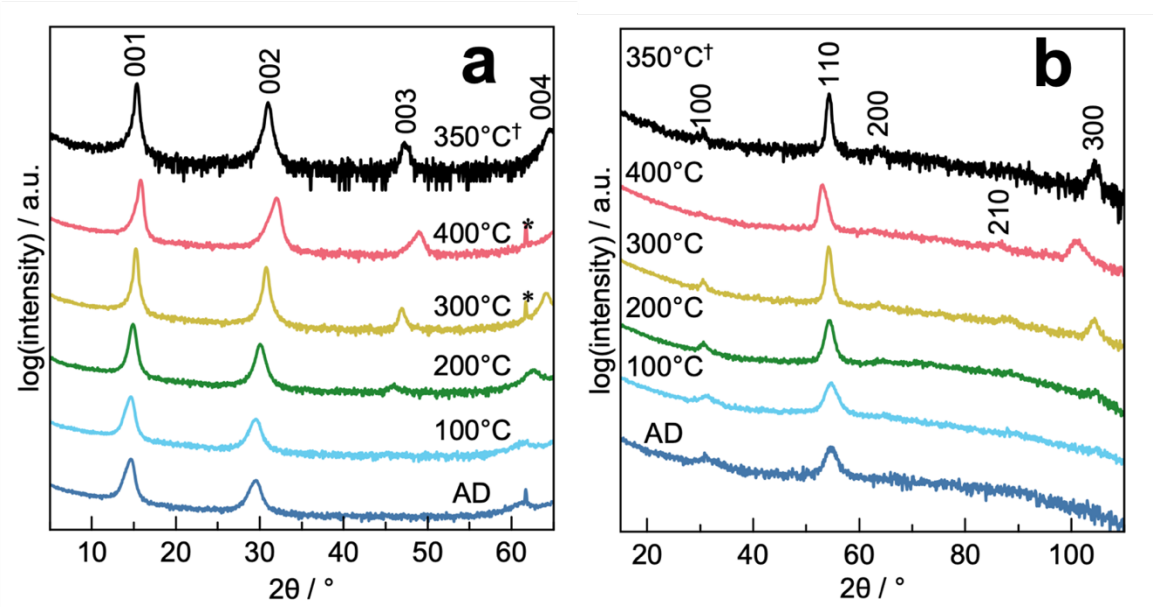

Fig. 7.2. Specular and in-plane XRD patterns collected on sample **8** after annealing at the indicated temperatures for 15 minutes. Reflections marked with * are due to the Si substrate. The 350°C anneal marked with † was carried out on an as-deposited piece of sample **8**.

Figure 3 contains plots of the change in the metal to selenium ratio and *a*- and *c*-axis lattice parameters as a function of annealing temperature for sample **8**. At lower annealing temperatures sample **8** contains excess Se atoms relative to a 1:2 ratio of metal to Se. After annealing at 300°C and 400°C, there are excess metal atoms relative to the amount of Se present. The *c*-axis lattice parameter decreases systematically with annealing temperature, while the *a*-axis lattice parameter remains relatively constant until abruptly increasing after the 400°C anneal. Changes in lattice parameters as a function of the amount of substitution and/or intercalation have been reported for quite a few different elements in several transition metal dichalcogenides.[28–33] Since a similar decrease in the *c*-axis lattice parameter and increase in the *a*-axis lattice parameter has previously been reported to occur for similar transition metal dichalcogenides intercalated with 3d metal atoms,[14,34,35] we suspect Fe atoms move from being substituted in the dichalcogenide to being intercalated as Se is lost. The

asymmetric reflection profiles contained in the specular and in-plane XRD patterns after annealing at 400°C are likely caused by a distribution of lattice parameters due to varying amounts of intercalation occurring in different van der Waal gaps and in different grains. Annealing the sample directly to 350°C for 15 min in a Se atmosphere reduced the amount of Se that was lost, leading to a composition of $Fe_{0.06}(Fe_{0.79}V_{0.21}Se_2)$, assuming that all the vanadium is substituted. Even though fewer atoms are intercalated in the sample annealed directly to 350°C, the *c*-axis lattice parameter was smaller than that of the sample annealed to 300°C, with the formula $Fe_{0.10}(Fe_{0.78}V_{0.22}Se_2)$. This highlights the ambiguity of using lattice parameters to distinguish between intercalation and substitution in TMDs because of the influence of processing parameters on the structure and composition.

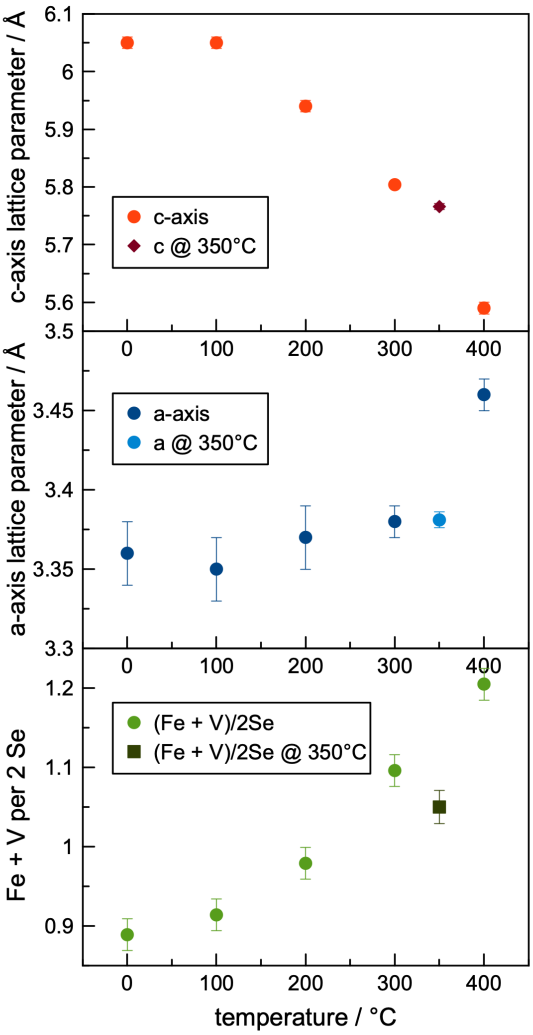

Fig. 7.3. Change in the *c*-axis (top) and *a*-axis (middle) lattice parameters and the ratio of metal to Se (bottom) in sample **8** as a function of annealing temperature.

A similar annealing study was carried out for sample **2** to explore the effect of processing parameters on structure in a sample that contains significantly less Fe than sample **8**. Sample **2** was annealed in an N_2 atmosphere at temperatures at or below 350°C, and in a Se partial pressure for the 400°C and higher temperature annealing steps. The diffraction patterns, contained in the SI, indicate that crystal growth of a dichalcogenide occurs during annealing. The XRF data indicate that sample **2** loses Se during the 200-400°C annealing steps. After the 400°C anneal, the sample is metal-rich relative to a stoichiometric M_1Se_2 compound, with the excess of 0.2 metal atoms per M_1Se_2 formula unit presumably occupying intercalation sites in the van der Waals gap between the M_1Se_2 layers, as no reflections from impurities are visible in the XRD patterns. At 450°C and 500°C, the amount of Se in the sample increases as the sample absorbs Se from the partial pressure provided by a Se pellet within the sample container. After annealing at 500°C, sample **2** has a nearly stoichiometric metal to Se ratio of 1:2. As shown in figure 4a, the *c*-axis lattice parameter steadily decreases with increasing temperatures when annealed in the absence of a Se partial pressure. This could be attributed to increasing amounts of intercalation, but the effect of processing parameters on the structure must also be considered (see Figure 4c). For example, the *c*-axis lattice parameters are significantly different for the 250°C and 500°C annealing steps even though the sample has nearly the same M_1Se_2 composition after both steps. Additionally, the *c*-axis lattice parameter decreases after annealing to 500°C even though the sample gained Se relative to the amount present after annealing to 450°C. These results suggest that metal atoms switch between being substituted or intercalated depending on the Se vapor pressure and the annealing temperature. The changes in structure for sample **2** also illustrate the challenges of using lattice parameters alone to determine the extent of intercalation or substitution, as the non-equilibrium distribution of defects and metal atom locations depend on the processing parameters.

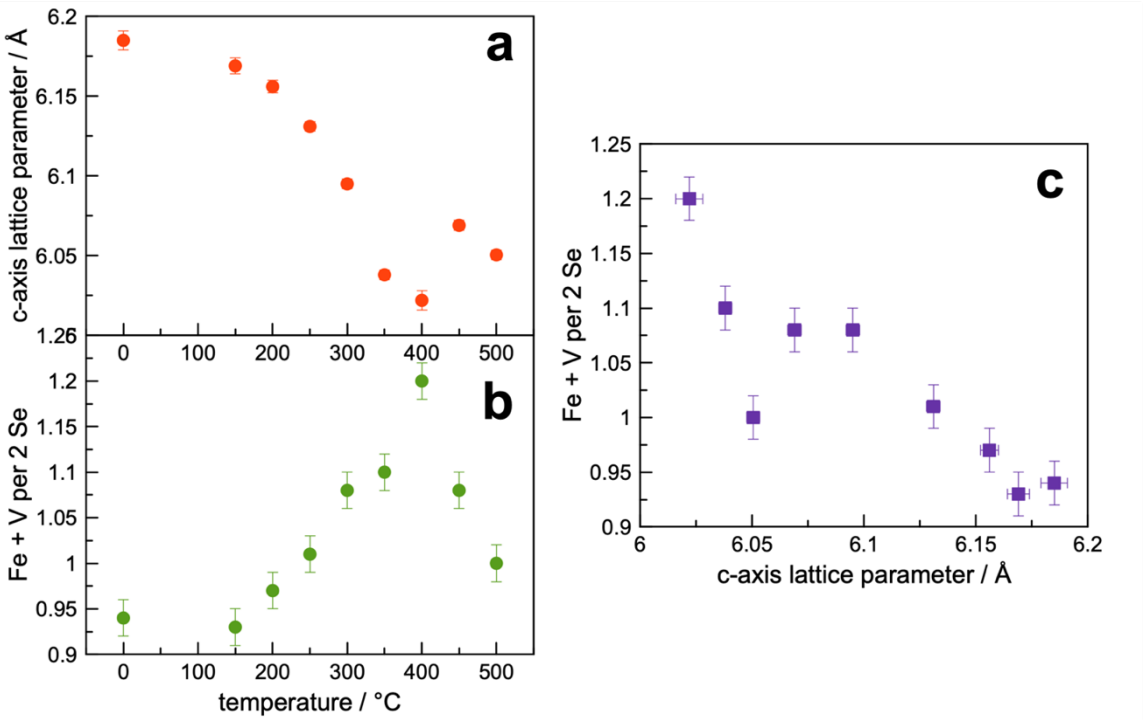

Fig. 7.4. Changes in the a) *c*-axis lattice parameter and b) composition as a function of annealing temperature and c) the change in the *c*-axis lattice parameter as a function of composition.

Based on the annealing studies for samples **2** and **8**, each of the as-deposited precursors were annealed to 350°C for 15 min in a Se atmosphere to promote growth of a mostly substituted dichalcogenide structure. The specular and in-plane XRD patterns collected after annealing are shown in Figure 5. The specular patterns for samples **1-8** each contain a family of 00*l* reflections, and the in-plane patterns can all be indexed with *hk*0 reflections from a hexagonal structure. Sample **9** is not included in this discussion, as its specular and in-plane XRD patterns contain reflections due to a hexagonal structure and reflections due to marcasite $FeSe_2$, indicating that the sample decomposes to a mixture of phases. The XRD data for samples **1-3** and **5-8** indicate that growth of a crystallographically aligned hexagonal structure occurs during annealing without any secondary phases forming. The data for sample **4** indicate that most of the sample is a crystallographically aligned hexagonal structure, but the presence of a weak reflection at ~32° 2θ suggests small grains of a secondary impurity phase also formed. Table 2 summarizes the lattice parameters

calculated for these samples along with the measured composition of the samples determined from XRF data.

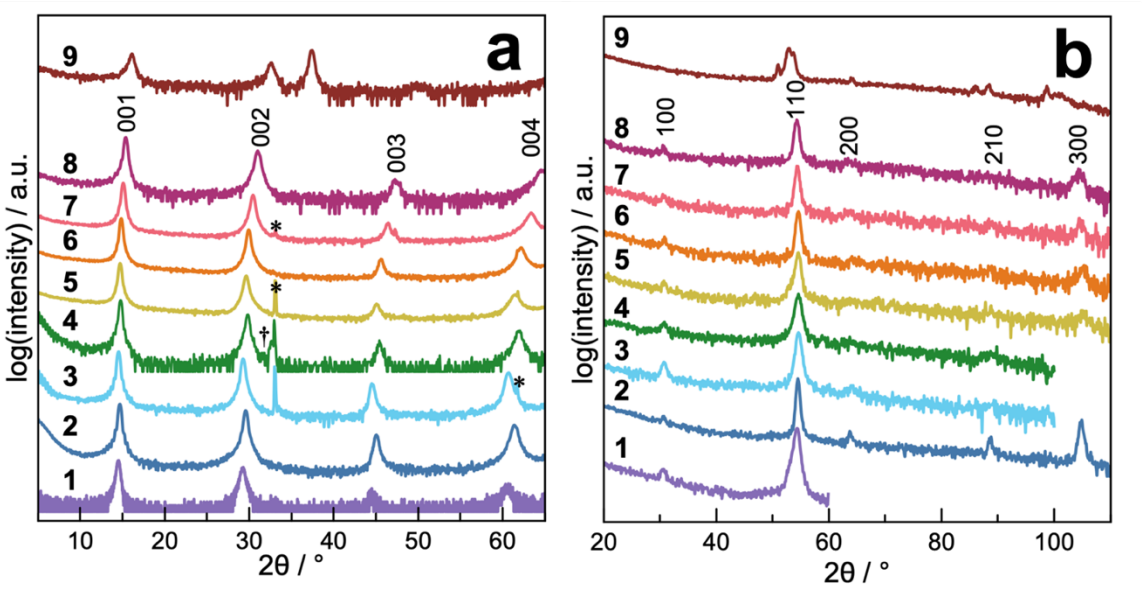

Fig. 7.5. a) Specular and b) in-plane XRD patterns for samples **1**-**8** annealed to 350°C for 15 min in a Se atmosphere. Reflections marked with * are due to the Si substrate. The reflection in the specular XRD for sample **4** marked with † is due to an unknown impurity phase.

Table 7.2. A summary of the composition and lattice parameters after annealing each sample to 350°C. The Fe/(Fe+V) values assume all Fe is substituted for V. The Fe + V per 2 Se values allow for an estimation of the amount of intercalated atoms.

Sample	Fe/(Fe+V)	*a*-axis lattice (Å)	*c*-axis lattice (Å)	Fe + V per 2 Se
1	0	3.371(1)	6.107(5)	1.02(2)
2	0.28	3.367(1)	6.092(1)	1.02(4)
3	0.32	3.346(6)	6.097(1)	1.02(6)
4	0.56	3.36(1)	5.980(1)	1.12(6)
5	0.57	3.362(2)	6.025(5)	1.07(5)
6	0.62	3.356(5)	5.968(3)	1.04(5)
7	0.71	3.371(1)	5.874(1)	1.04(5)
8	0.8	3.381(5)	5.766(5)	1.06(5)

Figure 6a graphs the lattice parameters determined from the XRD data in Figure 5 versus the amount of Fe in each sample measured using XRF and normalized as Fe/(Fe+V). The lattice parameter values reported for $Fe_xV_{1-y}Se_2$ samples from the literature are graphed on the same plots in different colors.[16,36] The trends in lattice parameters with composition are not linear, suggesting that the amounts of both substitution and intercalation change with composition. Figure 6b graphs the lattice parameters versus the amount of intercalation in each sample, which was approximated as (Fe+V)/(2Se). A clear trend is not observed based on the change in lattice parameter versus intercalation alone. Additionally, data point for the Fe-intercalated sample reported in the literature with nominal composition of $Fe_{0.33}VSe_2$ is an extreme outlier. Since lattice parameters have been reported to depend on the extent of both substitution and intercalation, nominal composition can lead to unreliable interpretations of the data, and more information is required to determine the distribution of Fe atoms in the samples. An additional complication is the impact of small amounts of an impurity phase on determining the extent of intercalation.

Our approach to this challenging problem is to combine composition data, analysis of Laue oscillations in specular XRD patterns, x-ray reflectivity data, cross-section STEM-EDS data, and Rietveld refinements of diffraction patterns to quantify the amounts of substitution and intercalation. The specular XRD patterns for samples **2**-**4** and **6**-**8** each contain Laue oscillations on either side of the 001 Bragg reflection (see Figure 7), which can be used to determine the average number of coherently diffracting unit cells of the dichalcogenide in each sample.[37] Patterns with Laue oscillations that extend to greater ranges of 2θ values around the Bragg peak, such as that for sample **2**, indicate that the majority of the crystalline domain thicknesses in the sample are narrowly distributed around the average, while patterns with Laue oscillations that damp out at narrower ranges of 2θ values around the Bragg peak, such as that for sample **8**, indicate a broader distribution of crystalline domain sizes.

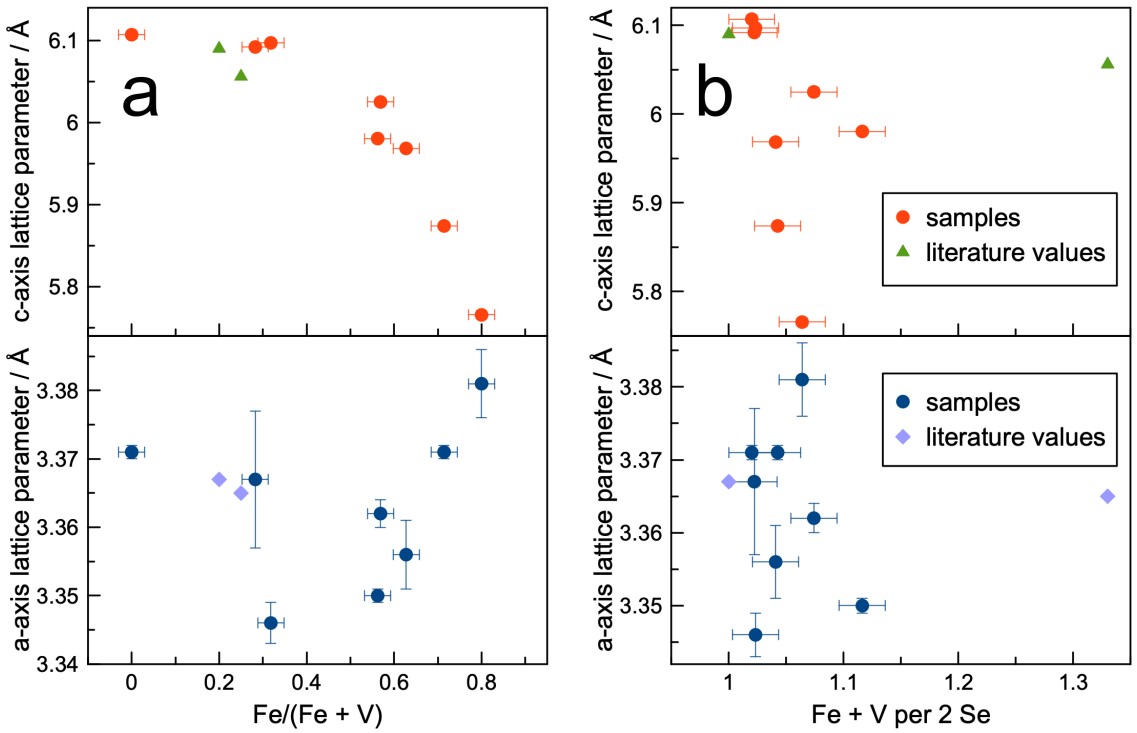

Fig. 7.6. Trends in the *c*-axis (top) and *a*-axis (bottom) lattice parameters versus a) the amount of Fe in the sample normalized as Fe/(Fe+V) and b) the amount of intercalation approximated as the ratio of total metal atoms per 2 Se atoms. The values for similar $Fe_x(Fe_yV_{1-y}Se_2)$ samples reported from the literature are shown in green for the *c*-axis lattice parameters and light purple for the *a*-axis lattice parameters.

Multiplying the average number of unit cells by the *c*-axis lattice parameter gives the average thickness of the crystalline dichalcogenide domains in each of the samples. The domain thicknesses can be compared to the total film thicknesses of each sample, derived from the Kiessig fringes in their XRR patterns (see SI). The total film thicknesses are each 2-6 Å larger than the average crystalline domain thicknesses, indicating small amounts of secondary phases are present above or below the crystalline domains. The impurity phases do not appear as extra reflections in the XRD patterns except for sample **4**.

The absolute number of atoms/Å^2 of each element in the samples, determined using XRF intensities, can be converted into the number of unit cells that can form by multiplying the number of atoms/Å^2 by the unit cell basal plane area. This can be compared to the average number of unit cells determined from the Laue oscillations. If we assume that V will

preferentially be in the dichalcogenide, the amount of substituted Fe is calculated by subtracting the number of V layers from the average number of unit cells. Assuming the amount of impurity phase is negligible, the amount of intercalation is the difference between total amount of Fe and the amount that is substituted. Since the calculated amount of intercalated Fe can be small, the presence of any impurity phase(s) can result in a significant overestimate of the amount of intercalation. The information determined from the combination of XRF, XRR, and Laue oscillation data is summarized in Table 3. Figure 8 contains a plot of the *a*- and *c*-axis lattice parameters versus the calculated Fe_x values, which indicates that there is a linear increase in the *a*-axis lattice parameter and decrease in the *c*-axis lattice parameter as the amount of intercalated Fe increases. The published literature values, shown in a different color, do not follow the same trend, illustrating that nominal composition alone cannot be used to rationalize changes in lattice parameters.

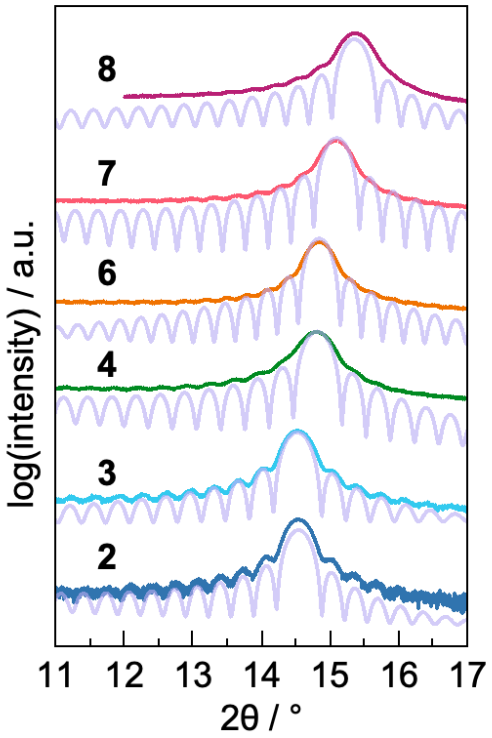

Fig. 7.7. Specular XRD patterns for samples **2**-**4** and **6**-**8** over the 2θ range 11-17° containing the 001 Bragg reflection with Laue oscillations on either side. The light purple curves are simulated fits of the Laue oscillations, and the other colored curves are experimental data for each sample.

Table 7.3. A summary of the sample information gained from combining the XRF, XRR, and Laue oscillation data used to estimate the values of x and y in the formula $Fe_x(V_{1-y}Fe_y)_2$.

Sample	Laue # Layers	# Layers Possible from XRF intensities			Impurity Layer Thickness (Å)	Excess Se Layers	Fe_x	Fe_y
		V	Fe	Se				
2	44(1)	33(1)	13(1)	45(1)	2	1	0.03(2)	0.25(2)
3	41(1)	30(1)	14(1)	43(2)	5	2	0.04(2)	0.27(2)
4	42(3)	21(1)	27(2)	43(2)	2	1	0.1(1)	0.50(2)
6	48(3)	19(1)	32(1)	49(2)	4	1	0.05(1)	0.60(2)
7	46(4)	14(1)	35(2)	47(2)	2	1	0.05(2)	0.70(2)
8	46(4)	10(1)	40(2)	47(2)	6	1	0.08(1)	0.78(2)

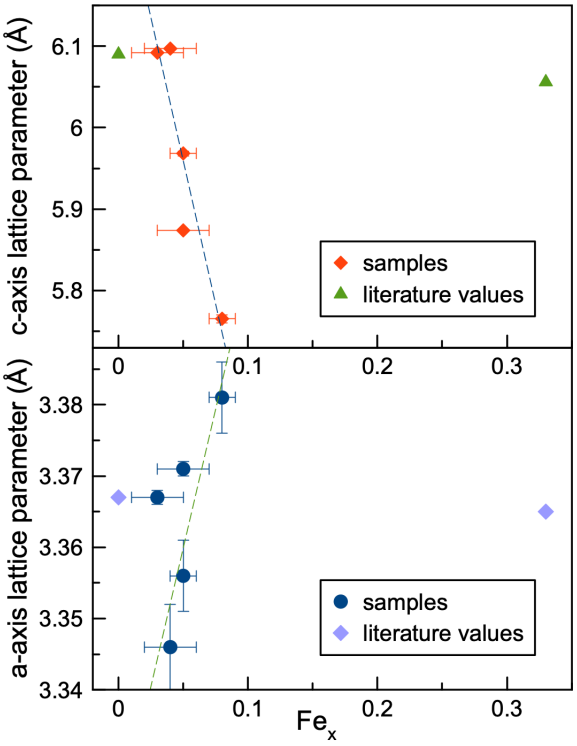

Fig. 7.8. Trend in the *c*-axis (top) and *a*-axis (bottom) lattice parameters versus the amount of intercalated Fe determined from the Laue oscillation and XRF data. Sample **4** is not included in this graph due to the presence of an impurity phase in its specular diffraction pattern. The values for similar $Fe_x(Fe_yV_{1-y}Se_2)$ samples reported from the literature are shown in green for the *c*-axis lattice parameters and light purple for the *a*-axis lattice parameters.

HAADF-STEM imaging and STEM-EDS measurements were carried out on a cross-section of sample **8** to directly measure the distribution of Fe atoms between substituted and intercalated sites to compare with the results discussed above. The HAADF-STEM images (Fig. 9) show a stack of 41+ unit cells that are crystallographically aligned perpendicular to the substrate. The image of the entire cross section (see SI) could not be used to determine the exact number of unit cells in the stack because of poor resolution in the layers near the surface of the sample. The unit cells that achieve atomic resolution clearly show a 1T hexagonal structure with van der Waals gaps between each layer. The average structure from the HAADF-STEM image can be compared with the average elemental intensities observed in the STEM-EDS elemental mapping (Fig. 9c) and indicate that the majority of the Fe atoms are located in the same plane as the V atoms. The STEM-EDS elemental intensity profile was collected along the axis perpendicular to the substrate for a section of the sample with atomic resolution in the HAADF-STEM image (Fig. 9d). This profile shows that a majority of the Fe is substituted, but some van der Waal gaps contain intensity from intercalated Fe atoms. To quantify the ratio of substituted to intercalated Fe, the intensity profiles of each element were averaged across the map by lattice translations of the unit cell, and the average peaks were fit to Gaussian distributions to give the background subtracted intensities along the *c*-axis of the unit cell as shown in Fig 9e.[38] The ratio of the integrated intensity of the intercalated Fe peak to the intensity of the substituted Fe peak indicates the intercalated Fe has x = 0.08(4). The HAADF-STEM and STEM-EDS data is consistent with the composition and structure determination the XRF, XRR, and Laue oscillation data.

A one-dimensional Rietveld refinement of the specular XRD pattern of sample **8** was carried out to confirm that the cross section was representative of the whole sample (Fig. 10). The atomic plane positions determined from the averaged EDS line profiles were used to construct a model of the unit cell for the refinement.[39] The Fe_x and Fe_y values determined from the combination of XRF, XRR, and Laue oscillation data were used to constrain the fractional occupancy for the initial model. The refinement provided a good fit of the experimental XRD data before and after releasing the constraints on the model. However, the Rietveld refinement was not expected to be very sensitive to a small amount of intercalated Fe or to the ratio of V to Fe due to their similar scattering power. Multiple refinements were carried out with a range of Fe to V ratios, which achieved similar goodness of fits (see SI).

This illustrates that Rietveld refinements alone cannot be used to determine whether atoms are incorporated via substitution or intercalation. It is necessary to use additional data on the structure and composition of samples to constrain the Rietveld refinement.

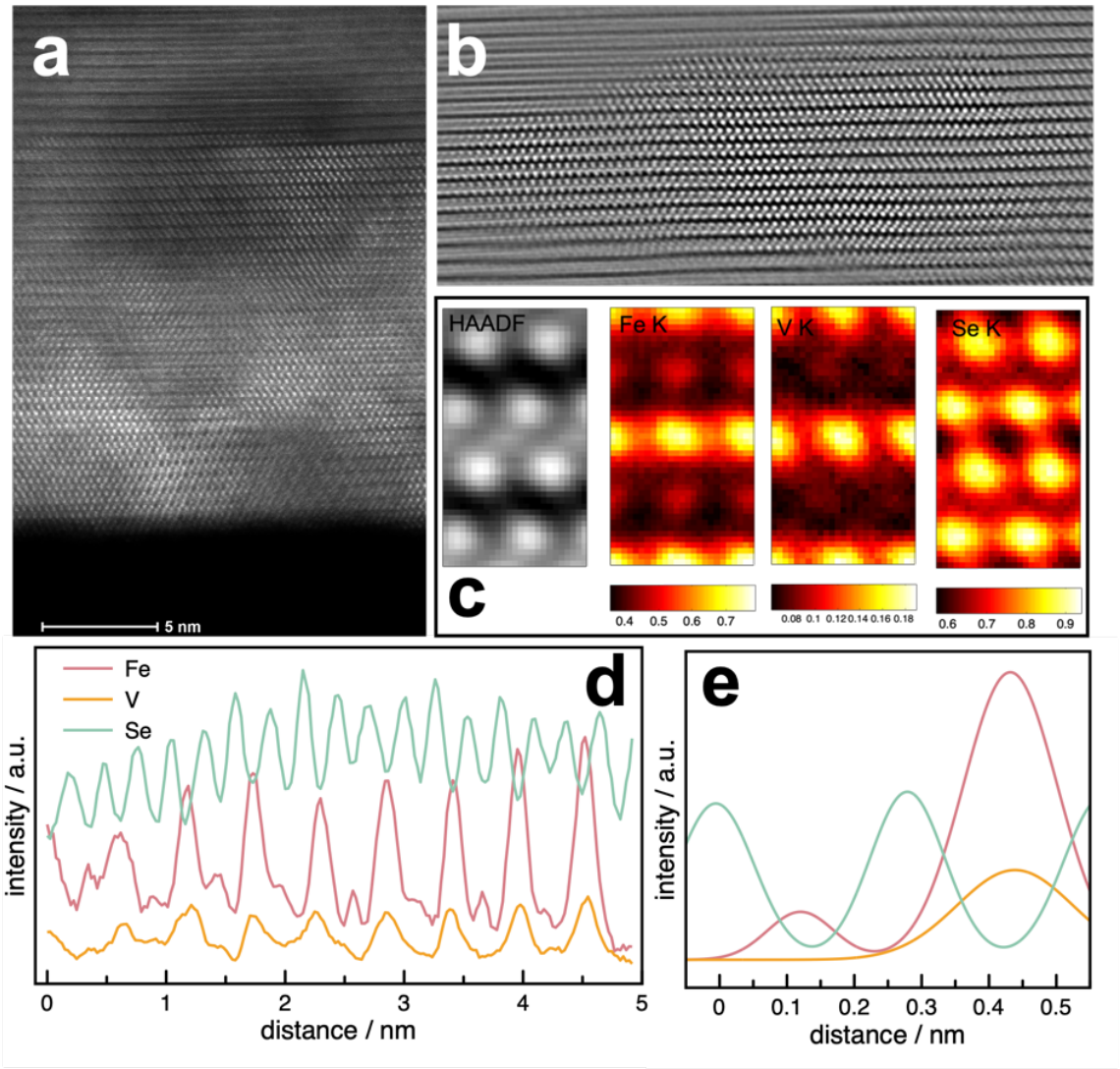

Fig. 7.9. HAADF-STEM images across a) a large area of the cross-section and b) a magnified section of the HAADF-STEM image which achieves atomic resolution. c) The average structure and elemental intensities from the HAADF-STEM image and EDS elemental map. d) EDS elemental line profiles collected along the axis perpendicular to the substrate. e) Elemental line profiles from a Gaussian fit of an averaged unit cell.

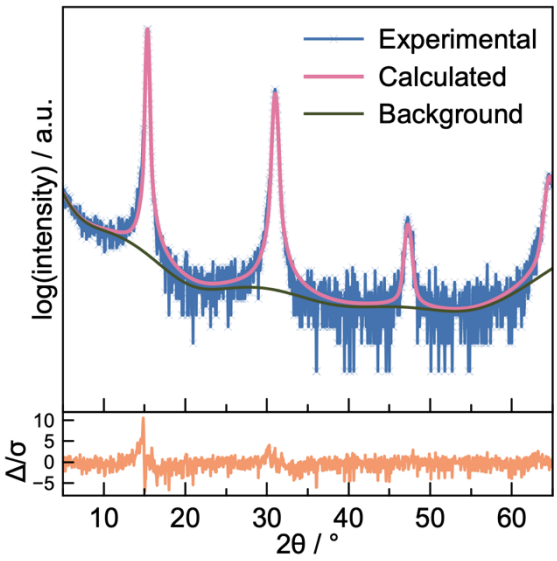

Fig. 7.10. One-dimensional Rietveld refinement of the specular XRD pattern of sample **8** annealed to 350°C.

7.3. Conclusions

We were able to expand the range of Fe substituted into the VSe_2 lattice up to x = 0.8. This was made possible by taking advantage of slow solid state diffusion rates which allowed for kinetic control over the formation of products from designed precursors. Formation of VSe_2 nucleation sites on deposit favored the addition of Fe into the lattice via substitution or intercalation rather than segregation into a binary Fe_xSe_y phase. The combination of substitution and intercalation caused two different effects on the lattice parameters.

Determining the amount and distribution of intercalated or substituted atoms is challenging, and we demonstrate that the determination cannot be accomplished using only a single analytical technique. A mixture of both types of incorporation can lead to different effects on the lattice, and the favored sites for incorporation can vary based on the overall composition. Furthermore, samples can be very sensitive to processing conditions, which can affect the lattice parameters, composition, and type of guest species incorporation. For example, the amount of intercalation in the samples presented here could be increased by annealing samples at temperatures high enough for them to lose Se. The Fe could also be moved from an intercalated site to a substituted site as the sample gained Se during annealing in a Se atmosphere.

We combined the data from several techniques that offer complementary information and give a self-consistent picture of what is occurring in each sample. Analysis and comparison of XRF, XRR, XRD, and Laue oscillation data leads to a more accurate determination of the amount and site of atom incorporation in the host lattice. For samples that do not contain Laue oscillations in their XRD patterns, HAADF-STEM imaging and STEM-EDS elemental mapping provide a direct measurement to quantify the amount of intercalation versus substitution. The results of this direct measurement on sample **8** agree with those from the combination of XRF, XRR, XRD, and Laue oscillation data.

7.4. Bridge

Chapter VII described an exploration of Fe-substituted or intercalated VSe_2 samples with high Fe content. Chapter VIII will focus on another ternary phase space containing Fe and Se. The following chapter will describe the investigation of the ternary Pb-Fe-Se phase space, which lead to the discovery of a novel ternary phase.

CHAPTER VIII

INVESTIGATION OF THE Pb-Fe-Se TERNARY SYSTEM AND THE SYNTHESIS OF A TERNARY $Pb_{1-x}Fe_xSe$ PHASE

8.0. Authorship Statement

Chapter VIII was published in *Chemistry of Materials* in 2022. F.G. Harvel is the primary author. I aided in writing, editing, and experimental work. R. Gannon, D. Bardgett, and M. Humphrey also contributed experimental work. D.C. Johnson provided editorial assistance.

8.1. Introduction

Computationally predicting potentially stable materials with desired properties has become an important tool to increase the rate of innovation, outlined by the rise of computational[1–3] and experimental material databases.[4–6] However, a major hurdle has been the actual synthesis of the predicted compounds.[7–10] The convex hull approach, which compares the heat of formation of predicted compounds to that of a mixture of the known thermodynamically stable compounds, is commonly used for assessing the potential stability of predicted materials.[9,11,12] The local free energy minima predicted in hull energy calculations, however, have systematic errors that depend on the functionals used. Furthermore, the ability to synthesize a given structure also depends on the magnitude of the energy barriers from a minima and the volume of configuration space occupied by the local free energy minima as well.[9,13,14] A second issue is the lack of experimental synthesis parameters and approaches that can be used to target a specific structure. Traditional synthesis approaches vary experimental parameters (composition, temperature, pressure, flux composition, etc.) to make the desired compound the most stable phase in the system. After the desired phase is formed, the reaction conditions are quickly altered, kinetically "trapping" the newly formed metastable phase before it can decompose.[15–17] Molecular beam epitaxy (MBE) is another approach to prepare metastable compounds by using the substrate surface structure as a template and controlling the experimental fluxes and substrate temperature to

find conditions where nucleation and growth of the targeted metastable compound is kinetically favored.[18–20] In both traditional and MBE synthesis, however, discovering the experimental conditions required to make a predicted compound thermodynamically stable is challenging and, with some exceptions, calculations do not include predictions of experimental conditions that would enhance the stability of predicted products.[9] The net result is that thousands of computationally stable structures remain unsynthesized.

A recent example of the attempted synthesis of $PbFe_2Se_3$, Pb_2FeSe_3, and Pb_2FeSe_4 highlights the challenges of synthesizing compounds predicted to be thermodynamically stable.[21] These compounds are interesting targets because there are no known ternary compounds in this phase diagram besides a ternary-alloy phase, and because of recent reports discussing the superconductivity of PbO-structured FeSe.[22,23] The compounds $PbFe_2Se_3$ and Pb_2FeSe_3 were predicted to be magnetic metals while Pb_2FeSe_4 was predicted to be a non-magnetic semiconductor. Conventional high temperature sealed tube reactions targeting these compounds yielded mixtures of PbSe and different iron selenide phases depending on the stoichiometry. Attempts to form them via MBE also were also unsuccessful, yielding mixtures of PbSe and Fe_3Se_4. While these results suggest that the materials are not thermodynamically stable in the ternary phase diagram with respect to binary compounds, it does not rule out the possibility that they are local free energy minima in the energy landscape that could be prepared under appropriate synthetic conditions.

Herein we attempted the synthesis of $PbFe_2Se_3$, Pb_2FeSe_3, and Pb_2FeSe_4 via modulated elemental reactants (MER).[24] As illustrated schematically in figure 1, MER differs from other synthesis methods by using low solid-state diffusion rates to limit the extent that a system can explore the free energy landscape. MER precursors are prepared by sequentially depositing elements on an unheated substrate. The elemental layer thicknesses can be less than a nanometer, resulting in ultrashort controllable interdiffusion distances. The low temperature of the substrate during deposition limits the extent atoms can diffusion on the surface or into the film. Low temperature annealing results in low solid state diffusion rates, but the short interdiffusion distances result in mixing of the elemental layers and/or nucleation and growth of crystalline solids. We expected that amorphous precursors would form during the deposition and anticipated that the predicted compounds might form during low temperature annealing, because disproportionation into a mixture of the stable binary

compounds would be inhibited by slow solid state diffusion rates. Instead, we formed a new metastable compound, $Pb_{1-x}Fe_xSe$ during the deposition of the precursors, where x ranges between at least 0.33 to 0.66.

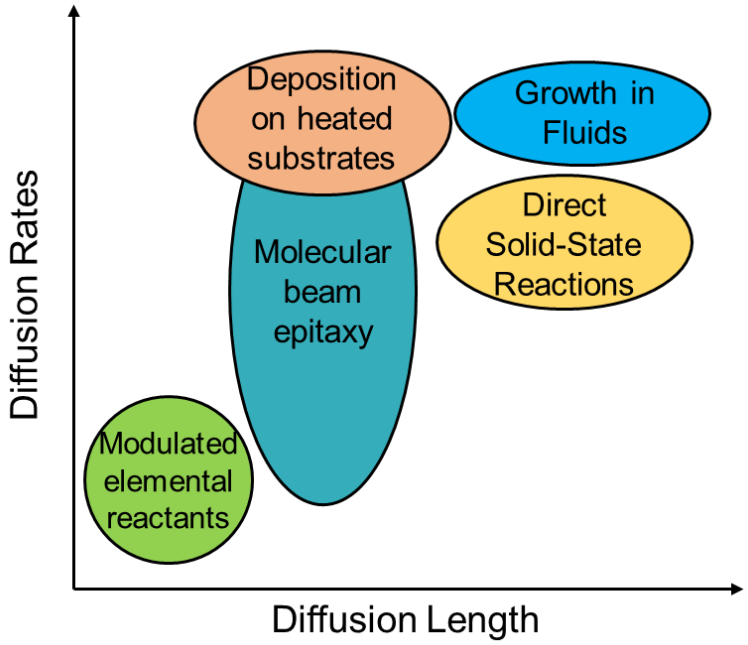

Fig. 8.1. A schematic of the relative diffusion rates and diffusion lengths found in solid state synthesis techniques in comparison to MER.

8.2. Methods and Materials

The multilayer thin-film precursors were deposited onto (100) oriented Si wafers using a custom-built high vacuum ($<10^{-6}$ Torr) physical vapor deposition (PVD) chamber from elemental sources. Electron-beam guns were used to evaporate Fe (99.95%) and Pb (99.99%) and a Knudson effusion cell was used to evaporate Se (99.99%). The deposition rates were monitored by quartz crystal microbalances located above each elemental source. Pneumatic shutters positioned between the elemental sources and the spinning substrate were programmed to open and close to control the sequence and amount of each element deposited. Thin layers of Pb, Fe, and Se were deposited in several different sequences and the sequence was repeated to yield a film thickness of approximately 300 Å. Prepared samples were stored in a nitrogen glovebox (>0.2 ppm O_2) to prevent oxidation.

Annealing of the samples took place inside an N_2 glovebox on a calibrated hot plate set to the desired temperature. The pieces were annealed for 15 minutes at each temperature. The samples were temporarily removed from the nitrogen glovebox as needed for characterization. Specular, grazing incidence and in-plane x-ray diffraction scans (XRD), x-ray reflectivity scans (XRR), and x-ray reflectivity (XRF) data were collected after each annealing step.

X-ray fluorescence spectroscopy (XRF) data was collected on a Rigaku Primus II spectrometer. A technique previously described by Hamman, et al was used to determine the proportionality constant between intensity and the absolute number of atoms per unit area.[25] X-ray reflectivity (XRR) data and specular X-ray diffraction (XRD) data were collected on a Bruker D8 diffractometer equipped with Cu Kα radiation in θ−2θ locked-coupled scan mode over a 2θ range of 0-11° for XRR and 5-65° for XRD. Film thicknesses were determined from the XRR patterns using a modified version of Bragg's law to account for refraction.[26] All of the in-plane and grazing incidence patterns and some of the XRR and XRD patterns were collected on a Rigaku Smartlab diffractometer with Cu Kα radiation and parallel-beam/parallel slit analyzer (PB/PSA) optics. Lebail fits of the specular, grazing and in-plane XRD patterns were carried out using the crystallography data analysis software, GSAS-II.[27]

8.3. Results and Discussion

Eleven MER precursors were made with a variety of layer sequences and a spread of compositions around those of the predicted Pb-Fe-Se compounds as shown in figure 2. The corresponding diffraction patterns are found in figures S1-11. The diffraction patterns of six of these as-deposited precursors contained reflections that could mostly be indexed to a tetragonal unit cell, as shown in figure 3, with a-axis lattice parameters of ~4.3 Å and *c*-axis lattice parameters of ~6.1 Å as summarized in Table 1. Two of these samples showed a broad, weak reflection that could not be indexed in the tetragonal unit cell. The number, intensity and line width of reflections varies between samples, indicating the level of crystallinity varies with composition. Two precursors (green dots) formed a significant impurity phase after annealing, which can be seen in figures S4-S6. Table 1 summaries the compositions, layering scheme, total thickness, estimated elemental layer thickness, and lattice parameters of the new tetragonal phase without any known binary compounds. The

layering sequence used in the precursor and the range of repeat layer thicknesses probed in our experiments did not affect the formation of this new compound. The compositions of the precursors that contained only the new tetragonal phase are found along the PbSe-FeSe tie line, suggesting that the stoichiometry of the new compound is $Pb_{1-x}Fe_xSe$.

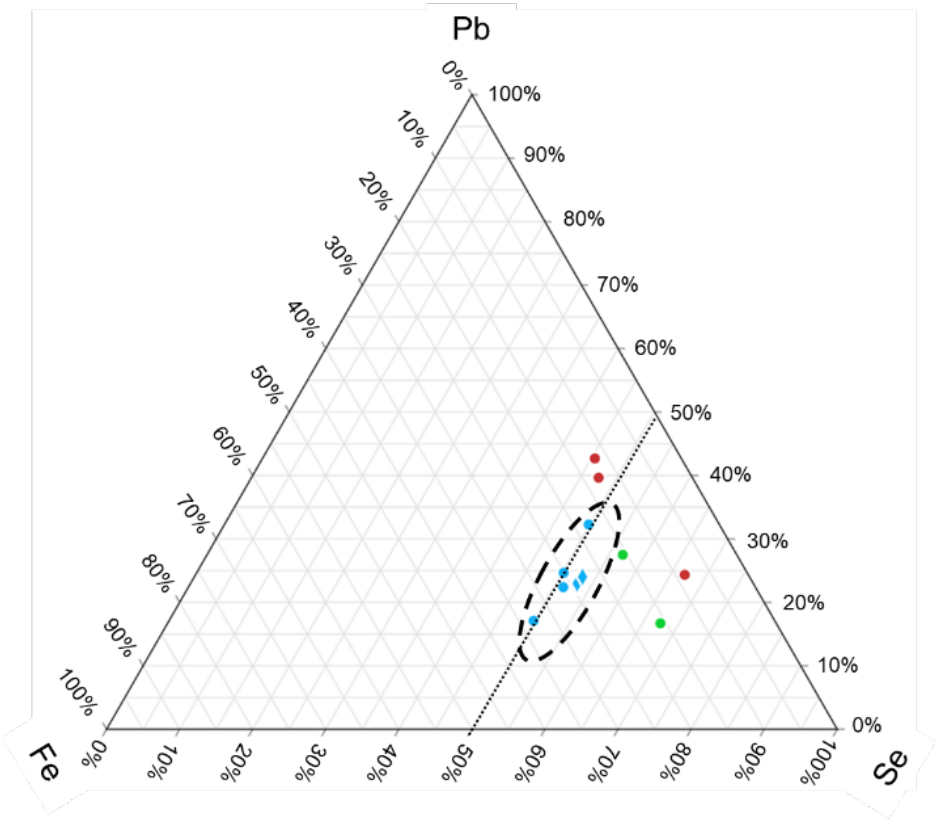

Fig. 8.2. The precursors made in this study imposed on a triangular composition space. The blue dots are precursors whose diffraction patterns contain only reflections from the new $Pb_{1-x}Fe_xSe$ phase. The blue diamonds are precursors whose diffraction patterns contain reflections from the new $Pb_{1-x}Fe_xSe$ phase and one additional broad reflection. The green dots are precursors whose diffraction patterns contain reflections from $Pb_{1-x}Fe_xSe$ phase and known binary compounds. The red dots are precursors whose diffraction patterns do not contain reflections from $Pb_{1-x}Fe_xSe$ phase. The dashed line is the $Pb_{1-x}Fe_xSe$ tie line.

Table 8.1. A summary of the characteristics of the as-deposited precursors that contained reflections from a new tetragonal phase in their diffraction patterns without any known binary compounds. Layer thickness were calculated by dividing the total film thickness by the number of layers deposited. Samples 2 and 3 contain a broad reflection from an unknown compound.

Sample	Layer Sequence	Composition	Film Thickness (Å)	Layer Thickness (Å)	*a*-lattice Parameter (Å)	c-lattice Parameter (Å)
1	Fe|Pb|Fe|Se	$Pb_{0.65}Fe_{0.36}Se_{1.00}$	455(1)	22.7(1)	4.302(2)	6.171(1)
2	Fe|Pb|Fe|Se	$Pb_{0.45}Fe_{0.43}Se_{1.00}$	373(1)	7.5(1)	4.43(1)	6.14(1)
3	Pb|Fe|Pb|Se	$Pb_{0.44}Fe_{0.46}Se_{1.00}$	290(1)	11.6(1)	4.25(1)	6.10(1)
4	Fe|Pb|Fe|Se	$Pb_{0.49}Fe_{0.50}Se_{1.00}$	376(1)	11.9(1)	4.34(2)	6.12(2)
5	Fe|Pb|Fe|Se	$Pb_{0.44}Fe_{0.51}Se_{1.00}$	297(1)	11.4(1)	4.34(1)	6.11(1)
6	Fe|Pb|Fe|Se	$Pb_{0.34}Fe_{0.66}Se_{1.00}$	388(1)	19.4(1)	4.39(1)	6.11(1)

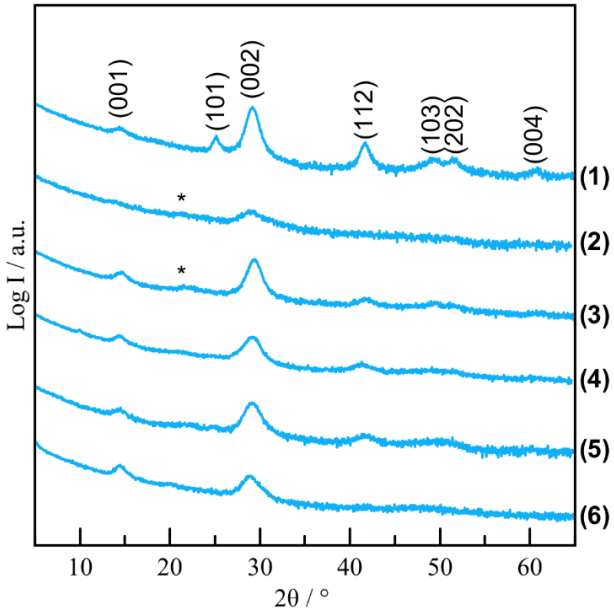

Fig. 8.3. Grazing-incidence x-ray diffraction patterns of the six as-deposited precursors where reflections can be indexed to a tetragonal unit cell without known binary compounds. The numbers refer to those in Table 1 and the * symbol marks a broad weak reflection from an unknown compound.

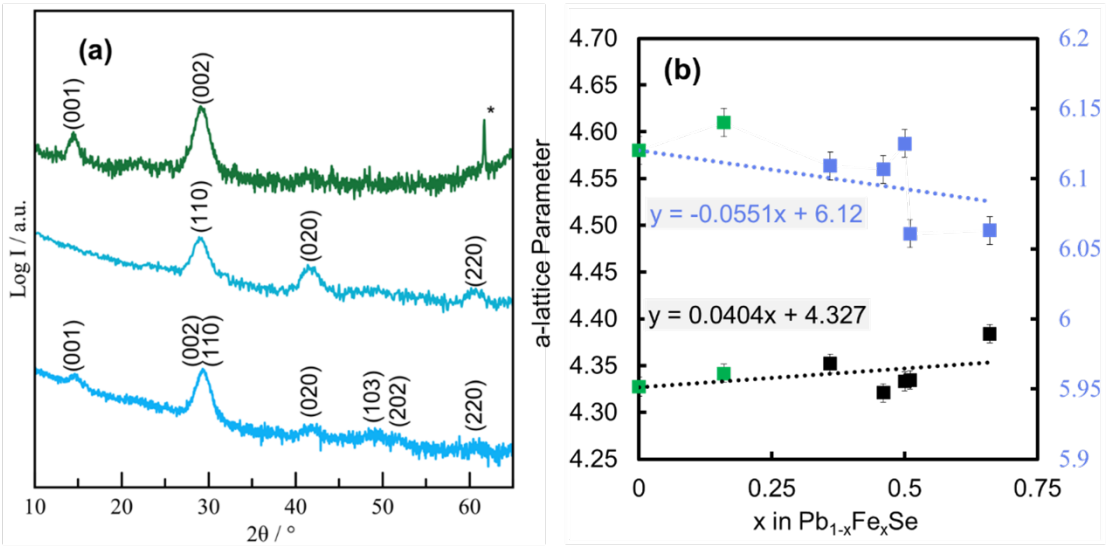

Fig. 8.4. a) Specular (green), in-plane grazing-incidence (teal), and grazing-incidence (blue) diffraction patterns of sample 5 after annealing at 150°C. b) *a*-axis and *c*-axis lattice parameters of samples **1** and **3-6** after annealing to 150°C. The green data points are from an $Pb_{1-x}Fe_xSe$ rock-salt structure previously reported.[28] The dotted lines are fits with the y-intercept constrained to the lattice parameters of PbSe.

The six samples in Table 1 were annealed to try to improve their crystallinity. As shown in Figure 4a for a representative film (sample 5), the reflections from the new phase sharpen and increase in intensity after annealing at 150°C. The impurity phase in sample 3 is no longer apparent in its diffraction pattern after annealing, while the intensity of the reflection from the impurity phase in sample 2 increased in intensity after annealing (figure S7). The low number of reflections in the specular pattern and the varying relative intensity of reflections in the different scans indicate that there is preferred crystallographic alignment. Figure 4b graphs the change in unit cell parameters after annealing obtained from simultaneous refinement of the diffraction patterns collected with different geometries as a function of iron content for the five samples with only reflections that could be indexed as tetragonal. The face-centered cubic (fcc) unit cell reported previously for PbSe and a low iron content $Pb_{1-x}Fe_xSe$ sample[28] were converted to body centered tetragonal unit cell to be included in this figure. While there is considerable scatter, the *a*-axis lattice parameter increases while the *c*-axis lattice parameter decreases as iron content increases.

The reflections observed for the new phase indicate that it has a primitive tetragonal unit cell. The position and intensity of reflections are similar to those of fcc PbSe, however, suggesting that Pb and Se are arranged as they are in PbSe. Since iron is divalent in both FeSe and $FeSe_2$ and the new tetragonal phase only forms near the $Pb_{1-x}Fe_xSe$ tie line, it is reasonable to expect Fe^{2+} to be substituting for Pb^{2+}, resulting in a tetragonal distortion from PbSe's rock-salt structure. Face-centered cubic structures are known to distort to tetragonal structures when subject to high temperatures or pressures.[29–32] Modeling the diffraction pattern as a function of iron position suggests that the iron occupies a set of partially occupied general position sites around the Pb^{2+} special position sites, presumably because of the smaller size of Fe^{2+} relative to Pb^{2+}. If the Fe^{2+} substitutes for Pb^{2+} and occupies a position off of the special position site, for example (0.55, 0.55, 0.7) instead of (0.5, 0.5, 0.5), significant intensity occurs for the 001 reflection in the diffraction pattern while the 100 reflection has very small intensity. This model increases the intensity of the (001) reflection as the amount of substituted Fe increases, which is consistent with the experimental data. Unfortunately, the preferred crystallographic alignment of the crystallites prevented a Rietveld refinement of the structure.

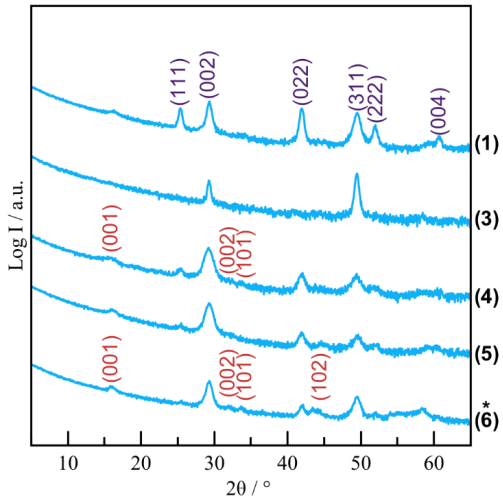

Fig. 8.5. The diffraction patterns of samples 1 and 3-6 after annealing at 200°C. The indices of the reflections correspond to lattice parameters and geometries consistent with PbSe (purple) and β-FeSe (red). Sample 6 was annealed to 250°C to induce full decomposition of the initial tetragonal phase.

The diffraction patterns from collected after annealing above 200°C indicate that the new tetragonal phase decomposed to mixtures of known binary compounds (Figure 5). There was no indication that the predicted compounds ($PbFe_2Se_3$, Pb_2FeSe_3, or Pb_2FeSe_4) formed as reaction intermediates (SI figures S5, S6, and S11). The diffraction patterns all contain relatively sharp reflections that can be indexed to a cubic unit cell with lattice parameters consistent with face-centered cubic (fcc) PbSe.[33] Samples 3-6 contain reflections that indicate tetragonal β-FeSe forms.[34] There were not enough reflections in sample 1 and 2 to identify the iron containing decomposition product, although the decomposition of the tetragonal $Pb_{1-x}Fe_xSe$ phase is evident from the disappearance of its 001 reflection at ~14.5° 2θ. Since the iron and lead atoms are intimately mixed in the new tetragonal phase, forming the predicted ternary compounds would involve only local rearrangements in the precursors that are close to their composition. The decomposition of $Pb_{1-x}Fe_xSe$ to the predicted ternary compounds might be expected to be kinetically favored at low temperatures where diffusion rates are small. The observed decomposition into binary compounds suggests that the predicted ternary compounds are metastable at best, and they will be very difficult to synthesize due to their large, complex unit cells.

8.4. Conclusions

The results presented highlight the challenges with predicting solid-state phases by using a hull energy approach without considering the volume of configuration space that will evolve into the predicted compounds.[9,21] Figure 6 presents a simplified three-dimensional schematic of a free energy landscape to illustrate how the volume of configuration space impacts the ability to prepare a compound. In this image, contour lines and color are used to indicate the relative energies of different configurations as a function of position. The ability to prepare a metastable product dependent on both the area of configuration space, shown as a dotted line around each yellow region and depth of the energy basin relative to the height of the saddle point between the metastable and thermodynamic phase. Our study suggests the $Pb_{1-x}Fe_xSe$ phase reported herein forms over a wide composition regime represented by the larger yellow region. Any starting point within the dotted line outlining the basin represents a configuration that will evolve into $Pb_{1-x}Fe_xSe$. Factors such as composition, diffusion distances, layering schemes and layer thicknesses in our study can be thought of as

experimental parameters that can be used to probe this configuration space. The smaller yellow region represents the computationally predicted phases. The yellow area is much smaller as specific stoichiometries were required for the proposed structures. The configurational area that will evolve into this minimum is much smaller, and probably overestimates the volume of configuration space that will form the predicted compounds. We expect this is a consequence of the very large unit cells of the predicted compounds. The energy barrier between this region and the mix of thermodynamic products is probably also small, making it experimentally more difficult to kinetically trap these metastable compounds.

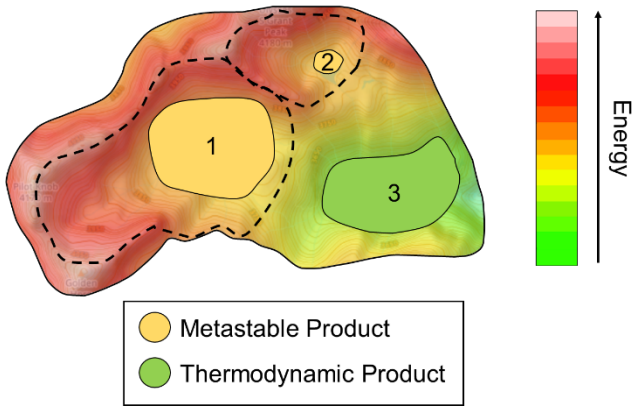

Fig. 8.6. A schematic of an energy landscape containing several potential products. The relative energy of each configuration is given by the color, with red being high energy and green low energy. The dotted regions show the area of configuration space that will evolve to form each of the metastable products.

This study illustrates areas in both theory and experiment where current understanding falls short of what is needed to accelerate materials discovery. Experimentally we need a better understanding of how to change reaction conditions in conventional synthetic approaches to make a targeted compound thermodynamically stable under the reaction conditions. For approaches that rely on controlling reaction kinetics, we need a better understanding of how experimental variables influence the configurational volumes of targeted compounds. Theory needs to address how predicted compounds might be synthesized. One advance would be to better define the configuration space around predicted compounds. Another, perhaps more challenging goal, would be to understand the relative

stability of different compounds in fluxes typically used in high temperature solid state reactions. Perhaps a first step would be to estimate the impact of pressure on the relative stability of predicted compounds. These and other experimental and theoretical advances are needed to increase our ability to prepare predicted compounds.

8.5. Bridge

Chapter VIII described the exploration of the Pb-Fe-Se phase space, which lead to the discovery of a novel ternary compound. The next chapter is focused on the continued investigation of this ternary phase space. Chapter IX presents a family of ternary misfit layered compounds with a novel 1T-$FeSe_2$ structure layer.

CHAPTER IX

1T-$FeSe_2$ LAYERS IN $(PbSe)_{1+\delta}(FeSe_2)_n$ – AN INTERLAYER STABILIZED 2D STRUCTURE

9.0. Authorship Statement

This chapter has been submitted to *Chemistry of Materials* and is awaiting review. F.G. Harvel and I are both the primary authors and carried out experimental work and data analysis. R.N. Gannon and H.R. Blackwood prepared lamella for collection of HAADF-STEM images and STEM-EDS that was done by P. Lu. S.P. Rudin carried out theoretical calculations. D.C. Johnson provided editorial assistance.

9.1. Introduction

The discovery that heterostructures have new properties that differ from those found in the constituents as bulk compounds has created a new field of research in the materials community.[1,2] These emergent properties of monolayers and heterostructures have been proposed for a variety of applications in electronic and optoelectronic devices such as photodetectors or field effect transistors.[3–5] Most heterostructures have been prepared by mechanical exfoliation and stacking of layers of the individual bulk constituents since they cannot be prepared via traditional high temperature solid state reactions.[6] However, there are ~50 known thermodynamically stable heterostructures, known as misfit compounds, that can be directly prepared by reaction of the elements at high temperatures – which is surprising given the structural mismatch between the constituent layers.[7,8] These misfit layer compounds contain two or more structurally different layers in each unit cell with a mutual modulation of their structures.[9] Stabilizing interlayer interactions in the known thermodynamically stable misfit layer compounds allow for the formation of 2D constituents with structures not found in the constituent binary phase diagrams. For example, the thermodynamically stable misfit compound $(BiSe)_{1+\delta}(CrSe_2)$ contains distorted, rock salt structured BiSe bilayers interwoven with 1T-structured $CrSe_2$ layers. Both these structural

units are not compounds found in the Bi-Se or Cr-Se phase diagrams but are favored in the heterostructure due to the stabilization from interlayer charge transfer.[10,11]

It is a reasonable hypothesis that other 2D layers with emergent structural motifs could be stabilized by the two-dimensional confinement and interlayer interactions within heterostructures. However, there are very few calculations of the formation energies of potential heterostructures in computational materials projects due to complications resulting from the lattice mismatch between constituents. The "island" approximation is a theoretical approach that has previously been used to computationally predict a novel constituent layer within a heterostructure that was successfully synthesized.[12] This approach approximates nuclei of constituent layers as 30-50 atom fragments, or "islands", of the structure being tested, which is confined between crystalline layers in the calculations. Relaxing this nucleus in a density functional (DFT) calculation tests its kinetic stability.[13] If the structure of the "island" remains ordered, it implies that the resultant heterostructure is a local free energy minimum in the energy landscape and experimentally one should be able to nucleate and grow it under the correct conditions.

Here we report our theoretical and experimental results from an investigation of potential heterostructures containing known or emergent iron selenide structures between layers of lead selenide. We chose to search the Pb-Fe-Se system because no thermodynamically stable ternary compounds – which would compete with the formation of a misfit layered compound – exist in the phase diagram and many known misfit layer compounds contain PbSe bilayers as constituents.[7,8] The kinetic stabilities of 36 different nuclei of potential iron selenide structures were explored between bilayers of PbSe with the "island" approach. Relaxing these "islands" in DFT calculations yielded several nuclei that retained their periodic structural motifs, suggesting they might be kinetically stable. For the iron selenide islands that retained their structural motifs, the thermodynamic stabilities of relaxed bulk compounds were calculated relative to the elements. The two lowest energy metastable structures were an FeSe in a three-monolayer Se-Fe-Se structure of Fe vertex-sharing octahedra with Se at the apexes, with the octahedra rotated against each other (-0.133 eV/atom) and a hexagonal 1T-$FeSe_2$ structure, similar to 1T-VSe_2 (-0.316 eV/atom), where the value in thermodynamically unstable with respect to the known binary iron selenides by 0.113 eV/atom. Figure 1 illustrates the sequence of calculations carried out for 1T-$FeSe_2$.

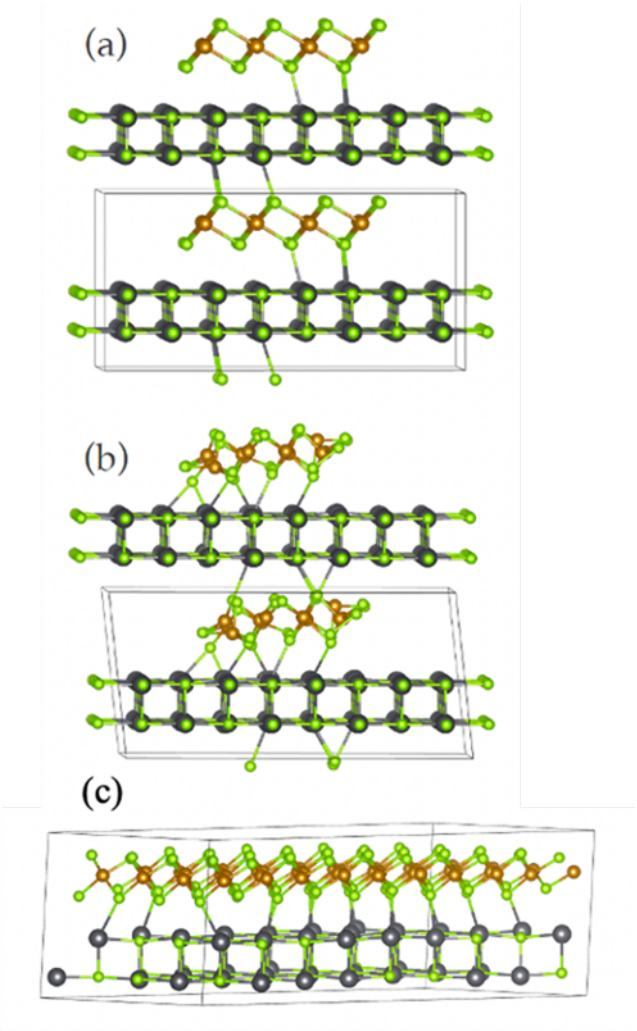

Fig. 9.1. The island structure of $FeSe_2$ is shown as it appears (a) before and (b) after relaxation. Based on the structure of (b), several approximate computational cells with complete PbSe and $FeSe_2$ layers were constructed. The full relaxed structure with the lowest formation energy is shown in (c).

9.2. Computational Methods

Theoretical calculations were carried out to search for potential metastable phases within the ternary Pb-Fe-Se phase diagram. The calculations were carried out using an "island" approximation in which potential layered Fe_xSe_y phases were modeled as finite nuclei located between infinite 2D slabs of the rock salt PbSe structure. The "islands" begin as an ordered configuration of atoms with various stoichiometries and structures. As the atoms are allowed to relax between the adjacent crystalline layers, the free space allows them

to diffuse into more favorable conditions to lower the overall free energy. The atoms will either form an ordered, periodic pattern – an "island of promise" – or a disordered dispersion – an "island of disaster".[13] The initial configuration and stoichiometry of the atoms in the island typically control the crystalline structure upon relaxation for "islands of promise" if the interfacial interactions with adjacent layers cause it to be kinetically favorable. The structures of the stable islands are used to estimate the potential crystalline layer's lattice constants. These are used to construct layered structures containing both crystalline constituent layers which are relaxed in DFT calculations to obtain formation energies. This provides information about the energy landscape of the system, which is used to target potential parameters (local compositions and predicted structures) for the design of precursors in MER synthesis.

9.3. Experimental Procedures

Samples were synthesized through the MER method. MER is carried out using a custom-built high vacuum physical vapor deposition chamber that is maintained at pressures $<3 \times 10^{-7}$ Torr during deposition. Precursors are deposited from elemental sources onto a room temperature spinning substrate. The precursors are deposited onto (100) oriented Si wafers with a passive SiO_2 layer at the substrate surface, which do not have an epitaxial relationship with the deposited layers. A Knudson effusion cell was used to evaporate Se (99.995%, Alfa Aesar) from an alumina crucible. Electron-beam guns were used to evaporate Fe (99.95%, Kurt J. Lesker) and Pb (99.8%, Alfa Aesar). Quartz crystal microbalances placed above the elemental sources were used to monitor the deposition rates, which were controlled to be 0.2-0.9 Å/sec. Pneumatic shutters positioned between the elemental sources and the unheated spinning substrate were programmed to open and close to control the sequence and thickness of the deposited elemental layers.

Precursors prepared to target the ternary heterostructure $(PbSe)_{1+\delta}(FeSe_2)_n$ were deposited with the sequence of elemental layers of Fe|Pb|Fe|Se for enough repeat units to target a total film thickness of ~30 nm (between 10-30 depending on n). The elemental layer thicknesses were designed to provide enough material to form a rock salt structured PbSe bilayer and n hexagonal structured FeSe2 layers in each repeat unit. Deposited samples were stored in a nitrogen glovebox (<0.2 ppm O_2) to prevent oxidation and were taken out as needed for characterization. Annealing studies were carried out by sequentially heating the

samples to temperatures ranging from 100°C-300°C for 15 minutes to monitor the reaction mechanism and determine the optimal temperature to crystallize the targeted phases. Samples were annealed on a calibrated hot plate in the nitrogen glovebox within a container with a Se atmosphere to prevent Se loss.

The samples were characterized using X-ray reflectivity (XRR), specular X-ray diffraction (XRD), in-plane grazing-incidence X-ray diffraction, and X-ray fluorescence (XRF) after each annealing step and as-deposited. X-ray fluorescence (XRF) spectroscopy scans were collected on a Rigaku Primus II spectrometer. The actual amount of each element deposited was determined by relating the measured intensity of an element's characteristic XRF signal to the total number of atoms per unit area using a proportionality constant, as outlined by Hamann et al.[26] The average local compositions of the layers in a repeat unit were calculated by dividing the total number of atoms of each element by the number of layers deposited.

The XRR and XRD patterns were collected on a Rigaku Smartlab diffractometer equipped with Cu Kα radiation. A θ−2θ locked-coupled scan mode was used to collect XRR and specular XRD patterns, with a 2θ range of 0-11° for XRR and 5-65° for XRD. Kiessig fringes in the XRR pattern were used to determine the total film thicknesses using a modified version of Bragg's law that accounts for refraction.[27] The in-plane XRD patterns were collected in grazing-incidence scan mode over a 2θ range of 15-110°. Lebail fits of the specular and in-plane XRD patterns were carried out to determine the unit cell lattice parameters. One-dimensional Rietveld refinements of the specular XRD patterns were carried out to determine whether the structure observed in the HAADF-STEM and STEM-EDS data was representative of the sample. All Lebail fits and Rietveld refinements were carried out using the crystallography data analysis software, GSAS-II.[28]
Cross-sections of the samples were prepared with an FEI Helios NanoLab 600i DualBeam focused ion beam scanning electron microscope (FIB-SEM) using standard lift out procedures. High-angle annular dark-field scanning transmission electron microscopy (HAADF-STEM) images and energy-dispersive X-ray spectroscopy (EDS) maps of the prepared cross-sections were obtained using a Titan G2 80-200 STEM with a Cs-probe corrector and ChemiSTEM technology (X-FEG and SuperX EDS with four windowless silicon drift detectors) at 200kV. The average atomic plane positions of the elements in the

unit cell were determined from the STEM-EDS data by lattice translations of the unit cell that were then fit to Gaussian distributions, in a method described by Lu et al.[15]

9.4. Results and Discussion

To experimentally synthesize the predicted $(PbSe)_{1+\delta}(FeSe_2)_n$ heterostructures, we used a diffusion-constrained synthetic approach that employs precursors composed of modulated elemental reactants (MER) to reduce diffusion distances. The predicted $(PbSe)_{1+\delta}(FeSe_2)_n$ structures consist of a bilayer of PbSe with a square in-plane unit cell alternating with *n* $FeSe_2$ hexagonal layers containing a central Fe sheet octahedrally coordinated by Se sheets above and below with a van der Waals gap between adjacent $FeSe_2$ layers. Layered precursors were prepared via sequential deposition of n x [Fe|Se] + Pb|Se elemental layers on a room temperature substrate, with the number of atoms of each element mimicking the number found in the unit cell of the targeted n = 1, 2, and 3 compounds. Our hypothesis was that the local compositions within the layered precursor would control what structures initially nucleate and that low diffusion rates during low temperature annealing would prevent long range rearrangement into more thermodynamically stable binary products.

The average number of atoms of each element deposited per repeating layer sequence in the precursors was determined using XRF and the number of deposited layer sequences. While the samples are all clustered near areas where the predicted compounds would be found based on estimates of the lattice parameters of the constituent layers (Fig S1), only Sample 1 formed a crystallographically aligned layered structure. The other samples formed $Pb_{1-x}Fe_xSe$ during the deposition and decomposed into PbSe and various iron selenides after low-temperature annealing (Fig. S3-S11).

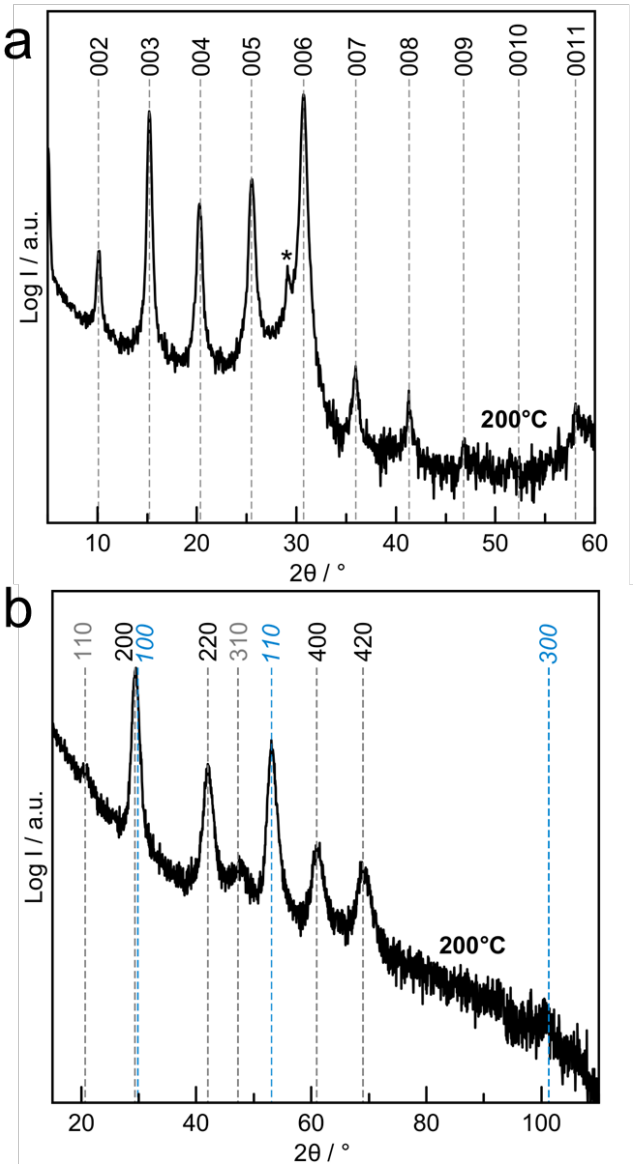

Fig. 9.2. a) The specular XRD and b) in-plane GIXRD patterns for Sample 1 annealed to 200°C. The lines correspond to the position of reflections determined from the lattice parameters of the indexed patterns. The 00*l* reflections yielded a c-axis lattice parameter of 17.463(6) Å. The black and grey lines for the *hk*0 reflections in the GIXRD pattern yielded a square in plane pattern for with an *a*-axis lattice parameter of 6.079 Å (black and grey lines) and an *a*-axis lattice parameter of 3.447(4) Å for a hexagonal structure (blue lines). The black lines correspond to allowed reflections and the grey lines correspond to forbidden reflections for a face centered cubic (fcc) structure.

The specular XRD and in-plane GIXRD patterns of Sample 1 after annealing at 200°C are shown in figures 2a and b. The specular diffraction pattern can be indexed to a family of 00*l* reflections from a heterostructure with a *c*-axis lattice parameter of 17.463(6) Å. All but one reflection in the in-plane GIXRD pattern can be indexed as *hk*0 reflections from a square lattice with an *a*-axis lattice parameter of 6.079(1) Å. The presence of weak 110 and 310 reflections indicate that the square phase is not isostructural with face-centered cubic (fcc) PbSe. The reflection at ~53° cannot be indexed to the square phase, but if indexed as a 110 reflection of a hexagonal layer it yields an *a*-axis lattice parameter of 3.447(4) Å. The heterostructure decomposes after annealing at 300°C (Fig. S2).

High-angle annular dark-field scanning transmission electron microscopy (HAADF-STEM) images and energy dispersive x-ray spectroscopy (EDS) maps on sample 1 annealed at 100°C were collected on cross sections of this sample to gain additional structural information. The HAADF-STEM images (Fig. S12) show a layered heterostructure with a repeat unit consisting of a brighter $Pb_{1-x}Fe_xSe$ layer and two darker Fe_xSe_y layers. Different zone axes are observed throughout the image, consistent with rotational disorder of the layers within the heterostructure. Clear [100] and [110] zone axes of the $Pb_{1-x}Fe_xSe$ layer are observed, however zone axes are not well defined for the Fe_xSe_y layers. The EDS intensity profiles (Fig. S13a) of each element suggest a repeat unit consisting of a $Pb_{1-x}Fe_xSe$ layer with Fe located between the Pb/Se planes and two Fe/Se layers containing a Se-Fe-Se sequence of elemental layers with a gap between adjacent Fe/Se trilayers. The presence of Fe in the $Pb_{1-x}Fe_xSe$ layer is consistent with the appearance of the forbidden reflection in the in-plane XRD pattern as previously reported for a metastable $Pb_xFe_{1-x}Se$ structure.[14] The EDS intensity profiles were averaged across the entire map and fit to Gaussian distributions in order to determine the average atomic plane positions in the heterostructure unit cell (Fig. S13b).[15] The Pb planes in the $Pb_{1-x}Fe_xSe$ layer are further apart (~2.2 Å) than the Se planes in the bilayer (~1.7 Å), which is a larger puckering distortion than observed for PbSe layers in misfit layer compounds.[16] The atomic plane positions from STEM-EDS data and the composition from the XRF data were used to create a starting model of the heterostructure for Rietveld refinements of the specular XRD. Refinements of this model, however, did not result in acceptable fits, which is likely due to defects in the sample such as local inclusions

of $FeSe_2$ in the PbSe layer or vice versa. These defects are known to occur when the local composition profiles differ from those required to form the heterostructure.[17]

We prepared a new set of precursors that targeted the amounts of Pb, Fe, and Se to form one layer of cubic PbSe and two layers of 1T-$FeSe_2$ per repeat unit based on the unit cell information determined from the XRD and STEM data collected on Sample 1 (Fig. S14). Each of the nine precursors deposited formed a layered structure during the room temperature deposition as indicated by the specular XRD patterns, but the intensity and width of the reflections varied based on the amount of nucleation and growth that occurred. Four of the samples had significantly broader heterostructure reflections and/or impurity phases as deposited and after annealing (Figs. S15-S20). The specular XRD patterns of five of the samples, however, contained more intense, narrower reflections. Sample 2, with an overall composition of $(PbSe)_{1.07}(FeSe_{1.94})_2$, is discussed in the following paragraphs as a representative sample from this set of 5.

An annealing study shows that the reflections in the specular and in-plane patterns for Sample 2 become sharper and more intense during annealing, and they were considerably sharper than those of Sample 1 at the same annealing temperatures (Fig 3 and Fig. S15). This suggests that the local composition profiles in Sample 2 were a better match to the targeted heterostructure. The lattice parameters calculated from the stepwise annealing process are found in Table S2. The $Pb_{1-x}Fe_xSe$ lattice parameter is 6.08(1) Å before annealing and increases to 6.118(3) Å after annealing at 200°C, which is significantly larger than what was observed in Sample 1. This could be due to the lower concentration of Fe in $Pb_{1-x}Fe_xSe$ present in Sample 2. The $FeSe_2$ *a*-axis lattice parameter is 3.38(2) Å before annealing and remains relatively constant, which also differs from what was observed for Sample 1. The specular XRD pattern for Sample 2 annealed to 200°C also contains Laue oscillations on several of the 00*l* reflections, which indicates that most of the sample is composed of similarly sized, crystallographically aligned, coherently diffracting crystalline domains. The Laue oscillations can be fit with a model consisting of a distribution of domains around a mean domain size of 18(2) unit cells. The *c*-axis lattice parameter of 17.618(2) Å multiplied by the number of layers determined from the Laue oscillations yields a thickness of the coherently diffracting crystalline domains of 317 Å, which is about 5% thinner than the total film thickness calculated from the XRR pattern of 338(5) Å. The XRF data show there are

enough Pb atoms present to form 19.6(2) PbSe layers, enough Fe atoms present to form 40.6(3) $FeSe_2$ layers, and enough Se atoms present to form 19.4(3) unit cells of the heterostructure. A broad impurity reflection present at ~28° 2θ in the specular XRD pattern after annealing at 200°C indicates that the 5% excess thickness is from small domains of PbSe, which form from the extra Pb and Se in the precursor.

HAADF-STEM images were collected on cross sections of Sample 2 to gain additional structural information (Fig. 4). The image of the full cross section shown in Figure 4a contains 17 $(PbSe)_{1+\delta}(FeSe_2)_2$ unit cells composed of one PbSe layer followed by two $FeSe_2$ layers, which is consistent with the number of unit cells determined from the Laue oscillations. A thin layer of the sample next to the substrate is $Pb_xFe_{1-x}Se$, which is consistent with the broad impurity phase peak present in the specular XRD data, the difference in total film thickness versus thickness of the coherently diffracting domain, and the excess material present calculated from the XRF data. While the majority of the sample is clearly $(PbSe)_{1+\delta}(FeSe_2)_2$, there are small domains in the sample where PbSe layers partially occupy sections within the $FeSe_2$ layers, which reflects the challenges in controlling the number of atoms deposited in each repeating sequence of elemental layers. Cubic PbSe and hexagonal 1T-$FeSe_2$ unit cells can be clearly identified by domains with aligned zone axes, such as those shown within the boxes in Fig 4b and expanded in Figs 4e and 4f. STEM-EDS elemental maps were obtained to probe the distribution of atoms in the film (Fig. 4c). The elemental line profiles are consistent with a periodic layering of a PbSe bilayer and two Se-Fe-Se trilayers. In contrast to the EDS map for Sample 1 at 100°C, the EDS map of Sample 2 at 200°C does not show Fe intensity between the Pb/Se layers. The puckering of the PbSe layer is similar to that found in thermodynamically stable misfit compounds, and likely stabilizes the structure by placing the Pb atoms nearer to the Se atoms in the $FeSe_2$ layer.[9] The atomic plane positions determined from the HAADF-STEM image and STEM-EDS elemental map were used to create a model for one-dimensional Rietveld refinements of the specular XRD data.[18] The constrained Rietveld refinements (Fig. S23) provided a reasonable fit of the data, indicating that the STEM data was representative of the bulk of the sample. These data confirm the formation of the $(PbSe)_{1.07}(FeSe_2)_2$ heterostructure containing 1T-$FeSe_2$ layers.

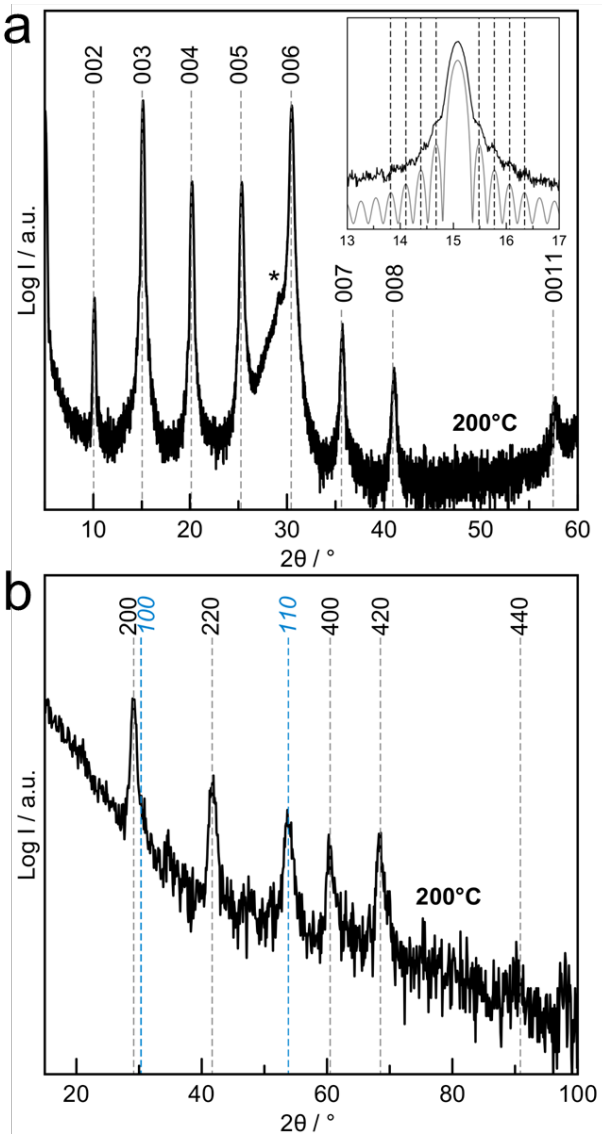

Fig. 9.3. The specular XRD (a), and in-plane GIXRD (b) patterns for Sample 2 annealed to 200°C. The 00*l* reflections yielded a c-axis lattice parameter of 17.618(2) Å. The black and grey lines for the *hk*0 reflections in the GIXRD pattern yielded a square in plane pattern for with an *a*-axis lattice parameter of 6.118(3) Å (black and grey lines) and an *a*-axis lattice parameter of 3.40(1) Å for a hexagonal structure (blue lines). The black lines correspond to allowed reflections and the grey lines correspond to forbidden reflections for a face centered cubic (fcc) structure. A zoomed in section of the specular XRD pattern shows Laue oscillations of the Bragg reflections which can be fit with the model consisting of 18-unit cells of the heterostructure, as shown in grey.

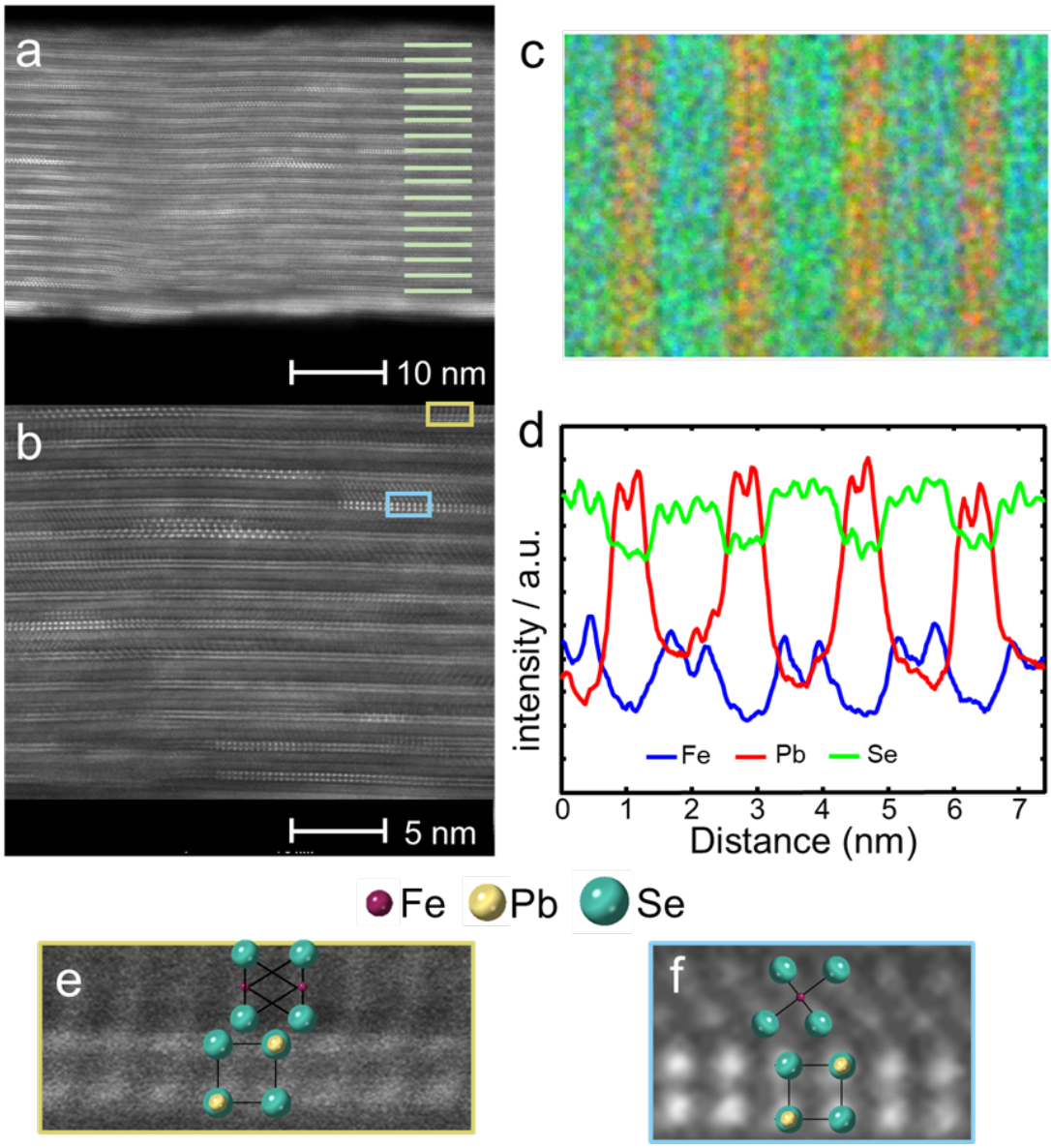

Fig. 9.4. HAADF-STEM images and STEM-EDS elemental maps are each for Sample 2 annealed to 200°C. a) A representative HAADF-STEM image showing 17 layers of the repeat unit as indicated by the green lines b) A closer view of a section of the HAADF-STEM image which achieves atomic resolution. The grains within the red boxes have a [100] orientation, allowing cubic PbSe and hexagonal $FeSe_2$ structures to be easily distinguished. c) An EDS elemental map and d) elemental line profiles of a portion of the sample with the elemental intensities mapped as a function of distance perpendicular to the substrate. e) Closer view of the [-100] zone axis of 1T-$FeSe_2$ and [100] of PbSe. f) Closer view of the [100] zone axis of 1T-$FeSe_2$ and [100] of PbSe.

With the structure and stoichiometry determined from Sample 2, we prepared precursors targeting $PbSe_{1.07}(FeSe_2)_1$ and $PbSe_{1.07}(FeSe_2)_3$ by decreasing and increasing the number of Fe|Se layers, respectfully. Annealing these precursors at 200°C resulted in their self-assembly into the targeted heterostructures, as indicated by their specular and in-plane XRD patterns (Fig. S24). The *c*-axis lattice parameters change by ~5.7 Å as *n* increases by 1 and the ratio of the intensities of the reflections in the in-plane diffraction patterns correlate with the ratio of the constituent layers. For the n = 3 heterostructure, the central 1T-$FeSe_2$ layer is surrounded by adjacent $FeSe_2$ layers and hence cannot be stabilized directly by the intralayer interaction with adjacent PbSe layers. This suggests that spatial confinement may also be an important factor in controlling the kinetics, as a layered 1T structure may have a lower surface energy than the pyrite structure found for bulk $FeSe_2$ and hence be easier to nucleate and more stable as a thin planar layer. The preparation and low temperature annealing of precursors with nanoarchitectures mimicking targeted metastable heterostructures kinetically traps the nucleation and growth of the targeted heterostructure, presumably because the low annealing temperatures prevent the segregation of the sample into separate domains of binary compounds.

9.5. Conclusions

The synthesis of targeted metastable compounds requires experimental parameters that favor the nucleation of a targeted structure while suppressing the nucleation of more thermodynamically stable products. The approach outlined herein uses predictions of potentially stable nuclei in a constrained geometry using the “island” approach to guide the experimental preparation of precursors with nanoarchitectures that favor the nucleation and growth of targeted compounds. The interactions between constituent layers are key to the kinetic stability of the constituent structures. The “island” approach computationally tests if 2D nuclei of novel structures of a constituent are likely to be kinetically stable between crystalline layers of a chosen second constituent, narrowing the experimental search to more likely candidates. The preparation of precursors with a nanoarchitecture (total number of atoms of each element per layer and deposited layer sequence) that matches that of a targeted compound experimentally increases the probability that it nucleates. Conceptually, the deposited precursors lie within the local minima of the targeted structures in the complex energy landscape, which enables the samples to lower their free energy by nucleating the

heterostructure. The local compositions within the nanoarchitecture control what structures nucleate, and low annealing temperatures limit long range diffusion, which prevents the samples from leaving their local free energy minima and segregating into mixtures of bulk binary constituents. Key to this experimental approach is the ability to control and measure the absolute number of atoms of each element deposited in each layer in the precursor. How close the nanoarchitecture needs to match that of a targeted structure is a key parameter for experimentalists and probably varies considerably depending on relative stabilities and local diffusion rates in the system being explored. Achieving kinetic control over the formation of targeted compounds by design of precursors provides an alternative approach to traditional synthetic approaches, which require discovering experimental conditions where the targeted compound is the thermodynamically most stable product in the reacting system.

9.6. Bridge

Chapter IX focused on the investigation of the ternary Pb-Fe-Se phase space and the formation of a novel ternary layered compound. Chapter X will focus on using the knowledge gained on the Pb-Fe-Se and V-Fe-Se ternary systems to explore the free energy landscape of the quaternary Pb-Fe-V-Se system.

CHAPTER X

EXPLORATION OF THE FREE ENERGY LANDSCAPE OF THE QUATERNARY Pb-Fe-V-Se SYSTEM

10.0. Authorship Statement

This chapter will be submitted to *Angewandte Chemie.* I am the primary author of this work. F. Harvel, N.Sagui, D. Bardgett, and S. Chu carried out annealing studies. R. Gannon prepared samples for HAADF-STEM imaging that was carried out by P. Lu. D.C. Johnson is my advisor and provided editorial assistance.

10.1. Introduction

There is a high motivation for researchers to discover novel materials for potential uses in technology. Among the search for new materials, ternary and higher order systems of compounds containing 3 or more elements have been far less synthetically realized than binary compounds.[1] Metastable multinary compounds are difficult to synthesize because a higher number of elemental combinations creates a higher likelihood that low-energy decomposition products exist in a broader minimum, increasing the probability of phase separation.[2] Synthesis of ternary or higher order compounds is particularly difficult using traditional high temperature synthesis techniques. High temperatures are typically necessary to overcome the energy barriers associated with solid state diffusion, but high temperatures also permit many intermediates to nucleate and grow. To lower reaction temperatures, researchers add additional components to create a melt. Compounds that are supersaturated nucleate and grow from the melt, but the lack of knowledge of the speciation in the fluids and the solubility products of potential compounds make it difficult to find conditions where ternary and higher order products nucleate and grow before binary compounds.[3]

The obvious challenges in synthesis of metastable phases are to have nucleation rather than diffusion be the rate limiting step to forming a crystalline solid and to find experimental parameters that directly control what nucleates. Molecular beam epitaxy (MBE) accomplishes the synthesis of metastable phases by templating growth with a substrate that

has an epitaxial relationship with a desired product. MBE also takes advantage of the differences in surface vs volume diffusion to target metastable compounds by confining the diffusion of atoms to only occur across the surface.[4–6] Controlling these parameters allows MBE synthesis to target kinetically favorable products rather than thermodynamic products. Many more novel phases have been predicted to be stable via theoretical calculations. To access more metastable products that can't be achieved by epitaxial growth, alternative solid-state synthesis methods must be developed that can achieve kinetic control over product formation. However, it is challenging to find the synthetic methods and parameters that would allow access to metastable compounds, which can lead to a lack of experimental verifiability of the proposed structures.[7]

In order to both predict and access potential novel phases, studies of energy landscapes that reveal generalized barriers between calculated minima are necessary.[8] An alternative synthesis approach, the modulated elemental reactants (MER) method, can be used to carry out studies of energy landscapes. MER relies on designed precursors prepared by depositing atomically thin elemental layers with designed thicknesses in specific sequences to control local composition. The controlled local compositions allow the reactions to attain a local thermodynamic equilibrium that is dictated by local chemical potentials before achieving a global equilibrium set by the average composition.[9] Therefore, the local compositions will control what nucleates because the fastest way for the system to lower its free energy is to form products close to nanoarchitecture of the precursor. For metastable phases that have been successfully synthesized, their persistence is due to the slow rates of solid-state diffusion, which raise the kinetic barrier for long-range chemical separation.[2] MER synthesis takes advantage of this by annealing the precursors at low enough temperatures to promote local structural rearrangements but prevent long range diffusion. This enables the exploration of ternary and quaternary free energy landscapes to discover both local free energy minima and the potential kinetic barriers between local and global minima.

An important aspect of the MER method is that the information learned about nucleation and growth of compounds from investigations of binary systems can be used to avoid binary compounds as reaction intermediates in ternary and higher order systems. For example, investigations of the Fe-Se, Pb-Se, V-Se and Mn-Se systems[10–13] enabled the

synthesis of the new compounds $Pb_xFe_{1-x}Se$[14] and $(PbSe)_{1+\delta}(FeSe_2)_n$,[15] many different $(PbSe)_n(VSe_2)_m$ compounds,[16–18] a broad range of Fe-substituted VSe_2 compounds,[19] and the $(Pb_2MnSe_3)_{0.6}(VSe_2)$ and $(Pb_3Mn_2Se_5)_{0.6}(VSe_2)$ compounds.[15,20] Here we extend these investigations by exploring the synthesis of compounds on the (FeSe-PbSe)VSe_2 and the PbSe($FeSe_2$-VSe_2) tie lines in the quaternary Fe-Pb-V-Se phase diagram. Precursors were prepared with local compositions and various nanoarchitectures to target new misfit compounds $(PbSe)_{1+\delta}(Fe_xV_{1-y}Se_2)_n$ and to target the Fe-analogs of $(Pb_nMn_mSe_{n+m})_{0.6}(VSe_2)$ compounds with Fe replacing Mn. Information gained from the study of related Pb-Fe-Se, Pb-V-Se, and Fe-V-Se ternary systems was used to guide the synthesis of the $(PbSe)_{1+\delta}(Fe_xV_{1-y}Se_2)_n$ intergrowths. These compounds formed readily, highlighting that information on reaction pathways in lower order systems can be applied to higher order compounds. Precursors designed to target $(Pb_2FeSe_3)_{0.6}(VSe_2)$ compounds rearranged to form more complex $(PbSe)_{1+\delta}(Fe_xV_{1-y}Se_2)_1(PbSe)_{1+\delta}(Fe_xV_{1-y}Se_2)_2$ unit cells. This unexpected rearrangement yields information about the free energy landscape of compounds within this quaternary system. The insight gained on reaction pathways and free energy landscapes from this investigation is additive and can be applied to a variety of phase systems which will lead to the formation of many more metastable compounds.

10.2. Results and Discussion

Previous studies have revealed that several $(PbSe)_{1+\delta}(VSe_2)_n$ intergrowths, $(PbSe)_{1+\delta}(FeSe_2)_n$ intergrowths, and highly substituted $Fe_xV_{1-y}Se_2$ compounds are metastable and can be formed from designed precursors.[15–19] Selected members of these families of intergrowths and alloys are represented on the PbSe-$FeSe_2$-VSe_2 phase plane shown in Figure 1. Based on the stability of these ternary compounds, we hypothesized that quaternary $(PbSe)_{1+\delta}(Fe_xV_{1-y}Se_2)_n$ intergrowths with compositions along the tie lines shown in Figure 1 also exist in local free energy minima. To test our hypothesis, five precursors were prepared to target $(PbSe)_{1+\delta}(Fe_xV_{1-y}Se_2)_n$ compounds within the PbSe-$FeSe_2$-VSe_2 phase plane. The precursors were deposited with a Pb|Se|(V|Fe|Se)$_n$ layering sequence. The amount of material in each Pb|Se sequence was targeted to be enough to form a single rock salt structured PbSe bilayer. The amount of material in each V|Fe|Se sequence was targeted to be enough Se and enough total metal (V + Fe) to form a hexagonal Se-Fe/V-Se trilayer. The amount of Fe

substitution targeted was x = 0.33 because compounds with this composition were found to decompose at higher temperatures than those with higher Fe content in a study of the Fe-V-Se ternary system. The number of atoms per unit area of each element in the as-deposited precursors were determined using x-ray fluorescence (XRF).[21] The calculated compositions for each of the 5 prepared precursors are displayed in the quaternary phase plane in Figure 1. The compositions of each of the as-deposited precursors were near the tie lines between the $(PbSe)_{1+\delta}(VSe_2)_n$ and $(PbSe)_{1+\delta}(FeSe_2)_n$ intergrowths with n = 1 or 2.

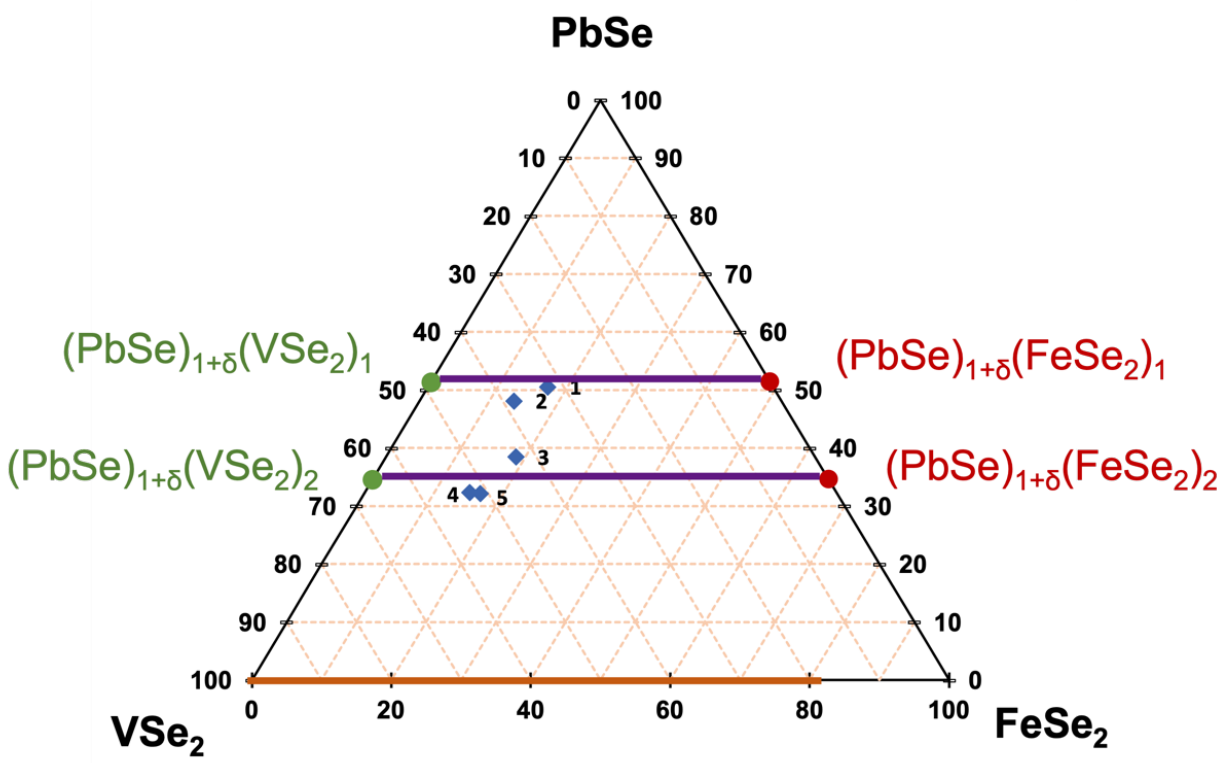

Fig. 10.1. PbSe-$FeSe_2$-VSe_2 phase plane from the quaternary Pb-Fe-V-Se phase diagram. The compounds marked with green circles represent $(PbSe)_{1+\delta}(VSe_2)_n$ intergrowths. The compounds marked with red circles represent $(PbSe)_{1+\delta}(FeSe_2)_n$ intergrowths. The orange tie line between the VSe_2 and $FeSe_2$ corners represents stable, substituted $Fe_xV_{1-y}Se_2$ compounds. The precursors prepared for this study targeted compositions along the purple tie lines between the $(PbSe)_{1+\delta}(VSe_2)_n$ and $(PbSe)_{1+\delta}(FeSe_2)_n$ intergrowths. The compositions of the as-deposited precursors are represented by the blue diamonds.

X-ray reflectivity (XRR) and specular and in-plane x-ray diffraction (XRD) patterns were collected on the as-deposited precursors, and the XRR and XRD patterns for samples **1** and **3** are shown in Figure 2. These samples are representative of the n =1 and n = 2 compounds, and the as-deposited data for the remaining samples which are very similar can be found in the SI. The XRR patterns of the as-deposited precursors contain artificial layering reflections due to the periodic modulation in electron density from the elemental layering sequences. This indicates that significant interdiffusion between repeat units did not occur during the deposition.

The specular XRD patterns contain several higher order Bragg reflections that can be indexed as families of 00*l* reflections, indicating that the samples begin to nucleate and grow crystallographically aligned to the substrate during the deposition. The *c*-axis lattice parameters of the n = 1 and n = 2 precursors on deposit were 12.33(1) Å and 18.46(2) Å, respectively. These are near those estimated for PbSe and $Fe_xV_{1-y}Se_2$ layers of ~6 Å each. The in plane XRD patterns contain *hk*0 reflections that can be indexed to a cubic phase and a hexagonal phase, further supporting the nucleation and growth of the structure aligned to the substrate during the deposition. No reflections due to an Fe_xSe_y impurity phase are present. The *a*-axis lattice parameters of the cubic and hexagonal phases of ~6.1 Å and ~3.4 Å, respectively, are near those expected for PbSe and VSe_2.

Annealing studies were carried out on samples **1** and **3** by sequentially annealing them to temperatures increasing by 100°C for 15 min. The samples were annealed in a partial pressure of Se for temperatures of 200°C and above to reduce Se loss through evaporation. XRF, XRR, and specular XRD data were collected after each annealing step, and in plane XRD data were collected when significant structural shifts occurred, as indicated by the specular XRD data. The annealing study for the n = 2 sample **3** is shown in Figure 3. The reflections in the specular and in plane XRD become narrower and more intense as the annealing temperature is increased up to 300°C, indicating the formation of larger grains crystallized perpendicular to the substrate. After annealing to 400°C, the reflections in the specular XRD pattern for sample **3** become broader and asymmetric, indicating that the sample has begun to decompose. At 500°C, the sample has fully decomposed into a mixture of thermodynamically stable binary products. The XRR and XRD patterns collected during the annealing study for the n = 1 sample **1** are shown in the SI and indicate the sample **1**

begins to decompose at 300°C, suggesting that the n = 2 structure may be more stable. This is likely due to the van der Waals gap between $Fe_xV_{1-y}Se_2$ layers, which allows excess metal atoms to intercalate. For temperatures of 300°C and below, no reflections due to iron impurity phases are present in the XRD patterns of either sample, indicating that the Fe atoms are incorporated into the intergrowth structure.

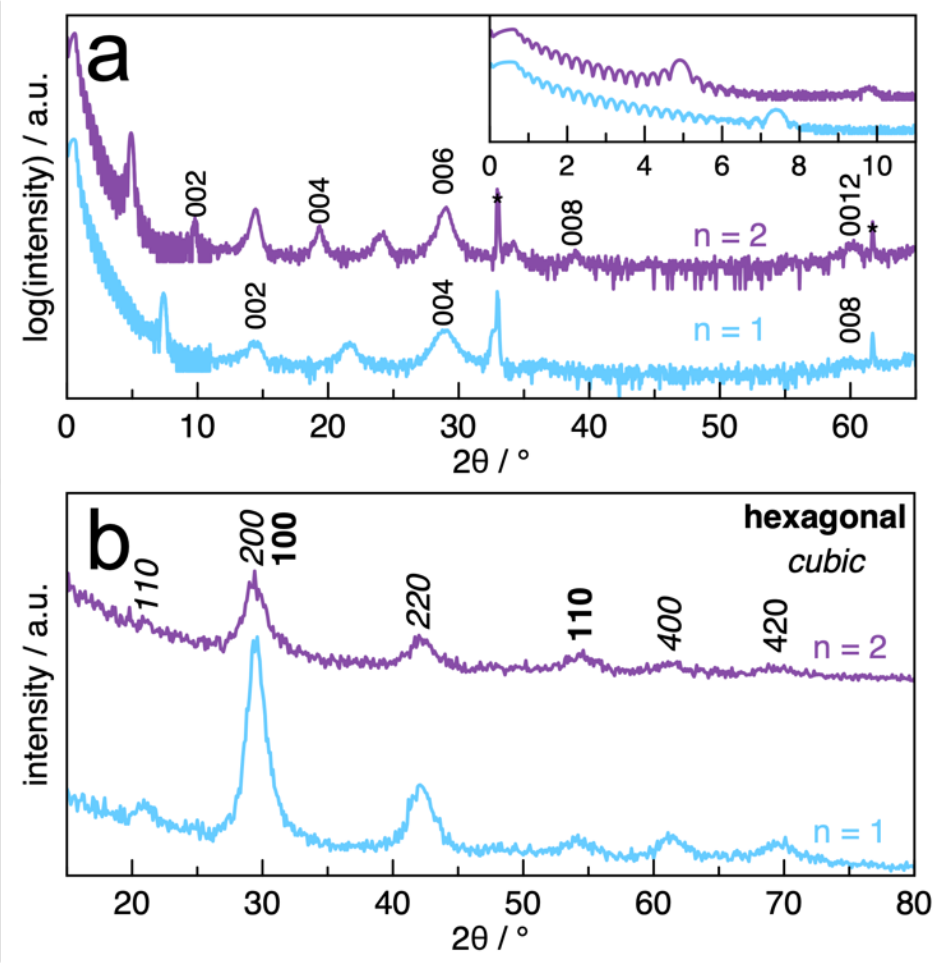

Fig. 10.2. a) XRR and specular XRD patterns and b) in-plane XRD patterns for the as-deposited n = 1 and n = 2 samples **1** and **3**. Reflections marked with * are due to the Si substrate. Selected miller indices are shown above their corresponding reflections.

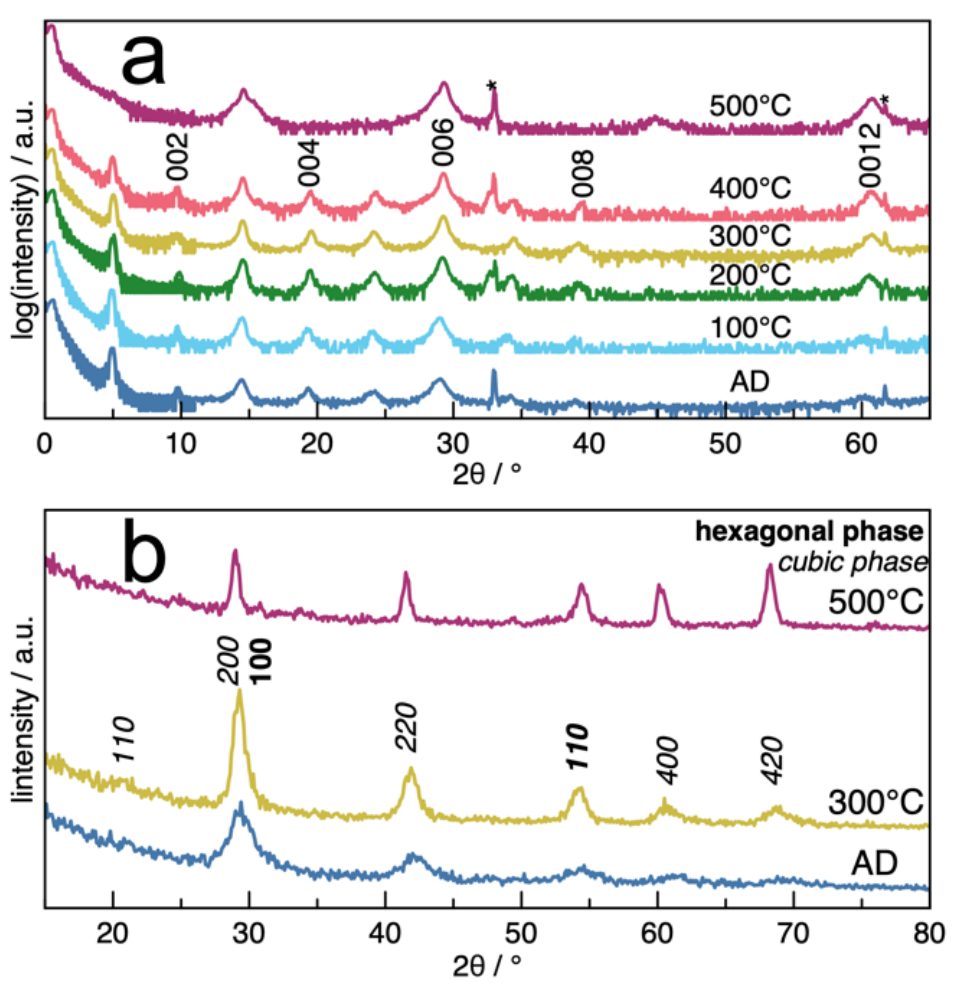

Fig. 10.3. a) XRR and specular XRD and b) in plane XRD patterns for sample **3** annealed to the temperatures indicated above each pattern. Reflections marked with * are due to the Si substrate. Selected miller indices are shown above their corresponding reflections.

Based on the results of the annealing studies, samples **1**-**5** were annealed to 300°C for 15 min in a partial pressure of Se vapor. Each sample formed the targeted n = 1 or n = 2 heterostructure during annealing. The XRR, specular XRD, and in plane XRD for the annealed samples are shown in Figure 4. The *a*- and *c*-axis lattice parameters calculated for each sample annealed to 300°C are summarized in Table 1. The specular and in plane XRD patterns for samples **2**-**5** contain only reflections due to the crystallographically aligned intergrowth composed of cubic and hexagonal phases. The in plane XRD pattern for sample

1 at 300°C contains asymmetric reflections at ~61 and ~68° 2θ, indicating that the sample has begun to decompose.

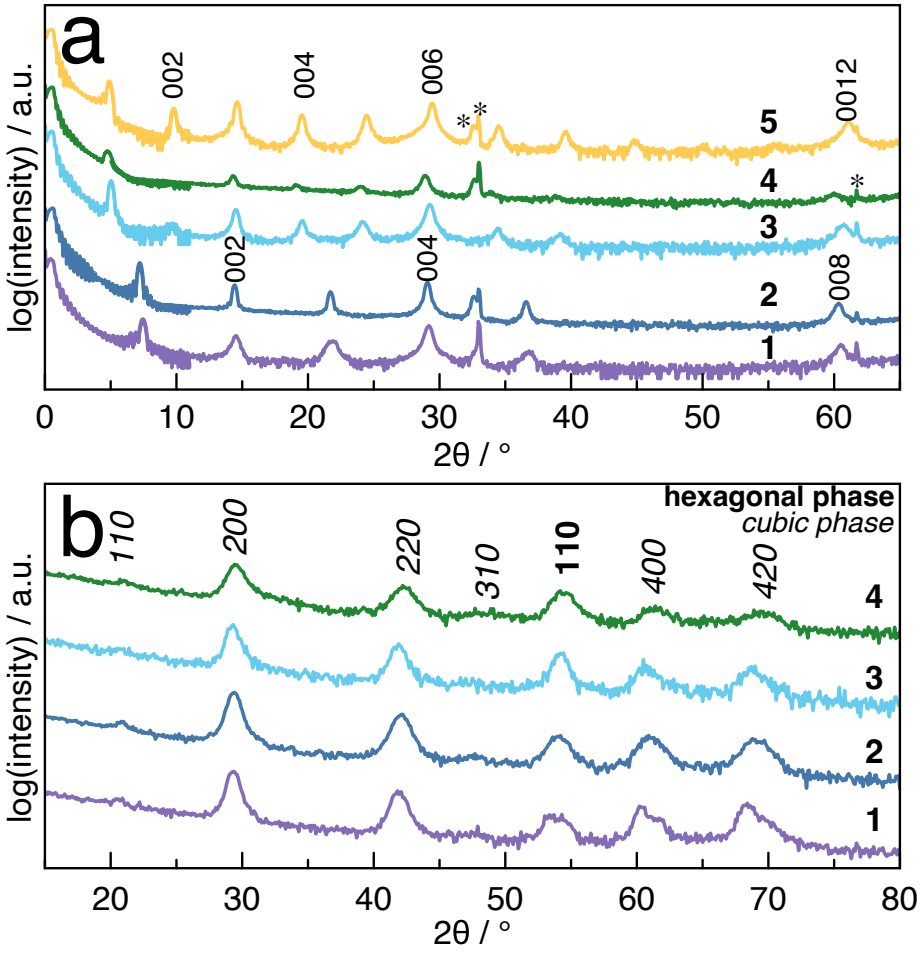

Fig. 10.4. a) XRR and specular XRD and b) in plane XRD patterns for the $(PbSe)_{1+\delta}(Fe_xV_{1-y}Se_2)_n$ samples annealed to 300°C. Reflections marked with * are due to the Si substrate. Selected miller indices are shown above their corresponding reflections.

Table 10.1. Summary of the lattice parameters and ratio of Fe + V to Se for samples annealed to 300°C.

Sample	Fe + V per 2 Se	c-axis (Å)	a-axis cubic (Å)	a-axis hexagonal (Å)
1	1.24	12.236(2)	6.13(3)	3.41
2	1.12	12.264(2)	6.06(2)	3.38
3	1.32	18.30(3)	6.08(2)	3.37
4	1.19	18.56(4)	6.04(2)	3.38
5	1.22	18.18(2)	-	-

To determine whether slight variations in composition affect the decomposition temperature, the XRF data were analyzed for each sample. To simplify the analysis, all Pb atoms were assumed to react in a 1:1 ratio with Se atoms, and the remaining Se atoms were assumed to react with V and Fe. The ratio of total Fe and V atoms to the remaining Se atoms was >1:2 for each of the samples (see Table 1). For the n = 2 samples, the excess metal atoms could be incorporated as intercalants in the van der Waals gap between $Fe_xV_{1-x}Se_2$ layers, but for the n = 1 samples, there is no van der Waals gap present for atoms to intercalate into. This likely affects the decomposition temperature as excess Fe atoms form impurity phases. Sample **1** lost enough Se during annealing that the ratio of Fe + V:Se was 1.24:2, which is likely why this sample began to break down at lower temperatures than samples **2**-**5**.

The XRR patterns for samples **1**, **2**, **3** and **5** and the specular XRD patterns for samples **2** and **5** contained Laue oscillations, as shown in Figure 5. Laue oscillations arise from a finite number of unit cells in coherently diffracting crystalline domains and can be used to calculate the average number of unit cells in the domain.[22] The number of unit cells can be multiplied by the *c*-axis lattice parameter to calculate the average thickness of the crystalline domains. This can be compared to the thickness calculated from the Kiessig fringes in the XRR pattern to determine the amount of the sample that is composed of impurity phase above or below the crystalline domains. For each of these samples, the difference between the total film thickness and crystalline domain thickness is significant, with 3-9% of each of the films composed of impurity phase. This can be compared to the XRF data, which shows that each sample is metal-rich based on the amount of Se present. The Se deficiency likely causes the high percentage of impurity phase, as the amount of material present is not enough to form the targeted product, so other phases with the stoichiometry of the remaining material will form instead. The XRF, Laue, and XRR data are summarized in Table 2.

The decomposition temperature for the $(PbSe)_{1+\delta}(Fe_xV_{1-y}Se_2)_n$ compounds was ~100°C higher than that of the similar ternary $(PbSe)_n(VSe_2)_m$ compounds and ~300°C higher than the similar $(PbSe)_{1+\delta}(FeSe_2)_n$ compounds.[15] This suggests that the substitution of Fe into the VSe_2 lattice causes the interlayer interactions with PbSe to be stronger, stabilizing the intergrowth. However, the $(PbSe)_{1+\delta}(Fe_xV_{1-y}Se_2)_n$ compounds decomposed at a lower temperature than the ternary $Fe_{0.33}V_{0.67}Se_2$ compound.[19] This suggests that the nucleation of

hexagonal VSe_2 sites may have a larger influence on the stabilization of $FeSe_2$ in the $(PbSe)_{1+\delta}(Fe_xV_{1-y}Se_2)_n$ structure than the interlayer interactions between PbSe and $FeSe_2$.

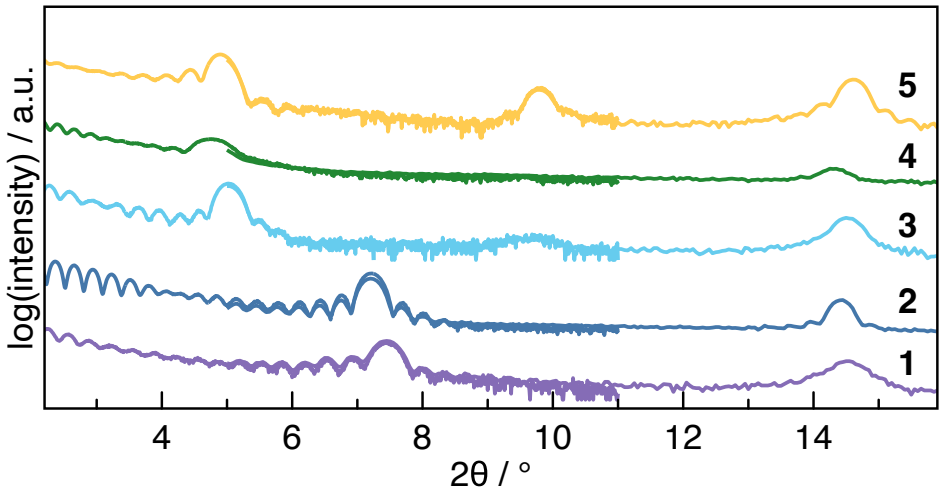

Fig. 10.5. Magnified section of the XRR and specular XRD patterns of samples **1**-**5** showing Laue oscillations for samples **1**-**3** and **5**.

Table 10.2. Summary of the number of layers determined from the XRF and Laue oscillation data and summary of the thicknesses determined from XRR and Laue oscillation data.

Sample	# PbSe layers	# V layers	# Fe layers	# V+Fe layers	# Se layers	# Laue layers	Laue Thick (Å)	XRR Thick (Å)	Impurity Phase Thick (Å)
1	23	16.5	8.7	25.2	20.3	21	257	273	16
2	24	20.9	7.4	28.3	25.3	23	282	293	11
3	17	10.7	4.6	15.3	12	14	256	264	8
5	16	14.1	4.5	18.6	15.3	14	255	279	24

To explore whether other quaternary Pb-Fe-V-Se compounds exist as local minima, a precursor (sample **6**) was prepared to target an analog of the $(Pb_2MnSe_3)_{0.6}(VSe_2)$ structure with Fe taking the place of Mn, as shown pictorially in Figure 6. Pure PbSe cannot form a trilayer structure in an intergrowth due to the puckering distortion that occurs at the interface with other layers,[23] but the Mn atoms were hypothesized to stabilize this structure due to their smaller radii compared to Pb.[20] Since Fe ions are smaller than Mn ions, as represented by the

ratio of ion sizes in Figure 6, we hypothesized that the formation of the $(Pb_2FeSe_3)_{0.6}(VSe_2)$ structure could be promoted from a designed precursor. Additionally, it was previously reported that alloying of Fe into a cubic PbSe structure was achieved from low temperature annealing of designed precursors, suggesting that Pb-Fe-Se cubic structures are metastable.[14]

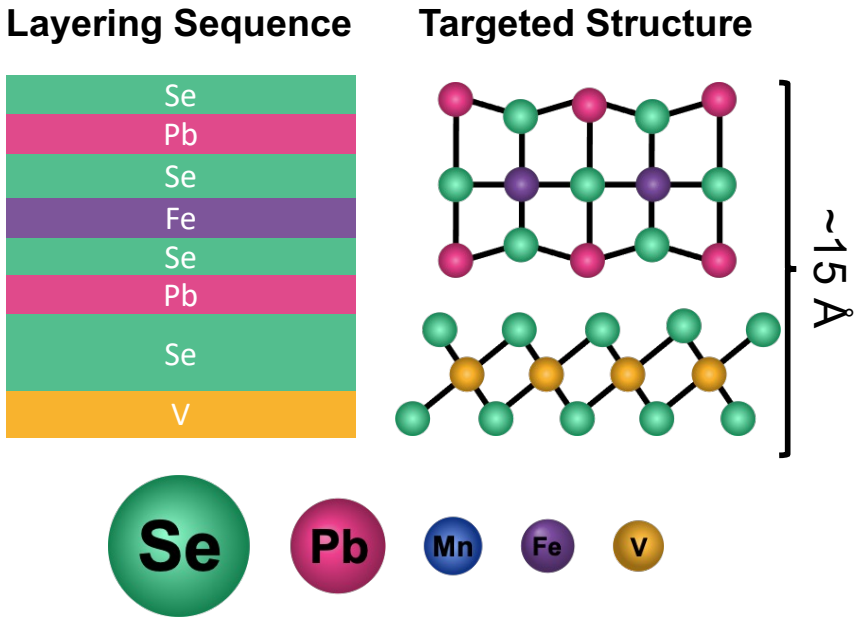

Fig. 10.6. Pictorial representation of the layering sequence of the as-deposited precursor and the targeted unit cell structure. The relative sizes of the atoms are represented by the scale of the legend.

The precursor for sample **6** was deposited with a V|Se|Pb|Se|Fe|Se|Pb|Se layering sequence, and the local compositions in each layering sequence were controlled to mimic the composition profile of the targeted unit cell. XRF, XRR, and specular XRD data were collected on the as-deposited precursor (Figure 7). The XRR pattern contains an artificial layering reflection corresponding to a d-spacing of ~15 Å, which is near that estimated for the targeted structure. The specular XRD contains very broad reflections which cannot be indexed to a single phase and do not relate to the artificial layering reflection. This indicates that the sample remains layered and mostly amorphous, and that significant nucleation and growth does not occur during the deposition.

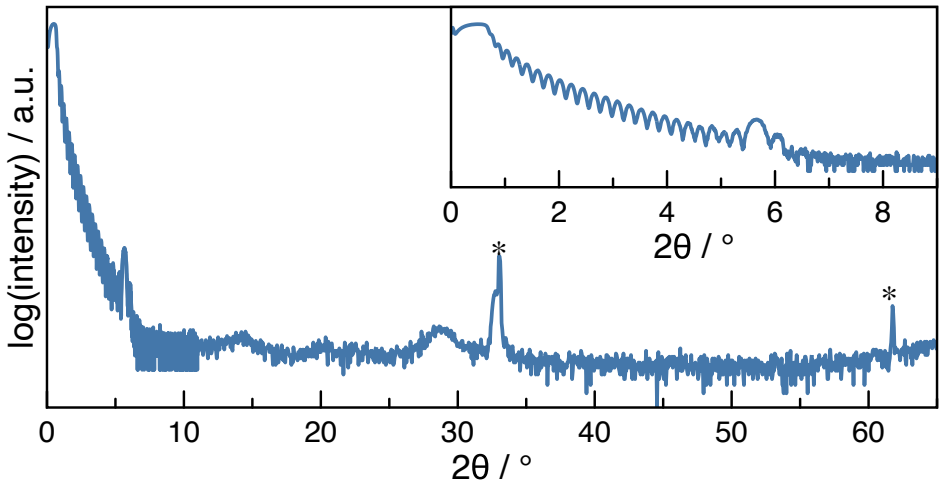

Fig. 10.7. As-deposited XRR and specular XRD patterns for sample **6.** Reflections marked with * are due to the Si substrate.

An annealing study was carried out on sample **6** with XRF, XRR, and specular XRD data collected after each sequential 50°C annealing step (Figure 8). The XRR patterns for the annealing study of sample 6 contain significant interference in the Kiessig fringes at temperatures of 150°C and above that is likely causes by domains of different thicknesses across the sample. Annealing the sample to 100°C and above, leads to the appearance of a second Bragg reflection at ~5.2° 2θ in the XRR pattern corresponding to a d-spacing of ~17 Å. This suggests that diffusion is occurring across repeat units and that modulated domains with different d-spacings are present. The peaks in the specular XRD pattern become narrower and more intense for annealing temperatures up to 350°C. The peaks can be indexed as a family of 00*l* reflections, indicating crystal growth perpendicular to the substrate. However, the calculated *c*-axis lattice parameter is ~30 Å, which is approximately double the size of the lattice estimated for the targeted structure. At temperatures of 150°C and above, the reflection in the XRR pattern at ~5.7° 2θ can be indexed as the 002 reflection of a ~30 Å unit cell. From these results, it is clear that the targeted structure was not able to form. Long-range diffusion to form a different compound with a much larger lattice parameter was favored. After annealing to 400°C, the XRR and XRD patterns do not contain reflections due to a heterostructure, indicating that the sample has decomposed into a mixture of known binary phases.

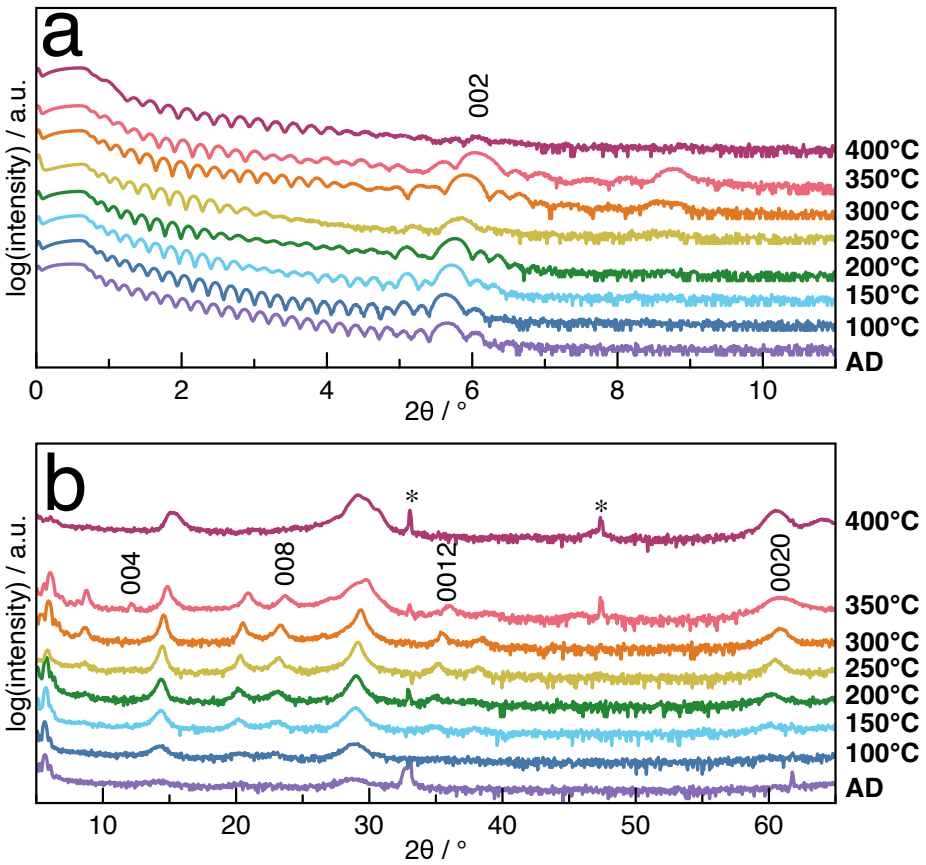

Fig. 10.8. a) XRR and b) specular XRD patterns collected during the annealing study of sample **6**. Reflections marked with * are due to the Si substrate. Selected miller indices are shown above their corresponding reflections.

Based on the rearrangement of sample **6** to a ~30 Å unit cell, we hypothesized that the structure that formed was a $(VSe_2)_1(PbSe)_{1+\delta}(VSe_2)_1(PbSe)_{1+\delta}(FeSe)_{1+\delta*}$ unit cell, which has an overall composition near that of the targeted $(Pb_2FeSe_3)_{0.6}(VSe_2)$ compound. To investigate the formation of this intergrowth, a precursor (sample **7**) was prepared with the layering sequence V|Se|Pb|Se|V|Se|Pb|Se|Fe|Se to mimic the local composition profile and nanoarchitecture of the targeted product. The amounts of V and Se in each V|Se sequence were targeted to be enough to form a layer of hexagonal VSe_2. The amounts of Pb and Se in each Pb|Se sequence and the amounts of Fe and Se in each Fe|Se sequence were targeted to be enough to form a bilayer of a cubic structure with lattice parameters near those of rock salt PbSe.

The as-deposited XRR and specular XRD patterns for sample **7** are shown in Figure 9. The as-deposited XRR pattern contains an artificial layering reflection and two higher order Bragg reflections, indicating that significant intermixing did not occur between repeat units. The specular XRD pattern contains several higher order Bragg peaks that can be indexed as a family of 00*l* reflections with a *c*-axis lattice parameter of ~30 Å. This indicates that the structure begins to nucleate and grow crystallographically aligned to the substrate during the deposition. The amount of nucleation and growth is significantly higher for sample **7** versus sample **6**. This suggests that the energy barrier for nucleation in sample **7** is much lower due to smaller diffusion distances for product formation created by the local composition profile and structure of the precursor.

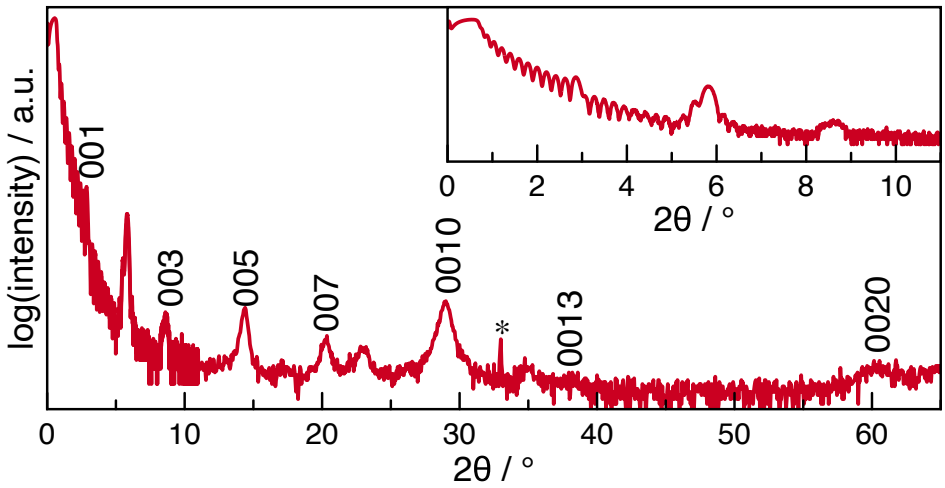

Fig. 10.9. As-deposited XRR and specular XRD patterns for sample 7. Reflections marked with * are due to the Si substrate.

An annealing study was carried out on sample **7**, and the XRR, specular XRD, and in plane XRD for the 250°C or 300°C annealing steps are shown in Figure 10. During annealing, the peaks in the XRR change shape and intensity, indicating that the modulation due to elemental layering is disappearing as the layers are becoming crystalline. The peaks in the specular XRD pattern become narrower and more intense with annealing and can be indexed with the peaks in the XRR pattern as a family of 00*l* reflections corresponding to a *c*-axis lattice parameter of 30.23(2) Å. This is near the estimated c-axis lattice parameter for the targeted intergrowth. The in plane XRD pattern for sample **7** annealed to 300°C contains

only reflections due to a hexagonal phase and a cubic phase. No reflections due to an Fe_xSe_y impurity phase are present. This indicates that the Fe atoms are incorporated into the intergrowth structure. Given the similarities in the overall composition and the *c*-axis lattice parameters for samples **6** and **7**, we hypothesized that both precursors formed the same structure during annealing.

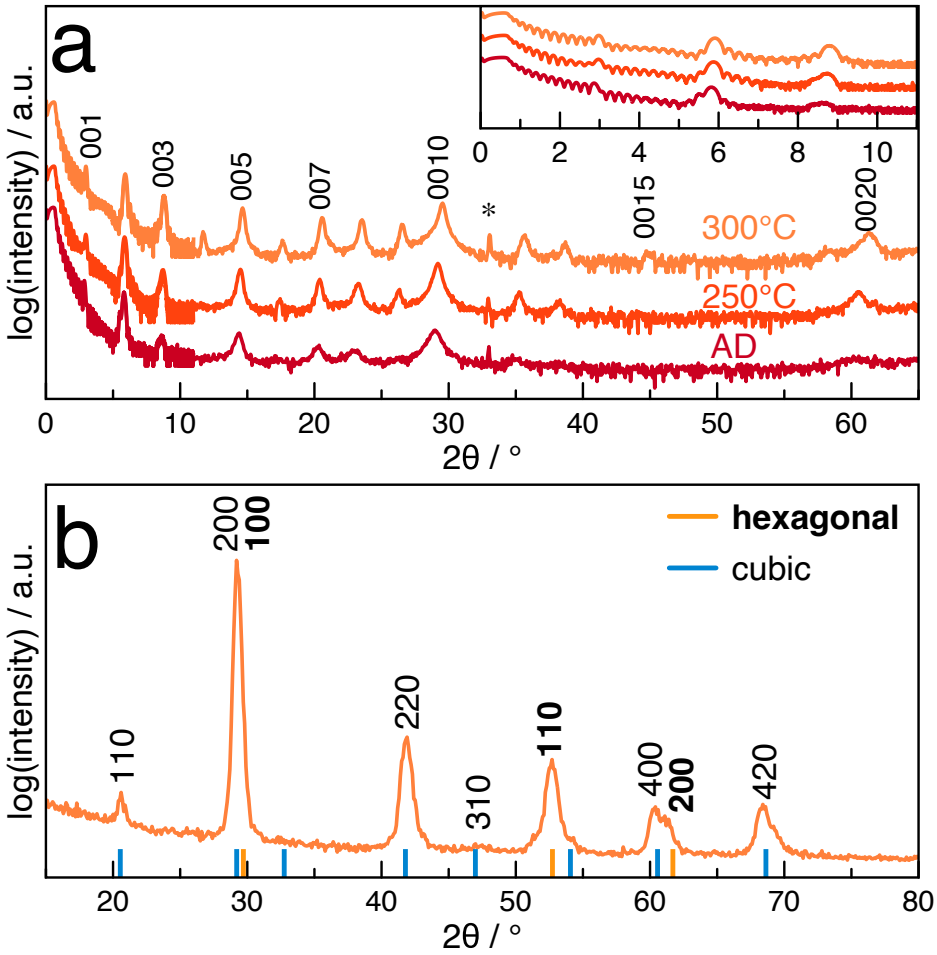

Fig. 10.10. a) XRR and specular XRD patterns for sample **7** as-deposited and annealed to 250°C and 300°C and b) in plane XRD pattern for sample **7** annealed to 300°C. Reflections marked with * are due to the Si substrate. The hexagonal and cubic indices are indicated below the reflections in the in plane pattern with orange or blue lines, respectively.

In order to determine the unit cell structure, a cross section of sample **7** was prepared for HAADF-STEM imaging and STEM-EDS elemental mapping. The STEM-EDS elemental line profile and HAADF-STEM images are shown in Figure 11. The cell structure shown in

the HAADF-STEM images consists of 5 individual layers that are arranged as cubic-hexagonal-cubic-hexagonal-hexagonal. This indicates that the precursor did not form the targeted $(VSe_2)_1(PbSe)_{1+\delta}(VSe_2)_1(PbSe)_{1+\delta}(FeSe)_{1+\delta*}$ unit cell and instead rearranged to a different unit cell. The HAADF-STEM image achieves atomic resolution, which allows the hexagonal and cubic structures to be clearly distinguished for some zone axes, such as the [100] zone axes shown in Figure 10b and c. The STEM-EDS elemental line profile shows that the cubic layers contain Pb and Se, and the hexagonal layers contain Se planes located on either side of V/Fe planes. For the two adjacent hexagonal layers, Fe intensity is visible within the gap between the layers. These data indicate that the precursor rearranges to form a $(PbSe)_{1+\delta}(Fe_xV_{1-y}Se_2)_1(PbSe)_{1+\delta}(Fe_xV_{1-y}Se_2)_2$ structure.

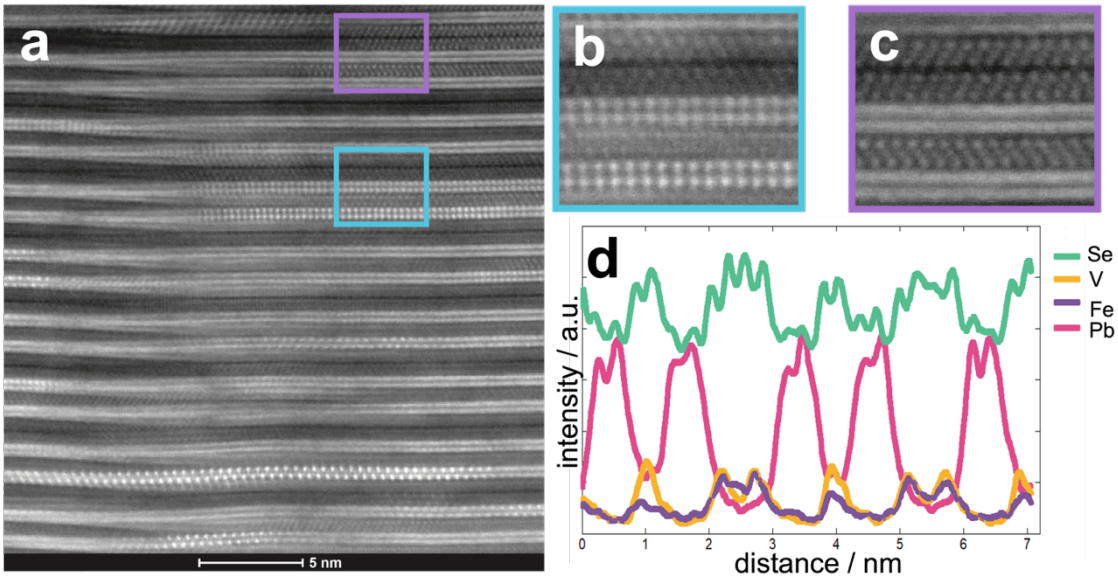

Fig. 10.11. a) HAADF-STEM image of the cross section of sample 7 with sections outlined in blue and purple that have been magnified to display the b) [100] axis of a cubic structure in the unit cell and c) [100] axis of a 1T hexagonal structure in the unit cell. d) The STEM-EDS elemental line profile collected across the axis perpendicular to the substrate.

Based on the similar unit cell size and relative intensities of the reflections in the specular XRD pattern, it is reasonable to assume that sample **6** rearranged to form the $(PbSe)_{1+\delta}(Fe_xV_{1-y}Se_2)_1(PbSe)_{1+\delta}(Fe_xV_{1-y}Se_2)_2$ structure shown for sample **7**. These compounds exist within the family of $(PbSe)_m(Fe_xV_{1-y}Se_2)_n$ intergrowths along the new tie

line in the PbSe-$FeSe_2$-VSe_2 quaternary phase plane shown in Figure 12. This suggests that the local minima of $(PbSe)_{1+\delta}(Fe_xV_{1-y}Se_2)_n$ intergrowths is very broad, and that diffusion of the Fe atoms to the VSe_2 nucleation sites does not create a large energy barrier to prevent the nucleation of $Fe_xV_{1-y}Se_2$ compounds over the nucleation of Pb_2FeSe_3. This also suggests that the larger difference in electronegativity between Pb and Mn is a significant factor in the stabilization of the trilayer Pb_2MnSe_3 structure, as the smaller Fe atoms did not stabilize the analog structure.

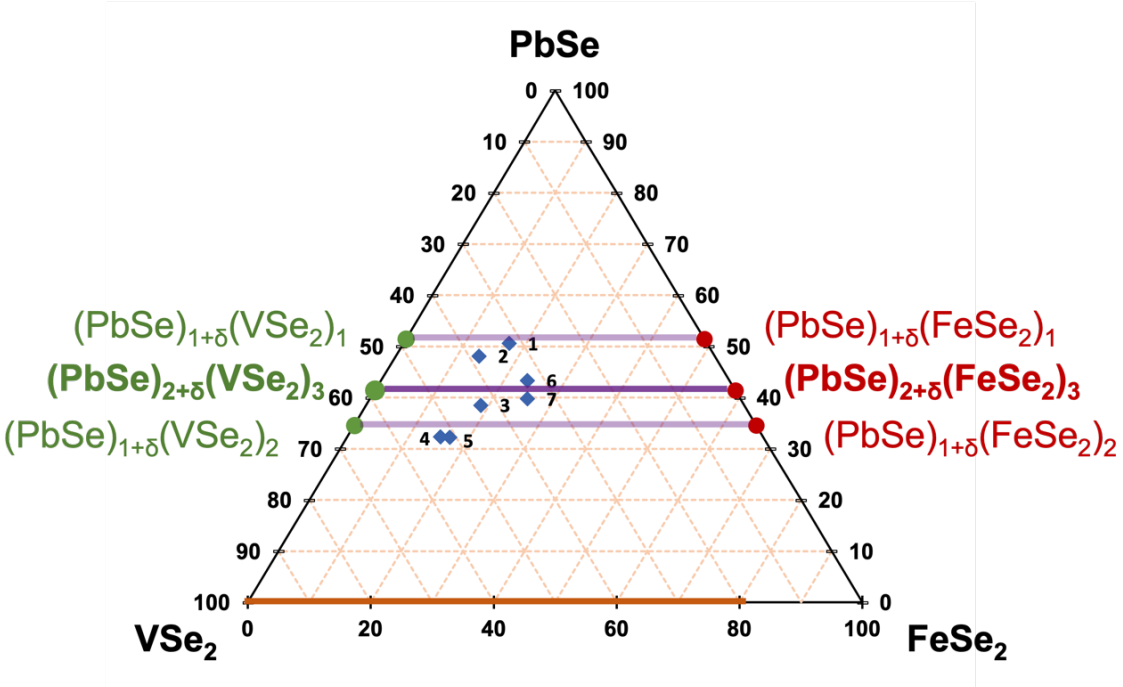

Fig. 10.12. PbSe-$FeSe_2$-VSe_2 phase plane from the quaternary Pb-Fe-V-Se phase diagram. The compounds marked with green circles represent $(PbSe)_{1+\delta}(VSe_2)_n$ intergrowths. The compounds marked with red circles represent $(PbSe)_{1+\delta}(FeSe_2)_n$ intergrowths. The orange tie line between the VSe_2 and $FeSe_2$ corners represents substituted $Fe_xV_{1-y}Se_2$ compounds. The dark purple tie line represents compounds with 2:3 ratios of cubic PbSe layers to hexagonal $Fe_xV_{1-y}Se_2$ layers. The compositions of the as-deposited precursors are represented by the blue diamonds. The compositions of samples **6** and **7** both fall along this tie line.

Since both Fe and Mn have been shown to alloy with PbSe,[14,24] the difference between their reaction pathways from quaternary precursors targeting $(Pb_nX_mSe_{n+m})_{0.6}(VSe_2)$ compounds reveals information about the stabilization of the $(Pb_nMn_mSe_{n+m})_{0.6}(VSe_2)$

structure. To further elucidate the difference between Mn and Fe reactants, we investigated the ternary Mn-V-Se system by preparing precursors targeting $Mn_xV_{1-y}Se_2$. Three precursors were prepared with a V|Mn|Se layering sequence, and the amount of material in each layering sequence was controlled to target enough total metal atoms and selenium atoms to form a 1T hexagonal layer with lattice parameters near those of VSe_2. The ratio of Mn to V atoms was varied to target substituted compounds with x = 0.1, 0.25, or 0.4 – samples **8**, **9**, and **10**, respectively.

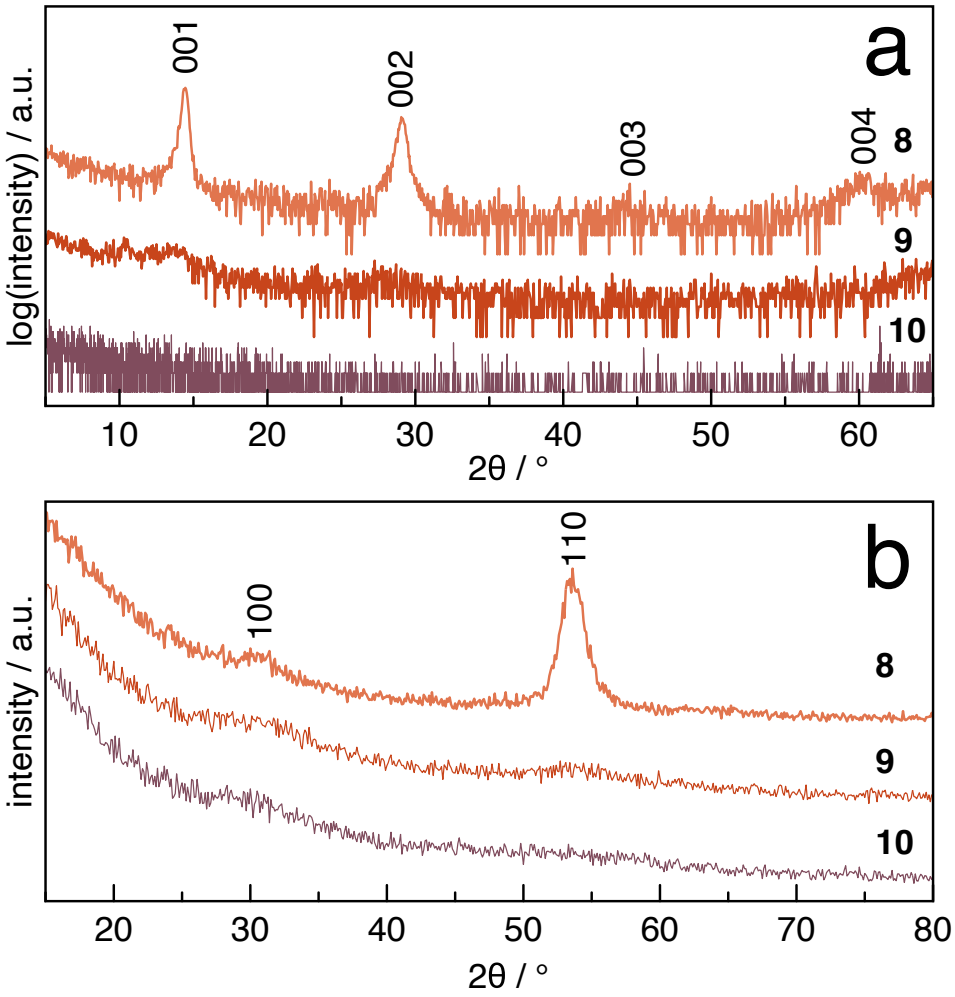

Fig. 10.13. As-deposited a) specular and b) in plane XRD patterns for samples **8-10**. Reflections marked with * are due to the Si substrate. Selected miller indices are shown above their corresponding reflections.

The as-deposited specular and in plane XRD patterns for samples **8**-**10** are shown in Figure 13. The specular XRD pattern for sample **8** targeting $Mn_{0.1}V_{0.9}Se_2$ contains a family of 00*l* reflections, indicating nucleation of the structure perpendicular to the substrate during deposition. The in plane XRD contains *hk*0 reflections that can be indexed to a hexagonal structure, further indicating nucleation of sample **8**. For samples **9** and **10**, the specular and in plane XRD patterns contain very broad, weak reflections that cannot be indexed to a single phase. This suggests that the presence of Mn atoms hinder the growth of VSe_2 grains during the deposition, implying that Mn atoms do not readily nucleate in a hexagonal structure off of VSe_2 nucleation sites.

An annealing study was carried out on sample **9** by sequentially annealing the sample to temperatures increasing by 100°C for 15 min. The specular and in plane XRD data collected after each annealing step are shown in Figure 14. At 100°C, the sample remains mostly amorphous, and at 200°C the specular XRD contains 00*l* reflections that can be indexed to a lattice parameter of 6.27(1) Å. However, the reflections are still relatively weak and broad, indicating the grains are small and heterogenous. After annealing the sample to 300°C, reflections due to a Mn_xSe_y impurity phase appear in both the specular and in plane XRD patterns. This is accompanied by the reflections indexing to a hexagonal unit cell becoming narrower and more intense. This further indicates that the presence of Mn atoms in the amorphous matrix around VSe_2 nucleation sites hinders crystal growth. The specular XRD data for samples **8** and **10**, shown in Figure 15, reveal similar results.

These data show that the energetic barrier to nucleate and grown Mn-substituted VSe_2 is larger than the barrier to diffuse to form a mixture of binary phases. This suggests that there was no competition for Mn incorporation into the VSe_2 lattice versus the PbSe lattice during the formation of $(Pb_nMn_mSe_{n+m})_{0.6}(VSe_2)$ compounds. This highlights the additive quality of information on phase systems, as formation of products in the Pb-Fe-V-Se and Pb-Mn-V-Se systems were directed by the reaction pathways in the Fe-V-Se and Mn-V-Se ternary systems.

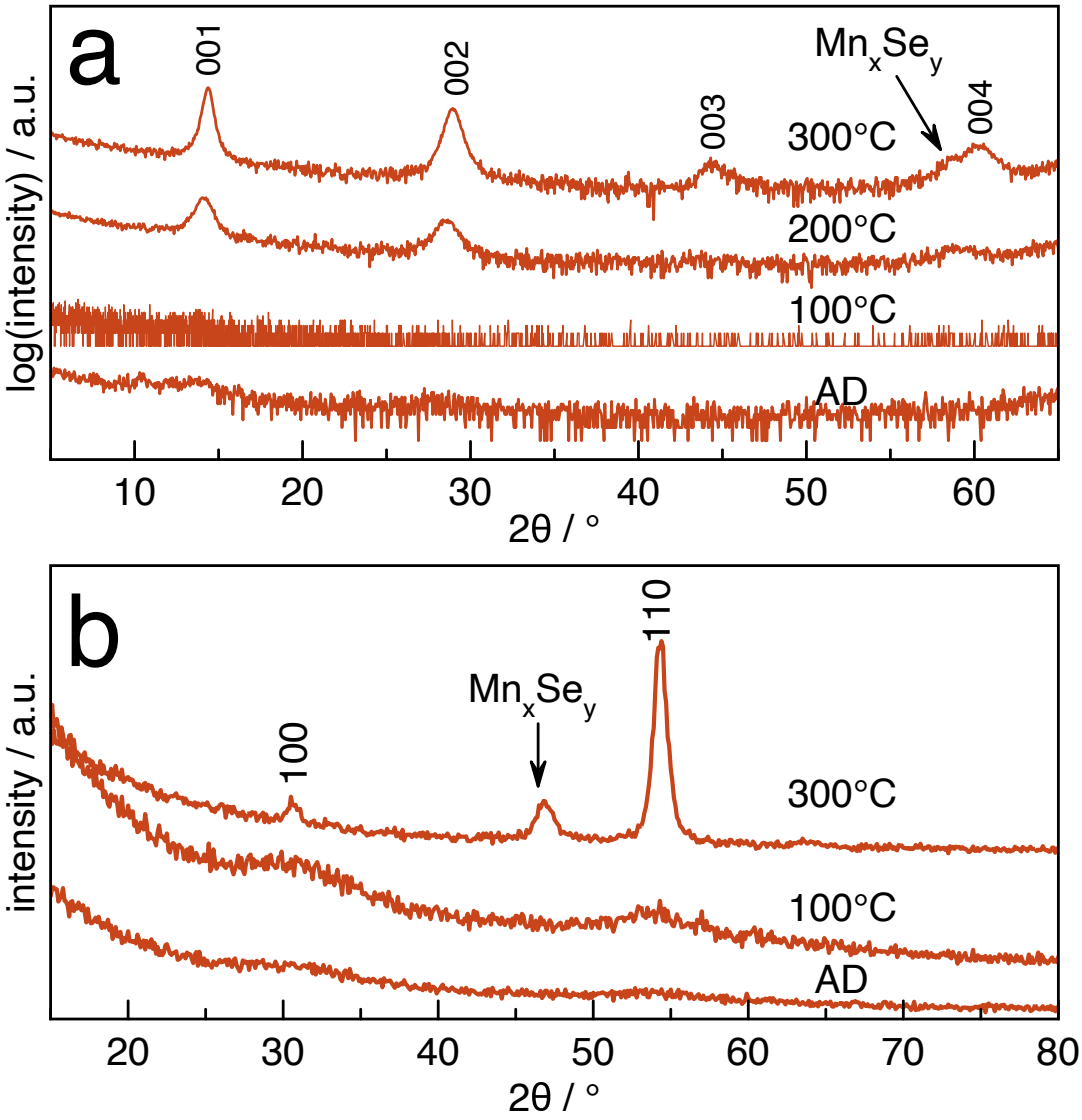

Fig. 10.14. In plane and specular XRD patterns collected during the annealing study of sample **9**. Reflections marked with * are due to the Si substrate. Selected miller indices are shown above their corresponding reflections.

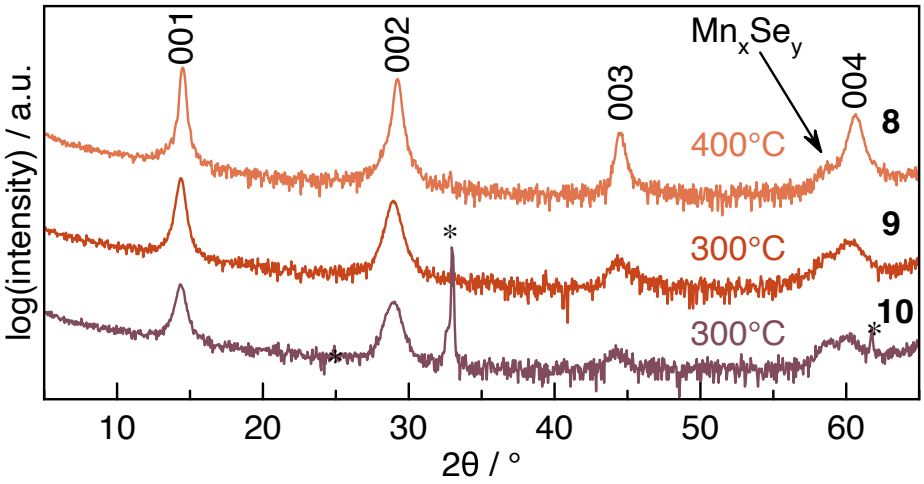

Fig. 10.15. Specular XRD patterns for sample **8-10** annealed to the indicated temperatures. Reflections marked with * are due to the Si substrate. Miller indices are shown above their corresponding reflections.

10.3. Conclusions

Synthesis via the modulated elemental reactants method enabled the formation of a family of novel, metastable quaternary compounds: $(PbSe)_m(Fe_xV_{1-y}Se_2)_n$. Targeting other quaternary Pb-Fe-V-Se compounds including the Fe analog of the metastable $(Pb_2MnSe_3)_{0.6}(VSe_2)$ intergrowth resulted in rearrangement of the precursors into members of the $(PbSe)_m(Fe_xV_{1-y}Se_2)_n$ family of intergrowths. This implies that the $(PbSe)_m(Fe_xV_{1-y}Se_2)_n$ compounds are located in a very broad well in the free energy landscape and that long-range diffusion doesn't create a large kinetic barrier for formation. This also implies that the stabilization of the puckering within the Pb_2MnSe_3 structure is due to the difference in electronegativity between Pb and Mn as well as the small size of Mn, since Fe is a smaller ion but has an electronegativity closer to Pb. An investigation of the ternary Mn-V-Se system was carried out to elucidate the difference between the reactions of Mn and Fe in precursors targeting $(Pb_2XSe_3)_{0.6}(VSe_2)$ with X = Mn or Fe. This study revealed that Mn is not stable as a substituted atom in the VSe_2 lattice, which reduces the drive to rearrange to form $Mn_xV_{1-y}Se_2$ in precursors targeting $(Pb_2MnSe_3)_{0.6}(VSe_2)$.

The synthesis of new metastable ternary and higher order compounds can be facilitated by studies of their lower order reactant phase systems. Information gained from studies of the lower order phase systems – i.e. Pb and Se, Pb, Fe, and Se, etc. – was applied

to target the metastable quaternary compounds in this investigation. This showcases that information on binary or ternary reaction pathways can be applied to direct synthetic efforts of higher order compounds. Studies of lower order systems can also reveal parameters, such as local composition profiles or layer thicknesses and sequences, that can be controlled to influence the formation of specific products. The information gained from these studies is additive and can be used to direct future synthetic efforts, which will lead to a better understanding of solid state free energy landscapes as well as the formation of a multitude of novel materials.

10.4. Bridge

Chapter X explored how the additive information gained from studies of binary and ternary phase systems could be applied to higher order phase systems. This enabled the synthesis of families of novel metastable compounds. Chapter XI will summarize the work presented in this dissertation as well as present conclusions and a future outlook.

CHAPTER XI

CONCLUSIONS

11.0. Authorship Statement

This chapter was written for this work alone with no intention of publishing it elsewhere. I am the primary author and wrote the following with assistance from my advisor David C. Johnson.

11.1 Conclusions

Layered materials are of high interest for technological applications because of the potential for novel, tunable properties that could be exploited for specific uses. Furthermore, the discovery of novel layered materials opens up the possibilities for a multitude of compounds with useful electronic, optical, or magnetic properties. However, both the discovery of novel materials and incorporation of layered materials like 2D heterostructures into real devices is hindered by limitations in current synthetic techniques. Fundamental knowledge of solid state reaction mechanisms is essential to gain insight into how to control the nucleation and growth of targeted products.

The modulated elemental reactants synthesis method offers unique advantages for investigating the reaction mechanisms of solid state systems and for forming low-dimensional layered materials such as 2D heterostructures. There are several tunable parameters for MER precursors such as the layer sequence, layer thickness, and post deposition processing parameters that can be systematically varied to gain insight into the nucleation and growth of products. This insight allows us to improve the design of the nanoarchitecture of MER precursors in order to target novel, metastable phases. Designed precursors have small diffusion distances created by the atomically thin elemental layers in the precursors and the low diffusion rate induced by low temperature annealing causes product formation to be dominated by kinetic stability rather than thermodynamic stability. This enables the formation of metastable products if they are local minima in the free energy landscape.

A pivotal development for the MER synthesis method is the use of XRF analysis to determine the number of atoms per unit area deposited in each of the precursors. This development has led to higher quality films prepared by the MER method, which is evidenced by the number of films prepared that contain Laue oscillations in their specular XRD patterns. The presence of Laue oscillations in XRD patterns presents an opportunity to gain significant structural information about the sample. Laue oscillations are particularly relevant for layered, thin films, which are key in modern devices. Developing a better understanding of the thin film structure through the advancement of Laue oscillation analysis can lead to insights on structure-function relationships. This is critical for targeting materials with specific chemical or physical properties for applications in modern technology.

This dissertation utilizes MER synthesis and Laue oscillation analysis in the investigation of several metastable, layered materials. This work begins with a brief overview of typical thin film synthesis methods before delving into an in-depth description of MER synthesis. Three initial examples are presented to demonstrate how parameters can be tuned in MER precursors to influence the nucleation and growth of metastable products. After a brief description of the experimental methods used, the advancement of Laue oscillation analysis via a method to extract structural information is presented. This method allows for the determination of the number of unit cells in the crystalline domain of the film. This is compared to the total film thickness to determine whether the film consists entirely of the crystalline material, which is useful for detecting small amounts of impurity phases that cannot be identified in XRD patterns. Further investigation into the factors that affect the intensities of Laue oscillations are then presented. These insights were used to develop and incorporate fitting software for patterns containing Laue oscillations into the crystallography data analysis software, GSAS-II. Laue oscillations were also essential for the development of a method to determine the site and amount of metal atoms incorporated into a layered TMD via substitution or intercalation.

The final section of this dissertation focuses on the investigation of several ternary or higher order phase systems containing Fe and Se. The method developed to determine the extent of substitution or intercalation in a TMD was used to explore $Fe_xV_{1-y}Se_2$ compounds with a broad range of Fe content (x = 0-0.9). The amount of Fe incorporated into the hexagonal VSe_2 lattice was expanded far beyond the previously achieved range (x = 0.33).

This work also demonstrates the importance of processing parameters and their influence on lattice parameters. The previously empty Pb-Fe-Se ternary phase diagram was then explored, which led to the formation of a novel $Pb_xFe_{1-x}Se$ phase. Further investigation of the Pb-Fe-Se phase diagram led to the formation of a family of $(PbSe)_{1.06}(FeSe_2)_n$ misfit-layered compounds with a novel, hexagonal $FeSe_2$ structure. The insights gained from investigating both the V-Fe-Se and Pb-Fe-Se phase spaces were used to design precursors for the synthesis of compounds in the quaternary Pb-Fe-V-Se system. A family of $(PbSe)_n(Fe_xV_{1-y}Se_2)_m$ compounds are reported. The reaction pathways to form the $(PbSe)_n(Fe_xV_{1-y}Se_2)_m$ products were elucidated through systematic variations in parameters such as the sequence and thickness of the elemental layers in the designed precursors. This understanding was applied to propose the topology of the free energy landscape.

This dissertation contributes towards the goal of materials discovery by developing and applying methods for the synthesis and characterization of layered thin film materials. Several advances in the analysis of Laue oscillations are presented and multiple metastable Fe-containing phases are reported. This work focuses on increasing our understanding of free energy landscapes through investigations of the nucleation and growth of metastable materials to improve the ability to target useful, metastable phases.

APPENDIX A
SUPPORTING INFORMATION FOR CHAPTER II

A. $Fe_xV_{1-x}Se_2$

For the annealing study carried out on the as-deposited $Fe_{0.8}V_{0.2}Se_2$ precursor, XRR, specular XRD, in-plane XRD, and XRF data were collected after each annealing temperature to follow changes in composition and structure. The thicknesses calculated from the Kiessig fringes in the XRR patterns (Figure S1) decrease steadily from as-deposited to 200°C as the sample crystallizes followed by a sharp decrease upon annealing to 300°C and 400°C when significant Se loss occurs (See Table 1). The decrease in thickness after the 300 and 400°C annealing steps is accompanied by increased film roughness, as evidenced by the Kiessig fringe decay at lower angles.

Table A.1. Thickness determined from Kiessig fringes in XRR pattern as a function of annealing.

Temperature (°C)	Thickness (Å)
As-deposited	308(1)
100	306(2)
200	297(1)
300	266(2)
400	242(1)

The peaks in the specular patterns collected after annealing at each temperature (Figure S1) can be indexed to a family of 00*l* reflections, indicating that the growing compound remains crystallographically aligned to the substrate. The reflections in the specular XRD pattern become narrower, have higher intensities and shift to higher angles as annealing temperatures are increased up to and including 300°C. The narrowing of the line widths indicates the growth of the size of coherently scattering domains after annealing at higher temperatures. The increase in intensity indicates that more of the film is becoming crystalline and/or more crystallographically aligned with the substrate. The shift of the reflections to higher angles indicates that the *c*-axis lattice parameters decrease with

increasing annealing temperature. After annealing at 400°C, the 00*l* reflections broaden and shift to even higher angles. This indicates that the size of the coherently scattering domains decreases, and the size of the *c*-axis lattice parameter decreases. The asymmetric reflection profiles after annealing at 400°C are likely caused by a distribution of lattice parameters due to variation of the distances between Se-M-Se trilayers caused by varying amounts of intercalation occurring in different van der Waal gaps, which is suggested by the XRF data.

XRF data collected after each temperature increase show that the samples lose Se during each annealing step. The Se loss occurring at 100°C and 200°C shifts the sample composition closer to a 1:2 ratio of metal to selenium atoms, suggesting that excess Se evaporates as the $Fe_xV_{1-x}Se_2$ hexagonal layers grow. Above 300°C, the ratio of metal atoms to selenium atoms becomes less than 1:2, which causes intercalation of Fe or V into the van der Waals gaps to occur. The changes in the composition and c-axis lattice parameter are summarized graphically in Figure S2.

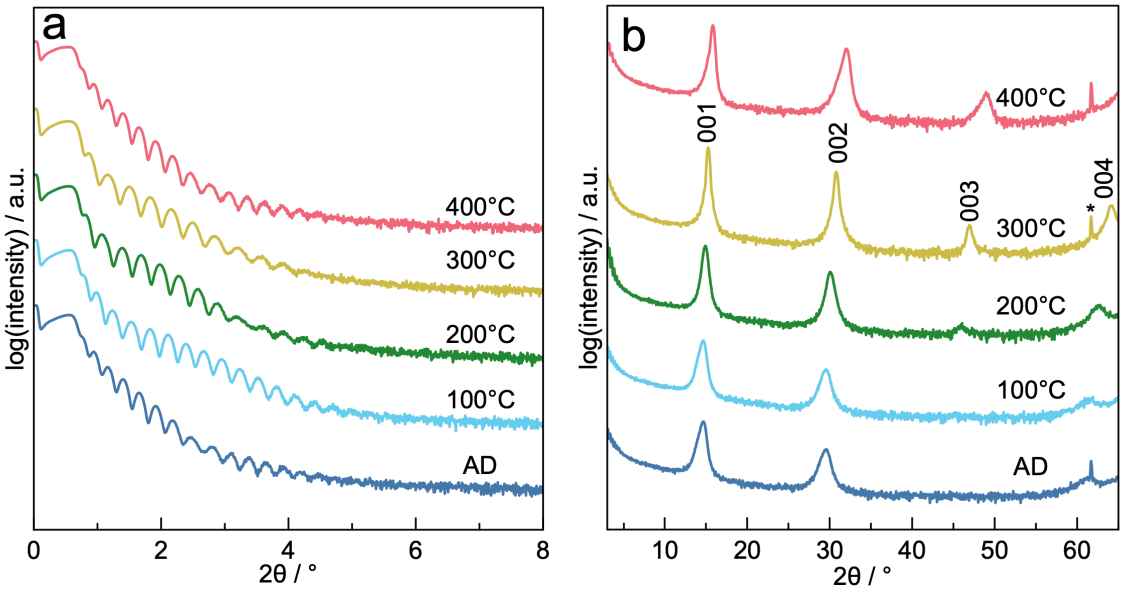

Fig. A.1. a) XRR patterns for the annealing study of the $Fe_{0.8}V_{0.2}Se_2$ sample b) Specular diffraction patterns of the $Fe_xV_{1-y}Se_2$ sample after annealing at the temperatures given above each of the scans. The indices of the reflections are given above the scan taken after annealing at 300°C.

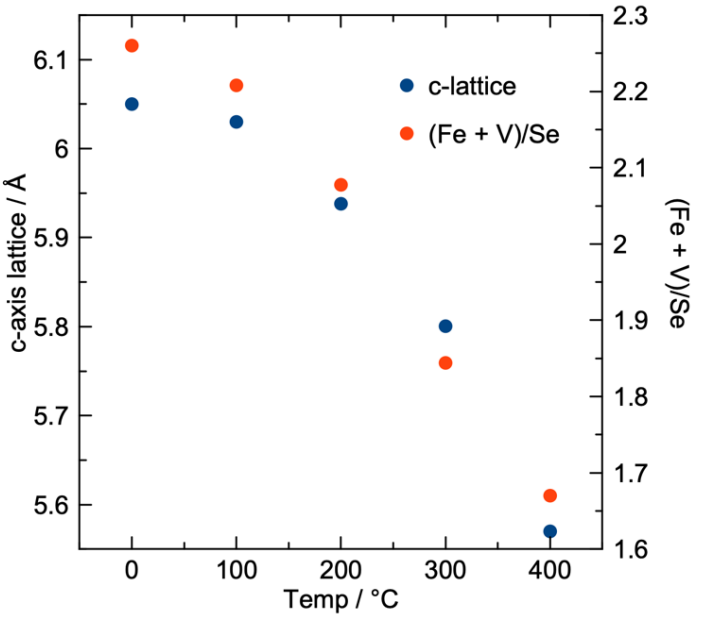

Fig. A.2. Trend in *c*-axis lattice parameter and composition changes for the $Fe_{0.8}V_{0.2}Se_2$ sample during annealing.

The in-plane XRD patterns collected after annealing the sample at each temperature are shown in Figure S3. The in-plane XRD patterns for each temperature below 400°C contain reflections that can be indexed as *hk*0 reflections of a hexagonal phase, and the position of the reflections remain constant as a function of annealing temperature. The resulting *a*-axis lattice parameters are all close to that reported for VSe_2. As the annealing temperature increases, the reflections of the hexagonal phase become narrower and more intense, indicating larger grain sizes and increased crystallinity and/or increased crystallographic alignment of the grains. At 300°C three additional reflections that can be indexed as *hk*0 reflections for the hexagonal phase are observed. At 400°C, the reflections shift to smaller angles, indicating that the *a*-axis lattice parameter increases as Fe or V intercalates into the van der Waals gaps. The increased line widths of the reflections after annealing at 400°C may be a result of variations in the amount of intercalation in different grains.

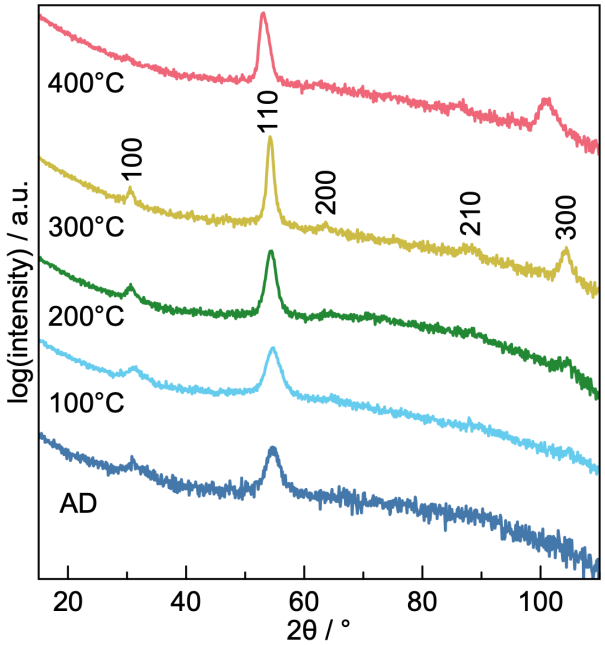

Fig. A.3. In-plane XRD scans collected after annealing the $Fe_{0.8}V_{02}Se_2$ sample at the temperatures given above each of the scans. The indices of the reflections are given above the scan taken after annealing at 300°C.

B. ***$(Pb_3Mn_2Se_5)_{0.6}VSe_2$***

An annealing study was carried out on the $(Pb_3Mn_2Se_5)_{0.6}VSe_2$ precursor, and XRR, specular XRD, in-plane XRD, and XRF data were collected after each annealing temperature. For the as-deposited sample, the XRR pattern contains eleven maxima and twelve minima before the first Bragg reflection, which is consistent with the 13 repeating sequences deposited. The XRR data at increasing temperatures (Figure S4) indicates that the sample remains layered at temperatures up to and including 350°C. The Bragg reflections from the elemental modulation shift to slightly lower angles after annealing at 100°C and shift very little when annealed at higher temperatures. Laue oscillations also appear between the 1st and 2nd order Bragg reflections after the 100°C annealing step, indicating that atoms in the majority of the sample diffuse to form uniformly sized, coherently scattering domains of a kinetically stable heterostructure. The 10 maxima and 11 minima of the Laue oscillations suggest that 12 unit cells of the heterostructure form during the 100°C annealing.

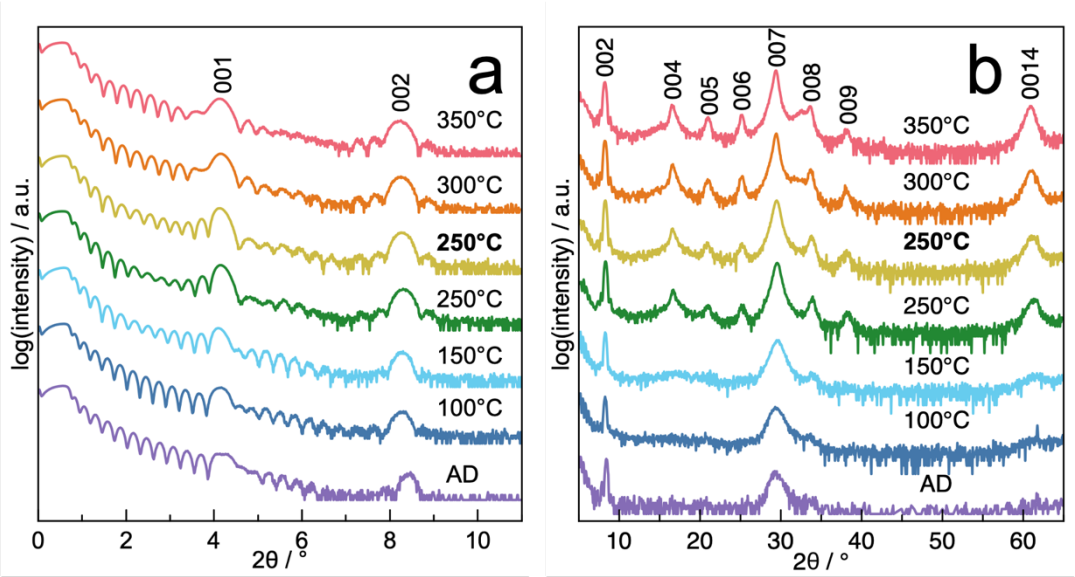

Fig. A.4. X-ray reflectivity (a) and specular XRD (b) data collected on the $(Pb_3Mn_2Se_5)_{0.6}VSe_2$ sample after annealing the sample at all nonbolded temperatures for 15 minutes and at the bolded temperature for 25 minutes.

The changes in the specular XRD data as a function of annealing temperature, Figure S4b, support the formation of a heterostructure. As annealing temperature is increased, new reflections appear in the specular scans that can be indexed as a family of 00*l* reflections. After annealing at 250°C, the reflections yield a *c*-axis lattice parameter of 21.21(1) Å, which is near the estimated value of the heterostructure based on expanding the $(Pb_2MnSe_3)_{0.6}VSe_2$ structure (c = 14.96 Å) by the addition of two ~3 Å thick rock salt structured monolayers. Annealing at temperatures above 250°C results in the growth of intensity at ~33° as impurity phases begin to grow. This intensity is most likely the 002 reflection of rock salt structured MnSe as it begins to segregate out of the heterostructure to form a separate binary phase, and its intensity increases as annealing temperature increases. The higher order 00*l* reflections remain broader than the first two Bragg reflections, presumably due to variations in the lattice parameters due to local composition fluctuations.

C. $(PbSe)_{1+\delta}(FeSe_2)_2$

An annealing study was carried out on the $(PbSe)_{1+\delta}(FeSe_2)_2$ precursor with XRR, XRD, and XRF data taken after each step. XRR and XRD data collected after annealing the precursor at sequentially increasing temperatures are shown in Figure S5. The XRR pattern of the as-deposited precursor (Figure S5) contains 18 Kiessig fringe maxima between the critical angle and the first order reflection, which is consistent with the 20 layering sequences deposited. The specular XRD pattern contains a family of 00*l* reflections. After each annealing step, the reflections become narrower and more intense. Additional 00*l* reflections become apparent the 150°C annealing step and become more intense after annealing to 200°C, which yield a *c*-axis lattice parameter of 17.592(5) Å. A peak due to an impurity phase – likely PbSe – becomes apparent at ~29° in the XRD pattern after annealing to 200°C.

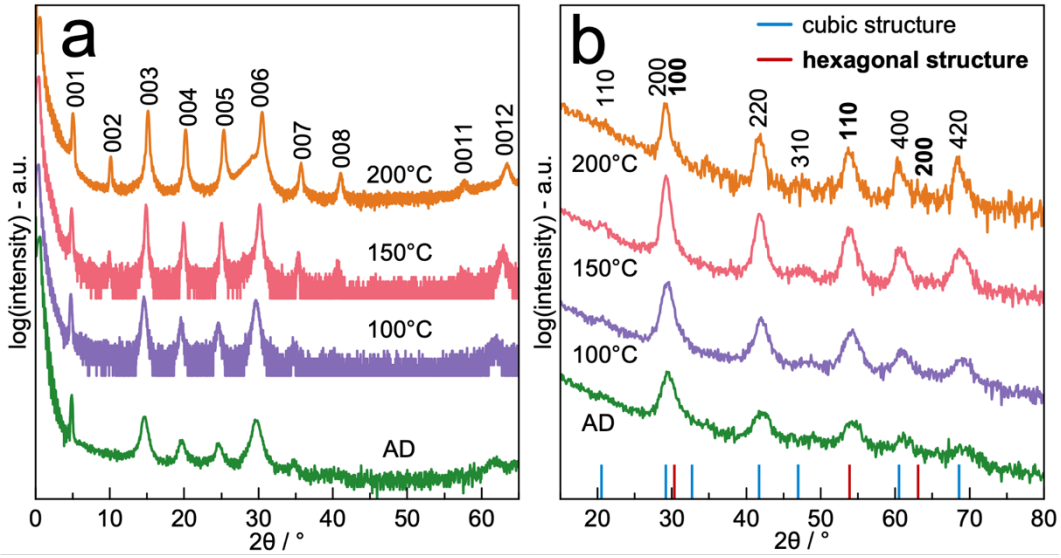

Fig. A.5. a) X-ray reflectivity and specular XRD data and b) in-plane XRD data collected on the $(PbSe)(FeSe_2)_2$ sample after each annealing step. Reflection locations determined from a Lebail fit of the 200°C XRD pattern are shown as tick marks below the in-plane pattern.

The reflections in the in-plane XRD pattern also become more intense and narrower after each increase in annealing temperature. Only *hk*0 reflections are present at each temperature, indicating that the sample remains crystallographically aligned to the substrate. The *a*-axis lattice parameter determined for the cubic phase of 6.115(5) Å is near that

expected for PbSe. Weak intensities observed for the 110 and 310 reflections, which are forbidden in the rock salt space group, indicate a distortion from the rock salt structure. The hexagonal phase has an *a*-axis lattice parameter of 3.40(2) Å, which is near that of the hexagonal VSe_2 compound.

APPENDIX B

SUPPORTING INFORMATION FOR CHAPTER VI

B.1. Annealing Study of Sample A

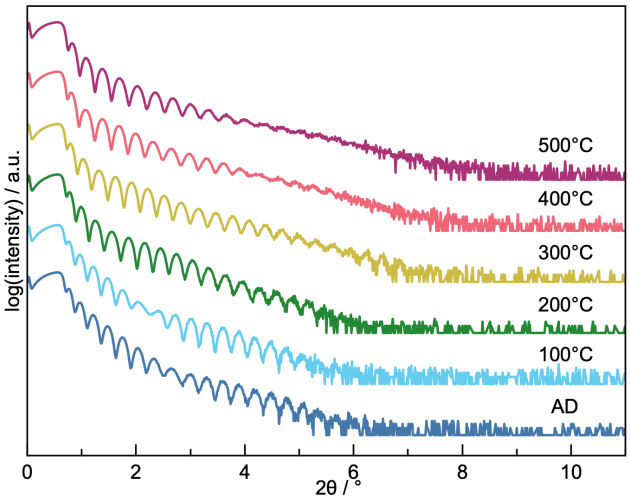

Fig. B.1. XRR patterns at each temperature for the annealing study of Sample A.

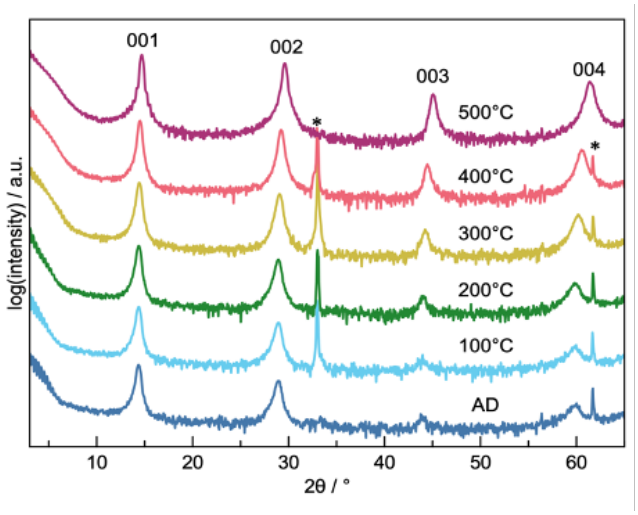

Fig. B.2. Specular XRD patterns at each temperature for the annealing study of Sample A. Reflections marked with * are from the Si substrate.

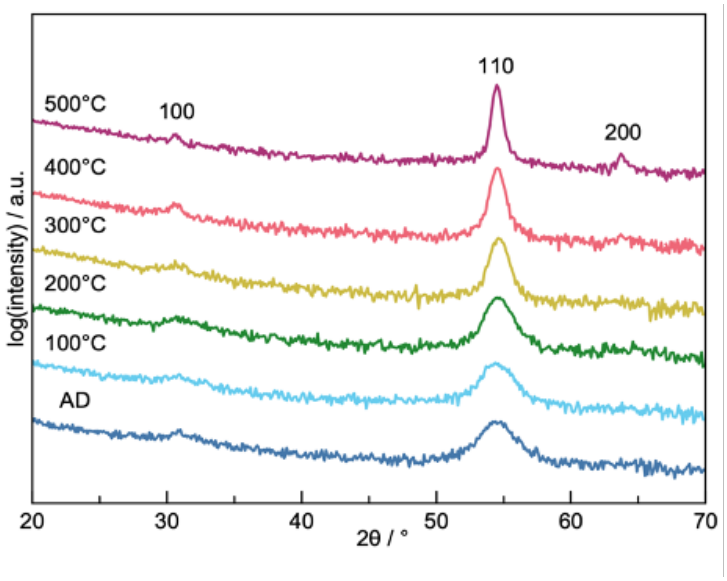

Fig. B.3. In-plane XRD patterns at each temperature for the annealing study of Sample A.

B.2. Rietveld Refinements - Sample A

The starting coordinates for the refinements of Sample A were chosen based on the z-coordinates calculated from HAADF-STEM and STEM-EDS data. The initial values for the fractional occupancy of Fe, V, and Se were chosen based on the compositional information given by the XRF data and Laue oscillations. The sum of the fractional occupancy of Fe and V was constrained to be 1, since the sample was expected to be substitutionally doped based on the XRF data. Given the interdependency of fractional occupancy on the atomic isotropic displacement parameter, U_{iso}, the effect of this parameter was explored by differing the treatment of U_{iso} as well as approaches to refining other parameters in each refinement. Four sample refinements are presented here. In the first refinement, all free parameters are refined independently. In the second, all U_{iso} values are fixed at an approximate expected value for dense phases of 0.01 $Å^2$. In the third, the U_{iso} values are constrained to a single refined value. In the fourth, the metal U_{iso} values are constrained to a single refined value and U_{iso} for Se is refined independently. Table SI-1 summarizes the results and Figures SI-4(A-D) shows the observed, fitted and difference patterns. Note that all refinements refined to quite similar minima, giving increased confidence in the results, with z-coordinates and fractional occupancies near to those expected from XRF, Laue, STEM-EDS, and HAADF-STEM data.

Table B.1. Summary of refinement results for Sample A. Note that the elemental composition is indicated as atoms/unit cell. U_{iso} values are in $Å^2$. The z coordinates are fractional, with $z_{Fe}=z_V=0$. GOF is the goodness of fit.

Parameter	Refinement 1	Refinement 2	Refinement 3	Refinement
Fe composition	0.296(5)	0.28(1)	0.289(2)	0.290(2)
V composition	0.708(8)	0.726(2)	0.710(2)	0.715(2)
Se composition	2.00(1)	1.99(4)	1.94(4)	2.00(1)
Fe Uiso	0.03(1)	0.01	0.0364(6)	0.029(2)
V Uiso	0.020(6)			
Se Uiso	0.044(4)			0.042(1)
Se z	0.2514(5)	0.246(1)	0.251(1)	0.249(1)
GOF	1.26	1.37	1.26	1.20

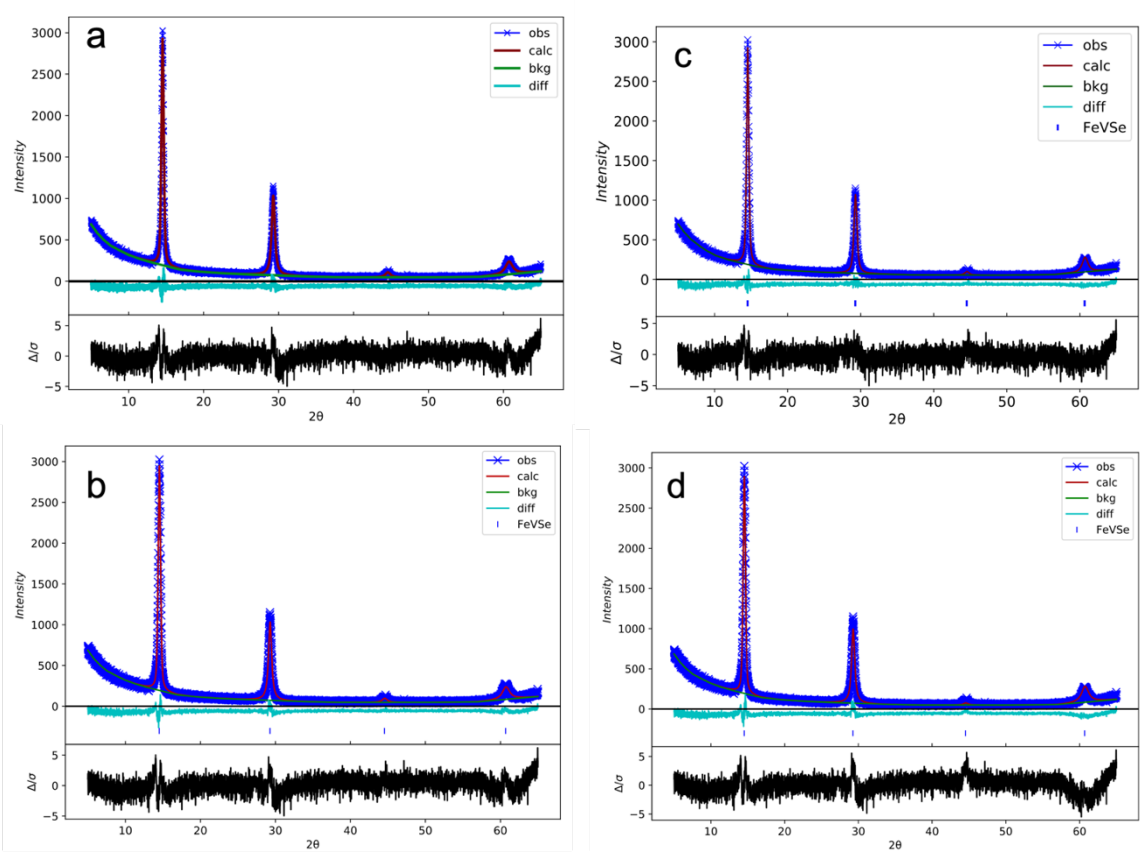

Fig. B.4. Rietveld refinement results for Sample A for refinement 1(A), 2(B), 3(C) and 4(D). The observed diffraction data are shown as blue crosses, the fitted result is shown as a red line, the differences between them is shown as a magenta line. The fitted background is a green line. The difference between the observed and fitted results, divided by the standard uncertainty for each point is shown in black in the lower box.

B.3. Annealing Study of Sample B

To further explore the stability of Sample B during annealing and to test the assumption that the stoichiometry controls the amount of substitution or intercalation, a piece of Sample B was annealed in Se vapor. At temperatures above 300°C, the sample begins to react with the Se atmosphere, and the lattice parameters calculated from the specular and in-plane XRD patterns shift towards those measured for Sample A. A weak reflection at ~33° also appears in the specular and in-plane XRD due to formation of an impurity phase [likely either marcasite structure $FeSe_2$ or δ-FeSe (P63/mmc)]. At 500°C, the lattice parameters for the piece of

Sample B annealed in Se vapor [a = 3.36(1) Å, c = 6.080(4) Å] are within error of those of Sample A, and the ratio of metal to Se is close to 1:2. This suggests that the TMD formed incorporates Fe mostly substitutionally. This illustrates that the stoichiometry of a sample is affected by annealing conditions that may cause incorporation of foreign atoms in the crystalline product to be different than that targeted by the initial stoichiometry.

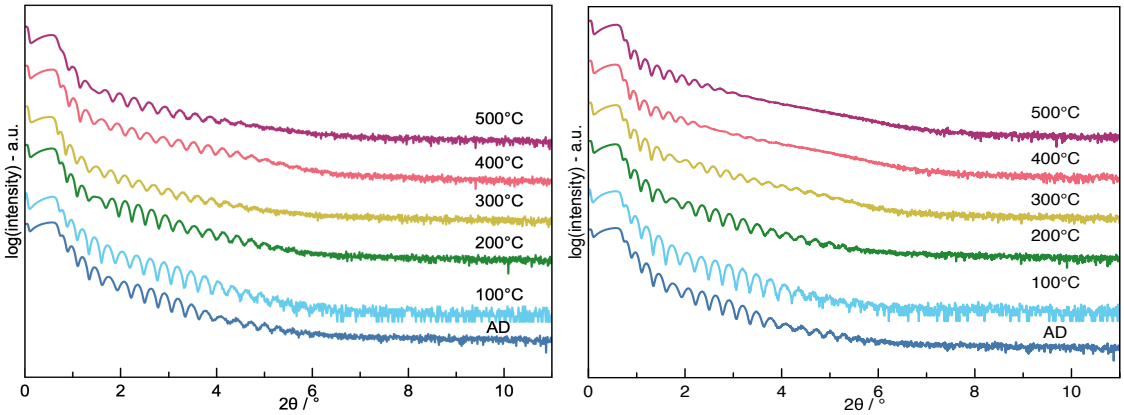

Fig. B.5. X-ray Reflectivity patterns from the study of Sample B, annealed under N_2 atmosphere (left) and Se atmosphere (right) to the indicated temperatures.

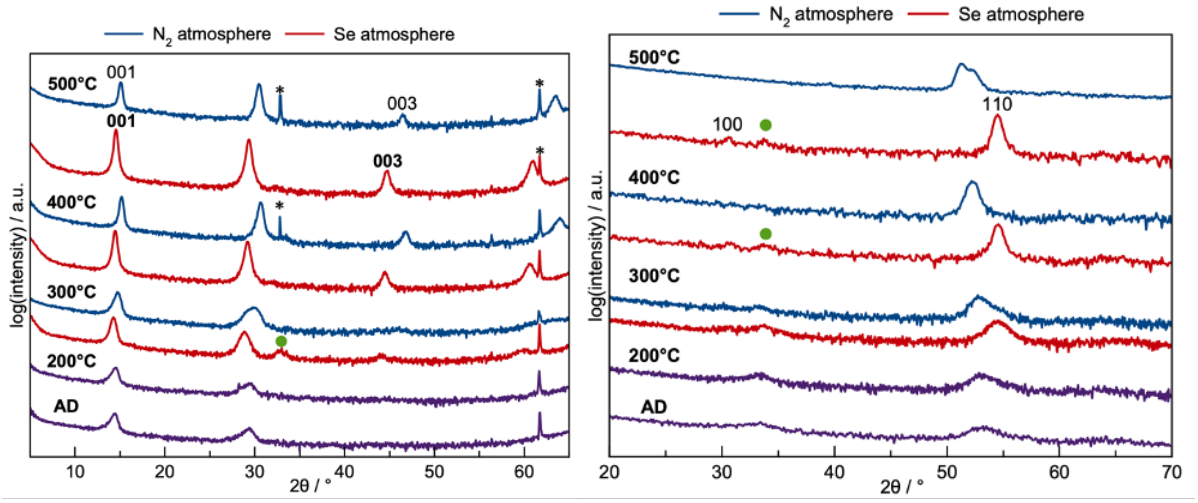

Fig. B.6. Specular (left) and in-plane (right) XRD patterns for the study of Sample B annealed under the indicated atmospheres and temperatures. Impurity phase reflections are marked with a green circle. Reflections marked with * are due to the Si substrate.

B.4. Rietveld Refinements - Sample B

Sample B had far fewer constraints for the refinement than Sample A, since the XRD pattern did not contain Laue oscillations and microscopy data was not taken. This led to multiple different structures that could be explored in the refinement with intercalated Fe or V, substituted Fe, or a mixture of both. Multiple starting models were explored to attempt to fit the XRD pattern, and several were able to reach a reasonable fit. Given the lack of available constraints, it is unclear which model gives the best refinement, and a single structural model cannot be determined. Three representative refinements are summarized below.

Refinement 1: Purely intercalated Fe

The starting model for this refinement had intercalated Fe with a fixed z-coordinate of 0.5. The initial fractional occupancy was based on the XRF stoichiometry ($Fe_{0.3}VSe_2$), but the refinement converged with less Fe than expected. However, the fractional occupancy of the Fe atom was highly correlated with the U_{iso} value To reduce these correlations, U_{iso} values were grouped for all atoms. Nevertheless, the refinement converged with a GOF value of 1.59 and the structure and stoichiometry summarized below.

Table B.2. Summary of refinement 1 of Sample B.

Element	Stoichiometry from Rietveld	U_{iso}	z
V	1.00(2)	0.041(1)	0.0
Se	1.95(1)	0.041(1)	0.2497(1)
Fe	0.121(3)	0.041(1)	0.5

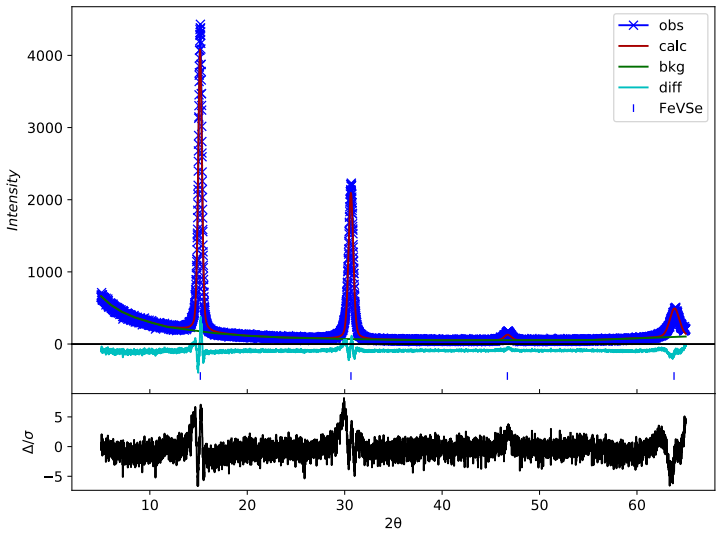

Fig. B.7. Rietveld refinement 1 of Sample B.

Refinement 2: Intercalated V and substituted Fe

This refinement started with substituted Fe and intercalated V, with a stoichiometry near that expected from XRF. The refinement converged with a GOF value of 1.58, but there are clear residuals shown in the XRD pattern and the stoichiometry has less Fe than expected from XRF. Again, a single U_{iso} value was used for all atoms.

Table B.3. Summary of refinement 2 of Sample B.

Element	Stoichiometry from Rietveld	U_{iso}	z
V	0.844(2)	0.047(1)	0.0
Fe	0.174(2)	0.047(1)	0.0
Se	2.02(1)	0.047(1)	0.249(1)
V	0.156(3)	0.047(1)	0.5

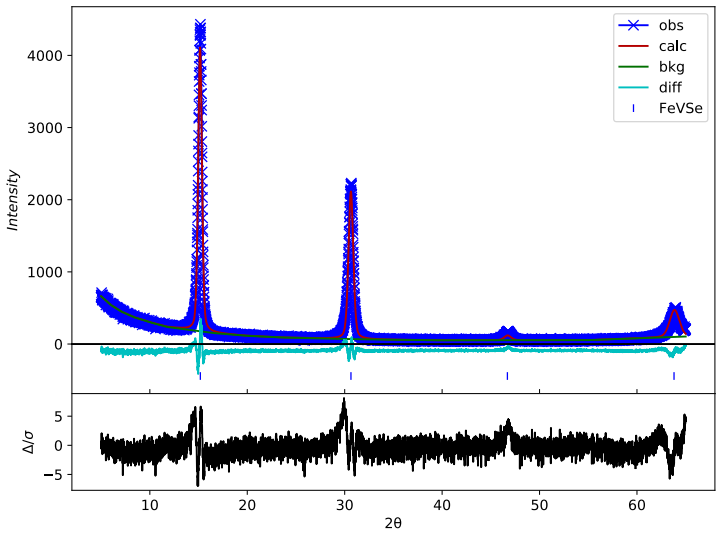

Fig. B.8. Rietveld refinement 2 of Sample B.

Refinement 3: Intercalated Fe and V and substituted Fe

This refinement started with substituted Fe and intercalated V and Fe, with a stoichiometry near that expected from XRF. The refinement converged with a GOF value of 1.55 with a reasonable stoichiometry.

Table B.4. Summary of refinement 3 of Sample B.

Element	Stoichiometry from Rietveld	U_{iso}	z
V	0.807(2)	0.0564(5)	0.0
Fe	0.250(2)	0.0564(5)	0.0
Se	2.04(1)	0.0564(5)	0.252(1)
V	0.100(3)	0.0564(5)	0.5
Fe	0.052(3)	0.0564(5)	0.5

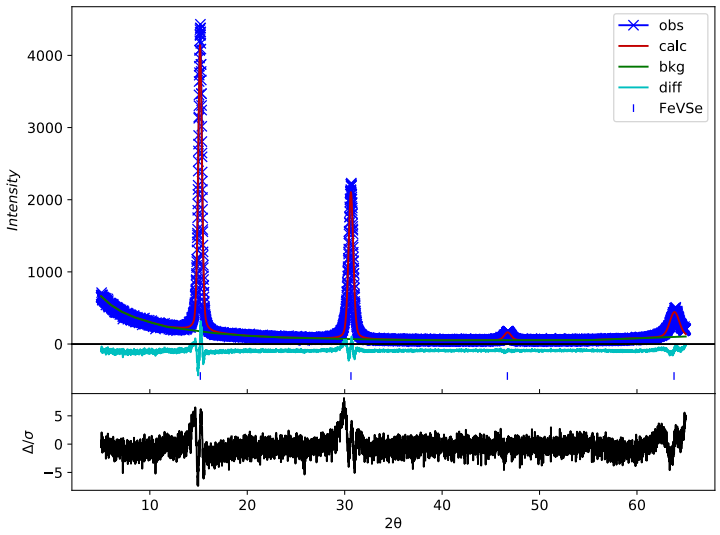

Fig. B.9. Rietveld refinement 3 of Sample B

Computational Calculations:

The DFT framework utilized here is comprised of the projector augmented wave (PAW)[1] method as implemented in the Vienna ab initio Simulation Package (VASP)[2,3] which has shown previous success when working with transition metal atoms and compounds.[4-6] In the PAW method all electrons appear as either adaptable in valance states or frozen in atomic core states. Many potentials are supplied within VASP, with this work utilizing those that treat the 4s and 4p of Se as valance electrons as well as the 4s and 3d electrons of both V and Fe. The PAW sphere radii are 1.16, 1.32, and 1.30 Å for Se, V, and Fe, respectively, which lead to no significant overlap between spheres. The plane wave energy cutoff is set to 520 eV, which converges energy differences to well below 1 meV/atom. Exchange and correlation are treated in the generalized gradient approximations (GGA) with the PBE functionals of Perdew, Burke, and Ernzerhof.[7] For each system the k-point mesh was altered until the total energy (calculated using the linear tetrahedron method with the corrections of Blochl et. al. converged within 1 meV/atom.[8] This was achieved by using a 3x3x3 mesh and was consistently applied throughout this work.

Unless otherwise stated, optimization of the individual superlattices began from the same basic pattern. Starting from the accepted, experimental lattice parameters of the simple, hexagonal cell of VSe_2, each lattice parameter was scaled up to produce a 4x4 superlattice consisting of 16 vanadium atoms and 32 selenium atoms in a monolayer of VSe_2. Next, this

monolayer was duplicated and placed 6.0 Å above the original. The conjugate gradient algorithm in VASP was then used to find the instantaneous ground state as a reference for pure VSe_2, which was used at the reference structure for subsequent calculations. The cell parameters and atomic positions undergo concurrent optimization. The spin and magnetic moments were optimized concurrently with structure. Two deposition schemes were considered, the first where individual vanadium atoms were sequentially replaced by iron up to approximately 13% iron by mass, as depicted in Fig. B.6(a). The second scheme involved sequentially intercalating iron atoms between the VSe_2 layers up to approximately 11% iron by mass. Both schemes add a total of 16 Fe atoms. In the intercalation scheme two potential insertion points were investigated. The first where the iron intercalated into the octahedral holes created by the two selenium layers. This arrangement, shown in Fig. SI-6(b), aligns the Fe atom with the vanadium atoms in each layer. The second scheme, designated as the "1T" position, shown in Fig. B.6(c), where the iron intercalates off center of the octahedral holes and is staggered between the V atoms in each layer. As the Fe mass fraction increases, a potentially large selection of structures in both mechanisms are possible based due to symmetry being broken by both substitution and intercalation. This work attempted to collect a reasonable sampling of structures at each mole fraction of iron observed. This ranged from those derived through chemical intuition, but also a random sampling of substitutions and intercalations. With each new concentration of iron, each structure was reoptimized and a new set of lattice parameters and formation enthalpy was determined.

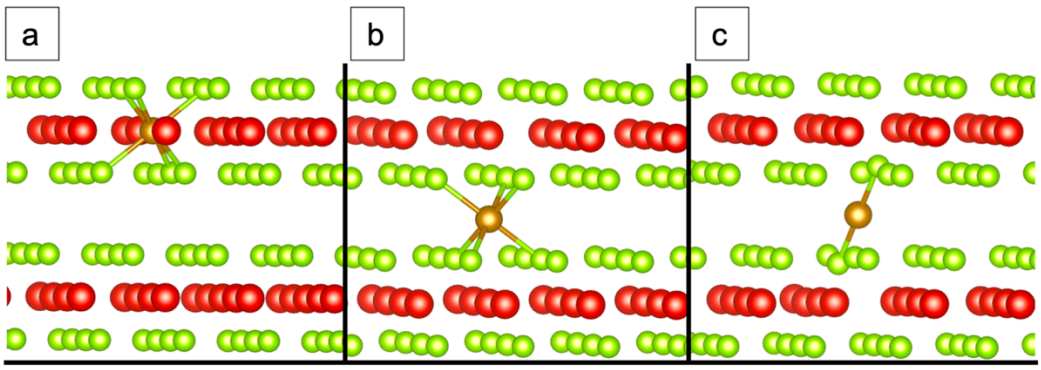

Fig. B.10. The three possible schemes for Fe addition to the VSe_2 bilayer: substitutional (a), octahedral intercalation (b), and "1T" intercalation (c).

Table B.5. Formation enthalpies of materials made from either substitutional or intercalated deposition of iron atoms. Also included are the *a* and *c* lattice parameters of the unit cell as a function of the mass percent of added iron.

Fe Atoms Deposited	Mass % Fe	Formation Enthalpy (meV/Atom)	Lattice Parameter *a*	Lattice Parameter *c*
Substitutional Replacement				
Pure VSe_2	0.00	-448	3.318	6.125
1	0.83	-437	3.312	6.126
3	2.50	-417	3.311	6.114
6	4.99	-381	3.317	6.070
8	6.64	-374	3.306	5.959
12	9.94	-327	3.296	5.937
16	13.21	-307	3.300	5.831
Intercalated Addition				
1 (1T)	0.83	-409	3.347	6.209
1 (Oct)		-440	3.319	6.113
3	2.45	-425	3.323	6.083
6	4.77	-397	3.347	6.062
8	6.27	-377	3.360	6.021
12	9.11	-333	3.391	5.872
16	11.79	-311	3.422	5.633

Table B.5 gives a summary of the most pertinent data from the theoretical calculations. The pure VSe_2 hexagonal crystal structure acts as an asymptote and reference point for both the substitutional and intercalated deposition mechanisms and is comprised of a VSe_2 bilayer, allowing for Fe substitution in two layers and two interstitial sites for Fe intercalation. The formation enthalpy of pure VSe_2 was calculated to be -448 meV/Atom. The lattice parameters *a* and *c* were calculated to be 3.318 and 6.125 Å, respectively, which

both agree reasonably well with the experimental values of 3.359 and 6.150 Å. Additionally, the spacing between vanadium atoms between layers was calculated to be 6.123 Å which agrees with the estimated value from experiment of 6.08 Å. The substitutional structure has a single, symmetry-unique structure with a formation enthalpy of -437 meV/Atom and the lattice parameters remain largely unchanged relative to VSe_2. Intercalation, however, has two possible structures depending on whether the 1T or octahedral structure is used. The octahedral configuration was energetically preferred relative to substitution and has a calculated formation energy of -440 meV/Atom. The 1T configuration, however, has the highest formation energy of -409 meV/Atom. This is coupled with large changes in both lattice parameters, implying significant energy for atomic displacement of the adjacent selenium atoms. For further computations, only intercalation into octahedral holes was considered as the energy difference and necessary Se displacement for 1T structures was considered too substantial to warrant further inquiry. The substitution scheme prefers to replace vanadium atoms in a single layer until 6.64% Fe by mass, which corresponds to two complete, adjacent rows of iron atoms. Sequential substitution shows the formation of these rows where each substitution replaces an adjacent V. The second and third most favored structures shown in figure SI-9 correspond to single and double atom deviations from the adjacent substitution scheme. In contrast, the intercalated scheme prefers to add iron atoms into both available layers until 6.27% Fe by mass, after which point it is energetically favorable to intercalate two rows in the same layer. Similar to the substitutional scheme, the second and third most favored structures are those with single and double atom displacements from adjacent addition. With further Fe addition, both deposition schemes favored completing rows in the second layer. It should be noted that in each deposition scheme there was little variance in energy between tested structures. For example, the energy range for the 2.50% iron by mass substitutional structures tested was 8.00 meV/Atom. This only increases to 16.21 meV/Atom at 9.94% despite there being a far greater number of possible configurations. Iron was added substitutionally up to a mass percent of 13.21%. At this point, half of the available vanadium has been substituted for iron. The lattice parameters *a* and *c* are 3.300 and 5.831 Å, respectively, which are trending to be closer to the lattice parameters of $FeSe_2$, which are 3.583 and 5.782 Å. Iron was intercalated up to a mass percent of 11.79%, which similarly has half of the available octahedral sites occupied. In a similar

fashion to the substitutional scheme, lattice parameters *a* and *c* are smoothly converging to the known values for $FeSe_2$. It is unlikely that the lattice constants for a fully intercalated material would match those of $FeSe_2$ and will likely reside somewhere between pure VSe_2 and $FeSe_2$. Experimentally determined values for the *c* lattice constant differ broadly between the intercalated and substitutional structures, which is not seen in theoretical simulations. To this end, a second set of calculations was conducted using the DFT-D2[9] method implemented in VASP to correct for potential errors with the default van der Waals radii in standard potentials. There was no significant difference between lattice parameters with or without this correction.

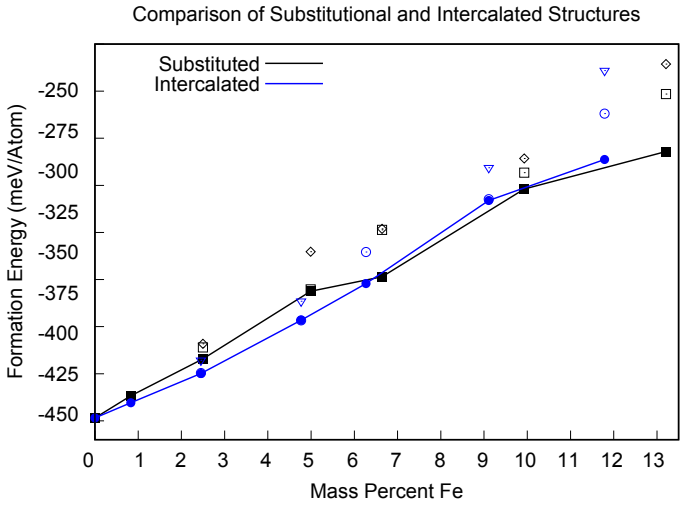

Fig. B.11 Formation energy in meV/Atom as a function of Fe mass %. The intercalated structures in blue are compared to the substitutional structures in black. Solid markers indicate the formation energy of the most stable structure tested. The hollow circles and squares mark the energy of the next highest energy conformation for the intercalated and substitutional structures respectively. The hollow triangles and diamonds represent the energy of the least stable conformers observed in both the intercalated and substitutional species respectively.

While at first glance it may appear that the intercalated method always provides lower formation enthalpies and would thus always be favored, it is necessary to plot formation energy as a function of the mass percent of Fe to observe the true trend. Figure SI-9 demonstrates the intriguing trend in formation energies of both deposition schemes. Low iron concentrations favor an intercalated scheme and are favored by an average of ~10 meV/Atom

which differs enough to make a definitive statement about the relative energetic favorability of both schemes given that there is no overlap in the ranges of energies for either mechanism when considering the second and third most favored structures. In many instances, it is difficult to distinguish between the ground state configuration and the second lowest configuration. However, at approximately 7% Fe by mass, when 8 iron atoms have been added, both deposition schemes are nearly degenerate accompanied by a crossover in the favored mechanism with the substitutional scheme being slightly preferred. Both schemes remain nearly degenerate throughout the remainder of the calculations. The above calculations suggest that even though there is little variance in calculated energies based on tested configurations, the energy difference is indeed large enough to imply that any kinetic effects could cause one mechanism to be favored over another given the increasing range of even the second lowest energies as the iron concentration increases above 10%. Further calculations are necessary to devise a sophisticated mechanism that would allow for the accurate description of the energetic crossover.

APPENDIX C

SUPPORTING INFORMATION FOR CHAPTER VII

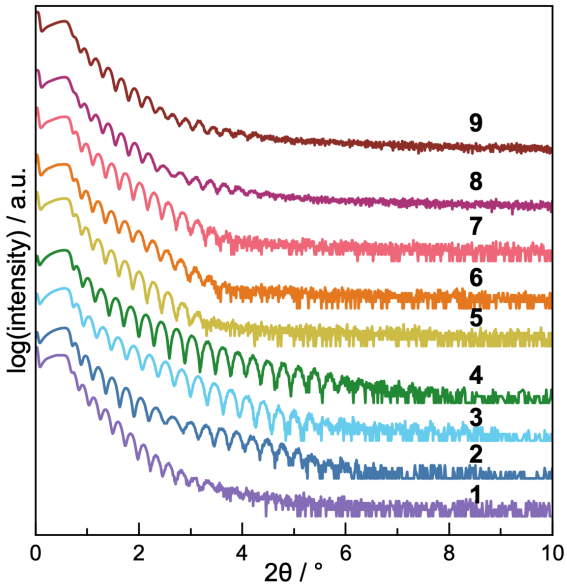

Fig. C.1. As-deposited XRR patterns for each sample.

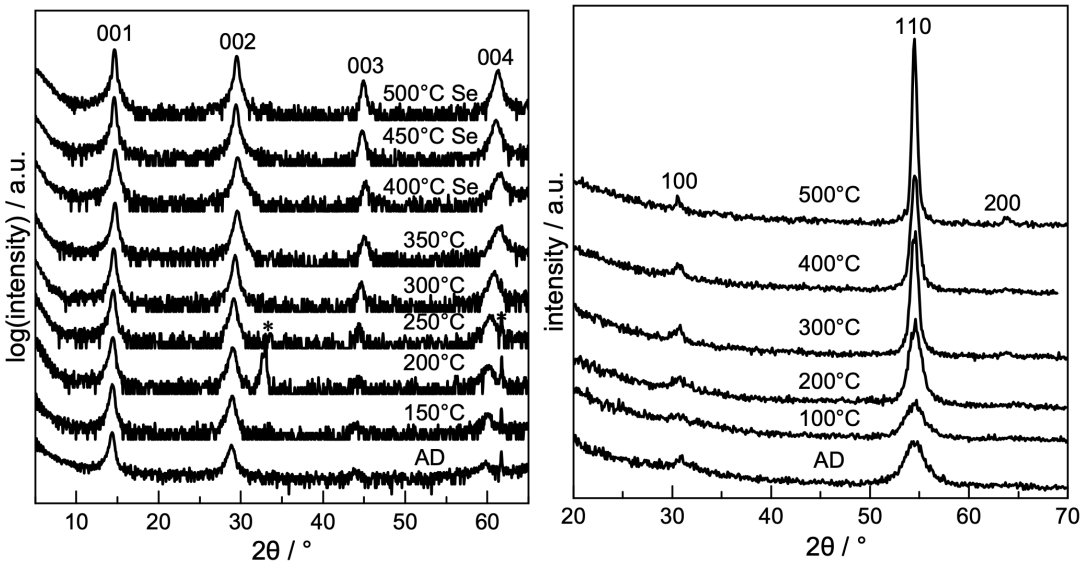

Fig. C.2. a) specular XRD and b) in plane XRD for annealing study of sample 2.

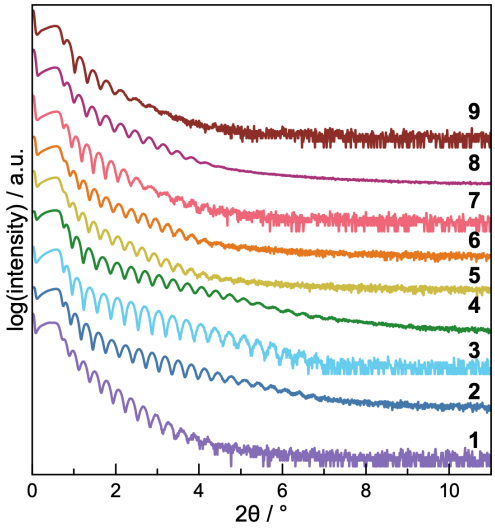

Fig. C.3. XRR patterns for each sample annealed to 350°C for 15 min.

Table C.1. Thicknesses determined from the XRR patterns and Laue oscillations for each sample.

Sample	XRR Thickness (Å)	Laue Thickness (Å)
2	270(2)	268(6)
3	255(2)	250(6)
4	254(2)	252(6)
6	291(2)	287(6)
7	272(2)	270(6)
8	271(2)	265(6)

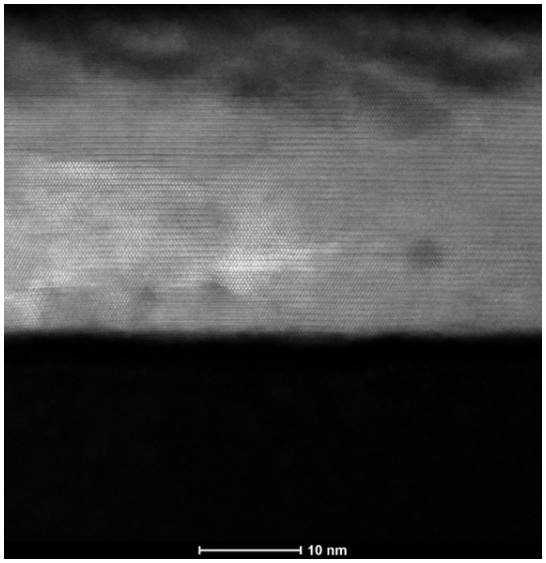

Fig. C.4. HAADF-STEM image across the entire cross-section of sample **8**.

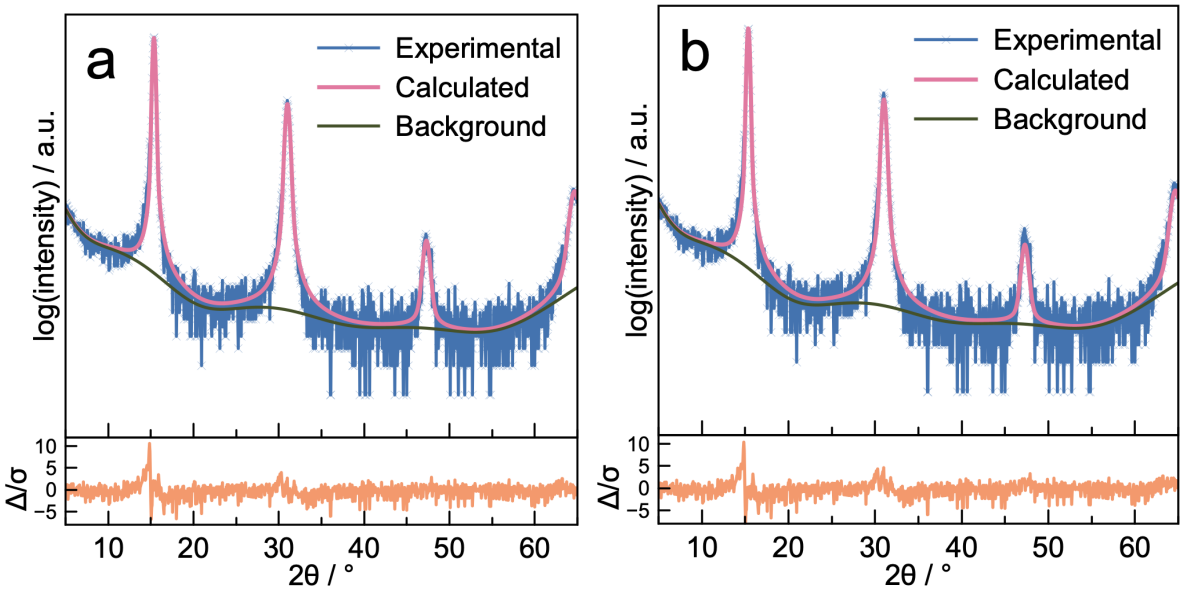

Fig. C.5. a) Rietveld refinements based on a model with the composition $Fe_{0.09}Fe_{0.65}V_{0.35}Se_2$ and b) Rietveld refinements based on a model with the composition $Fe_{0.79}V_{0.21}Se_2$

APPENDIX D

SUPPORTING INFORMATION FOR CHAPTER VIII

All substrate reflections are indicated by a *, due to the SiO_2/Si wafer.

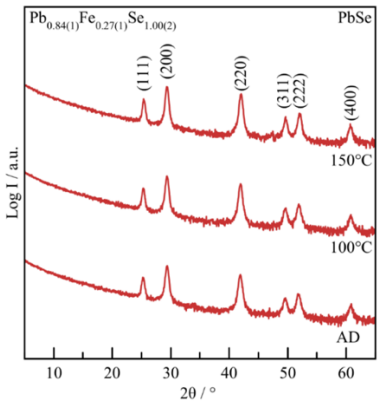

Fig. D.1. Grazing-incidence x-ray diffraction patterns of a film with a composition of $Pb_{0.84(1)}Fe_{0.27(1)}Se_{1.00(2)}$, annealed stepwise in N_2 atmosphere to 150°C. The reflections are indexed to a cubic phase with a lattice parameter of 6.121(2) Å with a face-centered geometry, which is consistent with PbSe.[1] There is no presence of the tetragonal $Pb_{1-x}Fe_xSe$ phase in the patterns.

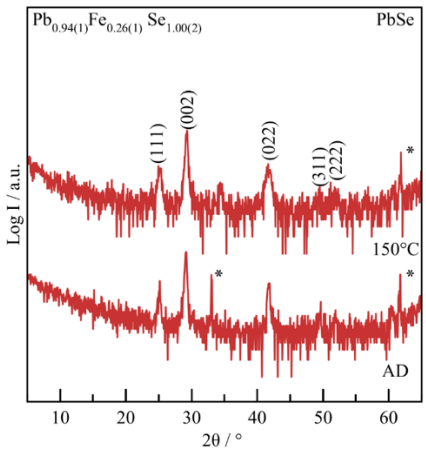

Fig. D.2. Specular locked-coupled x-ray diffraction patterns of a film with a composition of $Pb_{0.94(1)}Fe_{0.26(1)}Se_{1.00(2)}$, annealed in N_2 atmosphere to 150°C. The reflections are indexed to a cubic phase with a lattice parameter of 6.129(3) Å with a face-centered geometry, which is consistent with PbSe.[1] There is no presence of the tetragonal $Pb_{1-x}Fe_xSe$ phase in the patterns.

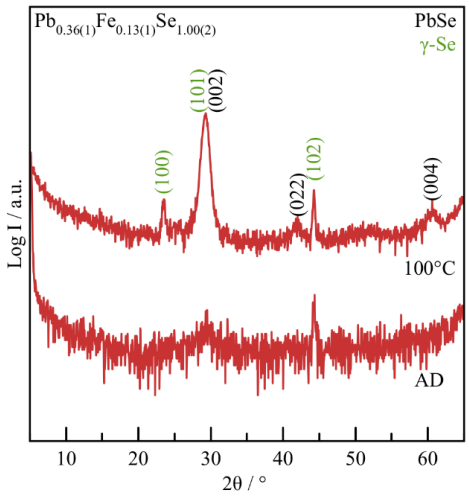

Fig. D.3. Specular locked-coupled x-ray diffraction patterns of a film with a composition of $Pb_{0.36(1)}Fe_{0.13(1)}Se_{1.00(2)}$, annealed in N_2 atmosphere to 100°C. The reflections are indexed to a cubic phase with a lattice parameter of 6.14(1) Å with a face-centered geometry, which is consistent with PbSe.[1] There is an additional set of reflections that can be indexed to a hexagonal unit cell with an a-lattice parameter of 4.40(1) Å and a c-lattice parameter of 4.91(1) Å, which is consistent with γ-Se.[2] There is no presence of the tetragonal $Pb_{1-x}Fe_xSe$ phase in the patterns.

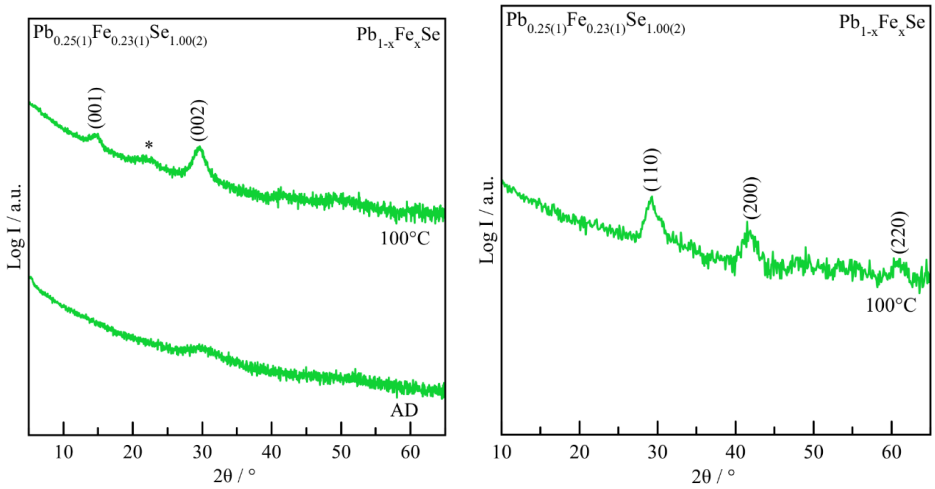

Fig. D.4. a) Grazing-incidence and b) in-plane grazing-incidence x-ray diffraction patterns of a film with a composition of $Pb_{0.25(1)}Fe_{0.23(1)}Se_{1.00(2)}$, annealed in N_2 atmosphere to 100°C. The reflections can be indexed to a tetragonal phase with an a and c-lattice parameter of 4.29(1) Å and 6.10(1) Å, corresponding to the $Pb_{1-x}Fe_xSe$ phase. There is an additional reflection indicated by the * in the grazing-incidence pattern, indicating an impurity phase.

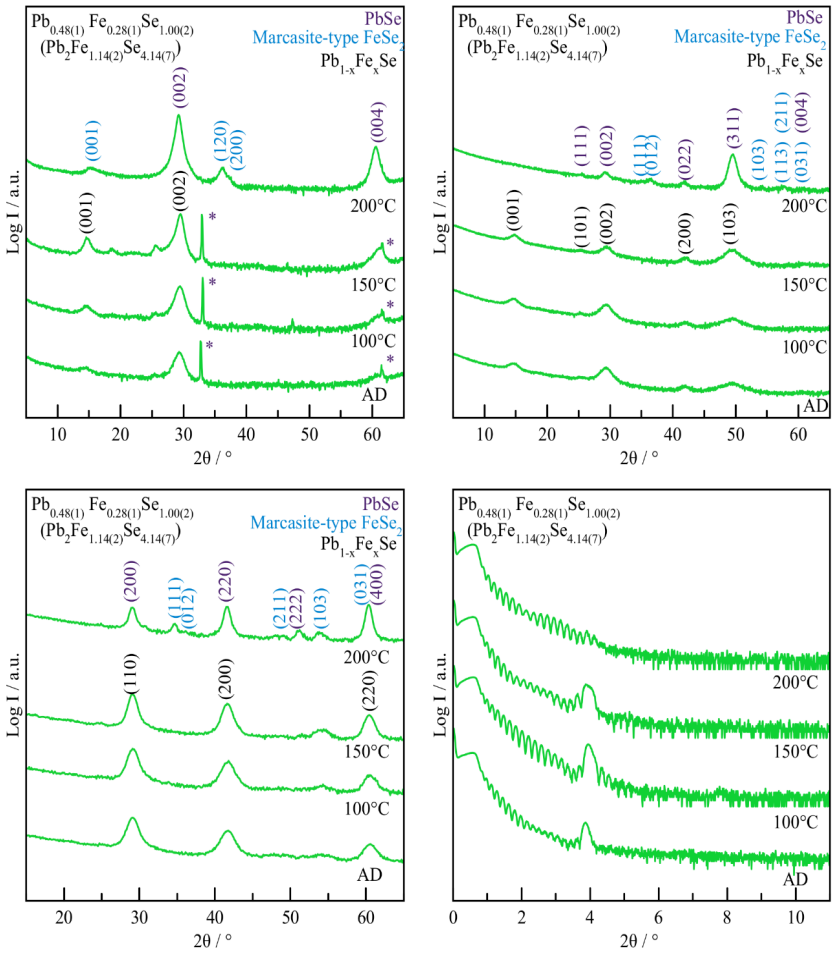

Fig. D.5. a) Specular locked-coupled, b) grazing-incidence, and c) in-plane grazing-incidence x-ray diffraction and d) low-angle x-ray reflectivity patterns of a film with a composition of $Pb_{0.48(1)}Fe_{0.28(1)}Se_{1.00(2)}$, annealed in N_2 atmosphere to stepwise to 200°C. This sample is close to composition of the predicted phase *Pb_2FeSe_4*[3], however there is no indication that it formed before breaking down to binary phases. The tetragonal $Pb_{1-x}Fe_xSe$ phase is present up to 150°C with a and c-lattice parameters of 4.33(1) Å and 6.10(1) Å, respectively, however there is an impurity phase indicated by reflections that are not indexed in the specular locked-coupled and in-plane grazing-incidence diffraction patterns. The patterns at 200°C show reflections that can be indexed to a cubic phase with a lattice parameter of 6.102(1) Å, consistent with PbSe.[1] They also show reflections that can be indexed to an orthorhombic phase with a, b, and c lattice parameters of 3.59(1) Å, 4.79(1) Å, and 5.77(1) Å, respectively, consistent with marcasite-type $FeSe_2$.[4] Impurity phases observed upon annealing is indicated by a ǂ.

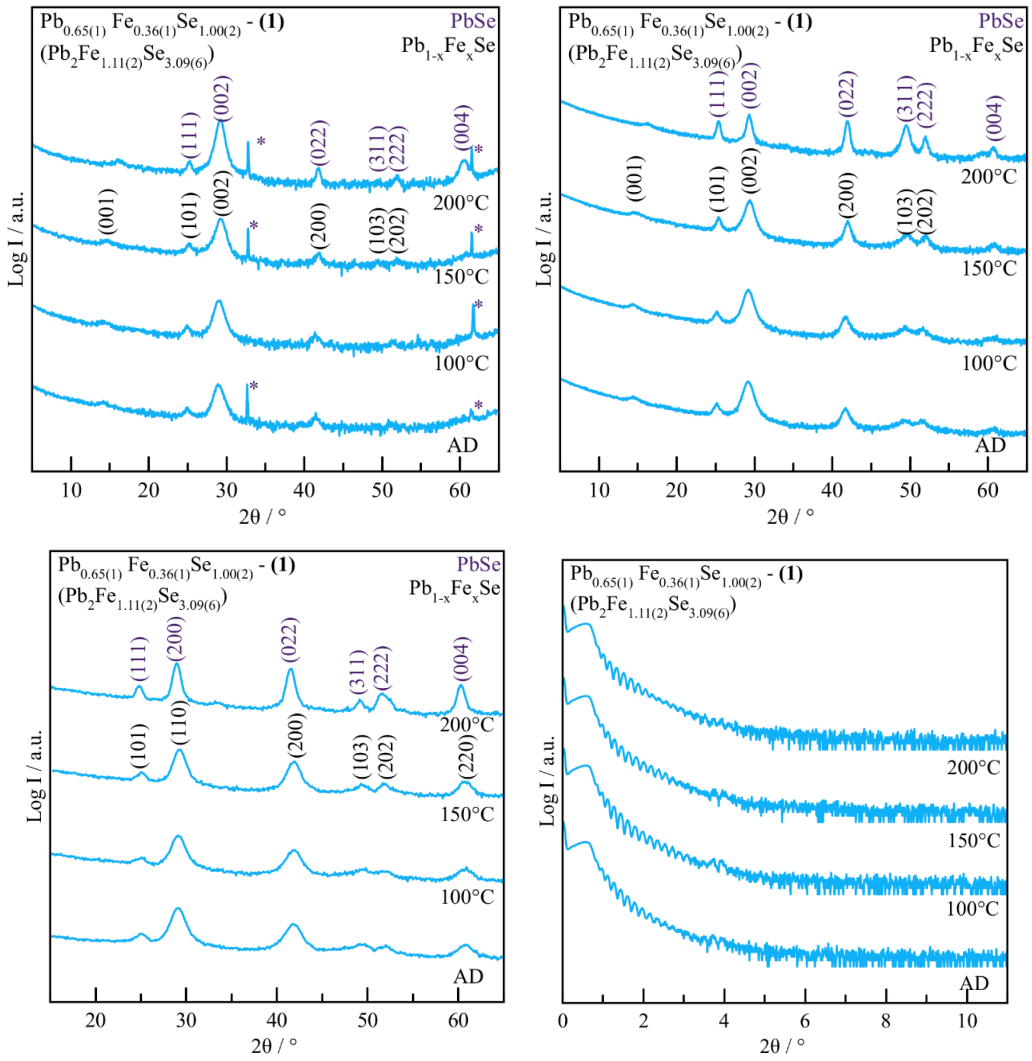

Fig. D.6. a) Specular locked-coupled, b) grazing-incidence, and c) in-plane grazing-incidence x-ray diffraction and d) low-angle x-ray reflectivity patterns of **film 1** with a composition of $Pb_{0.65(1)}Fe_{0.36(1)}Se_{1.00(2)}$, annealed in N_2 atmosphere to stepwise to 200°C. This sample is close to composition of the predicted phase Pb_2FeSe_3[3], however there is no indication that it formed before breaking down to binary phases. The tetragonal $Pb_{1-x}Fe_xSe$ phase is present up to 150°C with a and c-lattice parameters of 4.35(1) Å and 6.11(1) Å, respectively. The patterns at 200°C show reflections that can be indexed to a cubic phase with a lattice parameter of 6.096(1) Å, consistent with PbSe.[1] There are not enough reflections to accurately index the iron selenide phase present, although the breakdown of the initial $Pb_{1-x}Fe_xSe$ phase is evident from the shift of the (001) reflection to no longer index with the rest of the pattern.

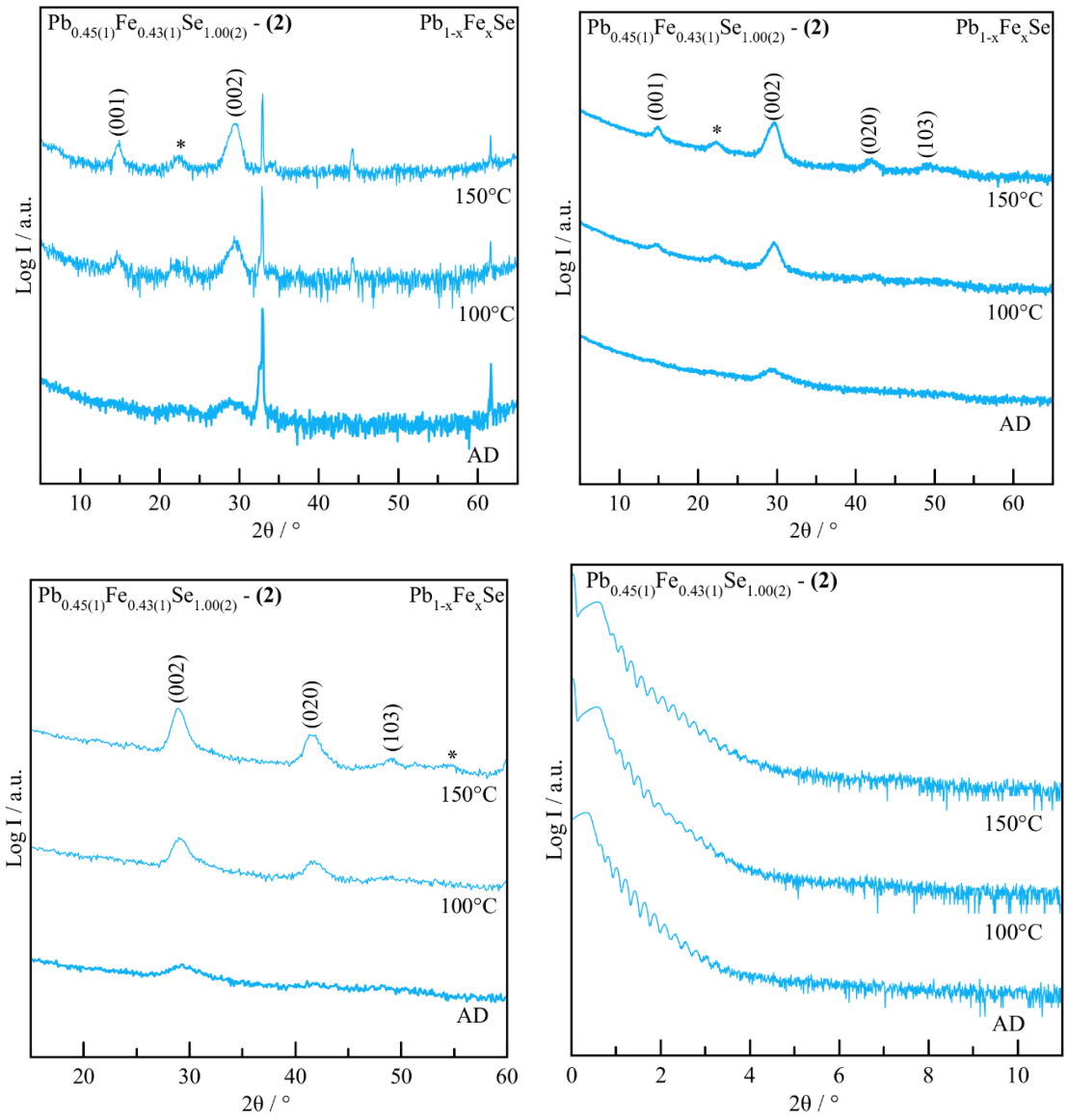

Fig. D.7. a) Specular locked-coupled, b) grazing-incidence, and c) in-plane grazing-incidence x-ray diffraction patterns and d) low-angle x-ray reflectivity of **film 2** with a composition of $Pb_{0.45(1)}Fe_{0.43(1)}Se_{1.00(2)}$, annealed in N_2 atmosphere to stepwise to 150°C. The tetragonal $Pb_{1-x}Fe_xSe$ phase is present up to 150°C with a and c-lattice parameters of 4.33(1) Å and 6.12(1) Å, respectively, however, there is an impurity phase present that grows through annealing, indicated by a ǂ.

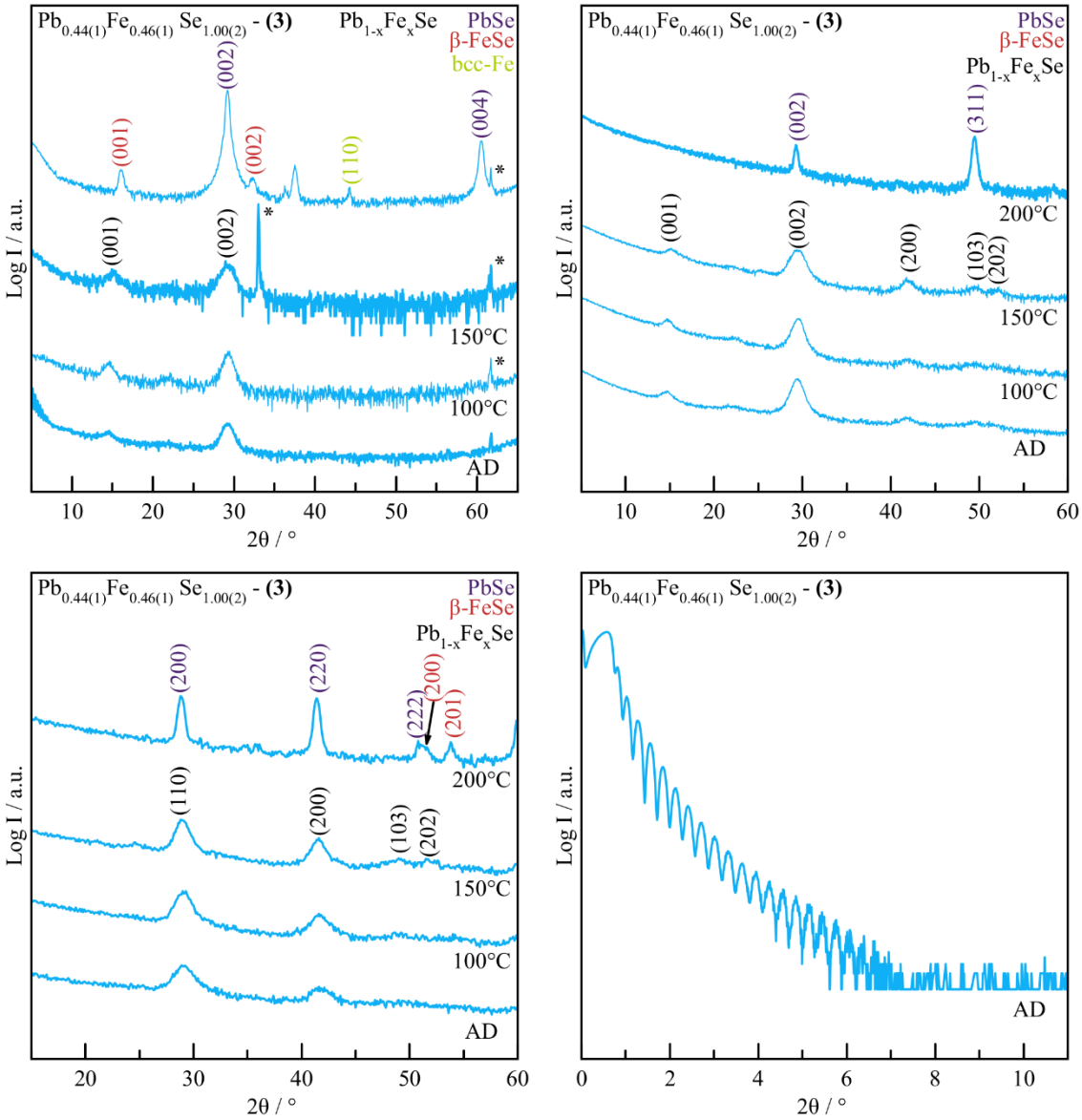

Fig. D.8. a) Specular locked-coupled, b) grazing-incidence, and c) in-plane grazing-incidence x-ray diffraction patterns and d) low-angle x-ray reflectivity of **film 3** with a composition of $Pb_{0.44(1)}Fe_{0.46(1)}Se_{1.00(2)}$, annealed in N_2 atmosphere to stepwise to 150°C. The tetragonal $Pb_{1-x}Fe_xSe$ phase is present up to 150°C with a and c-lattice parameters of 4.32(1) Å and 6.13(1) Å, respectively, however, there is an impurity phase present until it becomes minimal through annealing to 150°C, which is indicated by a ǂ. The initial phase decomposes at 200°C. The reflections can be indexed to a cubic phase with a lattice parameter of 6.119(3) Å, consistent with PbSe,[1] and a tetragonal structure with a and c-lattice parameters of 3.56(1) Å and 5.516 Å, respectively, consistent with tetragonal β-FeSe.[5]

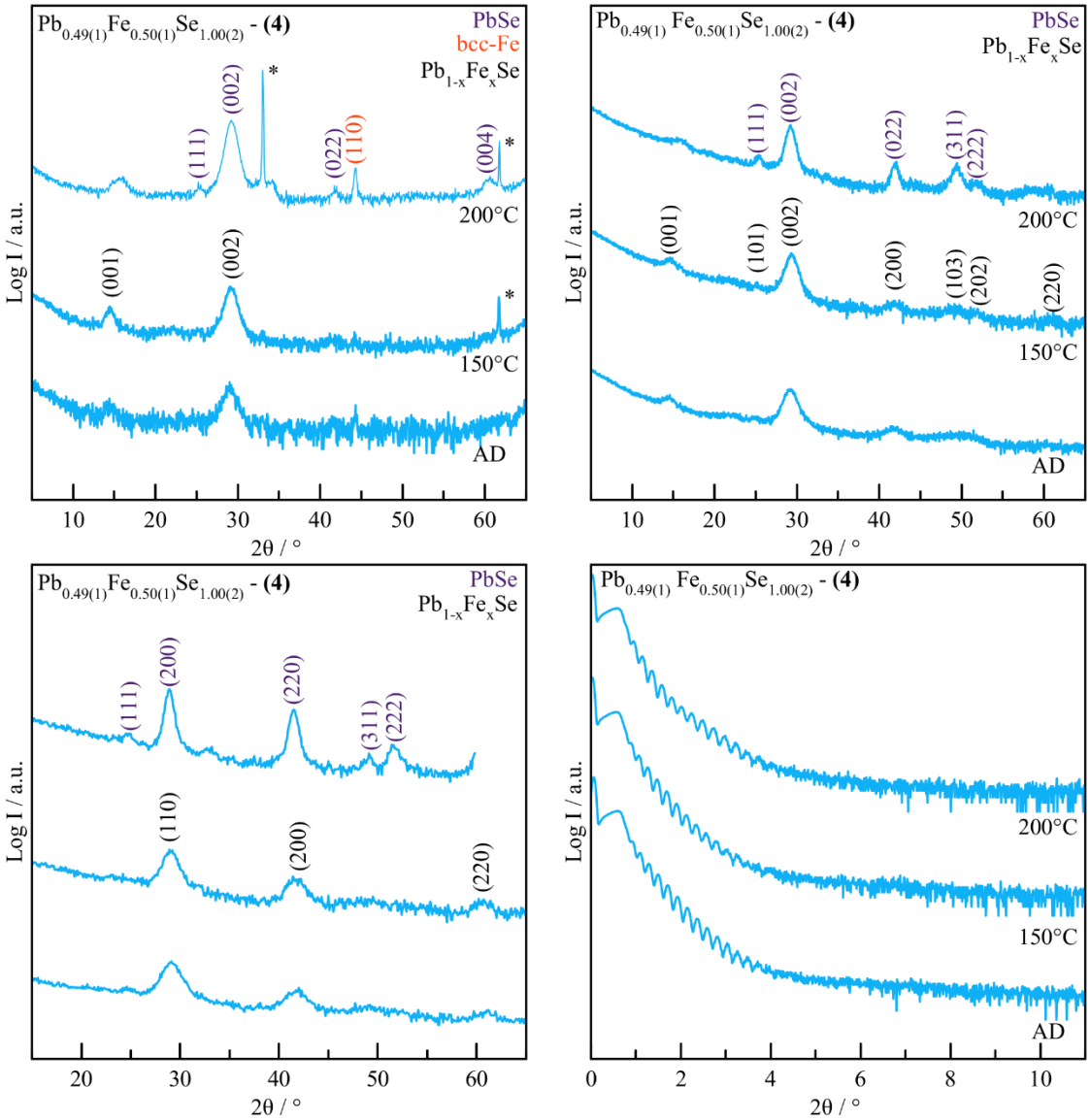

Fig. D.9. a) Specular locked-coupled, b) grazing-incidence, and c) in-plane grazing-incidence x-ray diffraction and d) low-angle x-ray reflectivity patterns of **film 4** with a composition of $Pb_{0.49(1)}Fe_{0.50(1)}Se_{1.00(2)}$, annealed in N_2 atmosphere to stepwise to 200°C. The tetragonal $Pb_{1-x}Fe_xSe$ phase is present up to 150°C with a and c-lattice parameters of 4.33(1) Å and 6.13(1) Å, respectively. The patterns at 200°C show reflections that can be indexed to a cubic phase with a lattice parameter of 6.125(1) Å, consistent with PbSe.[1] The remaining reflections could not be indexed to any known Fe_xSe_y compounds, although the decomposition of the initial phase is indicated by the shift of the (001) reflection to no longer index to the tetragonal unit cell.

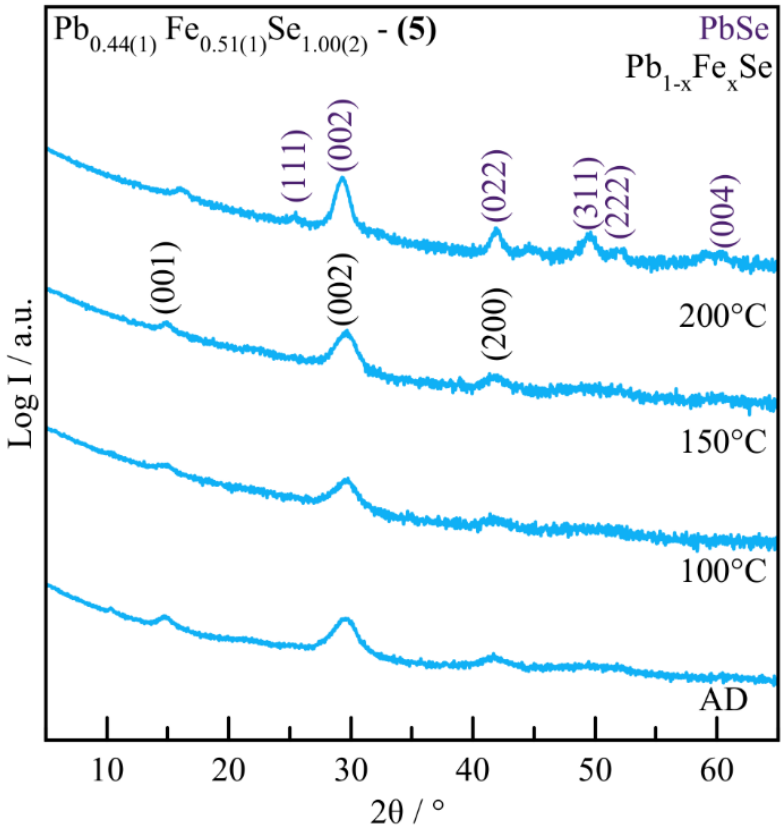

Fig. D.10. Grazing-incidence x-ray diffraction patterns of **film 5** with a composition of $Pb_{0.44(1)}Fe_{0.51(1)}Se_{1.00(2)}$, annealed in N_2 atmosphere to stepwise to 200°C. The tetragonal $Pb_{1-x}Fe_xSe$ phase is present up to 150°C with a and c-lattice parameters of 4.33(1) Å and 6.06(1) Å, respectively. The initial phase decomposes upon annealing to 200°C into binary phases. A cubic phase with a lattice parameter of 6.113(1) Å consistent with PbSe[1] is present, however, an iron selenide phase could not be identified. The other types of scans were not taken on this sample due to a limited amount of the sample, but the tetragonal phase and decomposition was still identified and characterized.

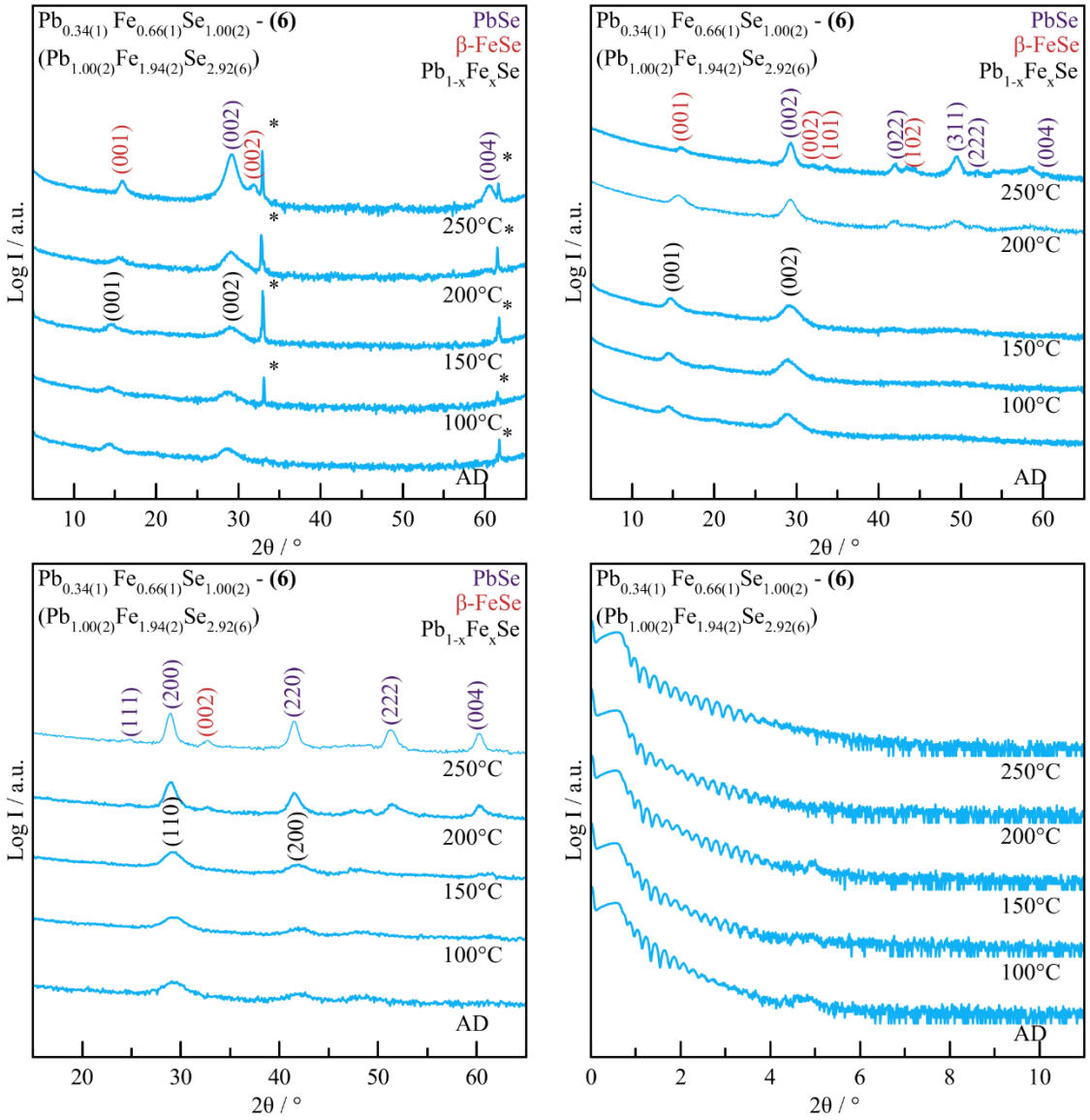

Fig. D.11. a) Specular locked-coupled, b) grazing-incidence, and c) in-plane grazing-incidence x-ray diffraction and d) low-angle x-ray reflectivity patterns of **film 6** with a composition of $Pb_{0.34(1)}Fe_{0.66(1)}Se_{1.00(2)}$, annealed in N_2 atmosphere to stepwise to 250°C. This sample is close to composition of the predicted phase $PbFe_2Se_3$[3], however there is no indication that it formed before breaking down to binary phases. The tetragonal $Pb_{1-x}Fe_xSe$ phase is present up to 150°C with a and c-lattice parameters of 4.38(1) Å and 6.06(1) Å, respectively. The patterns at 200°C show reflections that can be indexed to a cubic phase with a lattice parameter of 6.092(1) Å, consistent with PbSe.[1] Most of the remaining reflections can be indexed to a tetragonal unit cell with a and c-lattice parameters of 3.70(1) Å and 5.55(1), which is consistent with β-FeSe.[5]

APPENDIX E

SUPPORTING INFORMATION FOR CHAPTER IX

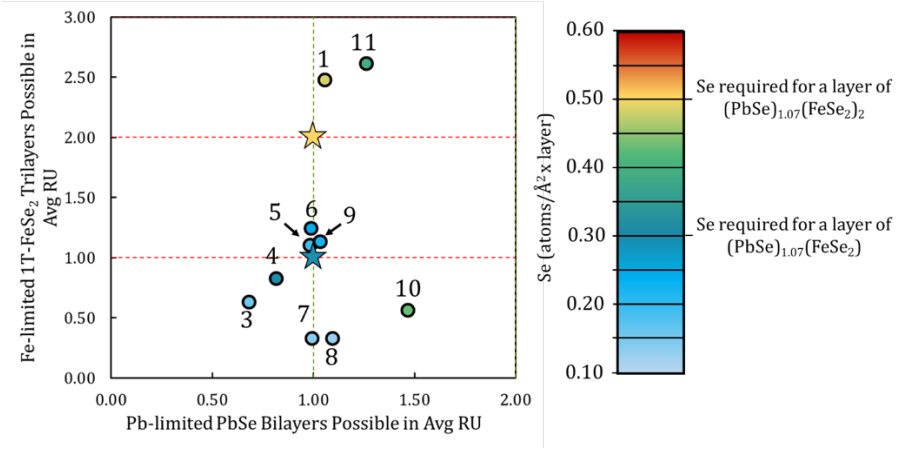

Fig. E.1. a) A three-dimensional representation of the composition of the precursors made in this study with respective sample numbers. The axes quantify the amount of Fe, Pb, and Se deposited per repeating sequence of layers normalized to that required per $FeSe_2$ or PbSe layer, respectively. The color of the points indicates the amount of Se deposited per layer. The stars show the estimated locations for $(PbSe)_{1.07}(FeSe_2)_1$ and $(PbSe)_{1.07}(FeSe_2)_2$ based on our calculations.

Table E.1. Description of sample **1** as a function of annealing including ternary composition relative to Pb content, total thickness of the film, comparison of c-lattice parameter of crystalline $(PbSe)_{1+\delta}(FeSe_2)_2$ to the layering thickness calculated via the first Bragg reflection in the x-ray reflectivity pattern, and lattice parameters of the constituents of the heterostructure. All thicknesses and lattice parameters are in Å.

Temp (°C)	**Ternary Comp.**	**Total Thick.**	**c-lattice**	**Layering Thick.**	**PbSe a-lattice**	**$FeSe_2$ a-lattice**
AD	$Pb_{1.00(1)}Fe_{2.44(2)}Se_{4.80(2)}$	379(2)	17.871(6)	18.61(3)	6.035(8)	3.42(1)
100	$Pb_{1.00(1)}Fe_{2.41(2)}Se_{4.80(2)}$	359(1)	17.824(3)	18.05(3)	6.052(3)	3.42(1)
200	$Pb_{1.00(1)}Fe_{2.46(2)}Se_{4.86(2)}$	337(4)	17.463(6)	17.59(4)	6.079(1)	3.447(4)
250	$Pb_{1.00(1)}Fe_{2.53(2)}Se_{4.89(2)}$	340(5)	17.086(6)	17.11(3)	6.130(2)	3.499(5)
300	$Pb_{1.00(1)}Fe_{2.39(2)}Se_{4.72(2)}$	320(6)	-	-	-	-

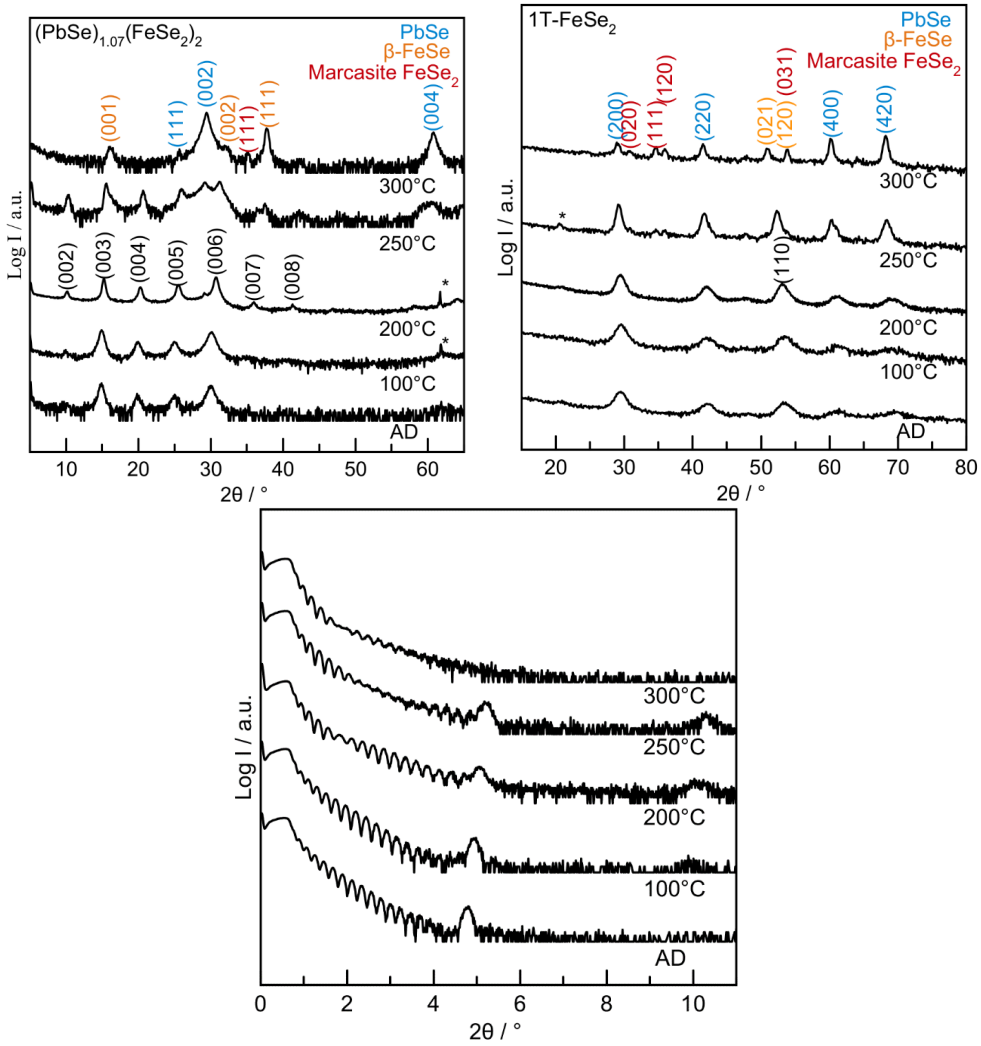

Fig. E.2. Specular (left), in-plane (right) x-ray diffraction, and x-ray reflectivity (bottom) patterns of the step-wise annealing study of sample **1**. The specular and in-plane diffraction patterns shows $(PbSe)_{1+\delta}(FeSe_2)_2$ persist until 300°C, where it decomposes into binary phases. The reflections at 300°C can be fit to a cubic structure with a lattice parameter of 6.128(1) Å, consistent with PbSe,[19] a tetragonal structure with an a-lattice parameter of 3.752(2) Å and c-lattice parameter of 5.594(3) Å consistent with β-FeSe,[20] and an orthorhombic structure with an a-lattice parameter of 4.775(1) Å, b-lattice parameter of 5.807(4) Å, and c-lattice parameter of 3.582(1) Å, consistent with marcasite-type $FeSe_2$.[21] The x-ray reflectivity patterns are consistent with the other two patterns, showing layering reflections until 300°C. In the specular patterns, a * indicates substrate reflections from Si/SiO_2. The in-plane pattern shows a forbidden reflection for face-centered cubic PbSe, indicated by a *, and is discussed in the manuscript.

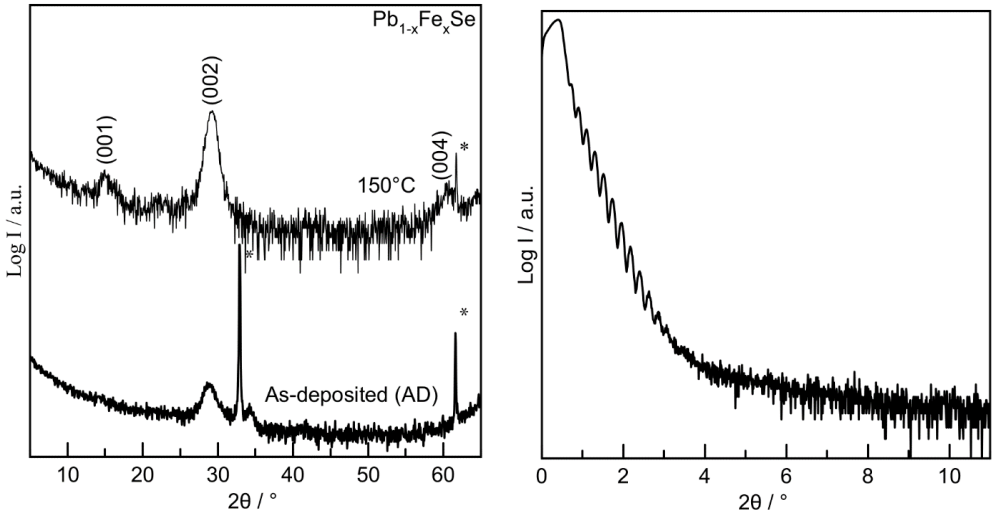

Fig. E.3. Specular x-ray diffraction (left) and x-ray reflectivity (right) patterns of sample **3** with a composition of $Pb_{1.00(1)}Fe_{0.86(1)}Se_{2.05(1)}$. The specular diffraction pattern at 150°C exhibits reflections consistent with tetragonal $Pb_{1-x}Fe_xSe$,[14] with a c-lattice parameter of 6.122(2) Å. Residual layering from the deposition is not observed in the XRR pattern indicated by the lack of a reflection in the XRR pattern. In the specular patterns, a * indicates substrate reflections from Si/SiO_2.

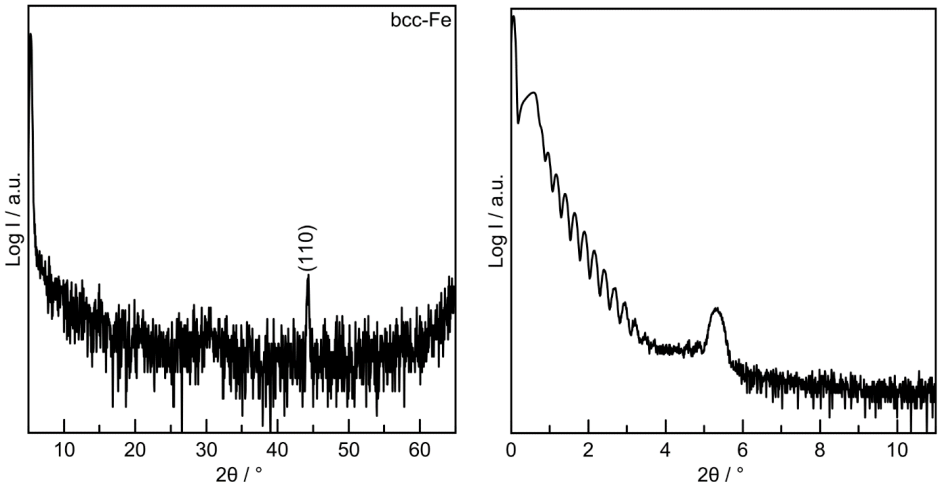

Figure S4: Specular x-ray diffraction (left) and x-ray reflectivity (right) patterns of sample **4** with a composition of $Pb_{1.00(1)}Fe_{0.94(1)}Se_{4.04\ (2)}$. The specular pattern shows a very broad reflection around 30° 2θ, although with the lack of other reflections is unable to be indexed. A reflection consistent with body-centered cubic (bcc) Fe is observed,[22] with a lattice parameter of 2.892(2) Residual layering from the deposition is seen in the XRR pattern, corresponding to a repeat thickness of ~16.5 Å.

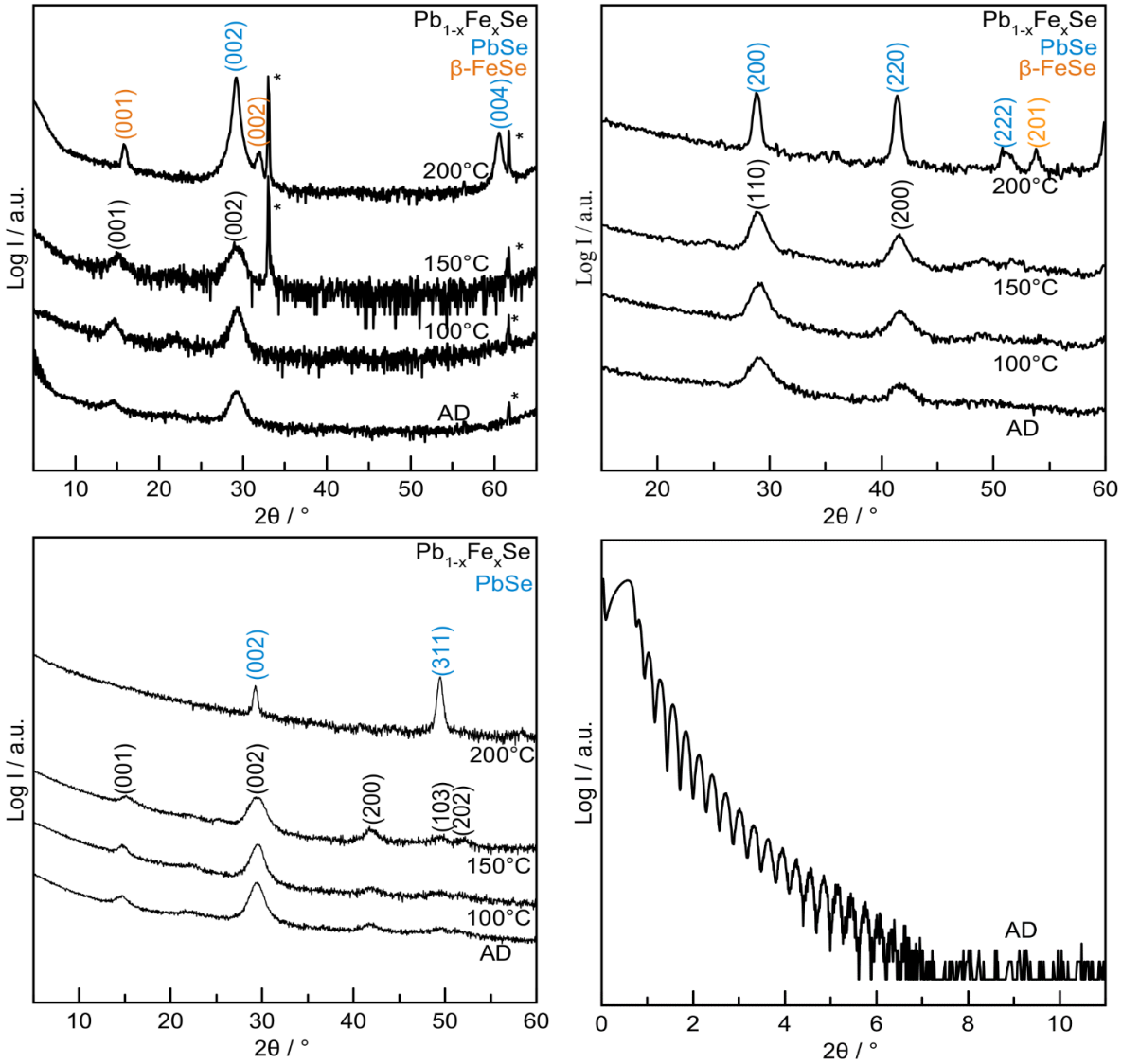

Fig. E.5. Specular (top-left), in-plane (top-right), grazing-incidence diffraction (bottom-left), and x-ray reflectivity (bottom-right) patterns of sample **5** with a composition of $Pb_{1.00(1)}Fe_{1.05(1))}Se_{2.30(1)}$. The XRR pattern shows no sign of residual layering. The specular, in-plane, and grazing-incidence patterns from show reflections consistent with tetragonal $Pb_{1-x}Fe_xSe$[14] with an a-lattice parameter of 4.321(4) Å and c-lattice parameter of 6.107(3) Å at 150°C. The initial phase decomposes after being annealed to 200°C, where the patterns show a cubic phase with a lattice parameter of 6.119(1) Å, consistent with PbSe,[23] and a tetragonal phase with an a-lattice parameter of 3.553(1) Å and c-lattice parameter of 5.519(2) Å, consistent with β-FeSe.. In the specular patterns, a * indicates substrate reflections from Si/SiO_2.

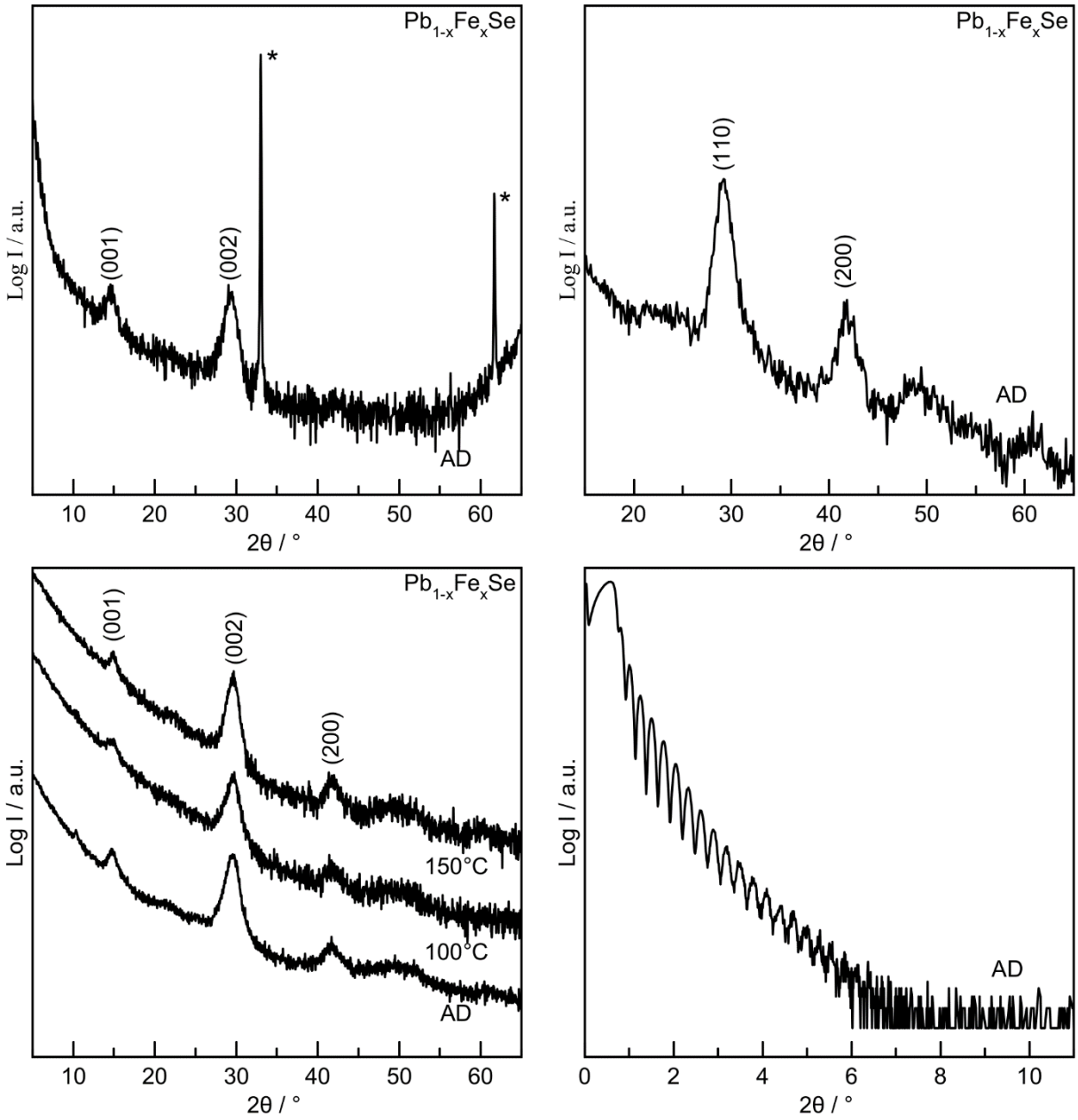

Fig. E.6. Specular (top-left), in-plane (top-right), grazing-incidence diffraction (bottom-left), and x-ray reflectivity (bottom-right) patterns of sample **6** with a composition of $Pb_{1.00(1)}Fe_{1.17(1))}Se_{2.29(1)}$. The XRR pattern show no sign of residual layering. The specular, in-plane, and grazing-incidence patterns from shows reflections consistent with tetragonal $Pb_{1-x}Fe_xSe$[14] with an a-lattice parameter of 4.34(2) Å and c-lattice parameter of 6.13(2) Å after deposition. In the specular patterns, a * indicates substrate reflections from Si/SiO_2.

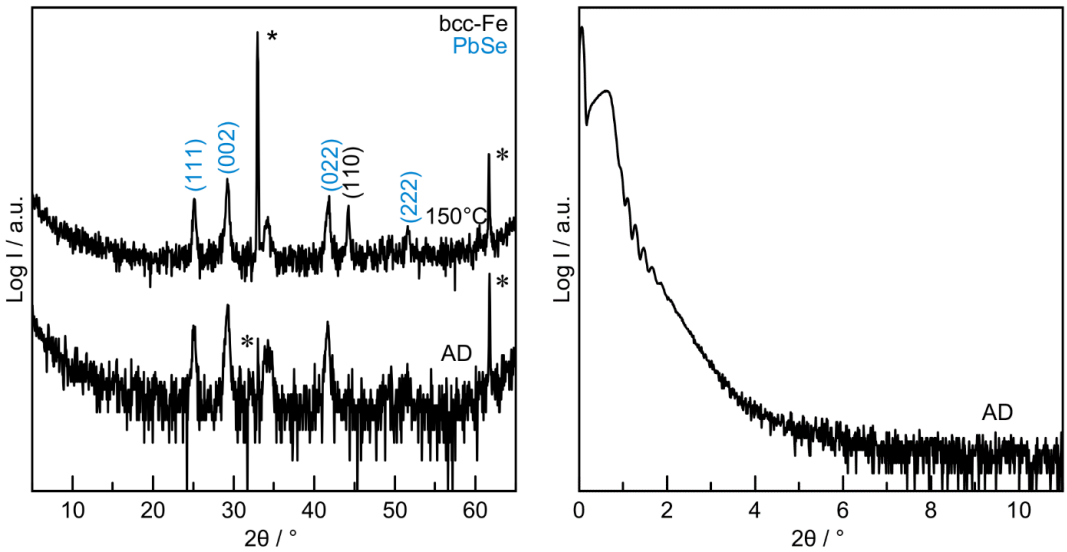

Fig. E.7. Specular (left) diffraction and x-ray reflectivity (right) patterns of sample **7** with a composition of $Pb_{1.00(1)}Fe_{0.31(1)}Se_{1.25(1)}$. The XRR pattern shows no sign of residual layering. The specular pattern shows reflections consistent with a cubic structure with a lattice parameter of 6.117(3) Å, consistent with PbSe.[23] A reflection consistent with bcc-Fe is also observed, with a lattice parameter of 2.895(1) Å.[22] In the specular patterns, a * indicates substrate reflections from Si/SiO_2.

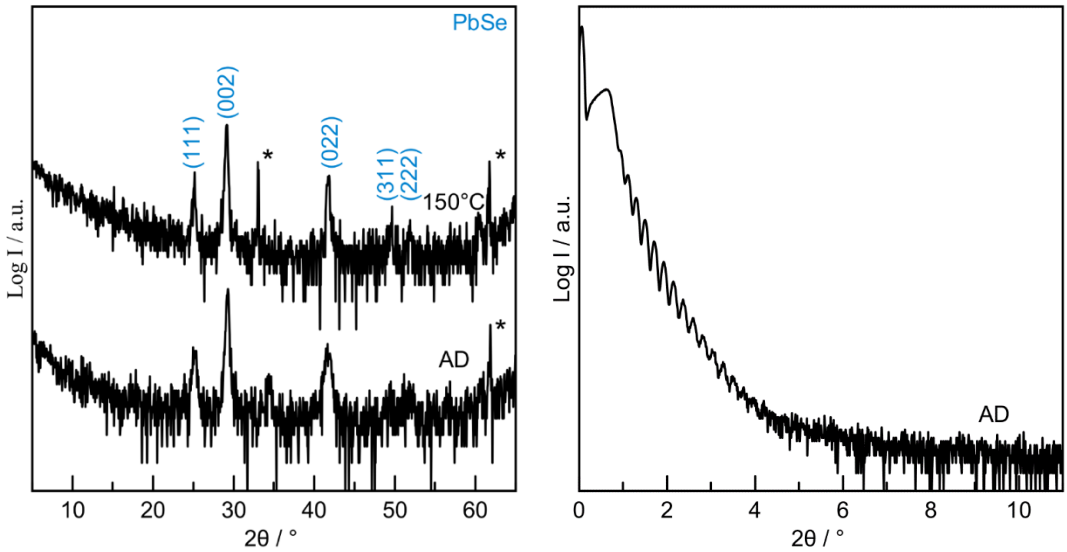

Fig. E.8. Specular (left) diffraction and x-ray reflectivity (right) patterns of sample **8** with a composition of $Pb_{1.00(1)}Fe_{0.28(1)}Se_{1.07(1)}$. The XRR pattern shows no sign of residual layering. The specular pattern shows reflections consistent with a cubic structure with a lattice parameter of 6.129(2) Å, consistent with PbSe.[24] In the specular patterns, a * indicates substrate reflections from Si/SiO_2.

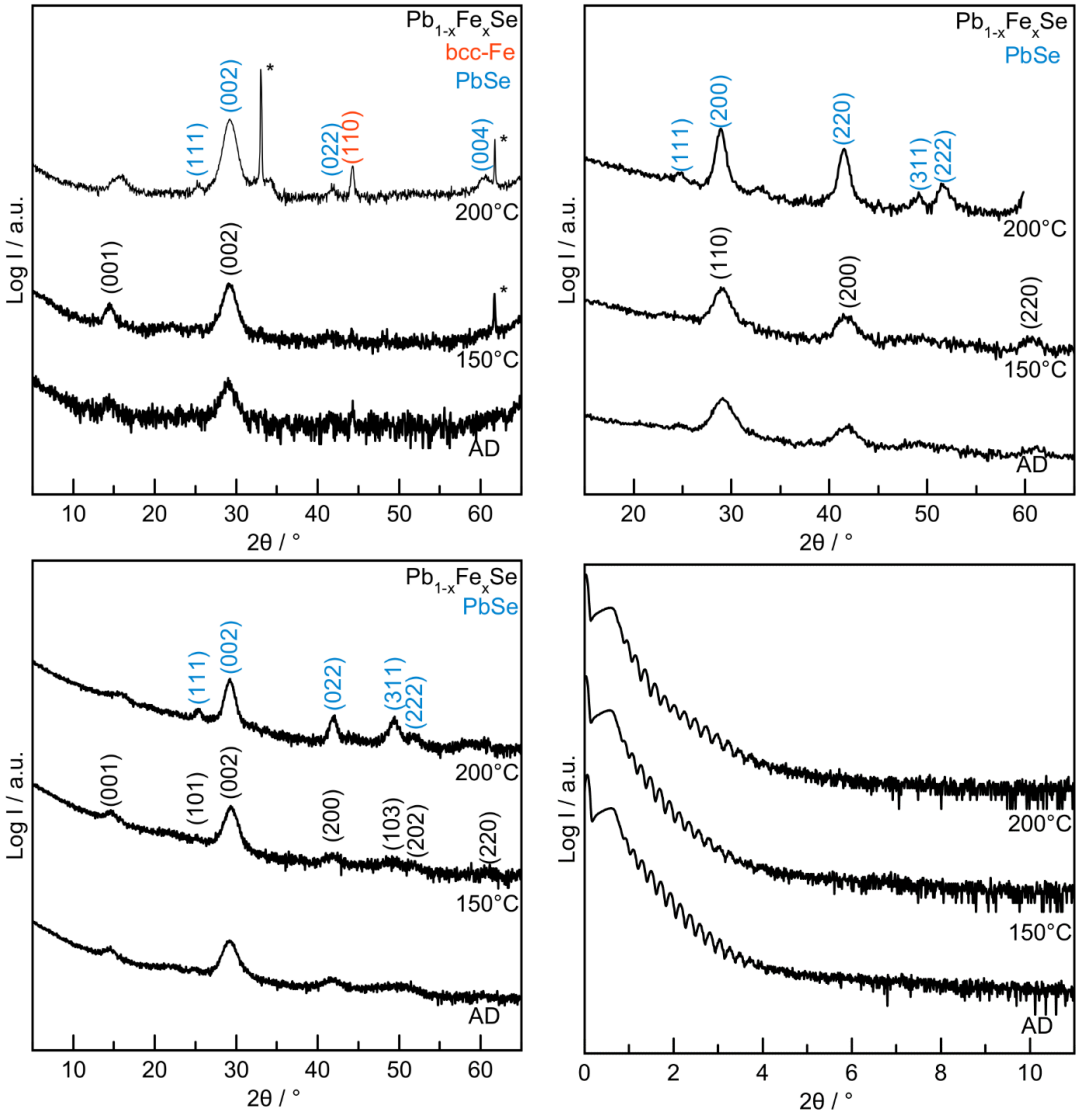

Fig. E.9. Specular (top-left), in-plane (top-right), grazing-incidence diffraction (bottom-left), and x-ray reflectivity (bottom-right) patterns of sample **9** with a composition of $Pb_{1.00(1)}Fe_{1.02(1)}Se_{2.04(1)}$. The XRR patterns shows no sign of residual layering. The specular, in-plane, and grazing-incidence patterns show reflections consistent with a tetragonal structure with an a-lattice parameter of 4.33(1) Å and a c-lattice parameter of 6.13(1) Å that persists up to annealing to 150°C, consistent with $Pb_{1-x}Fe_xSe$.[14] The initial phase decomposes after annealing to 200°C. The patterns exhibit reflections corresponding to a cubic phase with a lattice parameter of 6.125(1) Å, consistent with PbSe.[19] The remaining reflections could not be indexed to any know iron selenide compound, however the reflection around 16° 2θ does not correspond to any other reflections. In the specular patterns, a * indicates substrate reflections from Si/SiO_2.

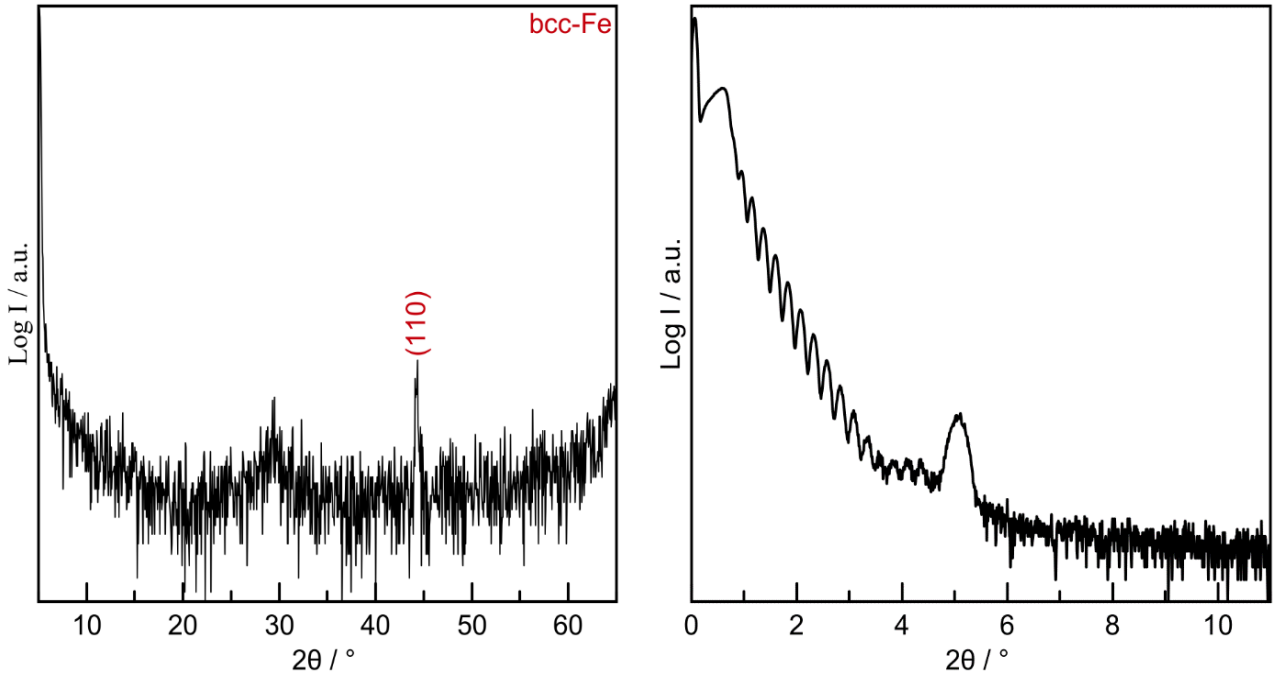

Fig. E.10. Specular x-ray diffraction (left) and x-ray reflectivity (right) patterns of sample **10** with a composition of $Pb_{1.00(1)}Fe_{0.36(1)}Se_{2.75(2)}$. The specular pattern shows a very broad reflection around 30° 2θ, although with the lack of other reflections is unable to be indexed. A reflection consistent with body-centered cubic (bcc) Fe is observed,[22] with a lattice parameter of 2.891(3) Å. Residual layering from the deposition is seen in the XRR pattern, corresponding to a repeat thickness of ~17.8 Å.

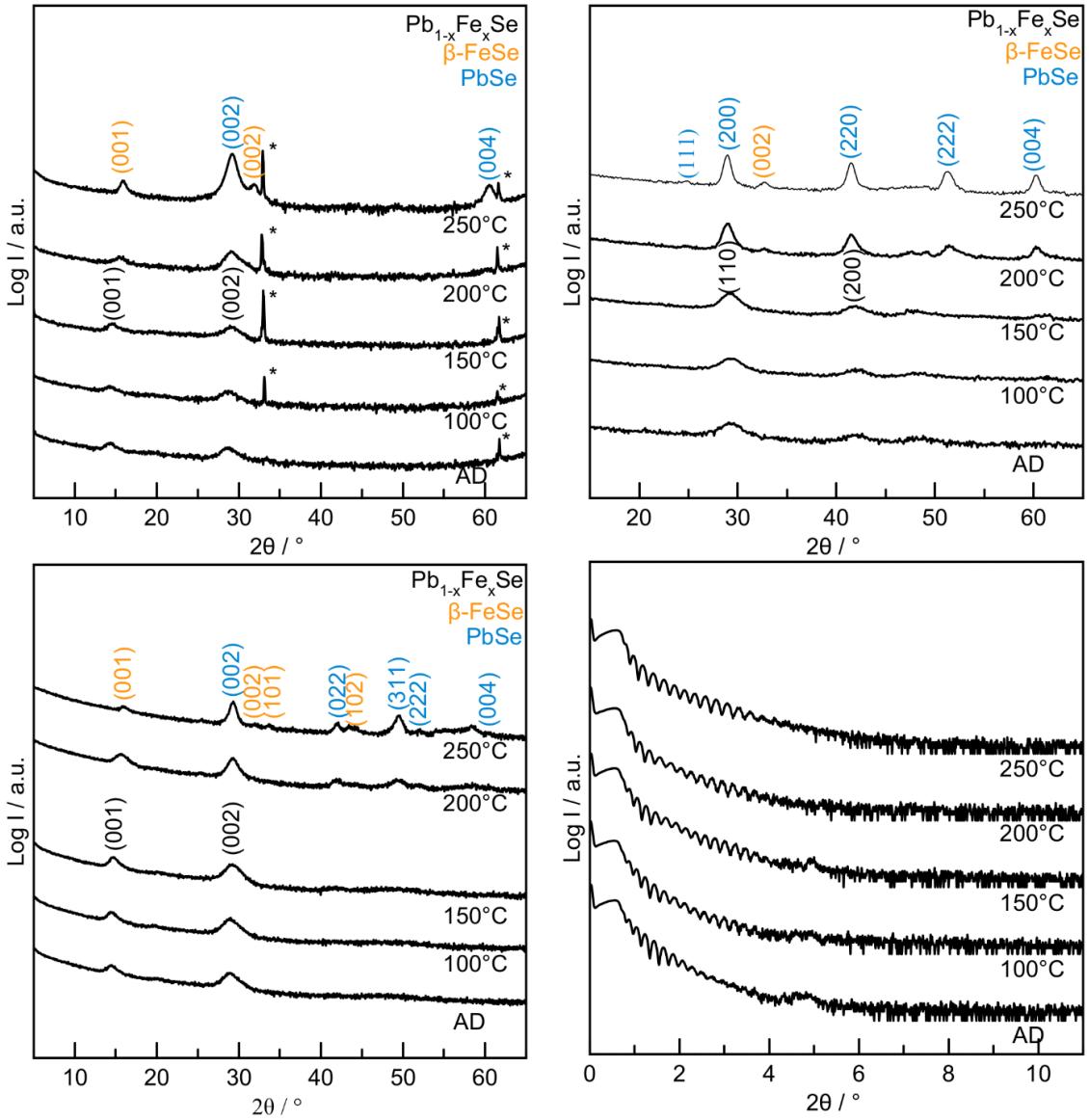

Fig. E.11. Specular (top-left), in-plane (top-right), grazing-incidence diffraction (bottom-left), and x-ray reflectivity (bottom-right) patterns of sample **11** with a composition of $Pb_{1.00(1)}Fe_{1.94(2)}Se_{2.92(1)}$. The XRR pattern shows no sign of residual layering. The specular, in-plane, and grazing-incidence patterns from show reflections consistent with tetragonal $Pb_{1-x}Fe_xSe$,[14] with an a-lattice parameter of 4.38(1) Å and c-lattice parameter of 6.06(1) Å at 150°C. The initial phase decomposes after being annealed to 200°C, where the patterns show a cubic phase with a lattice parameter of 6.092(1) Å, consistent with PbSe,[25] and a tetragonal phase with an a-lattice parameter of 3.70(1) Å and c-lattice parameter of 5.55(2) Å, consistent with β-FeSe.[20] In the specular patterns, a * indicates substrate reflections from Si/SiO_2.

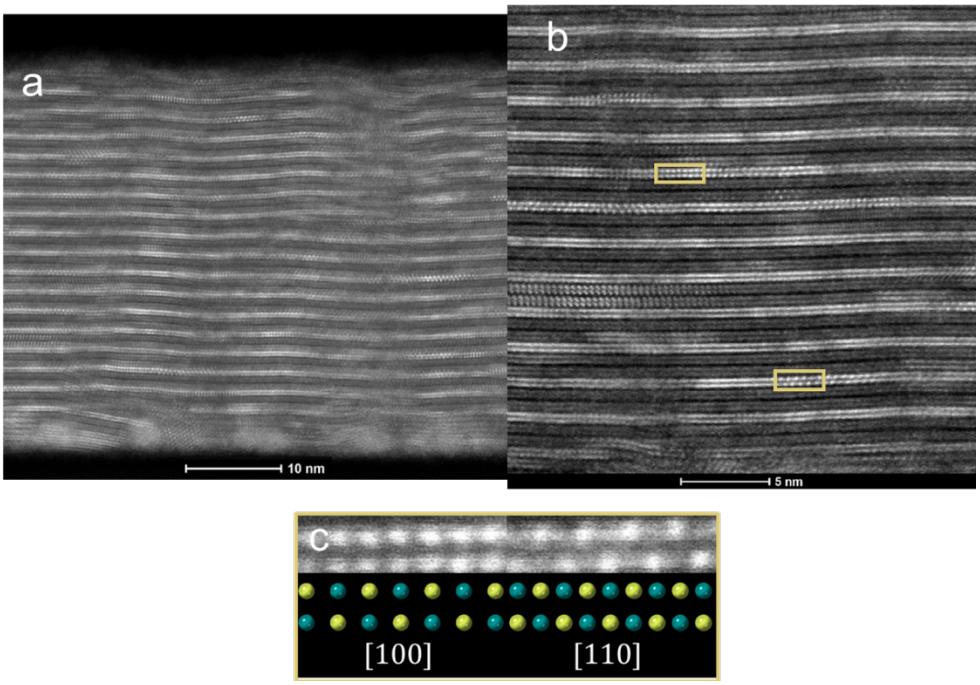

Fig. E.12. a) Top-to-bottom and b) zoomed cross-sectional high-angle annular dark field scanning transmission electron microscopy (HAADF-STEM) images of sample **1** annealed at 100°C for 15 minutes. c) Observed zone axes of the $Pb_{1-x}Fe_xSe$ layer. The yellow atoms and green atoms represent Pb and Se, respectively.

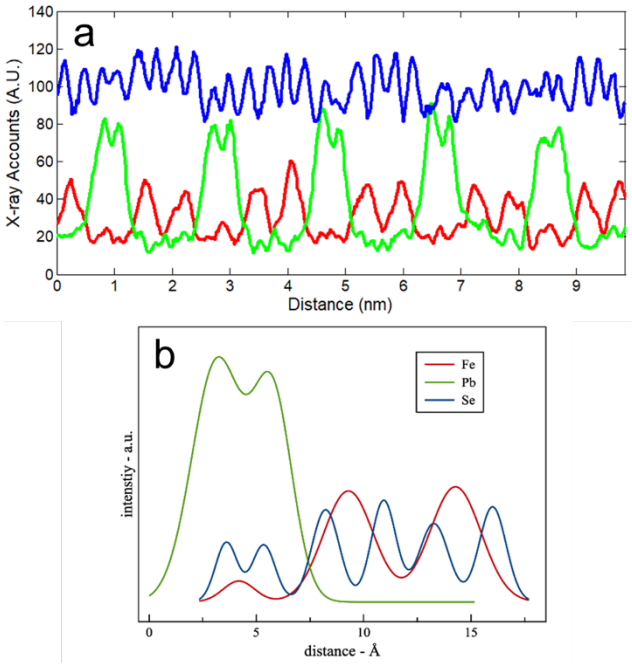

Fig. E.13. a) Raw and b) average energy dispersive spectroscopy (EDS) intensity profiles of sample **1** annealed at 100°C for 15 minutes.

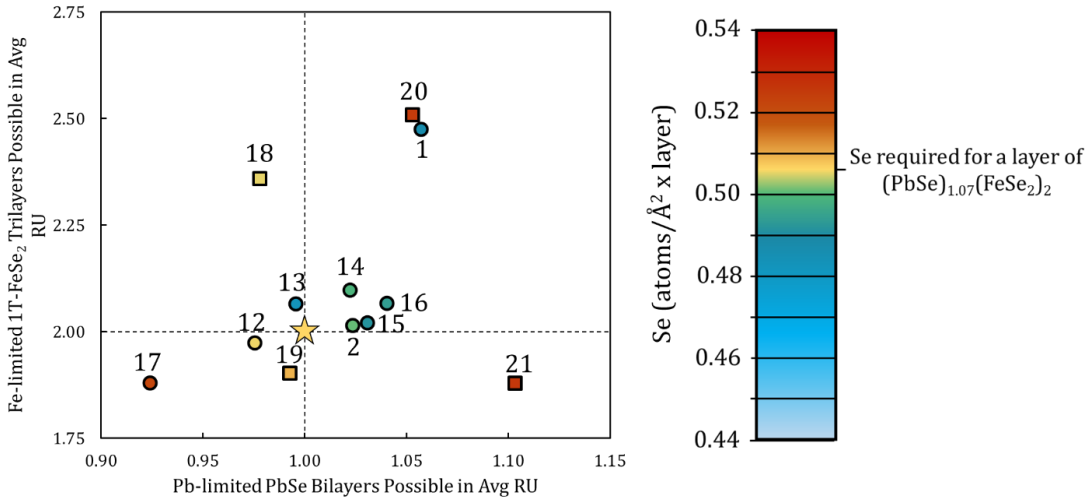

Fig. E.14. a) A three-dimensional representation of the composition of the precursors made in this study with respective sample numbers. The axes quantify the amount of Fe, Pb, and Se deposited per repeating sequence of layers normalized to that required per $FeSe_2$ or PbSe layer, respectively. The color of the points indicates the amount of Se deposited per layer. The star shows the estimated location for $(PbSe)_{1.07}(FeSe_2)_2$ based on our calculations. The circles represent samples that show crystalline layers before annealing, indicated in the specular reflections. The squares represent samples that show no crystalline layers before annealing, and form heterostructures with defects after annealing.

Table E.2. Description of sample **2** as a function of annealing including ternary composition relative to Pb content, total thickness of the film, comparison of c-lattice parameter of crystalline $(PbSe)_{1+\delta}(FeSe_2)_2$ to the layering thickness calculated via the first Bragg reflection in the x-ray reflectivity pattern, and lattice parameters of the constituents of the heterostructure. All thicknesses and lattice parameters are in Å.

Temp (°C)	Ternary Composition	Total Thickness	c-lattice	Layering Thickness	PbSe a-lattice	$FeSe_2$ a-lattice
AD	$Pb_{1.00(1)}Fe_{1.97(2)}Se_{4.90(2)}$	362(2)	17.991(6)	18.61(3)	6.08(1)	3.38(2)
100	$Pb_{1.00(1)}Fe_{1.97(2}Se_{4.97(2)}$	369(4)	17.935(5)	18.05(3)	6.104(6)	3.40(3)
150	$Pb_{1.00(1)}Fe_{1.97(2)}Se_{5.10(2)}$	336(5)	17.706(2)	17.59(4)	6.100(5)	3.40(1)
200	$Pb_{1.00(1)}Fe_{1.92(2)}Se_{5.02(2)}$	339(4)	17.618(2)	17.11(3)	6.118(3)	3.40(1)

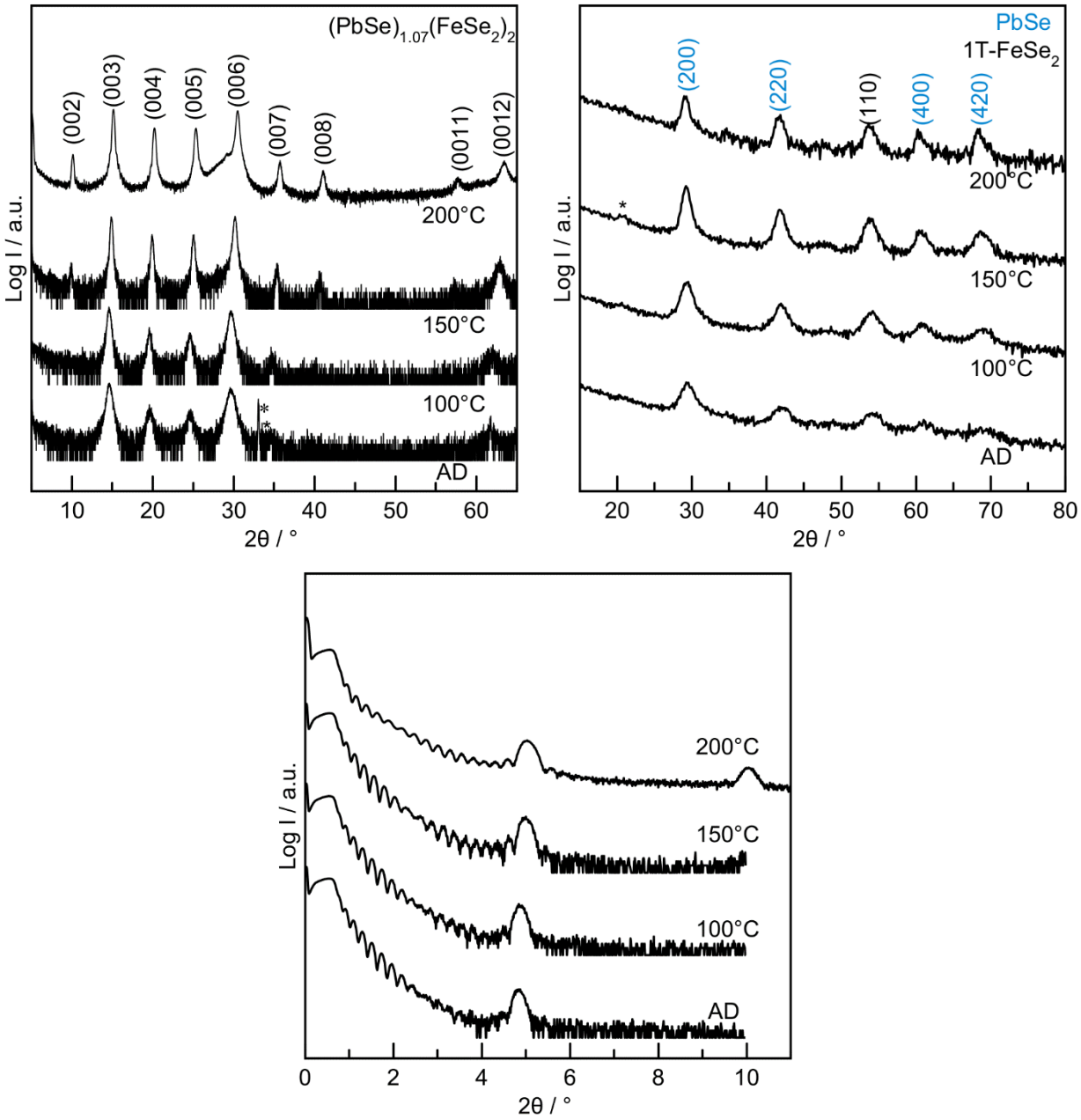

Fig. E.15. Specular (left), in-plane (right) x-ray diffraction, and x-ray reflectivity (bottom) patterns of the step-wise annealing study of sample **2**. The specular and in-plane diffraction patterns shows $(PbSe)_{1+\delta}(FeSe_2)_2$ persist until 200°C, where it decomposes into binary phases. The x-ray reflectivity patterns are consistent with the other two patterns, showing layering reflections until 200°C. In the specular patterns, a * indicates substrate reflections from Si/SiO_2. The in-plane pattern shows a forbidden reflection for face-centered cubic PbSe, indicated by a *, and is discussed in the manuscript. The lattice parameters of the heterostructure can be found in Table S2.

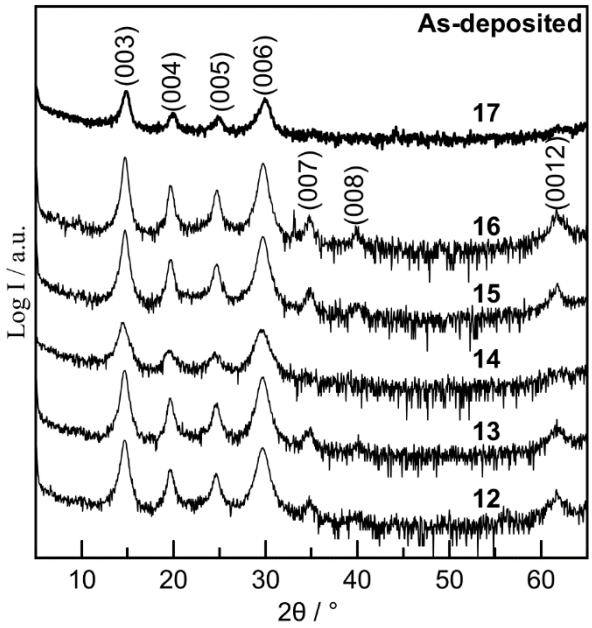

Fig. E.16. Specular x-ray diffraction patterns of samples **12-17** after deposition. In addition to samples 1 and 2, all 6 above showed crystalline layers before annealing. The samples are assumed to act similarly to sample **1** and **2** after annealing.

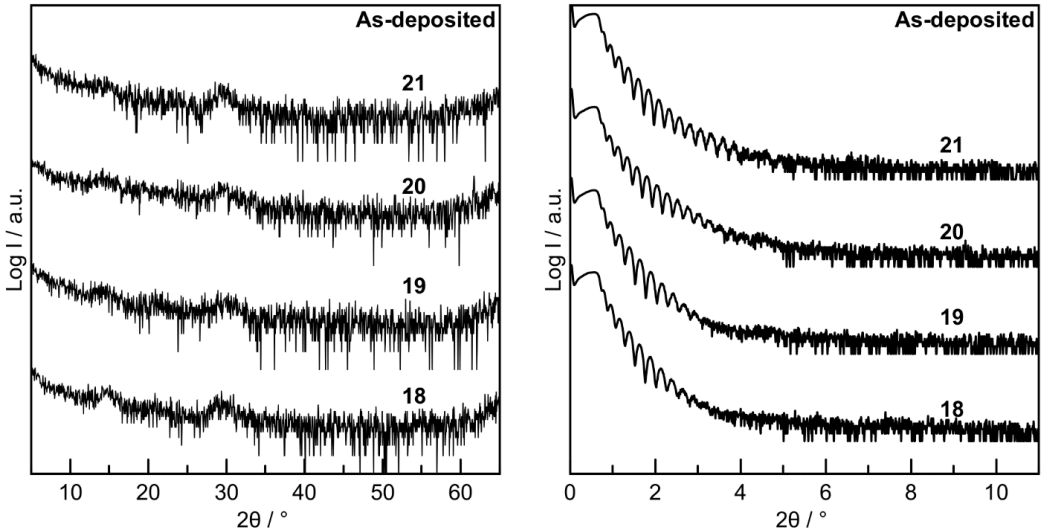

Fig. E.17. Specular x-ray diffraction (left) and x-ray reflectivity (right) patterns of samples **18-21** after deposition. These samples show little to no crystalline reflections in the specular diffraction pattern. Additionally, little to no layering from the initial deposition is present after the deposition indicated by the lack of reflections in the XRR pattern.

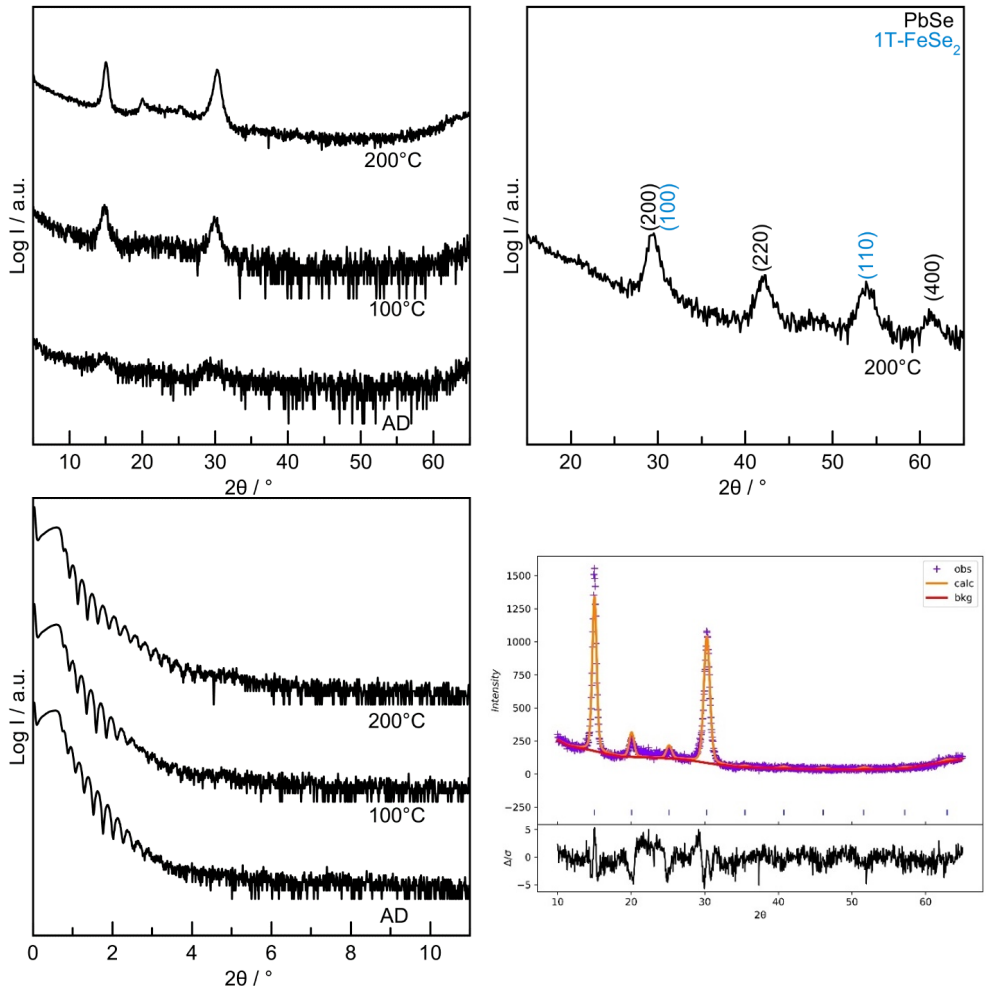

Fig. E.18. Specular (left), in-plane (top-right) x-ray diffraction (top-left), x-ray reflectivity (bottom-left), and Lebail refinement of the sample after annealing at 200°C (bottom-right) of sample **18** as a function of annealing stepwise to 200°C. The sample shows little to no crystalline layering upon deposition, followed by the growth of two strong reflections after annealing at 200°C. The four reflections are related by a c-lattice parameter of 17.71(1) Å, although likely contains less symmetry throughout the film in comparison to the samples that crystallized upon deposition. The in-place pattern after annealing to 200°C contains a cubic structure with a lattice parameter of 6.09(1) Å, consistent with PbSe,[25] and a hexagonal structure with an a-lattice parameter of 3.40(2) Å, consistent with previously discussed 1T-$FeSe_2$.

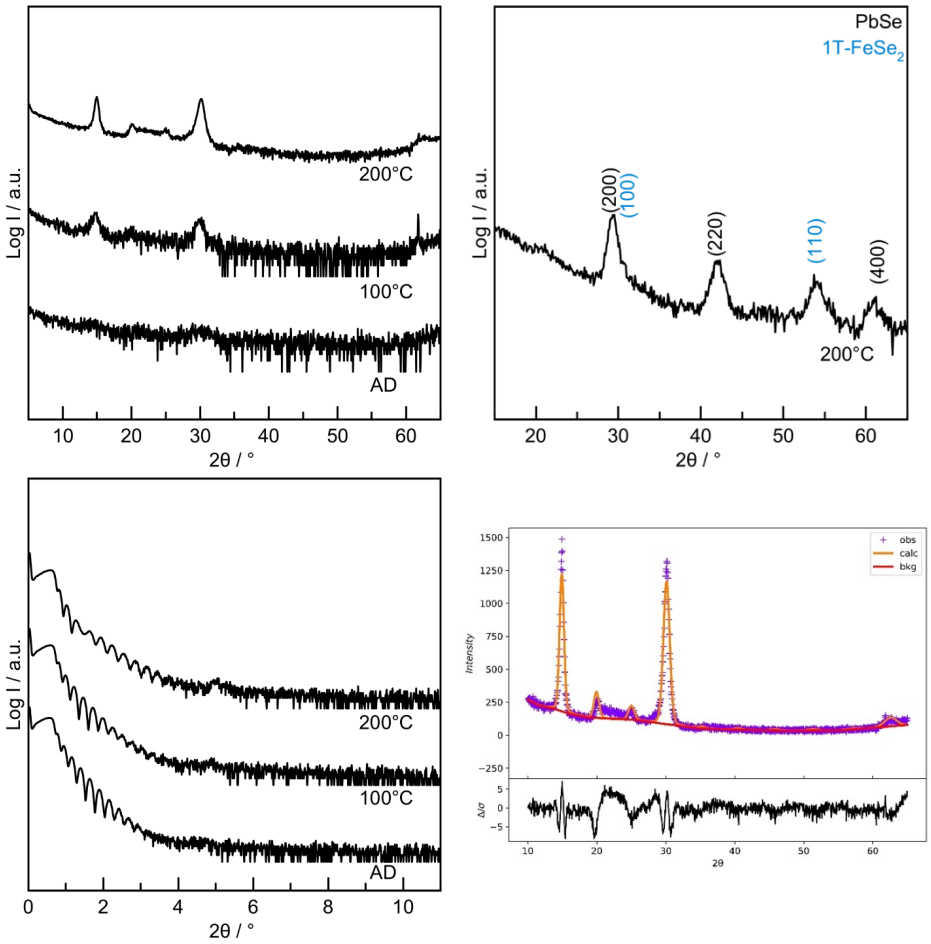

Fig. E.19. Specular (left), in-plane (top-right) x-ray diffraction (top-left), x-ray reflectivity (bottom-left), and Lebail refinement of the sample after annealing at 200°C (bottom-right) of sample **19** as a function of annealing stepwise to 200°C. The sample shows little to no crystalline layering upon deposition, followed by the growth of two strong reflections after annealing at 200°C. The four reflections are related by a c-lattice parameter of 17.81(1) Å, although likely contains less symmetry throughout the film in comparison to the samples that crystallized upon deposition. The in-place pattern after annealing to 200°C contains a cubic structure with a lattice parameter of 6.08(2) Å, consistent with PbSe,[25] and a hexagonal structure with an a-lattice parameter of 3.39(4) Å, consistent with previously discussed 1T-$FeSe_2$.

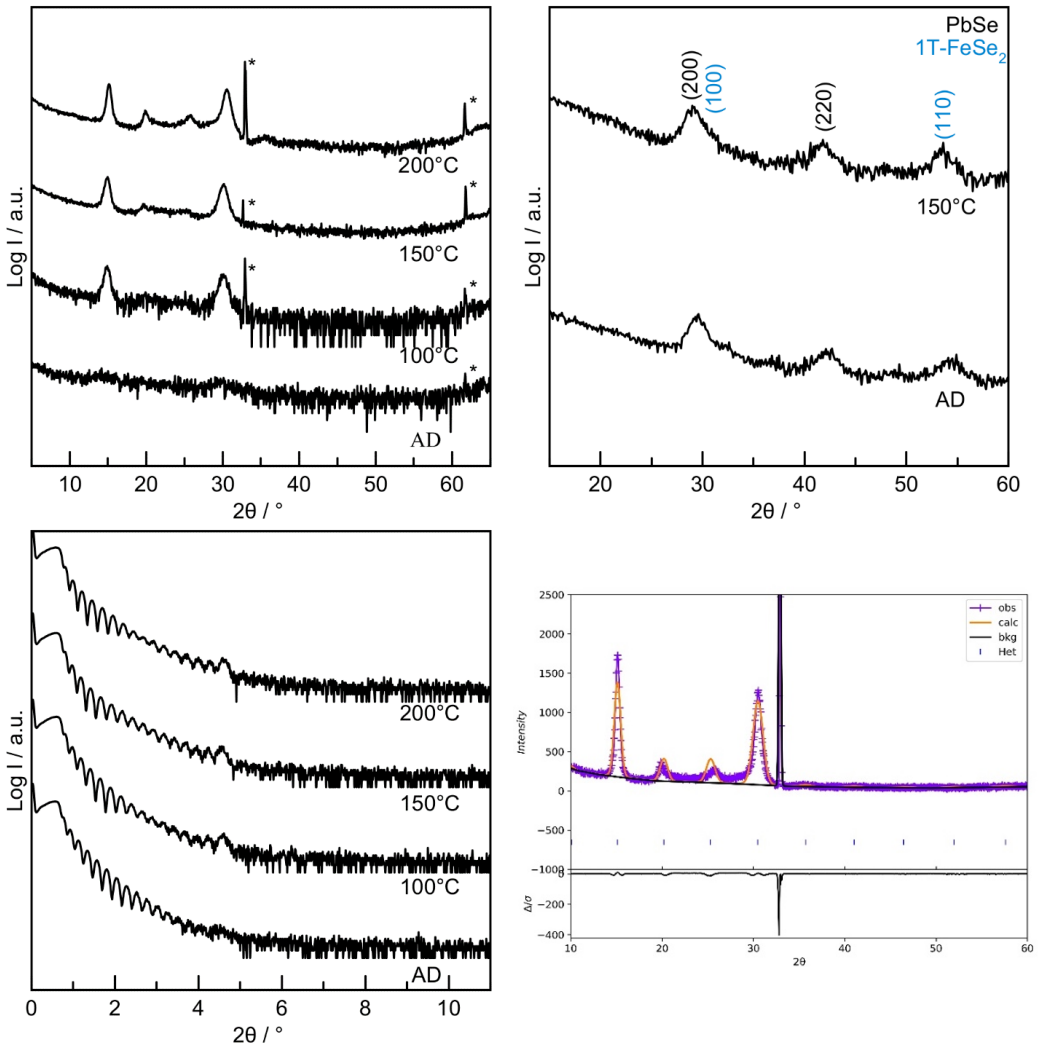

Fig. E.20. Specular (left), in-plane (top-right) x-ray diffraction (top-left), x-ray reflectivity (bottom-left), and Lebail refinement of the sample after annealing at 200°C (bottom-right) of sample **20** as a function of annealing stepwise to 200°C. The sample shows little to no crystalline layering upon deposition, followed by the growth of two strong reflections after annealing at 200°C. The four reflections are related by a c-lattice parameter of 17.58(3) Å, although likely contains less symmetry throughout the film in comparison to the samples that crystallized upon deposition. The in-place pattern after annealing to 200°C contains a cubic structure with a lattice parameter of 6.10(1) Å, consistent with PbSe,[25] and a hexagonal structure with an a-lattice parameter of 3.42(2) Å, consistent with previously discussed 1T-$FeSe_2$.

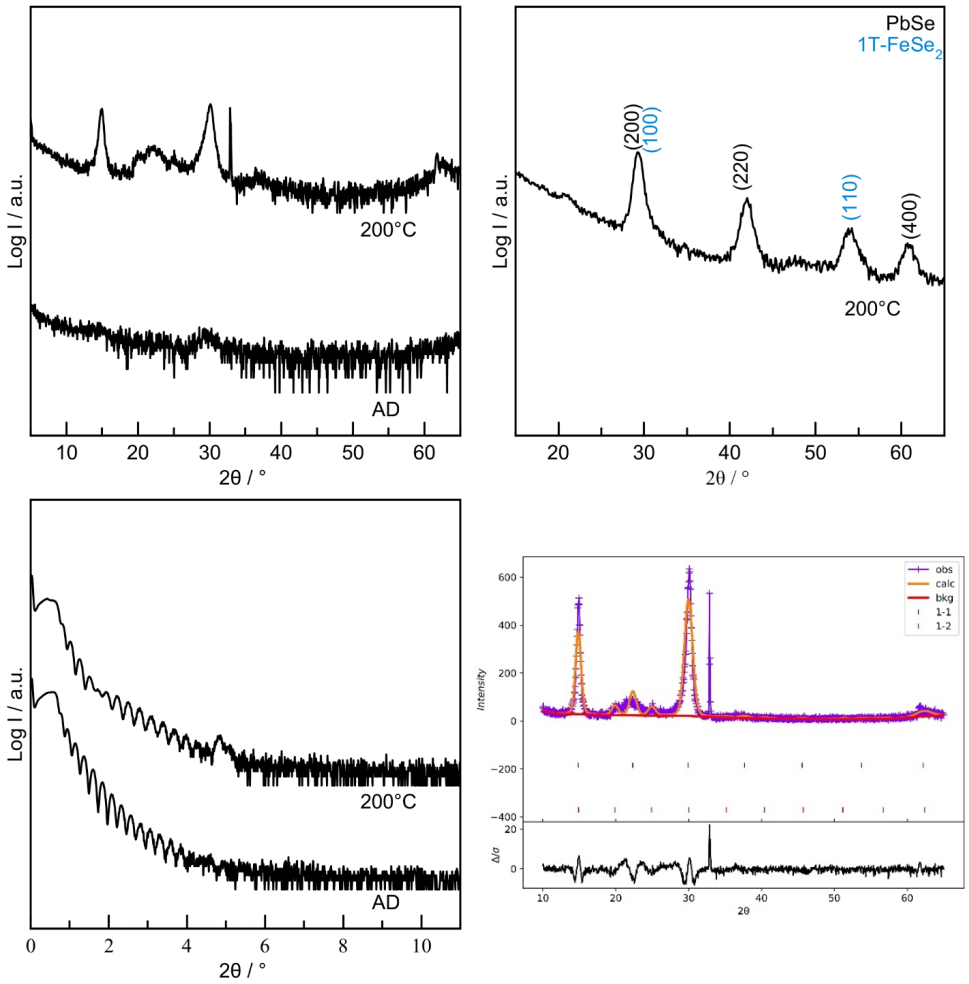

Fig. E.21. Specular (left), in-plane (top-right) x-ray diffraction (top-left), x-ray reflectivity (bottom-left), and Lebail refinement of the sample after annealing at 200°C (bottom-right) of sample **21** as a function of annealing to 200°C. The sample shows little to no crystalline layering upon deposition, followed by the growth of three reflections after annealing. Interestingly, the specular can be fit to two different c-lattice parameters of 17.84(3) Å and 11.93(1) Å, possibly indicating the formation of both $(PbSe)_{1+\delta}(FeSe_2)$ and $(PbSe)_{1+\delta}(FeSe_2)_2$. The in-place pattern after annealing to 200°C contains a cubic structure with a lattice parameter of 6.08(1) Å, consistent with PbSe,[25] and a hexagonal structure with an a-lattice parameter of 3.42(2) Å, consistent with previously discussed 1T-$FeSe_2$.

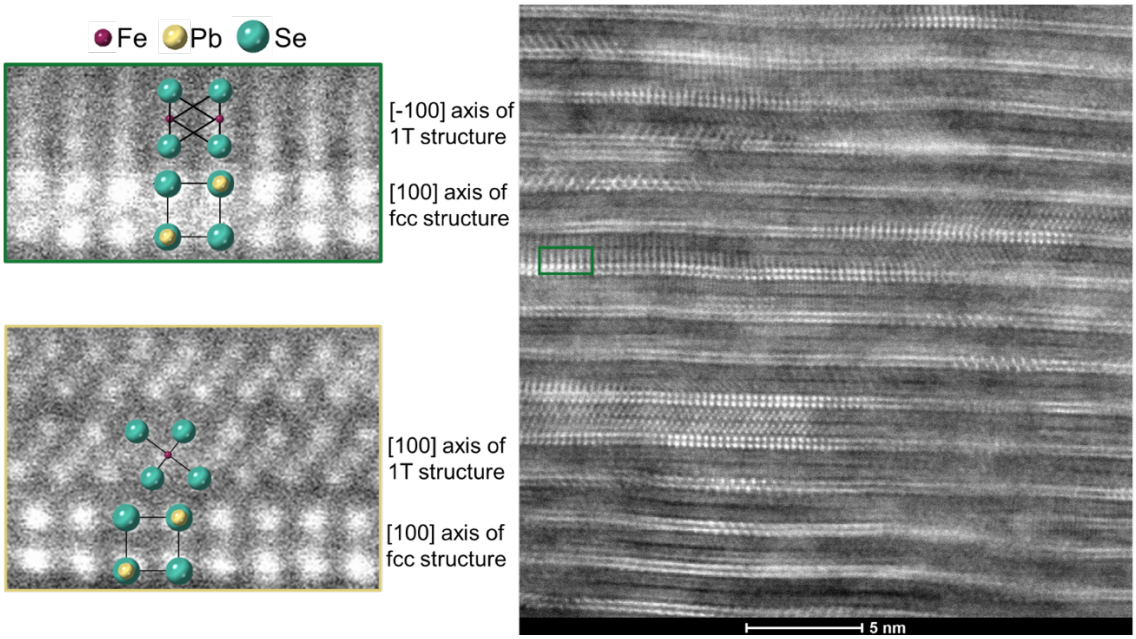

Fig. E.22. Another high-angle annual dark field scanning transmission electron microscope (HAADF-STEM) image of a cross section of sample **2**. Multiple zone axes of the film are shown on the left.

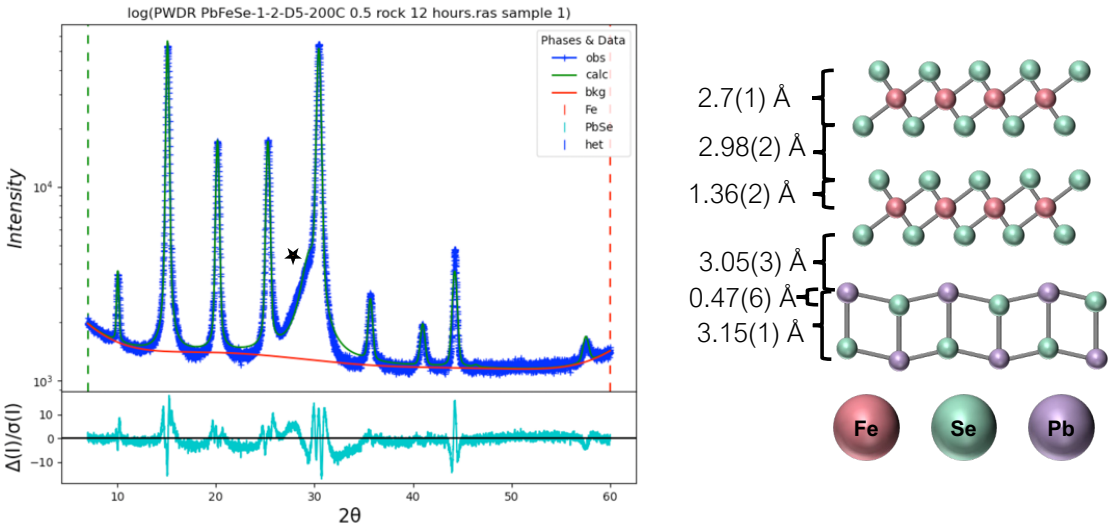

Fig. E.23. A representative Rietveld refinement of the specular XRD data (left) for sample 2 after annealing at 200°C. The peak marked with an orange star is due to PbSe and the peak marked with a yellow star is due to Fe. Interatomic plane distances determined from the refinement are shown on the right.

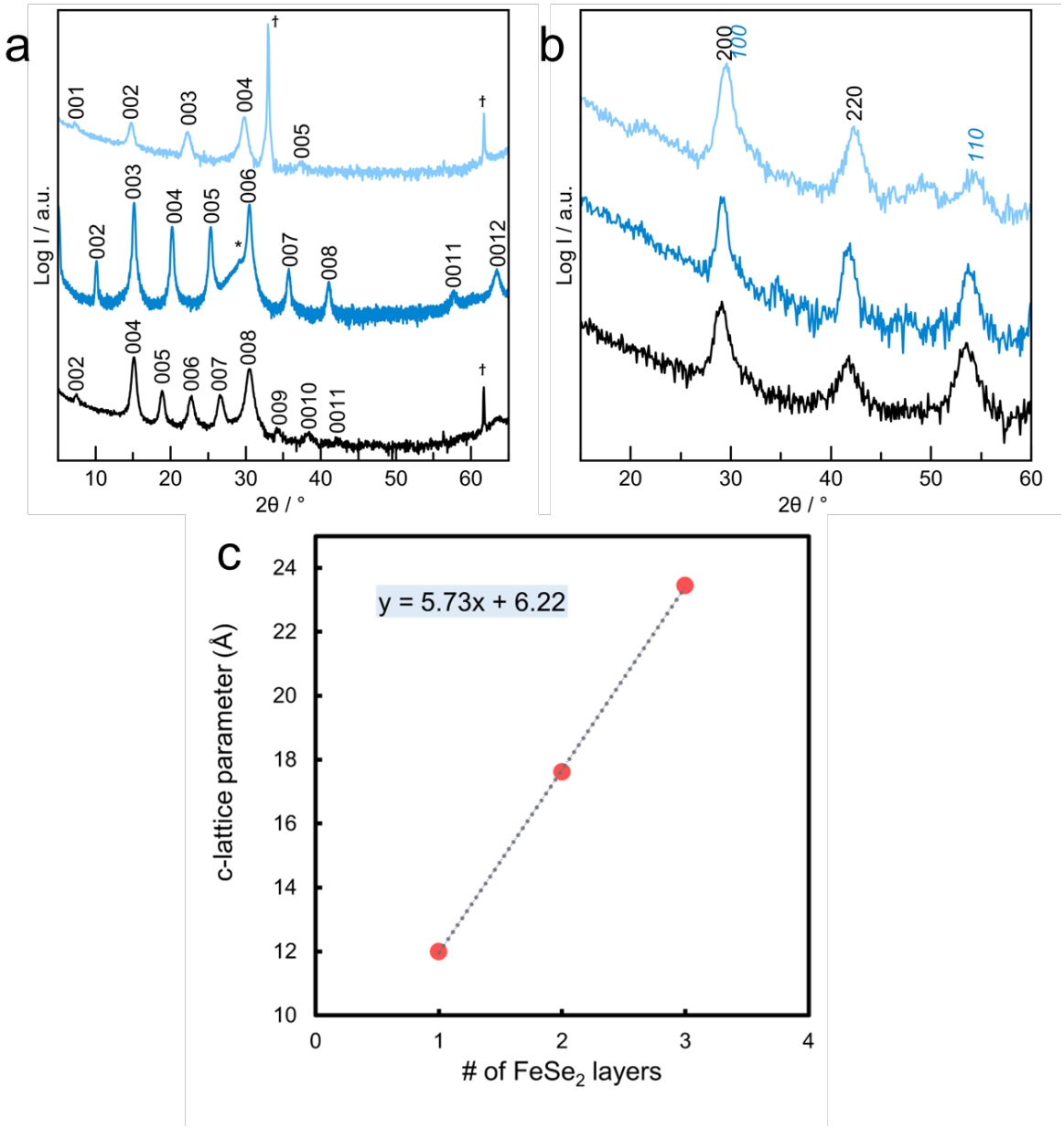

Fig. E.24. (a) Specular X-ray diffraction and (b) in-plane X-ray diffraction of samples with target structures of $(PbSe)_{1+\delta}(FeSe_2)$ (turquoise), $(PbSe)_{1+\delta}(FeSe_2)_2$ (blue, sample 2), and $(PbSe)_{1+\delta}(FeSe_2)_3$ (black) annealed at 200°C for 15 minutes in N_2 atmosphere. A plot of the c-lattice parameters versus number of $FeSe_2$ layers is displayed in (c).

APPENDIX F

SUPPORTING INFORMATION FOR CHAPTER X

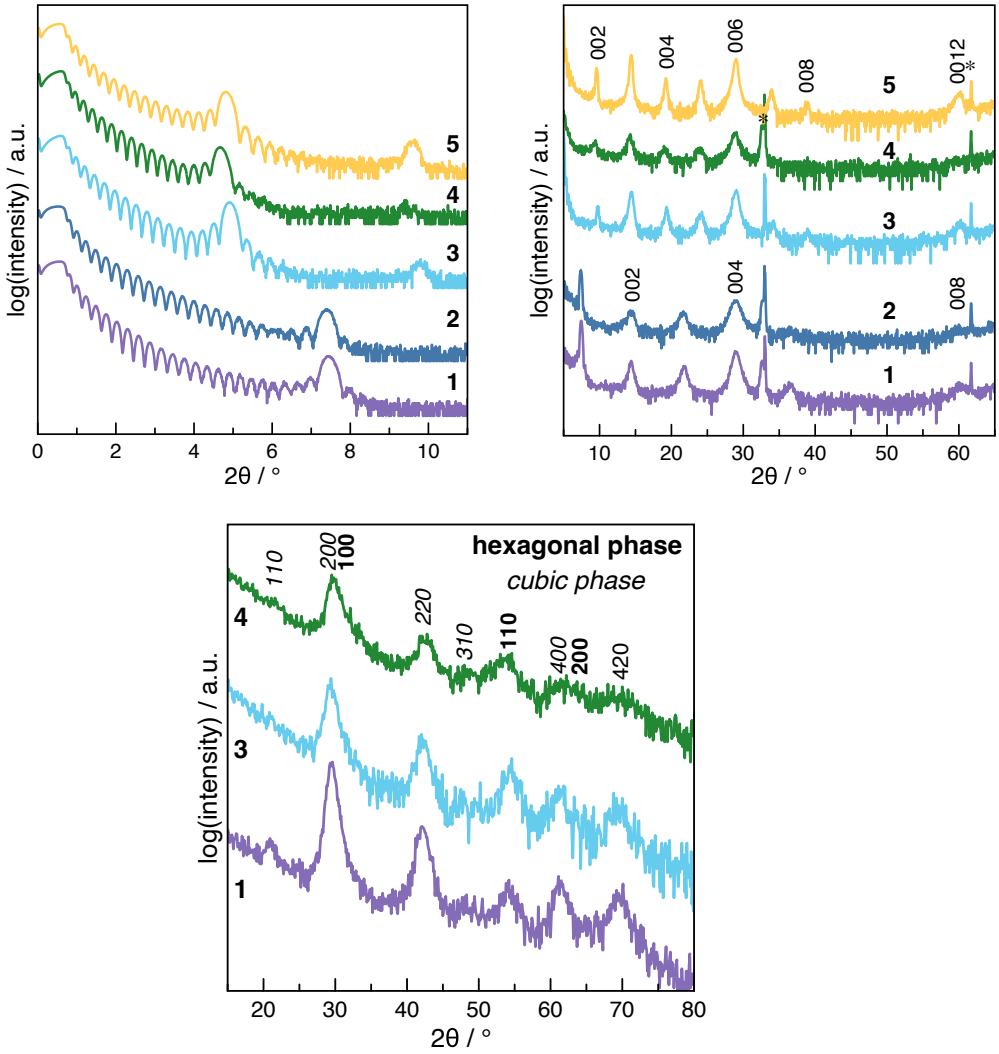

Fig. F.1. As-deposited XRR (left), specular XRD (right) and in plane XRD (bottom) patterns for samples 1-5.

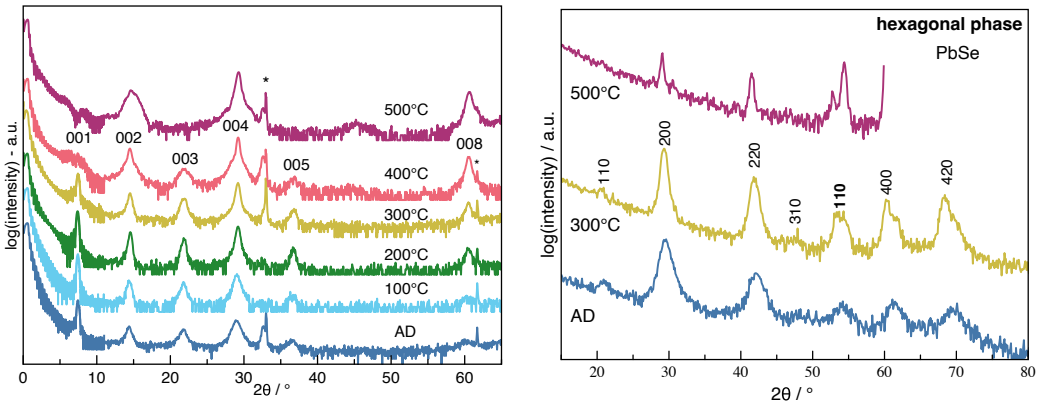

Fig. F.2. XRR and specular XRD (left) and in plane XRD (right) patterns collected during annealing study of sample 1.

REFERENCE CITED

CHAPTER I

(1) Oganov, A. R.; Pickard, C. J.; Zhu, Q.; Needs, R. J. Structure Prediction Drives Materials Discovery. *Nat Rev Mater* **2019**, *4*, 331–348. https://doi.org/10.1038/s41578-019-0101-8.

(2) Jain, A.; Shin, Y.; Persson, K. A. Computational Predictins of Energy Materials Using Density Functional Theory. *Nat Rev Mater* **2016**, *1*, 15004. https://doi.org/10.1038/natrevmats.2015.4.

(3) Aykol, M.; Hegde, V. I.; Hung, L.; Suram, S.; Herring, P.; Wolverton, C.; Hummelshøj, J. S. Network Analysis of Synthesizable Materials Discovery. *Nat Commun* **2019**, *10*, 2018. https://doi.org/10.1038/s41467-019-10030-5.

(4) Roberts, J.; Zurek, E. Computational Materials Discovery. *J Chem Phys* **2022**, *156*, 210401. https://doi.org/10.1063/5.0096008.

(5) Zakutayev, A.; Zhang, X.; Nagaraja, A.; Yu, L.; Lany, S.; Mason, T. O.; Ginley, D. S.; Zunger, A. Theoretical Prediction and Experimental Realization of New Stable Inorganic Materials Using the Inverse Design Approach. *J Am Chem Soc* **2013**, *135*, 10048–10054. https://doi.org/10.1021/ja311599g.

(6) Duan, C.; Liu, F.; Nandy, A.; Kulik, H. J. Putting Density Functional Theory to the Test in Machine-Learning-Accelerated Materials Discovery. *J Phys Chem Lett* **2021**, *12* (19), 4628–4637. https://doi.org/10.1021/acs.jpclett.1c00631.

(7) Zakutayev, A.; Bauers, S. R.; Lany, S. Experimental Synthesis of Theoretically Predicted Multivalent Ternary Nitride Materials. *Chem Mater* **2022**, *34*, 1418–1438. https://doi.org/10.1021/acs.chemmater.1c03014.

(8) Ho, Y. H.; Wu, J. Y.; Chiu, Y. H.; Wang, J.; Lin, M. F. Electronic and Optical Properties of Monolayer and Bilayer Graphene. *Phil Trans R Soc A* **2010**, *368*, 5445–5458. https://doi.org/10.1098/rsta.2010.0209.

(9) Mak, K. F.; Lee, C.; Hone, J.; Shan, J.; Heinz, T. F. Atomically Thin MoS2: A New Direct-Gap Semiconductor. *Phys Rev Lett* **2010**, *105*, 136805. https://doi.org/10.1103/PhysRevLett.105.136805.

(10) Balan, A. P.; Puthirath, A. B.; Roy, S.; Costin, G.; Oliveira, E. F.; Saadi, M. A. S. R.; Sreepal, V.; Friedrich, R.; Serles, P.; Biswas, A.; Iyengar, S. A.; Chakingal, N.; Bhattacharyya, S.; Saju, S. K.; Pardo, S. C.; Sassi, L. M.; Filleter, T.; Krasheninnikov, A.; Galvao, D. S.; Vajtai, R.; Nair, R. R.; Ajayan, P. M. Non-van Der Waals Quasi-2D Materials; Recent Advances in Synthesis, Emergent Properties and Applications. *Mater Today* **2022**, *58*, 164–200. https://doi.org/10.1016/j.mattod.2022.07.007.

(11) Splendiani, A.; Sun, L.; Zhang, Y.; Li, T.; Kim, J.; Chim, C. Y.; Galli, G.; Wang, F. Emerging Photoluminescence in Monolayer MoS2. *Nano Lett* **2010**, *10*, 1271–1275. https://doi.org/10.1021/nl903868w.

(12) Zhao, M.; Song, P.; Teng, J. Electrically and Optically Tunable Responses in Graphene/Transition-Metal-Dichalcogenide Heterostructures. *ACS Appl Mater Inter* **2018**, *10*, 44102–44108. https://doi.org/10.1021/acsami.8b12588.

(13) Zereshki, P.; Wei, Y.; Long, R.; Zhao, H. Layer-Coupled States Facilitate Ultrafast Charge Transfer in a Transition Metal Dichalcogenide Trilayer Heterostructure. *J Phys Chem Lett* **2018**, *9*, 5970–5978. https://doi.org/10.1021/acs.jpclett.8b02622.

(14) Stark, M. S.; Kuntz, K. L.; Martens, S. J.; Warren, S. C. Intercalation of Layered Materials from Bulk to 2D. *Adv Mater* **2019**, *31*, 1808213. https://doi.org/10.1002/adma.201808213.

(15) Zhao, X.; Song, P.; Wang, C.; Riis-Jensen, A. C.; Fu, W.; Deng, Y.; Wan, D.; Kang, L.; Ning, S.; Dan, J.; Venkatesan, T.; Liu, Z.; Zhou, W.; Thygesen, K. S.; Luo, X.; Pennycook, S. J.; Loh, K. P. Engineering Covalently Bonded 2D Layered Materials by Self-Intercalation. *Nature* **2020**, *581*, 171–177. https://doi.org/10.1038/s41586-020-2241-9.

(16) Zhou, J.; Lin, Z.; Ren, H.; Duan, X.; Shakir, I.; Huang, Y.; Duan, X. Layered Intercalation Materials. *Adv Mater* **2021**, *33*, 2004557. https://doi.org/10.1002/adma.202004557.

(17) Cordova, D. L. M.; Fender, S. S.; Kam, T. M.; Seyd, J.; Albrecht, M.; Lu, P.; Fischer, R.; Johnson, D. C. Designed Synthesis and Structure-Property Relationships of Kinetically Stable [(PbSe)1+d]m(VSe2)1 (m = 1, 2, 3, 4) Heterostructures. *Chem Mater* **2019**, *31* (20), 8473–8483. https://doi.org/10.1021/acs.chemmater.9b02826.

(18) Hite, O. K.; Falmbigl, M.; Alemayehu, M. B.; Esters, M.; Wood, S. R.; Johnson, D. C. Charge Density Wave Transition in (PbSe)1+δ(VSe2)n Compounds with n = 1, 2, and 3. *Chem Mater* **2017**, *29*, 5646–5653. https://doi.org/10.1021/acs.chemmater.7b01383.

(19) Li, H.; Li, Y.; Aljarb, A.; Shi, Y.; Li, L. J. Epitaxial Growth of Two-Dimensional Layered Transition-Metal Dichalcogenides: Growth Mechanism, Controllability, and Scalability. *Chem Rev* **2018**, *118* (13), 6134–6150. https://doi.org/10.1021/acs.chemrev.7b00212.

(20) Farrow, R. F. C. Stabilization of Metastable Phases By Epitaxy. *J Vac Sci Technol B Microelectron Nanom Struct* **1982**, *1* (2), 222–228. https://doi.org/10.1116/1.582491.

(21) Cai, Z.; Liu, B.; Zou, X.; Cheng, H. M. Chemical Vapor Deposition Growth and Applications of Two-Dimensional Materials and Their Heterostructures. *Chem Rev* **2018**, *118*, 6091–6133. https://doi.org/10.1021/acs.chemrev.7b00536.

(22) Gupta, A. Thin Film Synthesis of Metastable and Artificially Structured Oxides. *Curr Opin Solid State Mater Sci* **1997**, *2*, 23–31. https://doi.org/10.1016/S1359-0286(97)80101-5.

(23) Consonni, V. Self-Induced Growth of GaN Nanowires by Molecular Beam Epitaxy: A Critical Review of the Formation Mechanisms. *Phys Status Solidi - Rapid Res Lett* **2013**, *7* (10), 699–712. https://doi.org/10.1002/pssr.201307237.

(24) Schalk, N.; Tkadletz, M.; Mitterer, C. Hard Coatings for Cutting Applications: Physical vs. Chemical Vapor Deposition and Future Challenges for the Coatings Community. *Surf Coatings Technol* **2022**, *429*, 127949. https://doi.org/10.1016/j.surfcoat.2021.127949.

(25) Cho, A. Y. Growth and Properties of Iii-V Semiconductors By Molecular Beam Epitaxy. *Thin Solid Films* **1983**, *100*, 291–317. https://doi.org/10.1007/978-94-009-5073-3_6.

(26) Schlom, D. G.; Chen, L. Q.; Pan, X.; Schmehl, A.; Zurbuchen, M. A. A Thin Film Approach to Engineering Functionality into Oxides. *J Am Ceram Soc* **2008**, *91*, 2429–2454. https://doi.org/10.1111/j.1551-2916.2008.02556.x.

(27) Norton, D. P. Synthesis and Properties of Epitaxial Electronic Oxide Thin-Film Materials. *Mater Sci Eng R* **2004**, *43*, 139–247. https://doi.org/10.1016/j.mser.2003.12.002.

(28) Gorbenko, O. Y.; Samoilenkov, S. V.; Graboy, I. E.; Kaul, A. R. Epitaxial Stabilization of Oxides in Thin Films. *Chem. Mater.* **2002**, *14*, 4026–4043. https://doi.org/10.1002/chin.200251226.

(29) Xu, Y.; Park, J. H.; Yao, Z.; Wolverton, C.; Razeghi, M.; Wu, J.; Dravid, V. P. Strain-Induced Metastable Phase Stabilization in Ga 2 O 3 Thin Films. *ACS Appl Mater Inter* **2019**, *11*, 5536–5543. https://doi.org/10.1021/acsami.8b17731.

(30) Cho, A. Y.; Arthur, J. R. Molecular Beam Epitaxy. *Prog Solid State Ch* **1975**, *10* (PART 3), 157–191. https://doi.org/10.1016/0079-6786(75)90005-9.

(31) Vishwanath, S.; Dang, P.; Xing, H. G. *Challenges and Opportunities in Molecular Beam Epitaxy Growth of 2D Crystals*; Elsevier Inc., 2018. https://doi.org/10.1016/b978-0-12-812136-8.00017-7.

(32) Wang, J.; Li, T.; Wang, Q.; Wang, W.; Shi, R.; Wang, N.; Amini, A.; Cheng, C. Controlled Growth of Atomically Thin Transition Metal Dichalcogenides via Chemical Vapor Deposition Method. *Mater Today Adv* **2020**, *8*, 100098. https://doi.org/10.1016/j.mtadv.2020.100098.

(33) Hernandez Ruiz, K.; Wang, Z.; Ciprian, M.; Zhu, M.; Tu, R.; Zhang, L.; Luo, W.; Fan, Y.; Jiang, W. Chemical Vapor Deposition Mediated Phase Engineering for 2D Transition Metal Dichalcogenides: Strategies and Applications. *Small Sci* **2022**, *2*, 2100047. https://doi.org/10.1002/smsc.202100047.

CHAPTER II

[1] A. Zunger, Nat. Rev. Chem. **2**, 0121 (2018).

[2] S. Curtarolo, W. Setyawan, S. Wang, J. Xue, K. Yang, R.H. Taylor, L.J. Nelson, G.L.W. Hart, S. Sanvito, M. Buongiorno-Nardelli, N. Mingo, and O. Levy, Comp. Mater. Sci. **58**, 227 (2012).

[3] A. Jain, S.P. Ong, G. Hautier, W. Chen, W.D. Richards, S. Dacek, S. Cholia, D. Gunter, D. Skinner, G. Ceder, and K.A. Persson, APL Mater **1**, 011002 (2013).

[4] J.E. Saal, S. Kirklin, M. Aykol, B. Meredig, and C. Wolverton, Jom **65**, 1501 (2013).

[5] S. Curtarolo, G.L.W. Hart, M.B. Nardelli, N. Mingo, S. Sanvito, and O. Levy, Nat. Mater. **12**, 191 (2013).

[6] A. Narayan, A. Bhutani, S. Rubeck, J.N. Eckstein, D.P. Shoemaker, and L.K. Wagner, Phys. Rev. B **94**, 045105 (2016).

[7] E. Kim, K. Huang, A. Saunders, A. McCallum, G. Ceder, and E. Olivetti, Chem. Mater. **29**, 9436 (2017).

[8] J.C. Schön, Process. Appl. Ceram. **9**, 157 (2015).

[9] D.L.M. Cordova and D.C. Johnson, ChemPhysChem **21**, 1345 (2020).

[10] A. Stein, S.W. Keller, and T.E. Mallouk, Science **259**, 1558 (1993).

[11] A.Y. Cho and J.R. Arthur, Prog. Solid State Ch. **10**, 157 (1975).

[12] B.A. Joyce, Rep. Prog. Phys. **48**, 1637 (1985).

[13] W. Mortelmans, W. Mortelmans, A. Nalin Mehta, A. Nalin Mehta, Y. Balaji, Y. Balaji, S. Sergeant, R. Meng, M. Houssa, S. De Gendt, S. De Gendt, M. Heyns, M. Heyns, and C. Merckling, ACS Appl. Mater. Inter. **12**, 27508 (2020).

[14] D.S.H. Liu, M. Hilse, and R. Engel-Herbert, J. Vac. Sci. Technol. A **39**, 023413 (2021).

[15] T. Novet and D.C. Johnson, J. Am. Chem. Soc. **113**, 3398 (1991).

[16] H. Mehrer, *Diffusion in Solids: Fundamentals, Methods, Materials, Diffusion-Controlled Processes*, 155th ed. (Springer Series in Solid-State Sciences, 2007).

[17] M. Aykol, S.S. Dwaraknath, W. Sun, and K.A. Persson, Sci. Adv. **4**, eaaq0148 (2018).

[18] J.R. Williams, M.B. Johnson, and D.C. Johnson, J. Am. Chem. Soc. **125**, 3589 (2003).

[19] J.R. Williams, M.B. Johnson, and D.C. Johnson, J. Am. Chem. Soc. **123**, 1645 (2001).

[20] W. Ostwald, Z. Phys. Chem. **22**, 289 (1897).

[21] J.W. Cahn and J.E. Hilliard, J. Chem. Phys. **28**, 258 (1958).

[22] K.F. Kelton, Solid State Phys. **45**, 75 (1991).

[23] S.P. Rudin, ArXiv:1611.07510 [cond-mat.mtrl-sci] arXiv.org e-Print archive (2016).

[24] D.M. Hamann, S.P. Rudin, T. Asaba, F. Ronning, D.L.M. Cordova, P. Lu, and D.C. Johnson, Chem. Mater. **33**, 5076 (2021).

[25] G.A. Wiegers, Physica B & C **99**, 151 (1980).

[26] A.M. Miller, D.M. Hamann, E.C. Hadland, and D.C. Johnson, Inorg. Chem. **59**, 12536 (2020).

[27] N.T. Nguyen, B. Howe, J.R. Hash, N. Liebrecht, and D.C. Johnson, Adv. Mater. **18**, 118 (2006).

[28] D.L.M. Cordova, T.M. Kam, S.S. Fender, Y.H. Tsai, and D.C. Johnson, Phys. Status Solidi A **216**, 1800896 (2019).

[29] M.D. Anderson, C.L. Heideman, Q. Lin, M. Smeller, R. Kokenyesi, A.A. Herzing, I.M. Anderson, D.A. Keszler, P. Zschack, and D.C. Johnson, Angew. Chem. Int. Edit. **52**, 1982 (2013).

[30] R.N. Gannon, M.M. Choffel, H.R. Blackwood, N. Wolff, A. Lotnyk, L. Kienle, and D.C. Johnson, Z. Anorg. Allg. Chem. **648**, e202200015 (2022).

[31] T.C. Huang, R. Gilles, and G. Will, Thin Solid Films **230**, 99 (1993).

[32] B.H. Toby and R.B. Von Dreele, J. Appl. Crystallogr. **46**, 544 (2013).

[33] D.M. Hamann, D. Bardgett, D.L.M. Cordova, L.A. Maynard, E.C. Hadland, A.C. Lygo, S.R. Wood, M. Esters, and D.C. Johnson, Chem. Mater. **30**, 6209 (2018).

[34] M. Schaffer, B. Schaffer, and Q. Ramasse, Ultramicroscopy **114**, 62 (2012).

[35] G. Kresse and J. Furthmüller, Comp. Mater. Sci. **6**, 15 (1996).

[36] G. Kresse and J. Furthmüller, Phys. Rev. B **54**, 11169 (1996).

[37] P.E. Blöchl, Phys. Rev. B **50**, 17953 (1994).

[38] J.P. Perdew, K. Burke, and M. Ernzerhof, Phys. Rev. Lett. **77**, 3865 (1996).

[39] A. Tkatchenko and M. Scheffler, Phys. Rev. Lett. **102**, 6 (2009).

[40] F.J. Di Salvo and J. V. Waszczak, J. Phys. Colloques **37**, C4-157-C4-161 (1976).

[41] C. Wang, X. Wu, X. Zhang, G. Mu, P. Li, C. Luo, H. Xu, and Z. Di, Appl. Phys. Lett. **116**, 223901 (2020).

[42] M. Lemon, R.N. Gannon, P. Lu, S.R. Battey, S.P. Rudin, B.H. Toby, and D.C. Johnson, Chem. Mater. **34**, 8528 (2022).

[43] A.M. Miller, M. Lemon, M.A. Choffel, S.R. Rich, F. Harvel, and D.C. Johnson, Z. Naturforsch. B **77**, 313 (2022).

[44] C. Ern, W. Donner, H. Dosch, B. Adams, and D. Nowikow, Phys. Rev. Lett. **85**, 1926 (2000).

[45] E. Schierle, Antiferromagnetism in Thin Films Studied by Resonant Magnetic Soft X-Ray Scattering, Ph.D. Dissertation, Freie Univ. Berlin, Berlin, Germany (2006).

[46] NIST ICSD database: NIST Inorganic Crystal Structure Database, NIST Standard Reference Database Number 3, National Institute of Standards and Technology, Gaithersburg MD, 20899, https://doi.org/10.18434/M32147, (retrieved 8/22/2022)

[47] F. Harvel, M. Lemon, R.N. Gannon, D. Bardgett, M. Humphrey, and D.C. Johnson, Chem. Mater. **34**, 6339 (2022).

[48] X. Yang, M. Wang, Y. Li, H. Bai, J. Ma, X. Sun, Q. Tao, C. Dong, and Z.-A. Xu, Supercond. Sci. Tech. **31**, 125010 (2018).

[49] M. Esters, M.B. Alemayehu, Z. Jones, N.T. Nguyen, M.D. Anderson, C. Grosse, S.F. Fischer, and D.C. Johnson, Angew. Chem. Int. Edit. **54**, 1130 (2015).

[50] D.B. Moore, M. Beekman, S. Disch, P. Zschack, I. Häusler, W. Neumann, and D.C. Johnson, Chem. Mater. **25**, 2404 (2013).

[51] D.L.M. Cordova, S.S. Fender, T.M. Kam, J. Seyd, M. Albrecht, P. Lu, R. Fischer, and D.C. Johnson, Chem. Mater. **31**, 8473 (2019).

[52] C.M. Fang, A.R.H.F. Ettema, C. Haas, G.A. Wiegers, H. Van Leuken, and R.A. De Groot, Phys. Rev. B **52**, 2336 (1995).

[53] A.R.H.F. Ettema, C. Haas, and T.S. Turner, Phys. Rev. B **47**, 12794 (1993).

[54] A.R.H.F. Ettema and C. Haas, J. Phys.-Condens. Mat. **5**, 3817 (1993).

[55] M. Kalläne, K. Rossnagel, M. Marczynski-Bühlow, L. Kipp, H.I. Starnberg, and S.E. Stoltz, Phys. Rev. Lett. **100**, 065502 (2008).

[56] Y. Moelo, A. Meerschaut, J. Rouxel, and C. Auriel, Chem. Mater. **7**, 1759 (1995).

[57] G.A. Wiegers, Prog. Solid State Ch. **24**, 1 (1996).

[58] H. Liu and Y. Xue, Adv. Mater. **33,** 2008456 (2021).

[59] P. Lu, L. Zhou, M.J. Kramer, and D.J. Smith, Sci. Rep. **4**, 3945 (2014).

CHAPTER III

(1) Johnson, D. C. Controlled Synthesis of New Compounds Using Modulated Elemental Reactants. *Curr Opin Solid State Mater Sci* **1998**, *3*, 159–167. https://doi.org/10.1016/S1359-0286(98)80082-X.

(2) Noh, M.; Johnson, C. D.; Hornbostel, M. D.; Thiel, J.; Johnson, D. C. Control of Reaction Pathway and the Nanostructure of Final Products through the Design of Modulated Elemental Reactants. *Chem Mater* **1996**, *8*, 1625–1635. https://doi.org/10.1021/cm9601087.

(3) Hamann, D. M.; Bardgett, D.; Cordova, D. L. M.; Maynard, L. A.; Hadland, E. C.; Lygo, A. C.; Wood, S. R.; Esters, M.; Johnson, D. C. Sub-Monolayer Accuracy in Determining the Number of Atoms per Unit Area in Ultrathin Films Using X-Ray Fluorescence. *Chem Mater* **2018**, *30*, 6209–6216. https://doi.org/10.1021/acs.chemmater.8b02591.

(4) Huang, T. C.; Gilles, R.; Will, G. Thin-Film Thickness and Density Determination from x-Ray Reflectivity Data Using a Conventional Power Diffractometer. *Thin Solid Films* **1993**, *230*, 99–101. https://doi.org/10.1016/0040-6090(93)90499-F.

(5) Parratt, L. G. Surface Studies of Solids by Total Reflection of X-Rays. *Phys Rev* **1954**, *95* (2), 359–369. https://doi.org/10.1103/PhysRev.95.359.

(6) Tian, H. H.; Atzmon, M. Comparison of X-Ray Analysis Methods Used to Determine the Grain Size and Strain in Nanocrystalline Materials. *Philos Mag A Phys Condens Matter, Struct Defects Mech Prop* **1999**, *79* (8), 1769–1786. https://doi.org/10.1080/01418619908210391.

CHAPTER 1V

(1) James, R. W. *The Optical Principles of The Diffraction of X-Rays*; Ox Bow Press: Woodbridge, CT, 1982.

(2) Miyadera, T.; Auchi, Y.; Yamamoto, K.; Ohashi, N.; Koganezawa, T.; Yaguchi, H.; Yoshida, Y.; Chikamatsu, M. Insights into Microscopic Crystal Growth Dynamics of CH3NH3PbI3under a Laser Deposition Process Revealed by in Situ X-Ray Diffraction. *ACS Appl. Mater. Interfaces* **2021**, *13* (19), 22559–22566. https://doi.org/10.1021/acsami.1c04488.

(3) Forst, M.; Caviglia, A. D.; Scherwitzl, R.; Mankowsky, R.; Zubko, P.; Khanna, V.; Bromberger, H.; Wilkins, S. B.; Chuang, Y. D.; Lee, W. S.; Schlotter, W. F.; Turner, J. J.; Dakovski, G. L.; Minitti, M. P.; Robinson, J.; Clark, S. R.; Jaksch, D.; Triscone, J. M.; Hill, J. P.; Dhesi, S. S.; Cavalleri, A. Spatially Resolved Ultrafast Magnetic Dynamics Initiated at a Complex Oxide Heterointerface. *Nat. Mater.* **2015**, *14* (9), 883–888. https://doi.org/10.1038/nmat4341.

(4) Du, C.; Wang, H.; Yang, F.; Hammel, P. C. Systematic Variation of Spin-Orbit Coupling with d -Orbital Filling: Large Inverse Spin Hall Effect in 3d Transition Metals. *Phys. Rev. B - Condens. Matter Mater. Phys.* **2014**, *90* (14), 1–5. https://doi.org/10.1103/PhysRevB.90.140407.

(5) Tsuchiya, Y.; Norota, K.; Watabe, Y.; Kuroda, T.; Iwata, N.; Hashimoto, T.; Yamamoto, H. Growth Difference of LaFeO3 Thin Films by Pulsed Laser Deposition Method Using the Targets Prepared by Pechini and Conventional Solid Solution Methods. *Trans. Mater. Res. Soc. Japan* **2012**, *37* (3), 369–372. https://doi.org/10.14723/tmrsj.37.369.

(6) Iwata, N.; Watabe, Y.; Tsuchiya, Y.; Norota, K.; Hashimoto, T.; Huijben, M.; Rijnders, G.; Blank, D. Growth and Evaluation of [AFeOx/REFeO3] (A=Ca, Sr, RE=La, Bi) Superlattices by Pulsed Laser Deposition Method Using High Density Targets Prepared by Pechini Method. *Mater. Res. Soc. Symp. Proc.* **2012**, *1477*, 61–66. https://doi.org/10.1557/opl.2012.

(7) Grelet, E.; Dardel, S.; Bock, H.; Goldmann, M.; Lacaze, E.; Nallet, F. Morphology of Open Films of Discotic Hexagonal Columnar Liquid Crystals as Probed by Grazing Incidence X-Ray Diffraction. *Eur. Phys. J. E* **2010**, *31* (4), 343–349. https://doi.org/10.1140/epje/i2010-10586-2.

(8) Krauss, T. N.; Barrena, E.; Zhang, X. N.; De Oteyza, D. G.; Major, J.; Dehm, V.; Würthner, F.; Cavalcanti, L. P.; Dosch, H. Three-Dimensional Molecular Packing of Thin Organic Films of PTCDI-C 8 Determined by Surface X-Ray Diffraction. *Langmuir* **2008**, *24* (22), 12742–12744. https://doi.org/10.1021/la8030182.

(9) Abe, Y.; Kawamura, M.; Sasaki, K. Highly Textured (100) RuO2/(001) Ru Multilayers Prepared by Sputtering. *Japanese J. Appl. Physics, Part 1 Regul. Pap. Short Notes Rev. Pap.* **2002**, *41* (11 B), 6857–6861. https://doi.org/10.1143/JJAP.41.6857.

(10) Naito, M.; Karimoto, S.; Yamamoto, H.; Nakada, H.; Suzuki, K. Production of Double-Sided Large-Area High-Tc Wafers by Molecular Beam Epitaxy. *IEEE Trans. Appl. Supercond.* **2001**, *11* (1 III), 3848–3851. https://doi.org/10.1109/77.919904.

(11) Brangham, J. T.; Meng, K. Y.; Yang, A. S.; Gallagher, J. C.; Esser, B. D.; White, S. P.; Yu, S.; McComb, D. W.; Hammel, P. C.; Yang, F. Thickness Dependence of Spin Hall Angle of Au Grown on Y3 F E5 O12 Epitaxial Films. *Phys. Rev. B* **2016**, *94* (5), 6–11. https://doi.org/10.1103/PhysRevB.94.054418.

(12) Shu, X.; Zhou, J.; Liu, L.; Lin, W.; Zhou, C.; Chen, S.; Xie, Q.; Ren, L.; Xiaojiang, Y.; Yang, H.; Chen, J. Role of Interfacial Orbital Hybridization in Spin-Orbit-Torque Generation in Pt -Based Heterostructures. *Phys. Rev. Appl.* **2020**, *14* (5), 1. https://doi.org/10.1103/PhysRevApplied.14.054056.

(13) Xu, J.; Katoch, J.; Ahmed, A. S.; Pinchuk, I. V.; Young, J. R.; Johnston-Halperin, E.; Pelz, J.; Kawakami, R. K. Growth of Uniform CaGe2 Films by Alternating Layer Molecular Beam Epitaxy. *J. Cryst. Growth* **2017**, *460* (December 2016), 134–138. https://doi.org/10.1016/j.jcrysgro.2016.12.102.

(14) Song, Y.; Li, Z.; Li, H.; Tang, S.; Mu, G.; Xu, L.; Peng, W.; Shen, D.; Chen, Y.; Xie, X.; Jiang, M. Epitaxial Growth and Characterization of High Quality Bi2O2Se Thin Films on SrTiO3 Substrates by Pulsed Laser Deposition. *Nanotechnology* **2020**, *31* (16). https://doi.org/10.1088/1361-6528/ab6686.

(15) Switzer, J. A.; Hill, J. C.; Mahenderkar, N. K.; Liu, Y. C. Nanometer-Thick Gold on Silicon as a Proxy for Single-Crystal Gold for the Electrodeposition of Epitaxial Cuprous Oxide Thin Films. *ACS Appl. Mater. Interfaces* **2016**, *8* (24), 15828–15837. https://doi.org/10.1021/acsami.6b04552.

(16) Watabe, Y.; Iwata, N.; Oikawa, T.; Hashimoto, T.; Huijben, M.; Rijnders, G.; Yamamoto, H. Fabrication and Crystal Structure of [ABO3/REMO3] (A = Ca, La, B = Fe, Mn, RE = Bi, La, M = Fe, Fe0.8Mn0.2) Superlattices Grown by Pulsed Laser Deposition Method. *Jpn. J. Appl. Phys.* **2014**, *53* (5 SPEC. ISSUE 1). https://doi.org/10.7567/JJAP.53.05FB12.

(17) Onbasli, M. C.; Kehlberger, A.; Kim, D. H.; Jakob, G.; Kläui, M.; Chumak, A. V.; Hillebrands, B.; Ross, C. A. Pulsed Laser Deposition of Epitaxial Yttrium Iron Garnet Films with Low Gilbert Damping and Bulk-like Magnetization. *APL Mater.* **2014**, *2* (10). https://doi.org/10.1063/1.4896936.

(18) Peters, B.; Alfonsov, A.; Blum, C. G. F.; Hageman, S. J.; Woodward, P. M.; Wurmehl, S.; Büchner, B.; Yang, F. Y. Epitaxial Films of Heusler Compound Co2FeAl0.5Si 0.5 with High Crystalline Quality Grown by off-Axis Sputtering. *Appl. Phys. Lett.* **2013**, *103* (16), 0–5. https://doi.org/10.1063/1.4825338.

(19) Hauser, A. J.; Soliz, J. R.; Dixit, M.; Williams, R. E. A.; Susner, M. A.; Peters, B.; Mier, L. M.; Gustafson, T. L.; Sumption, M. D.; Fraser, H. L.; Woodward, P. M.; Yang, F. Y. Fully Ordered Sr2CrReO 6 Epitaxial Films: A High-Temperature Ferrimagnetic Semiconductor. *Phys. Rev. B - Condens. Matter Mater. Phys.* **2012**, *85* (16), 4–7. https://doi.org/10.1103/PhysRevB.85.161201.

(20) Switzer, J. A.; Gudavarthy, R. V.; Kulp, E. A.; Mu, G.; He, Z.; Wessel, A. J. Resistance Switching in Electrodeposited Magnetite Superlattices. *J. Am. Chem. Soc.* **2010**, *132* (4), 1258–1260. https://doi.org/10.1021/ja909295y.

(21) Asanuma, S.; Fukunaga, M.; Uesu, Y.; Haumont, R.; Dkhil, B.; Malibert, C.; Kiat, J. M. Fabrications of Pb(Sc1/2Nb1/2)O 3/XPbTiO3 Thin Films and Their Structural Characterizations. *Japanese J. Appl. Physics, Part 1 Regul. Pap. Short Notes Rev. Pap.* **2004**, *43* (9 B), 6581–6584. https://doi.org/10.1143/JJAP.43.6581.

(22) Dürr, A. C.; Schreiber, F.; Münch, M.; Karl, N.; Krause, B.; Kruppa, V.; Dosch, H. High Structural Order in Thin Films of the Organic Semiconductor Diindenoperylene. *Appl. Phys. Lett.* **2002**, *81* (12), 2276–2278. https://doi.org/10.1063/1.1508436.

(23) Ern, C.; Donner, W.; Dosch, H.; Adams, B.; Nowikow, D. Temperature-Dependent Interfacial Stiffness of the Disorder Layer in a Thin Cu3Au Alloy Film. *Phys. Rev. Lett.* **2000**, *85* (9), 1926–1929. https://doi.org/10.1103/PhysRevLett.85.1926.

(24) Mahenderkar, N. K.; Chen, Q.; Liu, Y.; Duchild, A. R.; Hofheins, S.; Chason, E.; Switzer, J. A. Epitaxial Lift-off of Electrodeposited Single-Crystal Gold Foils for Flexible Electronics. *Science (80-.).* **2017**, *355*, 1203–1206.

(25) Lu, W.; Yang, P.; Song, W. D.; Chow, G. M.; Chen, J. S. Control of Oxygen Octahedral Rotations and Physical Properties in SrRuO3 Films. *Phys. Rev. B - Condens. Matter Mater. Phys.* **2013**, *88* (21), 1–11. https://doi.org/10.1103/PhysRevB.88.214115.

(26) Xu, S. J.; Shi, Z.; Zhou, S. M. Clear Evidence of Interfacial Anomalous Hall Effect in Epitaxial L10 FePt and FePd Films. *Phys. Rev. B* **2018**, *98* (2), 1–5. https://doi.org/10.1103/PhysRevB.98.024413.

(27) Sojková, M.; Dobročka, E.; Hutár, P.; Tašková, V.; Pribusová Slušná, L.; Stoklas, R.; Píš, I.; Bondino, F.; Munnik, F.; Hulman, M. High Carrier Mobility Epitaxially Aligned PtSe2 Films Grown by One-Zone Selenization. *Appl. Surf. Sci.* **2021**, *538* (May 2020), 147936. https://doi.org/10.1016/j.apsusc.2020.147936.

(28) Lee, A. J.; Brangham, J. T.; Cheng, Y.; White, S. P.; Ruane, W. T.; Esser, B. D.; McComb, D. W.; Hammel, P. C.; Yang, F. Metallic Ferromagnetic Films with Magnetic Damping under 1.4 × 10-3. *Nat. Commun.* **2017**, *8* (1), 1–6. https://doi.org/10.1038/s41467-017-00332-x.

(29) Wormington, M.; Panaccione, C.; Matney, K. M.; Bowen, D. K. Characterization of Structures from X-Ray Scattering Data Using Genetic Algorithms. *Philos. Trans. R. Soc. A Math. Phys. Eng. Sci.* **1999**, *357* (1761), 2827–2848.

(30) Kiessig, von H. Interferenz von Röntgenstrahlen an Dünnen Schichten. *Ann. Phys.* **1931**, *402* (7), 769–788. https://doi.org/10.1002/andp.19314020702.

(31) Huang, T. C.; Gilles, R.; Will, G. Thin-Film Thickness and Density Determination from x-Ray Reflectivity Data Using a Conventional Power Diffractometer. *Thin Solid Films* **1993**, *230* (2), 99–101. https://doi.org/10.1016/0040-6090(93)90499-F.

(32) Wainfan, N.; Parratt, L. G. X-Ray Reflection Studies of the Anneal and Oxidation of Some Thin Solid Films. *J. Appl. Phys.* **1960**, *31* (8), 1331–1337. https://doi.org/10.1063/1.1735837.

(33) Schierle, E. Antiferromagnetism in Thin Films Studied by Resonant Magnetic Soft X-Ray Scattering, Freie Univ. Berlin, 2006.

(34) Zwiebler, M.; Hamann-Borrero, J. E.; Vafaee, M.; Komissinskiy, P.; Macke, S.; Sutarto, R.; He, F.; Büchner, B.; Sawatzky, G. A.; Alff, L.; Geck, J. Electronic Depth Profiles with Atomic Layer Resolution from Resonant Soft X-Ray Reflectivity. *New J. Phys.* **2015**, *17* (8). https://doi.org/10.1088/1367-2630/17/8/083046.

(35) Hamann, D. M.; Bardgett, D.; Cordova, D. L. M.; Maynard, L. A.; Hadland, E. C.; Lygo, A. C.; Wood, S. R.; Esters, M.; Johnson, D. C. Sub-Monolayer Accuracy in Determining the Number of Atoms per Unit Area in Ultrathin Films Using X-Ray Fluorescence. *Chem. Mater.* **2018**, *30*, 6209–6216. https://doi.org/10.1021/acs.chemmater.8b02591.

(36) Choffel, M. A.; Gannon, R. N.; Göhler, F.; Miller, A. M.; Medlin, D. L.; Seyller, T.; Johnson, D. C. Synthesis and Electrical Properties of a New Compound (BiSe)0.97(Bi2Se3)1.26(BiSe)0.97(MoSe2) Containing Metallic 1T-MoSe2. *Chem. Mater.* **2021**, *33* (16), 6403–6411. https://doi.org/10.1021/acs.chemmater.1c01623.

CHAPTER V

[1] G. Ozaydin-Ince, A.M. Coclite, and K.K. Gleason, Rep Prog Phys **75**, 016501 (2012).

[2] O. Shekhah, J. Liu, R.A. Fischer, and C. Wöll, Chem Soc Rev **40**, 1081 (2011).

[3] N. Choudhary and D. Kaur, Sensors Actuators A Phys **242**, 162 (2016).

[4] N. Setter, D. Damjanovic, L. Eng, G. Fox, S. Gevorgian, S. Hong, A. Kingon, H. Kohlstedt, N.Y. Park, G.B. Stephenson, I. Stolitchnov, A.K. Taganstev, D. V. Taylor, T. Yamada, and S. Streiffer, J Appl Phys **100**, 051606 (2006).

[5] D. Panda and T.Y. Tseng, Thin Solid Films **531**, 1 (2013).

[6] M. Fraga and R. Pessoa, Micromachines **11**, 799 (2020).

[7] M.C. Vasudev, K.D. Anderson, T.J. Bunning, V. V. Tsukruk, and R.R. Naik, ACS Appl Mater Inter **5**, 3983 (2013).

[8] N. Chen, D.H. Kim, P. Kovacik, H. Sojoudi, M. Wang, and K.K. Gleason, Annu Rev Chem Biomol Eng **7**, 373 (2016).

[9] C. Crivello, S. Sevim, O. Graniel, C. Franco, S. Pane, J. Puigmarti-Luis, and D. Munoz-Rojas, Mater Horizons **8**, 168 (2021).

[10] G. Gupta, R.K. Tyagi, S.K. Rajput, P. Saxena, A. Vashisth, and S. Mehndiratta, Mater Today Proc **38**, 259 (2020).

[11] P.J. McGinn, ACS Comb Sci **21**, 501 (2019).

[12] M. Smeller, Structural Studies of [(PbSe)0.99]m[WSe2]n, [(PbSe)1.00]m[MoSe2]n, and [(SnSe)1.03]m[MoSe2]n Misfit Layered Compounds, University of Oregon, 2011.

[13] A.M. Miller, M. Lemon, M.A. Choffel, S.R. Rich, F. Harvel, and D.C. Johnson, Z Naturforsch B **77**, 313 (2022).

[14] I. Vartanyants, E. Ern, W. Donner, H. Dosch, and W. Caliebe, Appl Phys Lett **77**, 3929 (2000).

[15] I.K. Robinson and I.A. Vartanyants, Appl Surf Sci **182**, 186 (2001).

[16] P. Komar and G. Jakob, J Appl Crystallogr **50**, 288 (2017).

[17] A.J. Ying, C.E. Murray, and I.C. Noyan, J Appl Crystallogr **42**, 401 (2009).

[18] S.J. Xu, Z. Shi, and S.M. Zhou, Phys Rev B **98**, 024413 (2018).

[19] A.J. Lee, J.T. Brangham, Y. Cheng, S.P. White, W.T. Ruane, B.D. Esser, D.W. McComb, P.C. Hammel, and F. Yang, Nat Commun **8**, 234 (2017).

[20] M. Sojková, E. Dobročka, P. Hutár, V. Tašková, L. Pribusová Slušná, R. Stoklas, I. Píš, F. Bondino, F. Munnik, and M. Hulman, Appl Surf Sci **538**, 147936 (2021).

[21] M. Lemon, R.N. Gannon, P. Lu, S.R. Battey, S.P. Rudin, B.H. Toby, and D.C. Johnson, Chem Mater **34**, 8528 (2022).

[22] M.H. Mendenhall, K. Mullen, and J.P. Cline, J Res Natl Inst Stand Technol **120**, 223 (2015).

[23] J.J. Denney, G.S. Mattei, M.H. Mendenhall, J.. Cline, P.G. Khalifah, and B.H. Toby, J Appl Crystallogr **55**, 289 (2022).

[24] G. Caglioti, A. Paoletti, and F.P. Ricci, Nucl Instruments **3**, 223 (1958).

[25] H.M. Rietveld, Acta Crystallogr **22**, 151 (1967).

[26] E. Prince, J Appl Crystallogr **14**, 157 (1981).

CHAPTER VI

(1) Wilson, J.A.; Yoffe, A.D. The transition metal dichalcogenides discussion and interpretation of the observed optical, electrical and structural properties. *Adv. Phys*. **1969**, *18*, 193–335.

(2) Doran, N.J. Electronic structure and band theory of transition metal dichalcogenides. *Physica B+C.* **1980**, *99*, 227–37.

(3) Krasnok, A.; Lepeshov, S.; Alú, A. Nanophotonics with 2D transition metal dichalcogenides. *Opt. Express.* **2018**, *26*, 15972-15994.

(4) Kong, D.; Cha, J.J.; Wang, H.; Lee, H.R.; Cui, Y. First-row transition metal dichalcogenide catalysts for hydrogen evolution reaction. *Energy Environ. Sci.* **2013**, *6*, 3553-3558.

(5) Pumera, M.; Loo, A. H. Layered Transition-Metal Dichalcogenides (MoS_2 and WS_2) for Sensing and Biosensing. *Trends Anal. Chem.* **2014**, *61*, 49–53.

(6) Wang, H.; Yuan, H.; Sae Hong, S.; Li, Y.; Cui, Y. Physical and chemical tuning of two-dimensional transition metal dichalcogenides. *Chem. Soc. Rev.* **2015**, *44*, 2664–80.

(7) Wang, Z.; Li, R.; Su, C.; Loh, K. P. Intercalated Phases of Transition Metal Dichalcogenides. *SmartMat.* **2020**, *1*, e1013.

(8) Loh, L.; Zhang, Z.; Bosman, M.; Eda, G. Substitutional Doping in 2D Transition Metal Dichalcogenides. *Nano Res.* **2021**, *14*, 1668–1681.

(9) Wang, S. Y.; Ko, T. S.; Huang, C. C.; Lin, D. Y.; Huang, Y. S. Optical and Electrical Properties of MoS_2 and Fe-Doped MoS_2. *Jpn. J. Appl. Phys.* **2014**, *53*, 04EH07.

(10) Shkvarina, E. G.; Titova, S. G.; Titov, A. N.; Shkvarin, A. S. The Mechanism of the Formation of One-Dimensional Chains of the Iron and Vanadium Atoms in the $TiSe_2$ Interlayer Space. *J. Alloys Compd.* **2017**, *717*, 286–293.

(11) Zhu, G.; Liu, J.; Zheng, Q.; Zhang, R.; Li, D.; Banerjee, D.; Cahill, D. G. Tuning Thermal Conductivity in Molybdenum Disulfide by Electrochemical Intercalation. *Nat. Commun.* **2016**, *7*, 13211.

(12) Morosan, E.; Zandbergen, H. W.; Dennis, B. S.; Bos, J. W. G.; Onose, Y.; Klimczuk, T.; Ramirez, A. P.; Ong, N. P.; Cava, R. J. Superconductivity in CuxTiSe2. *Nat. Phys.* **2006**, *2*, 544–550.

(13) Binnewies, M.; Glaum, R.; Schmidt, M.; Schmidt, P. Chemical Vapor Transport Reactions - A Historical Review. *Z. Anorg. Allg. Chem.* **2013**, *639*, 219–229.

(14) Tedstone, A. A.; Lewis, D. J.; O'Brien, P. Synthesis, Properties, and Applications of Transition Metal-Doped Layered Transition Metal Dichalcogenides. *Chem. Mater.* **2016**, *28*, 1965–1974.

(15) Shi, Y.; Li, H.; Li, L.-J. Recent Advances in Controlled Synthesis of Two-Dimensional Transition Metal Dichalcogenides via Vapour Deposition Techniques. *Chem. Soc. Rev.* **2015**, *44*, 2744–2756.

(16) Wang, S.; Robertson, A.; Warner, J. H. Atomic Structure of Defects and Dopants in 2D Layered Transition Metal Dichalcogenides. *Chem. Soc. Rev.* **2018**, *47* (17), 6764–6794.

(17) Friend, R. H.; Yoffe, A. D. Electronic Properties of Intercalation Complexes of the Transition Metal Dichalcogenides. *Adv. Phys.* **1987**, *36* (1), 1–94.

(18) Fujisawa, Y.; Shimabukuro, T.; Kojima, H.; Kobayashi, K.; Demura, S.; Sakata, H. Effect of Fe-Doping on CDW State in 1*T*-TaS_2 Investigated by STM/STS. *J. Phys. Conf. Ser.* **2017**, *871*, 012003.

(19) Di Salvo, F. J.; Waszczak, J. V. The Effect of Fe Substitution on the Charge Density Wave in VSe_2. *J. Phys. Colloq.* **1976**, *37*, C4-157-C4-161.

(20) Shkvarin, A. S.; Yarmoshenko, Y. M.; Merentsov, A. I.; Shkvarina, E. G.; Gubkin, A. F.; Píš, I.; Nappini, S.; Bondino, F.; Bobrikov, I. A.; Titov, A. N. Electronic Structures of the Vanadium-Intercalated and Substitutionally Doped Transition-Metal Dichalcogenides $Ti_xV_ySe_2$. *Inorg. Chem.* **2020**, *59*, 8543–8551.

(21) Liu, X.-C.; Zhao, S.; Sun, X.; Deng, L.; Zou, X.; Hu, Y.; Wang, Y.-X.; Chu, C.-W.; Li, J.; Wu, J.; Ke, F.-S.; Ajayan, P. M. Spontaneous Self-Intercalation of Copper Atoms into Transition Metal Dichalcogenides. *Sci. Adv.* **2020**, *6*, eaay4092.

(22) Parkin, S. S. P.; Friend, R. H. 3-*d* Transition-Metal Intercalates of the Niobium and Tantalum Dichalcogenides. I. Magnetic Properties. *Philoss. Mag. B* **1980**, *41*, 65–93.

(23) Baranov, N. V.; Pleshchev, V. G.; Selezneva, N. V.; Sherokalova, E. M.; Korolev, A. V.; Kazantsev, V. A.; Proshkin, A. V. Ferromagnetism and Structural Transformations Caused by Cr Intercalation into $TiTe_2$. *J. Phys.: Condens. Matter* **2009**, *21*, 506002.

(24) Yadav, C. S.; Rastogi, A. K. Transport and Magnetic Properties of $Fe_{1/3}VSe_2$. *J. Phys.: Condens. Matter* **2008**, *20*, 41521225.

(25) Susarla, S.; Kochat, V.; Kutana, A.; Hachtel, J. A.; Idrobo, J. C.; Vajtai, R.; Yakobson, B. I.; Tiwary, C. S.; Ajayan, P. M. Phase Segregation Behavior of Two-Dimensional Transition Metal Dichalcogenide Binary Alloys Induced by Dissimilar Substitution. *Chem. Mater.* **2017**, *29*, 7431–7439.

(26) Sirica, N.; Mo, S.-K.; Bondino, F.; Pis, I.; Nappini, S.; Vilmercati, P.; Yi, J.; Gai, Z.; Snijders, P. C.; Das, P. K.; Vobornik, I.; Ghimire, N.; Koehler, M. R.; Li, L.; Sapkota, D.; Parker, D. S.; Mandrus, D. G.; Mannella, N. Electronic Structure of the Chiral Helimagnet and 3d-Intercalated Transition Metal Dichalcogenide $Cr_{1/3}NbS_2$. *Phys. Rev. B* **2016**, *94*, 075141.

(27) Sohn, A.; Kim, C.; Jung, J.; Kim, J. H.; Byun, K.; Cho, Y.; Zhao, P.; Kim, S. W.; Seol, M.; Lee, Z.; Kim, S.; Shin, H. Precise Layer Control and Electronic State Modulation of a Transition Metal Dichalcogenide via Phase-Transition-Induced Growth. *Adv. Mater.* **2021**, 2103286.

(28) Lim, Y.R.; Han, J.K.; Yoon, Y.; Lee, J.; Jeon, C.; Choi, M.; et al. Atomic-Level Customization of 4 in. Transition Metal Dichalcogenide Multilayer Alloys for Industrial Applications. *Adv. Mater.* **2019**, *31*, 1901405.

(29) Ern, C.; Donner, W.; Dosch, H.; Adams, B.; Nowikow, D. Temperature-Dependent Interfacial Stiffness of the Disorder Layer in a Thin Cu_3Au Alloy Film. *Phys. Rev. Lett.* **2000**, *85*, 1926–1929.

(30) Schierle, E. Antiferromagnetism in Thin Films Studied by Resonant Magnetic Soft X-Ray Scattering, Ph.D. Dissertation, Freie Univ. Berlin, Berlin, Germany, 2006.

(31) Hamann, D. M.; Bardgett, D.; Cordova, D. L. M.; Maynard, L. A.; Hadland, E. C.; Lygo, A. C.; Wood, S. R.; Esters, M.; Johnson, D. C. Sub-Monolayer Accuracy in Determining the Number of Atoms per Unit Area in Ultrathin Films Using X-Ray Fluorescence. *Chem. Mater.* **2018**, *30*, 6209–6216.

(32) Huang, T. C.; Gilles, R.; Will, G. Thin-Film Thickness and Density Determination from x-Ray Reflectivity Data Using a Conventional Power Diffractometer. *Thin Solid Films* **1993**, *230*, 99–101.

(33) Toby, B.H.; Dreele, R.B. GSAS-II: The Genesis of a Modern Open-Source All Purpose Crystallography Software Package. *J. Appl. Crystallogr.* **2013**, *46*, 544-549.

(34) Schaffer, M.; Schaffer, B.; Ramasse, Q. Sample Preparation for Atomic-Resolution STEM at Low Voltages by FIB. *Ultramicroscopy.* **2012,** *114*, 62– 71.

(35) Blöchl, P. E. Projector Augmented-Wave Method. *Phys. Rev. B* **1994**, *50*, 17953–17979.

(36) Kresse, G.; Joubert, D. From Ultrasoft Pseudopotentials to the Projector Augmented-Wave Method. *Phys. Rev. B* **1999**, *59*, 1758–1775.

(37) Kresse, G.; Furthmüller, J. Efficient Iterative Schemes for *Ab Initio* Total-Energy Calculations Using a Plane-Wave Basis Set. *Phys. Rev. B* **1996**, *54*, 11169–11186.

(38) Coelho, P. M.; Nguyen Cong, K.; Bonilla, M.; Kolekar, S.; Phan, M.-H.; Avila, J.; Asensio, M. C.; Oleynik, I. I.; Batzill, M. Charge Density Wave State Suppresses Ferromagnetic Ordering in VSe_2 Monolayers. *J. Phys. Chem. C* **2019**, *123*, 14089–14096.

(39) Yi, M.; Wu, J.; Zheng, X.; Ming, X. Structural Transition from Marcasite to Pyrite Phase in $FeSe_2$ under High Pressure: A First-Principles Study. *Eur. Phys. J. B* **2020**, *93*, 179.

(40) Bianco, R.; Calandra, M.; Mauri, F. Electronic and Vibrational Properties of $TiSe_2$ in the Charge-Density-Wave Phase from First Principles. *Phys. Rev. B* **2015**, *92*, 094107.

(41) Perdew, J. P.; Burke, K.; Ernzerhof, M. Generalized Gradient Approximation Made Simple. *Phys. Rev. Lett.* **1996**, *77*, 3865–3868.

(42) Blöchl, P. E.; Jepsen, O.; Andersen, O. K. Improved Tetrahedron Method for Brillouin-Zone Integrations. *Phys. Rev. B* **1994**, *49*, 16223–16233.

(43) Miller, A.M.; Lemon, M.; Choffel, M.A.; Rich, S.R.; Harvel, F.; Johnson, D.C. Extracting information from X-ray diffraction patterns containing Laue oscillations. *Z. Naturforsch B,* **2022**, *77*, 313-322.

(44) Parratt, L. G. Surface Studies of Solids by Total Reflection of X-Rays. *Phys. Rev.* **1954**, *95*, 359–369.

(45) Lu, P.; Zhou, L.; Kramer, M. J.; Smith, D. J. Atomic-Scale Chemical Imaging and Quantification of Metallic Alloy Structures by Energy-Dispersive X-Ray Spectroscopy. *Sci. Rep.* **2015**, *4*, 3945.

(46) Smeller, M. Structural Studies of $[(PbSe)_{0.99}]_m[WSe_2]_n$, $[(PbSe)_{1.00}]_m[MoSe_2]_n$, and $[(SnSe)_{1.03}]_m[MoSe_2]_n$ Misfit Layered Compounds, Ph.D. Dissertation, University of Oregon, Eugene, OR, 2011.

CHAPTER VII

(1) Zhang, H. Introduction: 2D Materials Chemistry. *Chem Rev* **2018**, *118*, 6089–6090. https://doi.org/10.1021/acs.chemrev.8b00278.

(2) Pham, P. V.; Bodepudi, S. C.; Shehzad, K.; Liu, Y.; Xu, Y.; Yu, B.; Duan, X. 2D Heterostructures for Ubiquitous Electronics and Optoelectronics: Principles, Opportunities, and Challenges. *Chem Rev* **2022**, *122*, 6514–6613. https://doi.org/10.1021/acs.chemrev.1c00735.

(3) Han, S. A.; Bhatia, R.; Kim, S. W. Synthesis, Properties and Potential Applications of Two-Dimensional Transition Metal Dichalcogenides. *Nano Converg* **2015**, *2*, 17. https://doi.org/10.1186/s40580-015-0048-4.

(4) Wilson, J. A.; Yoffe, A. D. The Transition Metal Dichalcogenides Discussion and Interpretation of the Observed Optical, Electrical and Structural Properties. *Adv Phys* **1969**, *18* (73), 193–335. https://doi.org/10.1080/00018736900101307.

(5) Manzeli, S.; Ovchinnikov, D.; Pasquier, D.; Yazyev, O. V.; Kis, A. 2D Transition Metal Dichalcogenides. *Nat Rev Mater* **2017**, *2*. https://doi.org/10.1038/natrevmats.2017.33.

(6) Thakar, K.; Lodha, S. Optoelectronic and Photonic Devices Based on Transition Metal Dichalcogenides. *Mater Res Express* **2019**, *7* (1). https://doi.org/10.1088/2053-1591/ab5c9c.

(7) Mak, K. F.; Shan, J. Photonics and Optoelectronics of 2D Semiconductor Transition Metal Dichalcogenides. *Nat Photonics* **2016**, *10* (4), 216–226. https://doi.org/10.1038/nphoton.2015.282.

(8) Wang, Q. H.; Kalantar-Zadeh, K.; Kis, A.; Coleman, J. N.; Strano, M. S. Electronics and Optoelectronics of Two-Dimensional Transition Metal Dichalcogenides. *Nat Nanotechnol* **2012**, *7* (11), 699–712. https://doi.org/10.1038/nnano.2012.193.

(9) Hu, H.; Zavabeti, A.; Quan, H.; Zhu, W.; Wei, H.; Chen, D.; Ou, J. Z. Recent Advances in Two-Dimensional Transition Metal Dichalcogenides for Biological Sensing. *Biosens Bioelectron* **2019**, *142*, 111573. https://doi.org/10.1016/j.bios.2019.111573.

(10) Wang, L.; Xu, D.; Jiang, L.; Gao, J.; Tang, Z.; Xu, Y.; Chen, X.; Zhang, H. Transition Metal Dichalcogenides for Sensing and Oncotherapy: Status, Challenges, and Perspective. *Adv Funct Mater* **2021**, *31*, 2004408. https://doi.org/10.1002/adfm.202004408.

(11) Yun, Q.; Li, L.; Hu, Z.; Lu, Q.; Chen, B.; Zhang, H. Layered Transition Metal Dichalcogenide-Based Nanomaterials for Electrochemical Energy Storage. *Adv Mater* **2020**, *32*, 1903826. https://doi.org/10.1002/adma.201903826.

(12) Wang, H.; Yuan, H.; Sae Hong, S.; Li, Y.; Cui, Y. Physical and Chemical Tuning of Two-Dimensional Transition Metal Dichalcogenides. *Chem Soc Rev* **2015**, *44* (9), 2664–2680. https://doi.org/10.1039/c4cs00287c.

(13) Bertolazzi, S.; Gobbi, M.; Zhao, Y.; Backes, C.; Samorì, P. Molecular Chemistry Approaches for Tuning the Properties of Two-Dimensional Transition Metal Dichalcogenides. *Chem Soc Rev* **2018**, *47*, 6845–6888. https://doi.org/10.1039/c8cs00169c.

(14) Baranov, N. V; Pleshchev, V. G.; Selezneva, N. V; Sherokalova, E. M.; Korolev, A. V; Kazantsev, V. A.; Proshkin, A. V. Ferromagnetism and Structural Transformations Caused by Cr Intercalation into TiTe 2 . *J Phys - Condens Mat* **2009**, *21* (50), 506002. https://doi.org/10.1088/0953-8984/21/50/506002.

(15) Liu, W.; Li, S.; Wu, H.; Dhale, N.; Koirala, P.; Lv, B. Enhanced Superconductivity in the Se-Substituted 1T- PdTe2. *Phys Rev Mater* **2021**, *5*, 14802. https://doi.org/10.1103/PhysRevMaterials.5.014802.

(16) Wang, C.; Wu, X.; Zhang, X.; Mu, G.; Li, P.; Luo, C.; Xu, H.; Di, Z. Iron-Doped VSe 2 Nanosheets for Enhanced Hydrogen Evolution Reaction. *Appl Phys Lett* **2020**, *116* (22), 223901. https://doi.org/10.1063/5.0008092.

(17) May, A. F.; Yan, J.; McGuire, M. A. A Practical Guide for Crystal Growth of van Der Waals Layered Materials. *J Appl Phys* **2020**, *128*, 051101. https://doi.org/10.1063/5.0015971.

(18) Martinolich, A. J.; Kurzman, J. A.; Neilson, J. R. Circumventing Diffusion in Kinetically Controlled Solid-State Metathesis Reactions. *J Am Chem Soc* **2016**, *138* (34), 11031–11037. https://doi.org/10.1021/jacs.6b06367.

(19) Wang, S.; Robertson, A.; Warner, J. H. Atomic Structure of Defects and Dopants in 2D Layered Transition Metal Dichalcogenides. *Chem Soc Rev* **2018**, *47* (17), 6764–6794. https://doi.org/10.1039/c8cs00236c.

(20) Shi, Y.; Li, H.; Li, L. J. Recent Advances in Controlled Synthesis of Two-Dimensional Transition Metal Dichalcogenides via Vapour Deposition Techniques. *Chem Soc Rev* **2015**, *44* (9), 2744–2756. https://doi.org/10.1039/c4cs00256c.

(21) Lim, Y. R.; Han, J. K.; Yoon, Y.; Lee, J. B.; Jeon, C.; Choi, M.; Chang, H.; Park, N.; Kim, J. H.; Lee, Z.; Song, W.; Myung, S.; Lee, S. S.; An, K. S.; Ahn, J. H.; Lim, J. Atomic-Level Customization of 4 in. Transition Metal Dichalcogenide Multilayer Alloys for Industrial Applications. *Adv Mater* **2019**, *31* (29), 1–14. https://doi.org/10.1002/adma.201901405.

(22) Sohn, A.; Kim, C.; Jung, J. H.; Kim, J. H.; Byun, K. E.; Cho, Y.; Zhao, P.; Kim, S. W.; Seol, M.; Lee, Z.; Kim, S. W.; Shin, H. J. Precise Layer Control and Electronic State Modulation of a Transition Metal Dichalcogenide via Phase-Transition-Induced Growth. *Adv Mater* **2022**, *34* (48), 1–7. https://doi.org/10.1002/adma.202103286.

(23) Sirica, N.; Mo, S. K.; Bondino, F.; Pis, I.; Nappini, S.; Vilmercati, P.; Yi, J.; Gai, Z.; Snijders, P. C.; Das, P. K.; Vobornik, I.; Ghimire, N.; Koehler, M. R.; Li, L.; Sapkota, D.; Parker, D. S.; Mandrus, D. G.; Mannella, N. Electronic Structure of the Chiral Helimagnet and 3d -Intercalated Transition Metal Dichalcogenide C R1/3Nb S2. *Phys Rev B* **2016**, *94* (7), 1–19. https://doi.org/10.1103/PhysRevB.94.075141.

(24) Sasaki, M.; Ohnishi, A.; Kikuchi, T.; Kitaura, M.; Shimada, K.; Kim, H. J. Anomalous Transport Properties in Fe Intercalation Compound Fe x TiSe 2 Single Crystals. *J Low Temp Phys* **2010**, *161* (3–4), 375–386. https://doi.org/10.1007/s10909-010-0196-1.

(25) Norris, D. J.; Efros, A. L.; Erwin, S. C. Doped Nanocrystals. *Science* **2008**, *319* (5871), 1776–1779. https://doi.org/10.1126/science.1143802.

(26) Hamann, D. M.; Bardgett, D.; Cordova, D. L. M.; Maynard, L. A.; Hadland, E. C.; Lygo, A. C.; Wood, S. R.; Esters, M.; Johnson, D. C. Sub-Monolayer Accuracy in Determining the Number of Atoms per Unit Area in Ultrathin Films Using X-Ray Fluorescence. *Chem Mater* **2018**, *30*, 6209–6216. https://doi.org/10.1021/acs.chemmater.8b02591.

(27) Friend, R. H.; Yoffe, A. D. Electronic Properties of Intercalation Complexes of the Transition Metal Dichalcogenides. *Adv Phys* **1987**, *36* (1), 1–94. https://doi.org/10.1080/00018738700101951.

(28) Zhang, Q.; Mei, L.; Cao, X.; Tang, Y.; Zeng, Z. Intercalation and Exfoliation Chemistries of Transition Metal Dichalcogenides. *J Mater Chem A* **2020**, *8* (31), 15417–15444. https://doi.org/10.1039/d0ta03727c.

(29) Zhang, P.; Cheng, N.; Li, M.; Zhou, B.; Bian, C.; Wei, Y.; Wang, X.; Jiang, H.; Bao, L.; Lin, Y.; Hu, Z.; Du, Y.; Gong, Y. Transition-Metal Substitution-Induced Lattice Strain and Electrical Polarity Reversal in Monolayer WS2. *ACS Appl Mater Inter* **2020**, *12* (16), 18650–18659. https://doi.org/10.1021/acsami.9b22004.

(30) Tang, B.; Zhou, J.; Sun, P.; Wang, X.; Bai, L.; Dan, J.; Yang, J.; Zhou, K.; Zhao, X.; Pennycook, S. J.; Liu, Z. Phase-Controlled Synthesis of Monolayer Ternary Telluride with a Random Local Displacement of Tellurium Atoms. *Adv Mater* **2019**, *31* (23), 1–8. https://doi.org/10.1002/adma.201900862.

(31) Onofrio, N.; Guzman, D.; Strachan, A. Novel Doping Alternatives for Single-Layer Transition Metal Dichalcogenides. *J Appl Phys* **2017**, *122* (18). https://doi.org/10.1063/1.4994997.

(32) Yazdani, S.; Yarali, M.; Cha, J. J. Recent Progress on in Situ Characterizations of Electrochemically Intercalated Transition Metal Dichalcogenides. *Nano Res* **2019**, *12*, 2126–2139. https://doi.org/10.1007/s12274-019-2408-6.

(33) Sherokalova, E. M.; Pleschov, V. G.; Baranov, N. V.; Korolev, A. V. Magnetic Properties of Titanium Diselenide Intercalated with Gadolinium. *Phys Lett Sect A Gen At Solid State Phys* **2007**, *369* (3), 236–242. https://doi.org/10.1016/j.physleta.2007.04.084.

(34) Spiecker, E.; Schmid, A. K.; Minor, A. M.; Dahmen, U.; Hollensteiner, S.; Jäger, W. Self-Assembled Nanofold Network Formation on Layered Crystal Surfaces during Metal Intercalation. *Phys Rev Lett* **2006**, *96* (8), 3–6. https://doi.org/10.1103/PhysRevLett.96.086401.

(35) Miller, A. M.; Lemon, M.; Choffel, M. A.; Rich, S. R.; Harvel, F.; Johnson, D. C. Extracting Information from X-Ray Diffraction Patterns Containing Laue Oscillations. *Z Naturforsch B* **2022**, *77* (4–5), 313–322. https://doi.org/10.1515/znb-2022-0020.

(36) Lu, P.; Zhou, L.; Kramer, M. J.; Smith, D. J. Atomic-Scale Chemical Imaging and Quantification of Metallic Alloy Structures by Energy-Dispersive X-Ray Spectroscopy. *Sci Rep - UK* **2014**, *4*, 3945. https://doi.org/10.1038/srep03945.

(37) Smeller, M. Structural Studies of [(PbSe)0.99]m[WSe2]n, [(PbSe)1.00]m[MoSe2]n, and [(SnSe)1.03]m[MoSe2]n Misfit Layered Compounds, University of Oregon, 2011.

CHAPTER VIII

(1) *Materials Project*. https://materialsproject.org/ (accessed 2022-06-18).

(2) *The Open Quantum Materials Database*. https://oqmd.org/ (accessed 2022-06-18).

(3) *Novel Materials Discovery Centre of Excellence.* https://nomad-coe.eu/ (accessed 2022-06-18).

(4) *National Institute of Standards and Technology.* https://www.nist.gov/ (accessed 2022-06-18).

(5) *Inorganic Crystal Structure Database*. https://icsd.products.fiz-karlsruhe.de/ (accessed 2022-06-18).

(6) *Pauling File*. https://paulingfile.com/ (accessed 2022-06-18).

(7) Szczypiński, F. T.; Bennett, S.; Jelfs, K. E. Can We Predict Materials That Can Be Synthesized? *Chem. Sci. J.* **2021**, *12*. https://doi.org/10.1039/d0sc04321d.

(8) Butler, K. T.; Frost, J. M.; Skelton, J. M.; Svane, K. L.; Walsh, A. Computational Materials Design of Crystalline Solids †. *Chem. Soc. Rev.* **2016**, *45*, 6138. https://doi.org/10.1039/c5cs00841g.

(9) Therrien, F.; Jones, E. B.; Stevanović, V. Metastable Materials Discovery in the Age of Large-Scale Computation. *Appl. Phys. Rev*. **2021**, *8*(3), 1310. https://doi.org/10.1063/5.0049453.

(10) Chamorro, J. R.; Mcqueen, T. M. Progress toward Solid State Synthesis by Design. *Acc. Chem. Res.* **2018,** *51*, 11, 2918–2925. https://doi.org/10.1021/acs.accounts.8b00382.

(11) Blum, V.; Zunger, Prediction of Ordered Structures in the bcc Binary Systems of Mo, Nb, Ta, and W From First-Principles Search of Approximately 3,000,000 Possible Configurations. *Phys. Rev. B*. **2005**, *72*(2), 104. https://doi.org/10.1103/PhysRevB.72.020104.

(12) Wang, HC., Botti, S. & Marques, M.A.L. Predicting stable crystalline compounds using chemical similarity. *npj Comput Mater*. **2021**, *7***,** 12. https://doi.org/10.1038/s41524-020-00481-6.

(13) Pandey, S.; Qu, J.; Stevanović, V.; St. John, P.; Gorai, P. Predicting Energy and Stability of Known and Hypothetical Crystals Using Graph Neural Network. *Patterns.* **2021**, *2* (11). https://doi.org/10.1016/J.patter.2021.100361.

(14) Packwood, D. M. Exploring the Configuration Spaces of Surface Materials Using Time-Dependent Diffraction Patterns and Unsupervised Learning. *Sci. Rep*. **2020**, *10*, 5868 https://doi.org/10.1038/s41598-020-62782-6.

(15) Kim, Y. J.; Perepezko, J. H. Formation of a Metastable Ferromagnetic τ Phase during Containerless Melt Processing and Rapid Quenching in Mn-Al-C Alloys. *J. Appl. Phys.* **1992**, *71*, 676. https://doi.org/10.1063/1.351326.

(16) Golizadeh, M.; Mendez Martin, F.; Wurster, S.; Mogeritsch, J. P.; Kharicha, A.; Kolozsvári, S.; Mitterer, C.; Franz, R. Rapid Solidification and Metastable Phase Formation during Surface Modifications of Composite Al-Cr Cathodes Exposed to Cathodic Arc Plasma. *J. Mater. Sci. Technol.* **2021**, *94*, 147–163. https://doi.org/10.1016/J.JMST.2021.03.059.

(17) Vitta, S.; Greer, A. L.; Somekh, R. E. Metastable Phases Formed by Nanosecond Laser-Quenching of Metals and Binary Alloys. *Mater. Sci. Eng.* **1988.** *98*, 105-109. https://doi.org/10.1016/0025-5416(88)90136-X.

(18) Constantin, C.; Al-Brithen, H.; Haider, M. B.; Ingram, D.; Smith, A. R. ScGaN Alloy Growth By Molecular Beam Epitaxy: Evidence for a Metastable Layered Hexagonal Phase. *Phys. Rev. B*. **2004**. *70*(19), 3309. https://doi.org/10.1103/PhysRevB.70.193309.

(19) Pukite, P. R.; Harwit, A.; Iyer, S. S. Molecular Beam Epitaxy of Metastable, Diamond Structure Sn_xGe_{1-x} Alloys. *Appl. Phys. Let.* **1989**, *54*, 2142–2144. https://doi.org/10.1063/1.101152.

(20) Gibson, J. M. Metastable Phases and the Molecular Beam Epitaxy of Metal Silicides. *MRS. Proc*. **1988**; *104*. 613-616. https://doi.org/10.1557/proc-104-613.

(21) Narayan, A.; Bhutani, A.; Rubeck, S.; Eckstein, J. N.; Shoemaker, D. P.; Wagner, L. K. Computational and Experimental Investigation for New Transition Metal Selenides and Sulfides: The Importance of Experimental Verification for Stability. *Phys. Rev. B.* **2016**, *94*(4). https://doi.org/10.1103/PhysRevB.94.045105.

(22) Ying, T.; Chen, X.; Wang, G.; Jin, S.; Lai, X.; Zhou, T.; Zhang, H.; Shen, S.; Wang, W. Superconducting Phases in Potassium-Intercalated Iron Selenides. *J. Am. Chem. Soc.* **2013**, *135*(8), 2951-2954. https://doi.org/10.1021/ja312705x.

(23) Song, Y.; Chen, Z.; Zhang, Q.; Xu, H.; Lou, X.; Chen, X.; Xu, X.; Zhu, X.; Tao, R.; Yu, T.; Ru, H.; Wang, Y.; Zhang, T.; Guo, J.; Gu, L.; Xie, Y.; Peng, R.; Feng, D. High Temperature Superconductivity at FeSe/$LaFeO_3$ Interface. *Nat. Commun.* **2021**, *12*(1), 1–8. https://doi.org/10.1038/s41467-021-26201-2.

(24) Johnson, D. C. Controlled Synthesis of New Compounds Using Modulated Elemental Reactants. *Curr. Opin. Solid State Mater. Sci.* **1998**, *3*(2), 159–167. https://doi.org/10.1016/S1359-0286(98)80082-X.

(25) Hamann, D. M.; Bardgett, D.; Leo, D.; Cordova, M.; Maynard, L. A.; Hadland, E. C.; Lygo, A. C.; Wood, S. R.; Esters, M.; Johnson, D. C. Sub-Monolayer Accuracy in Determining the Number of Atoms per Unit Area in Ultrathin Films Using X-Ray Fluorescence. *Chem. Mater.* **2018**. *30*(18), 6209-6216. https://doi.org/10.1021/acs.chemmater.8b02591.

(26) Xu, M.; Yang, T.; Yu, W. X.; Yang, N.; Liu, C. X.; Mai, Z. H.; Lai, W. Y.; Tao, K. Accurate Determination of Film Thickness by Low-Angle X-Ray Reflection. *Chin. Phys. Lett.* **2000**, *9* (11), 833–836. https://doi.org/10.1088/1009-1963/9/11/007.

(27) Toby, B. H.; von Dreele, R. B. GSAS-II: The Genesis of a Modern Open-Source All Purpose Crystallography Software Package. *J. Appl. Crystallogr.* **2013**, *46* (2), 544–549. https://doi.org/10.1107/S0021889813003531.

(28) Bhardwaj, A.; Varadarajan, E.; Srivastava, P.; Sehgal, H. K. Structural, Optical and Electrical Properties of Chemically Grown $Pb_{1-x}Fe_xSe$ Nanoparticle Thin Films. *Solid State Commun.* **2008**, *146* (1–2), 53–56. https://doi.org/10.1016/j.ssc.2008.01.021.

(29) Quan, Z.; Wu. D.; Zhu, J.; Evers, W. H.; Boncella, J. M.; Siebbeles, L. D. A.; Wang, Z.; Navrotsky, A.; Xu, H. Energy Landscape of Self-Assembled Superlattices of PbSe Nanocrystals. *Proc. Natl. Acad. Sci.* **2014**, *111*(25). https://doi.org/10.1073/pnas.1408835111.

(30) Durandurdu, M. Fcc-to-Bct Phase Transformation of Aluminum under Triaxial Stresses: An Ab Initio Constant Pressure Study. *Eur. Phys. J. B* **2009**, *72*, 241–245. https://doi.org/10.1140/epjb/e2009-00342-9.

(31) Gao, Y.; Wang, Y. Hidden Pathway during Fcc to Bcc/Bct Transformations: Crystallographic Origin of Slip Martensite in Steels. *Physical Review Materials* **2018**, *2*, 93611. https://doi.org/10.1103/PhysRevMaterials.2.093611.

(32) Grant, P. M. Electronic Properties of Rocksalt Copper Monoxide: A Proxy Structure for High Temperature Superconductivity. *J. Phys. Conf. Ser.* **2008**, *129*. https://doi.org/10.1088/1742-6596/129/1/012042.

(33) Noda, Y.; Ohba, S.; Sato, S.; Saito, Y. Charge Distribution and Atomic Thermal Vibration in Lead Chalcogenide Crystals. *Acta. Cryst*. **1983**, *39*(B), 312-317. https://doi.org/10.1107/S0108768183002463.

(34) Koz, C.; Schmidt, M.; Borrmann, H.; Burkhardt, U.; Rößler, S.; Carrillo-Cabrera, W.; Schnelle, W.; Schwarz, U.; Grin, Y. Synthesis and Crystal Growth of Tetragonal β-$Fe_{1.00}Se$. *Z. Anorg. Allg. Chem.* **2014**, *640*(8–9), 1600–1606. https://doi.org/10.1002/zaac.201300670.

CHAPTER IX

[1] Huang, B.; McGuire, M. A.; May, A.F.; Xiao, D.; Jarillo-Herrero, P.; Xu, X. Emergent phenomena and proximity effects in two-dimensional magnets and heterostructures. *Nat. Mater.* **2020**, 19, 1276–1289.

[2] Bao, C.; Tang, P.; Sun, D; & Zhou, S. Light-induced emergent phenomena in 2D materials and topological materials. *Nat. Rev. Phys.* **2022***,* 4, 33–48.

[3] Tan, J.; Li, S; Liu, B.; & Cheng, H.-M. Structure, Preparation, and Applications of 2D Material-Based Metal–Semiconductor Heterostructures. *Small Struct.* **2021,** 2, 2000093.

[4] Wang, H.; Liu, F.; Fu, W.; Fang, Z.; Zhou, W.; Liu, Z. Two-dimensional heterostructures: Fabrication, characterization, and application. **2014**, 6, 12250–12272.

[5] Chiu, K. C.; Zhang, X. Q.; Liu, X. Menon,; V. M. Chen, Y.F. Wu, J. M. Lee, Y. H. Synthesis and Application of Monolayer Semiconductors. *IEEE J. Quantum Electron.* **2015,** 51,

[6] Y. Gao, J. Ding. *Synthesis of heterostructures based on two-dimensional materials*. *Synthesis, Modelling and Characterization of 2D Materials and their Heterostructures, vol. 2* (Eds.: D. Datta, J. Ding, G. Hader, E-H Yang), Elsevier. 2020.

[7] Rouxel, J., Meerschaut, A. & Wiegers, G. A. Chalcogenide misfit layer compounds. *J Alloys Compd*. 229, 144–157.

[8] Ng, N. & McQueen, T. M. Misfit layered compounds: Unique, tunable heterostructured materials with untapped properties. *APL. Mater.* **2022**, 10.

[9] Wiegers, G. A. Misfit layer compounds: Structures and physical properties. *Prog. Solid State.* **1996**, ch. 24, 1–139.

[10] Esters, M., Hennig, R. G. & Johnson, D. C. Insights into the Charge-Transfer Stabilization of Heterostructure Components with Unstable Bulk Analogs. *Chem. Mater.* **2018**, 30, 4738–4747.

[11] Clarke, S. M. & Freedman, D. E. $(BiSe)_{1.23}CrSe_2$ and $(BiSe)_{1.22}(Cr_{1.2}Se_2)_2$: Magnetic anisotropy in the first structurally characterized Bi-Se-Cr ternary compounds. *Inorg. Chem.* **2015**. 54, 2765–2771.

[12] Hamann, D. M. Rudin, S. P. Asaba, T. Ronning, F. Cordova, D. L. M. Lu, P. Johnson, D. C. Predicting and synthesizing interface stabilized 2D layers. *Chem. Mater.* **2021**, 33, 5076–5084.

[13] Rudin, S. P. A Density Functional Theory Calculations-Based Approach that Predicts Layered Materials with Emergent Structures. *arXiv:1611.07510.* **2016**, 1–12.

[14] Harvel, F.; Lemon, M.; Gannon, R. N.; Bardgett, D.; Humphrey, M.; Johnson, D.C. Investigation of the Pb-Fe-Se Ternary System and the Synthesis of a Ternary $Pb_{1-x}Fe_xSe$ Phase. *Chem. Mater.* **2022**, 34, 6339–6344.

[15] Lu, P., Zhou, L., Kramer, M. J. & Smith, D. J. *Sci. Rep. – UK.* **2014**, 4, 1–5.

[16] Anderson, M.D; Heideman, C. L.; Lin, Q.; Smeller, M.; Kokenyesi, R.; Herzing, A. A.; Anderson, I. M.; Keszler, D. A.; Zschack, P.; Johnson, D. C. *Angew. Chem. Int. Edit.* **2013**. 52, 1982–1985.

[17] Falmbigl, M.; Putzky, D.; Ditto, J.; Esters, M.; Bauers, S.; Ronning, F.; D. C. Johnson. *ACS Nano.* **2015**, 9, 8440–8448.

[18] Smller, M. Structural Studies of $[(PbSe)_{0.99}]_m[WSe_2]_n$, $[(PbSe)_{1.00}]_m[MoSe_2]_n$, and $[(SnSe)_{1.03}]_m[MoSe_2]_n$ Misfit Layered Compounds. *Dissertation, University of Oregon*. **2011**.

[19] Noda, Y.; Ohba, S.; Sato, S. & Saito, Y. *Acta Crystallogr. Section B.* **1983,** 39, 312–317.

[20] Kumar, R. S.; Zhang, Y.; Sinogeikin, S.; Xiao, Y.; Kumar, S.; Chow, P.; Cornelius, A. L.; Chen, C. *J. Phys. Chem.* **2010**, 114, 12597–12606.

[21] Lavina, B.; Downs, R. T. Sinogeikin, S.; *Crystals.* **2018**, 8.

[22] Rei, R. P.; Owen, A.; Williams, G. I. *ARER.* **1936***,* 49, 1053.

[23] Noda, Y.; Masumoto K.; Ohba, S.; Saito, Y.; Toriumi, K.; Iwata, W Y.; Shibuya, I. *Acta. Crystallogr.* **1987**. *C* 43, 1443–1445.

[24] Mariano, A. N.; Chopra, K. L. *Appl. Phys. Lett.* **1967**, 10, 282–284.

[25] Knight, K. S.; Gibbs, A. S.; Bull, C. L.; Powell, A. V.; Funnell, N. P.; Ridley, C. J. *Mater. Adv.* **2022**, 3, 2077.

[26] Hamann, D. M.; Bardgett, D.; Cordova, D. L. M.; Maynard, L. A.; Hadland, E. C.; Lygo, A. C.; Wood, S. R.; Esters, M.; Johnson, D. C. *Chem. Mater.* **2018**, 30, 6209–6216.

[27] Huang, T. C.; Gilles, R.; Will, G. *Thin Solid Films.* **1993**, 230, 99–101.

[28] Toby, B. H.; Von Dreele, R. B. *J. Appl. Crystallogr.* **2013**. 46, 544–549.

CHAPTER X

(1) Cordova, D. L. M.; Johnson, D. C. Synthesis of Metastable Inorganic Solids with Extended Structures. *ChemPhysChem* **2020**, *21* (13), 1345–1368. https://doi.org/10.1002/cphc.202000199.

(2) Sun, W.; Dacek, S. T.; Ong, S. P.; Hautier, G.; Jain, A.; Richards, W. D.; Gamst, A. C.; Persson, K. A.; Ceder, G. The Thermodynamic Scale of Inorganic Crystalline Metastability. *Sci Adv* **2016**, *2*, e1600225. https://doi.org/10.1126/sciadv.1600225.

(3) Stein, A.; Keller, S. W.; Mallouk, T. E. Turning Down the Heat: Design and Mechanism in Solid-State Synthesis. *Science* **1993**, *259* (9), 1558–1564.

(4) Cho, A. Y.; Arthur, J. R. Molecular Beam Epitaxy. *Prog Solid State Ch* **1975**, *10* (PART 3), 157–191. https://doi.org/10.1016/0079-6786(75)90005-9.

(5) Gupta, A. Thin Film Synthesis of Metastable and Artificially Structured Oxides. *Curr Opin Solid State Mater Sci* **1997**, *2*, 23–31. https://doi.org/10.1016/S1359-0286(97)80101-5.

(6) Farrow, R. F. C. Stabilization of Metastable Phases By Epitaxy. *J Vac Sci Technol B Microelectron Nanom Struct* **1982**, *1* (2), 222–228. https://doi.org/10.1116/1.582491.

(7) Narayan, A.; Bhutani, A.; Rubeck, S.; Eckstein, J. N.; Shoemaker, D. P.; Wagner, L. K. Computational and Experimental Investigation for New Transition Metal Selenides and Sulfides: The Importance of Experimental Verification for Stability. *Phys Rev B* **2016**, *94* (4), 1–15. https://doi.org/10.1103/PhysRevB.94.045105.

(8) Schön, J. C. Nanomaterials - What Energy Landscapes Can Tell Us. *Process Appl Ceram* **2015**, *9* (3), 157–168. https://doi.org/10.2298/PAC1503157S.

(9) Neilson, J. R.; McDermott, M. J.; Persson, K. A. Modernist Materials Synthesis: Finding Thermodynamic Shortcuts with Hyperdimensional Chemistry. *J Mater Res* **2023**, *38*, 2885–2893. https://doi.org/10.1557/s43578-023-01037-2.

(10) Bardgett, D.; Gannon, R. N.; Hamann, D. M.; Roberts, D. M.; Bauers, S. R.; Lu, P.; Johnson, D. C. Understanding the Reactions between Fe and Se Binary Diffusion Couples. *Chem Mater* **2021**, *33* (7), 2585–2592. https://doi.org/10.1021/acs.chemmater.1c00303.

(11) Gannon, R. N.; Choffel, M. M.; Blackwood, H. R.; Wolff, N.; Lotnyk, A.; Kienle, L.; Johnson, D. C. Growth of Crystallographically Aligned PbSe Films of Controlled Thickness on Amorphous Substrates. *Z Anorg Allg Chem* **2022**, *648* (15), e202200015. https://doi.org/10.1002/zaac.202200015.

(12) Choffel, M. A.; Hamann, D. M.; Joke, J. A.; Cordova, D. L. M.; Johnson, D. C. The Reaction between Mn and Se Layers. *Z Anorg Allg Chem* **2018**, *644* (24), 1875–1880. https://doi.org/10.1002/zaac.201800378.

(13) Overbay, M.; Novet, T.; Johnson, D. C. The Low Temperature Synthesis of Vanadium Selenides Using Superlattice Reactants. *J Solid State Chem* **1996**, *123* (2), 337–343. https://doi.org/10.1006/jssc.1996.0189.

(14) Harvel, F.; Lemon, M.; Gannon, R. N.; Bardgett, D.; Humphrey, M.; Johnson, D. C. Investigation of the Pb-Fe-Se Ternary System and the Synthesis of a Ternary Pb1- XFe XSe Phase. *Chem Mater* **2022**, *34* (14), 6339–6344. https://doi.org/10.1021/acs.chemmater.2c00799.

(15) Lemon, M.; Harvel, F. G.; Gannon, R. N.; Lu, P.; Rudin, S. P.; Johnson, D. C. Targeted Synthesis of Predicted Metastable Compounds Using Modulated Elemental Reactants. *J Vac Sci Technol A* **2023**, *41* (2), 022203. https://doi.org/10.1116/6.0002260.

(16) Cordova, D. L. M.; Kam, T. M.; Fender, S. S.; Tsai, Y. H.; Johnson, D. C. Strong Non-Epitaxial Interactions: Crystallographically Aligned PbSe on VSe2. *Phys Status Solidi A* **2019**, *216* (15), 1–7. https://doi.org/10.1002/pssa.201800896.

(17) Cordova, D. L. M.; Fender, S. S.; Kam, T. M.; Seyd, J.; Albrecht, M.; Lu, P.; Fischer, R.; Johnson, D. C. Designed Synthesis and Structure-Property Relationships of Kinetically Stable [(PbSe)1+d]m(VSe2)1 (m = 1, 2, 3, 4) Heterostructures. *Chem Mater* **2019**, *31* (20), 8473–8483. https://doi.org/10.1021/acs.chemmater.9b02826.

(18) Hite, O. K.; Falmbigl, M.; Alemayehu, M. B.; Esters, M.; Wood, S. R.; Johnson, D. C. Charge Density Wave Transition in (PbSe)1+δ(VSe2)n Compounds with n = 1, 2, and 3. *Chem Mater* **2017**, *29*, 5646–5653. https://doi.org/10.1021/acs.chemmater.7b01383.

(19) Lemon, M.; Gannon, R. N.; Lu, P.; Battey, S. R.; Rudin, S. P.; Toby, B. H.; Johnson, D. C. Method to Determine the Distribution of Substituted or Intercalated Ions in Transition-Metal Dichalcogenides: Fe. *Chem Mater* **2022**, *34* (19), 8528–8535. https://doi.org/10.1021/acs.chemmater.2c00431.

(20) Hamann, D. M.; Rudin, S. P.; Asaba, T.; Ronning, F.; Cordova, D. L. M.; Lu, P.; Johnson, D. C. Predicting and Synthesizing Interface Stabilized 2D Layers. *Chem Mater* **2021**, *33* (13), 5076–5084. https://doi.org/10.1021/acs.chemmater.1c01064.

(21) Hamann, D. M.; Bardgett, D.; Cordova, D. L. M.; Maynard, L. A.; Hadland, E. C.; Lygo, A. C.; Wood, S. R.; Esters, M.; Johnson, D. C. Sub-Monolayer Accuracy in Determining the Number of Atoms per Unit Area in Ultrathin Films Using X-Ray Fluorescence. *Chem Mater* **2018**, *30*, 6209–6216. https://doi.org/10.1021/acs.chemmater.8b02591.

(22) Miller, A. M.; Lemon, M.; Choffel, M. A.; Rich, S. R.; Harvel, F.; Johnson, D. C. Extracting Information from X-Ray Diffraction Patterns Containing Laue Oscillations. *Z Naturforsch B* **2022**, *77* (4–5), 313–322. https://doi.org/10.1515/znb-2022-0020.

(23) Cordova, D. L. M.; Fender, S. S.; Hooshmand, M. S.; Buchanan, M. R.; Davis, J.; Kam, T. M.; Gannon, R. N.; Fischer, R.; Lu, P.; Hanken, B. E.; Asta, M.; Johnson, D. C. The Instability of Monolayer-Thick PbSe on VSe2. *Chem Mater* **2020**, *32* (18), 7992–8003. https://doi.org/10.1021/acs.chemmater.0c02922.

(24) Kiyosawa, T.; Takahashi, S.; Koguchi, N. Partial Phase Diagram of New Quarternary Semiconductor Pb1- XMnxS1- YSeyfor Mid-Infrared Lasers. *J Mater Sci* **1992**, *27* (19), 5303–5305. https://doi.org/10.1007/BF02403834.

APPENDIX B

(1) Blöchl, P. E. Projector Augmented-Wave Method. *Phys. Rev. B* **1994**, *50*, 17953–17979.

(2) Kresse, G.; Joubert, D. From Ultrasoft Pseudopotentials to the Projector Augmented-Wave Method. *Phys. Rev. B* **1999**, *59*, 1758–1775.

(3) Kresse, G.; Furthmüller, J. Efficient Iterative Schemes for *Ab Initio* Total-Energy Calculations Using a Plane-Wave Basis Set. *Phys. Rev. B* **1996**, *54*, 11169–11186.

(4) Coelho, P. M.; Nguyen Cong, K.; Bonilla, M.; Kolekar, S.; Phan, M.-H.; Avila, J.; Asensio, M. C.; Oleynik, I. I.; Batzill, M. Charge Density Wave State Suppresses Ferromagnetic Ordering in VSe_2 Monolayers. *J. Phys. Chem. C* **2019**, *123*, 14089–14096.

(5) Yi, M.; Wu, J.; Zheng, X.; Ming, X. Structural Transition from Marcasite to Pyrite Phase in $FeSe_2$ under High Pressure: A First-Principles Study. *Eur. Phys. J. B* **2020**, *93*, 179.

(6) Bianco, R.; Calandra, M.; Mauri, F. Electronic and Vibrational Properties of $TiSe_2$ in the Charge-Density-Wave Phase from First Principles. *Phys. Rev. B* **2015**, *92*, 094107.

(7) Perdew, J. P.; Burke, K.; Ernzerhof, M. Generalized Gradient Approximation Made Simple. *Phys. Rev. Lett.* **1996**, *77*, 3865–3868.

(8) Blöchl, P. E.; Jepsen, O.; Andersen, O. K. Improved Tetrahedron Method for Brillouin-Zone Integrations. *Phys. Rev. B* **1994**, *49*, 16223–16233.

(9) Grimme, S. Semiempirical GGA-type density functional constructed with a long-range dispersion correction, *J. Comp. Chem*, **2006**, *27*, 1787-1799.

APPENDIX D

1. Noda, Y.; Ohba, S.; Sato, S.; Saito, Y. Charge Distribution and Atomic Thermal Vibration in Lead Chalcogenide Crystals. *Acta. Cryst*. **1983**, *39*(B), 312-317. https://doi.org/10.1107/S0108768183002463.

2. Keller, R.; Holzapfel, W. B.; Schulz, H. Effect of Pressnre on the Atom Positions in Se and Te. *Phys. Rev. B*. **1977,** *16*(10), 4404-4412. https://doi.org/10.1103/PhysRevB.16.4404.

3. Narayan, A.; Bhutani, A.; Rubeck, S.; Eckstein, J. N.; Shoemaker, D. P.; Wagner, L. K. Computational and Experimental Investigation for New Transition Metal Selenides and Sulfides: The Importance of Experimental Verification for Stability. *Phys. Rev. B.* **2016**, *94*(4). https://doi.org/10.1103/PhysRevB.94.045105.

4. Lavina, B., Downs, R. T. & Sinogeikin, S. The structure of ferroselite, $FeSe_2$, at pressures up to 46 GPa and temperatures down to 50 K: A single-crystal micro-diffraction analysis. *Crystals.* **2018**, *8*(7)*,* 289. https://doi.org/10.3390/cryst8070289.

5. Koz, C.; Schmidt, M.; Borrmann, H.; Burkhardt, U.; Rößler, S.; Carrillo-Cabrera, W.; Schnelle, W.; Schwarz, U.; Grin, Y. Synthesis and Crystal Growth of Tetragonal β-$Fe_{1.00}Se$. *Z. Anorg. Allg. Chem.* **2014**, *640* (8–9), 1600–1606. https://doi.org/10.1002/zaac.201300670.